REPORT DOCUMENTATION PAGE

Form Approved
OMB No. 0704-0188

1. AGENCY USE ONLY (Leave Blank)	2. REPORT DATE 1995	3. REPORT TYPE AND DATES COVERED Final

4. TITLE AND SUBTITLE
Particle Dispersion and Inter-Phase Kinetic Energy Transfer in a Turbulent, Two-Phase Shear Layer

5. FUNDING NUMBERS

6. AUTHORS
Kenneth T. Kiger

7. PERFORMING ORGANIZATION NAME(S) AND ADDRESS(ES)
University of California, San Diego

PERFORMING ORGANIZATION

AFRL-SR-BL-TR-98-

0023

9. SPONSORING/MONITORING AGENCY NAME(S) AND ADDRESS(ES)
AFOSR/NI
110 Duncan Avenue, Room B-115
Bolling Air Force Base, DC 20332-8080

11. SUPPLEMENTARY NOTES

12a. DISTRIBUTION AVAILABILITY STATEMENT
Approved for Public Release

12b. DISTRIBUTION CODE

13. ABSTRACT *(Maximum 200 words)*
See attached.

19980115 222

14. SUBJECT TERMS			15. NUMBER OF PAGES
			16. PRICE CODE

17. SECURITY CLASSIFICATION OF REPORT	18. SECURITY CLASSIFICATION OF THIS PAGE	19. SECURITY CLASSIFICATION OF ABSTRACT	20. LIMITATION OF ABSTRACT
Unclassified	Unclassified	Unclassified	UL

UNIVERSITY OF CALIFORNIA, SAN DIEGO

PARTICLE DISPERSION AND INTER-PHASE KINETIC ENERGY TRANSFER IN A TURBULENT, TWO-PHASE SHEAR LAYER

A dissertation submitted in partial satisfaction of the

requirements for the degree Doctor of Philosophy

in Engineering Sciences (Mechanical Engineering)

by

Kenneth T. Kiger

Committee in charge:

Professor Juan C. Lasheras, Chairperson
Professor Laurence Armi
Professor Charles Van Atta
Professor Said Elghobashi
Professor Eckart Meiburg
Professor Sutanu Sarkar
Professor Forman A. Williams

1995

The dissertation of Kenneth Kiger is approved, and
it is acceptable in quality and form for publication on
microfilm:

_____

_____

_____

_____

_____

_____

_____ Chair

University of California, San Diego

1995

TABLE OF CONTENTS

LIST OF TABLES

LIST OF FIGURES

Acknowledgment

I would like to acknowledge the support and encouragement that my parents gave me while I was growing up and throughout my academic career. Without their patience for my endless questions, tinkering with household appliances, and the countless Lego sets, I would probably not have had the inclination to pursure a career in engineering and science. They have done a remarkable job in providing me with unhindered opportunities to grow and explore the world around us, and I can only hope to repay them by someday providing those same opportunities to others. I am also indebted to the rest of my family - my sisters Kris[1] and Amy, my grandparents Dorothy, Eleanor and Leonard, my late grandfather Tom, my in-laws Jane and Ed Davis, and my Aunts, Uncles, and Cousins who all took an interest and concern in my academic pursuits.

I also wish to thank my wife, Sarah, for her unwavering dedication and support since we first met in England one autumn long ago. Her smile, laughter, and reassurance have been a source of inspiration at times when my confidence and spirits were flagging. Her companionship has provided me with years of happiness and has helped me to keep a balanced life between the sometimes conflicting demands of graduate research and a fulfilling personal life interacting with the rest of humanity.

This dissertation would not be complete without a tremendous acknowledgement to my advisor and friend, Juan Lasheras. His concern for his students, both in their academic/professional progress and personal well-being, has made for a very gratifying experience at UCSD. His consummate ability as an advisor provided me with the right amount of support to maintain steady progress when I needed it without stifling the development of independent growth and creativity. As a friend, he is always there to listen and to share his personal experiences. I am very grateful for all of the opportunities, educational and otherwise, that he has provided. I would also like to thank all of the AMES faculty at

---

[1]Thanks go to Kris for her suggested utilization of the under-employed oompa-loompa workforce and for pointing out the concerns and effects of sneezes on an open-section wind tunnel.

UCSD that made for such an intellectually stimulating graduate program. In particular, I found the discussions and coursework with professors Forman A. Williams, Chuck van Atta, Sutanu Sarkar, Larry Armi (of Scripps Institute of Oceanography), Costas Pozrikidis, and Daniel B. Olfe have provided me with a comprehensive overview and insight into the many wonders of fluid mechanics.

This dissertation also owes a debt to the hard work of professor Benigno J. Lázaro and his original intellectual contribution in the field of turbulent two-phase flows. His efforts have provided a lucid vantage point and framework from which the conception and timely completion of this dissertation has hinged.

Finally, I would like to acknowledge all of the many friends I have made through the years in the lab and at UCSD for their support, discussion and companionship which makes for such enjoyable working conditions. Thanks should be made explicitly to: Paul M. Rightley for his advice, discussion (which was invaluable during the gestation and clairi-fication of many of the ideas within this thesis), and unique sense of humor which I looked forward to sparring with every day; his wife, Maria L. J. Rightley, for keeping Paul in line and for her kind advice; Eugene Pawlak, for his friendship, comradarie, surfing lessons, and for providing me with the enlightenment as to the importance and meaning of the Pawlak number; Professor Sigidur Thordensen and Dr. Dave Showalter for showing me the ropes around the lab and making my adjustment to graduate school a pleasant experience; Francis D. Petach, for his technical advice around the lab and the good lunchtime discussions; as well as Dr. Antonio Sanchez, Kurt Keller, Kathy Prestridge, Carlos Martinez, Brent Wilt-shire and all of my other classmates. I will complete my tenure at UCSD feeling as though I have extended my family, and I look foward to keeping these relationships throughout my career and into the distant future.

VITA

1991	B.S., Aerospace Engineering University of Southern California
1993	Teaching Assistant, Department of Applied Mechanics and Engineering Science, University of California, San Diego
1993	M.S. Engineering Science (Aerospace) University of California, San Diego
1991–1995	Research Assistant, University of California, San Diego
1995	Doctor of Philosophy University of California, San Diego

PUBLICATIONS

"Effect of Vortex Pairing on Particle Dispersion and Kinetic Energy Transfer in a Two-Phase Turbulent Shear Layer." Journal of Fluid Mechanics, In Press.

"Vortex Pairing and Droplet Dispersion in a Turbulent Free Shear Layer." 25th International Symposium on Combustion, The Combustion Institute, Pittsburgh, PA, pp. 407–412, 1994.

"Conditional-averaged Droplet Size Number Frequency Evolution During Vortex Pairing in a Two-Phase, Turbulent Free Shear Flow." ICLASS 94, Bergell House Inc., New York, Yule and Dumouchel, eds. pp. 126–133, 1994.

FIELDS OF STUDY

Major Field: Engineering

Studies in Fluid Mechanics.
Professors Juan Lasheras, Dan Olfe, and Charles Van Atta

Studies in Thermodynamics and Gas Dynamics.
Professors Juan Lasheras and Forman Williams

Studies in Numerical Methods.
Professors Constantine Pozrikidis and Sutanu Sarkar

Studies in Applied Mathematics.
Professors Forman A. Williams and Jeffery Rabin

ABSTRACT OF THE DISSERTATION

Particle Dispersion and Inter-Phase Kinetic

Energy Transfer in a Turbulent,

Two-Phase Shear Layer

by

Kenneth T. Kiger

Doctor of Philosophy in Engineering Sciences (Mechanical Engineering)

University of California, San Diego, 1995

Professor Juan C. Lasheras, Chair

The transport of heavy, polydispersed particles and the inter-phase transfer of kinetic energy is measured experimentally in a turbulent shear layer. Specifically, fundamental/subharmonic forcing and conditional-averaging techniques were used to study the particle/turbulence interaction with the large-scale, spanwise, coherent vortices, starting from their initial roll-up through the first pairing event. It is shown that the pairing event plays a homogenizing role on the particulate field, but the amount of homogenization is strongly dependent upon the particle's viscous relaxation time, the eddy turnover time, as well as the time the particles are allowed to interact with each scale prior to a pairing event. Thus, even though the smaller size particles become well-mixed across the structure, the larger sizes are still dispersed in an inhomogeneous fashion. The dispersed/carrier phase coupling was examined through the measurement of conditionally-averaged kinetic energy transfer (which results from the work done to accelerate or decelerate the dispersed phase), as well as the conditionally-averaged particle dissipation (energy dissipated by shear deformation in the carrier phase due to the relative slip between the particles and the carrier fluid). It

is found that the kinetic energy transfer between the phases occurs inhomogeneously with energy being exchanged predominantly in a sublayer just outside the region of maximum turbulence intensity. The kinetic energy transfer is shown to exhibit notable positive and negative peaks beneath the cores and stagnation points of the large-scale eddy field, and these peaks are shown to result from the irrotational velocity perturbations created by the vortices. The particle dissipation is also found to be localized in the same regions of prominent kinetic energy transfer, but shifted slightly towards the center of the mixing region owing to its dependence on the square of the slip velocity. The magnitude of the particle dissipation is typically around 10% of the kinetic energy transfer levels and about 1% of the estimated turbulent dissipation of the base flow. These energy exchange mechanisms remain a prominent process as long as the Stokes number of the particles relative to the large-scales is of order unity.

Chapter 1

General Introduction

It is the goal of this work to characterize the dispersion and interaction of heavy particulates within a turbulent free shear layer. Specifically, this work focuses on the role of the vortex pairing process and the kinetic energy transfer between the dispersed phase and the continuous carrier flow.

Dispersed particulate flows are a special case of the more generalized field of multi-phase flow. These systems are characterized by the presence of sharp interfacial boundaries which separate two or more immiscible liquids or different states of matter (gas, liquid, solid, or plasma). Each phase itself is typically governed by its own single-phase continuum equations which describe the conservation of mass, momentum, and energy within the region bounded by the interface. A *dispersed* multi-phase flow is defined as a system in which one of the phases is not spatially contiguous, but is separated into many discrete parcels of material and is completely bounded by the other (continuous) phase or a solid boundary.

There are many practical applications for which an understanding of turbulent, dispersed, multi-phase flow is essential to improvement of engineering design and prognostication. Among the many examples are liquid and solid fuel dispersal in combustion processes, sediment transport, cloud physics, particle separators and pollutant scrubbers. Design and prediction of these processes requires that certain aspects regarding the state of the system can be determined. In the most direct method, this could be obtained by solving the single-phase conservation equations that are applicable within the domain of the specific phase and using interfacial conservation relations (also known as jump conditions)

1

to couple the phases, thus providing a complete solution for the system. This, in fact, turns out to be very impractical (if not impossible) for general multi-phase flow problems as the interface is a dynamic discontinuous feature of the flow field. Tracking such a singularity and ensuring the proper conservation across its boundary is a difficult problem, and currently works well for only a few simplified problems (such as flow around isolated droplets or flow over a smooth, laminar interface).

It is clear then, that an alternative multi-phase flow description is required if many of the important problems are to be solved. Although the complete instantaneous solution is helpful to understanding the physics of the interaction, it is not always necessary for the design of engineering devices. For someone concerned with the pressure drop or heat transfer rate along a pipe carrying a two-phase system, knowing the instantaneous velocity at every location is far more information than is needed to size the pipe and select the proper material. In many of these cases, it is sufficient to obtain a statistical description of the system which would specify the mean and fluctuating intensity of quantities such as the velocity, concentration, temperature, pressure, etc. This has prompted the development of averaging techniques which simplify the flow description by making temporal, spatial, or ensemble averages across the interfacial boundaries, giving a set of macroscopic averaged conservation equations (Ishii, 1975; Soo, 1967; Delhaye et al., 1981). Averaging across the interface removes the distinct identities of the phases and results in a description which is equivalent to two (or more) inter-penetrating and co-existing fluids. The averaging necessarily results in a loss of the microscopic information within the flow field and thus presents a closure problem whereby the details of the interfacial exchanges must now be described in terms of the macroscopic averaged variables. Formulation of the constitutive closure relations are usually completed through judicious postulation, subject to experimental validation and the constraints of guiding principles such as the second law of thermodynamics and frame indifference (Drew, 1983). This is by far the most serious difficulty in utilizing the two-fluid formulation as the models tend to depend heavily on an *a priori* knowledge of the typical interface geometry and there is also great difficulty ensuring that the models are complete. Nevertheless, this type of description has proved itself useful in several applications, namely bubbly pipe flow and other aspects important to the nuclear power industry. Thus, although

this approach has to contend with the complex difficulties of describing the closure relations before it can be considered complete, it does show promise as an engineering tool and has the benefit of a rigorous mathematical formulation from first principles. It is the intent of this work to provide a set of data with which future models can be verified, in addition to providing insight into mechanisms which result from the interfacial transfer in order to improve upon current models.

If the turbulent two-phase flow problem is restricted to the case of a very dilute, dispersed second phase, then Lagrangian particle tracking methods can be used as an alternative to the two-fluid model. In this method, the equation of motion for a single particle is solved directly for every particle in the system (Martin and Meiburg, 1994; Elghobashi and Truesdell, 1993; Wang and Maxey, 1993b), or solved as a statistically averaged equation representative of many particles (Lu et al., 1993). Due to its simplicity, this method has been used extensively in many numerical simulations of various turbulent flows, and has even allowed for an analytical statistical treatment of certain special cases (Hinze, 1972). This has shed some light into the possible form of spectra and correlations for both the particles and continuous fluid, and has been the formulation primarily used to study particle/turbulence interaction. The most significant drawbacks to this approach are the restrictions and uncertainties imposed by the equation describing the motion of the particle. Currently, this equation is only valid for an isolated particle in uniform shear, which implies that the particles must be smaller than the smallest flow scale and that the inter-particle spacing must be much greater than the particle's diameter. In addition to this, there is also a significant amount of debate as to the proper form for the expression of the lift force acting on the particulates, due to the poor agreement observed between predictions and experimental observation.

In contrast to the two-fluid model, the effects of two-way inter-phase coupling are often implemented by including a momentum source term in the continuous phase momentum equation. The momentum source is usually postulated to have a form similar to the forcing term acting on the particle and is averaged over some discrete volume or represented as singular point sources (Maxey et al., 1994). The lack of rigorous coupling formulation has been a critique for this method in addition to the severe restrictions imposed

4

by the particulate momentum equation. Nevertheless, the method is useful when used within the regimes for which it is applicable due to the fact that the interaction terms are unambiguous and straightforward to interpret. It is within the limits of this conceptual framework that the results of this analysis will be examined. This will hopefully allow for the clearest insight into the physical mechanisms of the interaction (as compared to the tenuous models used for the two-fluid closure relations).

In addition to the problems associated with describing interfacial transport, most two-phase flow applications are also faced with the difficulty that at least one of the phases is dominated by turbulent fluctuations. The work of this thesis is focused upon the interaction and dispersion of particulates in a specific category of prototypical turbulent flows, namely that of the turbulent free shear layer. This classification of flow is an important key to understanding many fundamental questions of turbulence in addition to having many applications in industry and nature. They are also good candidates for dispersed two-phase flow studies due to the fact that they are extensively studied as a single-phase flow, and can be manipulated by controlled perturbations to isolate specific large-scale turbulent mechanisms in the near field of the mixing layer.

This type of flow is formed by allowing two uniform streams of different velocities to mix together, such as whenever flow separates from a sharp corner or in two-layer exchange flows. Without any turbulent fluctuations, the two streams try to equilibrate with one another and exchange momentum through steady viscous diffusion. In practice, however, this is an unstable situation which rapidly transitions to the formation of two-dimensional spanwise vortices whose initial size and spacing is on the order of the mixing layer thickness (Winant and Browand, 1974; Brown and Roshko, 1974). As the development continues, additional instabilities manifest themselves and result in a dynamical evolution towards a self-similar turbulent state. One of the most important of these events is vortex pairing, whereby neighboring large-scale vortices begin to orbit around one another due to their mutual induction and amalgamate to form a larger structure twice the size and spacing of the original vortices (Winant and Browand, 1974). This pairing event is responsible for the linear growth rate of the shear layer (as opposed to the $x^{1/2}$ growth rate for the laminar case), and controls the bulk entrainment and transport processes. Other

mechanisms result in the amplification of streamwise vorticity embedded in the high-strain region between neighboring vortices (Corcos and Lin, 1984; Lasheras and Maxworthy, 1987; Lasheras and Choi, 1988), which stems from a convective diffusive balance and vorticity amplification within the imposed strain field. This initiates the three-dimensional cascade to a fully-developed, turbulent field, and creates a small-scale structure that becomes very effective in aiding the molecular mixing of the constituents from either stream within the shear layer. The small scales mainly contribute to the viscous dissipation of the flow kinetic energy and contribute very little to the overall turbulent transport. Thus, from a bulk mixing perspective, understanding the role of the large-scales and their pairing event is a fundamental first step to understanding how the particulates are dispersed in the fully developed turbulent flow. Within this thesis, experimental techniques which utilize forcing and conditional sampling are used which allow for a detailed structural view of the large-scale interaction between the phases and provides many insights into the physical mechanisms involved. While it is true that this approach neglects the important two-way coupling effects closely linked to the smallest scales, the dispersed phase concentrations are limited to sufficiently dilute levels to prevent this from being a problem, while at the same time giving an indication of where and how these effects may become important within the larger scales at larger concentrations.

Chapter 2

Formulation of Dilute Two-Phase Flow

The description of two-phase flows is typically approached from two different perspectives. The first and more general method utilizes averaging procedures to generate a set of averaged conservation equations in which none of the information of the instantaneous, local flow is retained. As pointed out in Chapter 1, this greatly simplifies the description of the flow but is incomplete in the sense that constitutive relations linking the averaged variables to the local fluctuations must be modeled to make any progress. The second method, and the one adopted in this chapter, starts with a Lagrangian description of an isolated particle, and heuristically extends the conservation equation of the continuous carrier fluid to account for the presence of the particles.

2.1 Motion of an Isolated Droplet

The study of unsteady particle motion in a turbulent fluid is generally considered to have its modern origins in the work of Tchen (Tchen, 1947), who extended the unsteady creeping flow solutions of Basset, Boussinesq, and Oseen to a non-uniform and variable flow velocity. Since that time, there has been substantial debate about the proper form of several terms in the equation of motion, in particular the effect of the far-field pressure gradients within the gas (Corrsin and Lumley, 1956), the added mass (Auton et al., 1988),

6

the Basset history term (Mei et al., 1991), and the generation of a lift force (Auton, 1987; Saffman, 1965; Mei, 1992). Maxey and Riley (Maxey and Riley, 1983) have derived a consistent equation of particle motion which is the most commonly agreed upon equation to describe the motion of a small, spherical particle in the presence of a non-uniform, unsteady flow. This formulation will form a basis for the analysis of the current work, and hence their procedure is outlined below to render a clear understanding of the assumptions and limitations imposed by the derivation.

The framework of the derivation begins with the description of a specified base flow field of the continuous carrier fluid without any particle present, which is assumed to satisfy

$$\rho_g\Big(\frac{\partial u}{\partial t} + u\cdot\nabla u\Big) = -\nabla p + \rho_g g + \mu\nabla^2 u, \tag{2.1}$$

$$\nabla \cdot u = 0. \tag{2.2}$$

The spherical particle is then placed in the uniform base flow, and the no-slip boundary condition on the surface of the particle results in a new flow field, $\tilde{u}$. This flow also satisfies the incompressible Navier-Stokes equations,

$$\rho_g\Big(\frac{\partial \tilde{u}}{\partial t} + \tilde{u}\cdot\nabla \tilde{u}\Big) = -\nabla p + \rho_g g + \mu\nabla^2 \tilde{u} \tag{2.3}$$

$$\nabla \cdot \tilde{u} = 0, \tag{2.4}$$

now subject to the boundary conditions:

$$\tilde{u} = u \qquad \text{as } \mathbf{r} \to \infty \tag{2.5}$$

$$\tilde{u} = v + \Omega \times \mathbf{r} \quad \text{at } |\mathbf{r}| = a. \tag{2.6}$$

The above description allows the flow field to be decomposed into the specified base and disturbance flow specified by

$$\tilde{u} = u + u_c \tag{2.7}$$

where $\boldsymbol{u}_\varepsilon$ is the disturbance flow. The difference of equations (2.1) and (2.3) gives the conservation equation for the disturbance flow, and can be simplified to the case of Stokes flow

$$\frac{\partial \boldsymbol{u}_\varepsilon}{\partial t} = -\nabla p_\varepsilon + \mu \nabla^2 \boldsymbol{u}_\varepsilon \tag{2.8}$$

provided that

$$\frac{\Delta U a}{\nu} \ll 1 \tag{2.9}$$

and

$$\frac{a^2}{\nu} \frac{U_0}{L} \ll 1. \tag{2.10}$$

Equation (2.9) and (2.10) stipulate that the Reynolds number based on both the slip velocity and the due to the velocity gradient across the particle must be small for (2.8) to be valid. The acceleration of the particle is then balanced by the external body forces $(m_p \boldsymbol{g})$, and the integral of the stress tensor over its surface,

$$\begin{aligned}
m_p \frac{\mathrm{d}\boldsymbol{v}}{\mathrm{d}t} &= m_p \boldsymbol{g} + \oint_s \boldsymbol{n} \cdot \tilde{\boldsymbol{\sigma}} \, \mathrm{d}S \\
&= m_p \boldsymbol{g} + \oint_s \boldsymbol{n} \cdot (\boldsymbol{\sigma} + \boldsymbol{\sigma}_\varepsilon) \, \mathrm{d}S \\
&= m_p \boldsymbol{g} + \boldsymbol{f} + \boldsymbol{f}_\varepsilon
\end{aligned} \tag{2.11}$$

where

$$\tilde{\boldsymbol{\sigma}} = -\tilde{p} + \mu \left[\nabla \tilde{\boldsymbol{u}} + (\nabla \tilde{\boldsymbol{u}})^T \right], \tag{2.12}$$

$m_p = \frac{4}{3}\pi a^3$ is the mass of the particle, and $(^T)$ indicates the transpose. The solution for $\boldsymbol{f}$ is obtained by using Gauss's theorem to change from an integral over the droplet's surface to a volume integral, substituting (2.1), and finally assuming that all second order derivatives of the undisturbed flow, $\nabla^2 \boldsymbol{u}$, are negligible, giving

$$\boldsymbol{f} = -m_f \boldsymbol{g} + m_g \frac{D\boldsymbol{u}}{Dt}. \tag{2.13}$$

The last assumption places an additional restriction that the gradients of velocity must be approximately constant across the particle, requiring that

$$\frac{a}{L} \ll 1. \tag{2.14}$$

The solution for f_ε is determined using equation (2.8), a Stokes flow symmetry relation, and the solution for an unsteady point force (see Maxey and Riley (1983) for details) to give

$$
f_\varepsilon = -\frac{1}{2} m_g \frac{d}{dt} \left(v - u - \frac{1}{10} a^2 \nabla^2 u \right)
$$
$$
- 6\pi \mu a \left(v - u - \frac{1}{6} a^2 \nabla^2 u \right) - 6\pi a^2 \mu \int_0^t \frac{\frac{d}{d\tau} \left(v - u - \frac{1}{6} a^2 \nabla^2 u \right)}{[\pi \nu (t - \tau)]^{\frac{1}{2}}} d\tau. \quad (2.15)
$$

The final form of the equation is given by

$$
m_p \frac{dv}{dt} = \underbrace{(m_p - m_g) g}_{(1)} + \underbrace{m_g \frac{Du}{Dt}}_{(2)} - \underbrace{\frac{1}{2} m_g \frac{d}{dt} \left(v - u - \frac{1}{10} a^2 \nabla^2 u \right)}_{(3)}
$$
$$
- \underbrace{6\pi \mu a \left(v - u - \frac{1}{6} a^2 \nabla^2 u \right)}_{(4)} - \underbrace{6\pi a^2 \mu \int_0^t \frac{\frac{d}{d\tau} \left(v - u - \frac{1}{6} a^2 \nabla^2 u \right)}{[\pi \nu (t - \tau)]^{\frac{1}{2}}} d\tau}_{(5)}, \quad (2.16)
$$

The various terms in the above equation represent forces due to (1) buoyancy, (2) far field pressure gradients, (3) the effect of added mass owing to the acceleration of the fluid surrounding the particle, (4) Stokes drag force, and (5) Basset viscous history term. The higher-order terms which appear as $a^2 \nabla^2 u$ are called the Faxen corrections and account for the non-uniformity of the far field.

Several calculations have been made for the lift force acting on a sphere due to uniform shear. In the limit of zero Reynolds number, no lateral force can be generated by an an imposed shear flow. However, Saffman (Saffman, 1965) did a perturbation analysis in terms of a large viscosity (small Reynolds number) to obtain

$$
|\mathbf{F}_{L_{\text{Saffman}}}| = 81.2 \, a^2 \rho_g \sqrt{\nu \kappa} \, |(u - v)|, \quad (2.17)
$$

where κ is the magnitude of the uniform velocity gradient. The above expression requires a uniform velocity in the far field as well as in the vicinity of the droplet, and is valid in the range of small Reynolds numbers. Auton (Auton, 1987) gave results for the lift on a droplet in an inviscid weak shear flow (large Reynolds number), in which the lift force results from a redistribution of the free-stream vorticity by the potential flow about the sphere. Secondary flow due to the vorticity is calculated using Biot-Svart law, giving the resultant lift force to

be

$$\mathbf{F}_{L_{\text{Auton}}} = -\frac{1}{2}\, m_f\, (\boldsymbol{u} - \boldsymbol{v}) \times \boldsymbol{\omega}. \tag{2.18}$$

Equation (2.18) requires that $|\boldsymbol{u} - \boldsymbol{v}| \gg a|\boldsymbol{\omega}|$ to preserve the linearity of the potential flow calculation.

Excluding lift force and gravity (which will be checked for applicability in the current experiment in Chapter 4), the effect of the various terms on the particle response can be examined in frequency space. Hinze (Hinze, 1972) and Hjelmfelt and Mockros (Hjelmfelt and Mockros, 1966) have approached the problem by expressing $\boldsymbol{u}$ and $\boldsymbol{v}$ as a Fourier transform and substituting in (2.16) excluding the buoyancy term and the effect of lift. The transforms for one dimension are defined by

$$\begin{aligned}
u_g(t) &= \int_0^\infty \Lambda_g(\omega)\exp(i\omega t)d\omega \\
u_p(t) &= \int_0^\infty \Lambda_p(\omega)\exp(i\omega t)d\omega
\end{aligned} \tag{2.19}$$

where Λ_g and Λ_p are complex functions of the frequency. The particle response is then determined by

$$\begin{aligned}
\frac{u_p}{u_g} &= \left[\frac{\Lambda_p \Lambda_p^\star}{\Lambda_g \Lambda_g^\star}\right]^{\frac{1}{2}} = \sqrt{(1 + \mathbf{f_1})^2 + \mathbf{f_2}} \\
\Phi &= \tan^{-1}\left[\frac{\mathbf{f_2}}{1 + \mathbf{f_1}}\right]
\end{aligned} \tag{2.20}$$

where

$$\begin{aligned}
\mathbf{f_1} &= \frac{(1 + C)(B - 1)}{(A + C)^2 + (1 + C)^2} \\
\mathbf{f_2} &= \frac{(A + C)(B - 1)}{(A + C)^2 + (1 + C)^2}
\end{aligned} \tag{2.21}$$

The coefficients A, B, and C are assigned different values depending upon which terms are retained in the equation of motion. For the general case

$$A = \frac{1}{2\pi\, St\, (1 + \frac{\gamma}{2})}, \quad B = \frac{3\gamma}{2\,(1 + \frac{\gamma}{2})}, \quad C = \frac{3}{2\,(1 + \frac{\gamma}{2})}\left[\frac{\gamma}{2\pi\, St}\right]^{\frac{1}{2}}. \tag{2.22}$$

Eliminating the Basset term gives

$$A = \frac{1}{2\pi\, St\, (1 + \frac{\gamma}{2})}, \quad B = \frac{3\gamma}{2\,(1 + \frac{\gamma}{2})}, \quad C = 0. \tag{2.23}$$
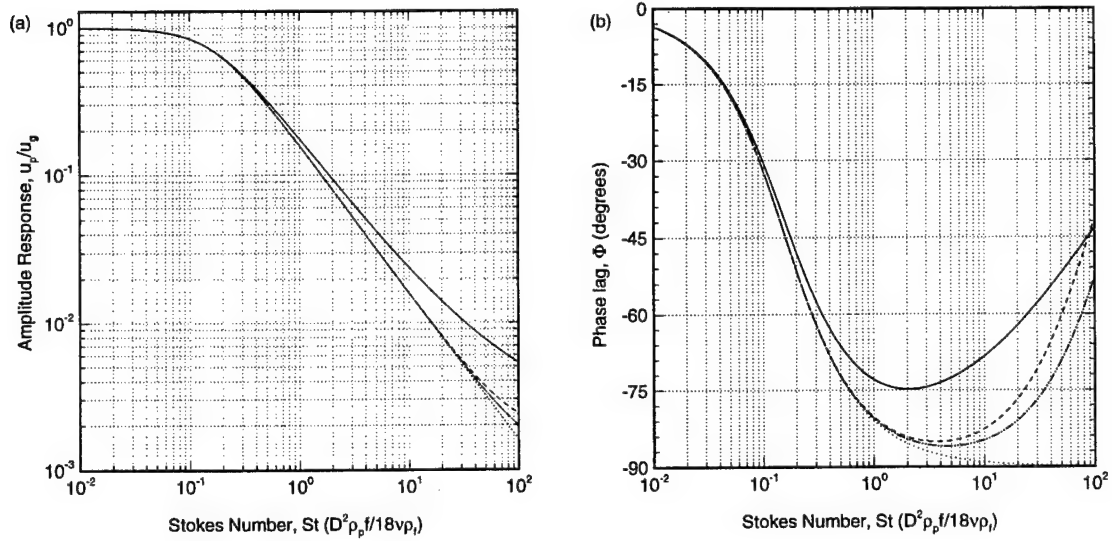
Figure 2.1: Steady state response of an isolated droplet. $\gamma = \rho_g/\rho_p = 0.0012$. (*a*) Amplitude ratio, u_p/u_g. (*b*) Phase angle. ——— , All terms; – – – , no Basset; —··— , no Basset, added mass; ········ , no Basset, added mass, pressure. From Hjelmfelt and Mockros (1966).

Neglecting the Basset and the added mass term

$$A = \frac{1}{2\pi\, St}, \quad B = \gamma, \quad C = 0. \tag{2.24}$$

Retaining only the Stokes drag gives

$$A = \frac{1}{2\pi\, St}, \quad B = 0, \quad C = 0. \tag{2.25}$$

where $\gamma = \rho_g/\rho_p$ is the density ratio between the gas and the particle, and St is the Stokes number as defined by

$$St = \tau_p f = \frac{2}{9}\frac{a^2}{\gamma\nu}\frac{\omega}{2\pi} \tag{2.26}$$

The steady-state droplet response for a water droplet in air ($\gamma = 0.0012$) is shown in figure 2.1. For Stokes numbers less than 1, there is virtually no influence on the droplet response by the terms other than the Stokes drag (less than 10% deviation in amplitude and phase). At high frequencies (large St), the solution which retains only Stokes drag underestimates

the amplitude of the general response by approximately 60%, while the phase lag deviates less than 20%. Neglect of the Basset term is observed to make the greatest deviation at high frequency, but the overall agreement of all four curves indicates that the assumption of dominant drag is certainly valid for Stokes numbers less than 1. This curve can also be used to help asses the selection of a seeding particle cut-off value, as will be done in chapter 3.

2.2 Effect of Weak Two-way Coupling on Carrier Gas

The above analysis for the motion of an isolated droplet can be used to find the force exerted on the continuous phase for the case of weak coupling. By weak coupling it is meant that the volume fraction is low enough that there is no significant effect on the continuity equation of the gas phase, and each droplet can be considered to act in isolation with the carrier gas. If one then considers a single droplet contained within an intermediate meso-scale averaging volume of characteristic dimension L_o, smaller than the smallest scale of the carrier gas motion (η_κ) and larger than the droplet diameter ($D = 2a$), then the momentum conservation equation for the undisturbed component of the gas will be modified by the addition of a reaction force between the particle and the gas:

$$\frac{\partial \boldsymbol{u}}{\partial t} + \boldsymbol{u} \cdot \nabla \boldsymbol{u} = -\frac{1}{\rho_g} \nabla p_g + \boldsymbol{g} + \nu \nabla^2 \boldsymbol{u} - \boldsymbol{f}_\varepsilon \tag{2.27}$$

Where $\boldsymbol{f}_\varepsilon$ is the force due to the disturbance flow created by the presence of the droplet. Only this force is transmitted back to the carrier gas, as the force acting on the droplet due to the undisturbed velocity field, $\boldsymbol{f} = m_g \boldsymbol{g} + m_g D\boldsymbol{u}/Dt$, is already accounted for in the equation of motion of the undisturbed field. For a more detailed analysis this formulation, the reader is referred to the work of Rightley (Rightley, 1995) and Maxey and Chang (Maxey et al., 1994). If there are now N particles per unit volume of size D within the averaging volume, then assuming that all particles in that volume have the same velocity and acceleration, equation (2.27) will be

$$\frac{\partial \boldsymbol{u}}{\partial t} + \boldsymbol{u} \cdot \nabla \boldsymbol{u} = -\frac{1}{\rho_g} \nabla p_g + \boldsymbol{g} + \nu \nabla^2 \boldsymbol{u} - N\boldsymbol{f}_\varepsilon. \tag{2.28}$$

This approach has been used by Marble (Marble, 1970) in the context of studying dusty gases, such as rocket nozzles and shock waves. In his applications, the problem is typically quasi-one-dimensional and the effects of the turbulence are ignored. In general, though, the assumption that all of the particle velocities are the same will only be valid in turbulent flows when the particle's viscous relaxation time is much less than the convective time scales of the smallest fluid motion. Consider, for example, the case of a stagnation flow of two opposing streams. At the separation boundary, heavy particles which cannot follow the straining motion will move into the opposing stream, where particles will be moving with the opposite velocity. For the general case, then, f_ε must represent a force averaged over the meso-scale volume. Equation (2.28) can be extended to a distribution of different sized droplets by summing the contribution from each size range $D_i \pm dD$. This results in a similar evolution equations for each size class (D_k) of the dispersed phase (see (Lázaro, 1989)),

$$\frac{\partial v_k}{\partial t} + v_k \cdot \nabla v_k = -\frac{1}{\rho_p}\nabla p_g + g + \nu\nabla^2 v_k + N f_{\varepsilon k}. \tag{2.29}$$

The constraints imposed on the above formulation and the equation of motion for the particle are summarized as follows.

1. The flow must be dilute ($\alpha_p \ll 1$) to keep higher-order coupling terms from being important, and to ensure that the inter-particle spacing is great enough for the solution (2.16) to be valid.

2. The meso-scale averaging volume and particle diameters must be much smaller than the smallest scale of the fluid motion $D < L_o < \eta_\kappa$. This ensures uniform velocity gradients in the vicinity of the droplet, as required by equation (2.13).

3. The droplet's Reynolds number based on its relative motion and shear velocity must be small ($\text{Re}_D = \omega D^2/\nu \ll 1$) so that the unsteady Stokes flow solution may be used to find the disturbance force acting on the droplet.

Chapter 3

Measurement Techniques and Instrumentation

3.1 Measurement of Two-Phase Flows

The discontinuous nature of multi-phase flows presents many difficulties in the measurement of the flow characteristics. Until the last several decades, most measurements were limited to bulk average quantities such as the pressure drop along two-phase pipe flow. The reason for the lack of precise measurements is due to the problems caused by the sharp changes in the fluid properties (density, thermal conductivity, heat capacity, etc.) across the interface, rendering most of the traditional single-phase techniques useless. For example, pitot tubes measure the dynamic pressure, $\overline{\rho u^2}$, and can be used to estimate the mean velocity, u, provided the flow is incompressible and the density is known. Aside from the mechanical difficulties associated with using this probe in multi-phase flow (e.g. inlet port blockage due to surface tension effects of an air/water interface), the large difference in density between the phases ($\rho_l/\rho_g \approx 10^3$) would prevent any meaningful measurement. Hot wires are met with a similar fate due to the large change in thermal capacity and conductance between the liquid and the gas, in addition to the fact that the drops may wet the probe's surface for a significant period of time after impact. This technique has been used, however, with marginal success in a dilute two-phase turbulent jet (Hetsroni and Sokolov, 1971) by essentially filtering the portion of the data contaminated by the impact of

14

the droplets. Measurement of particulate size and mass flux have also proved problematic. Historically measurements of the dispersed phase mass flow rate were performed through the use of patternators (sub-divided catch-basins) and iso-kinetic suction probes, which only allow for long-time average quantification. All of the above intrusive methods also suffer from the fact that they alter the flow due to their mechanical presence. Although this disruption can often be minimized, ideally the use non-intrusive techniques is by far much more desirable.

It is clear then, that the development of non-intrusive, spatially and temporally re-solved optical techniques could be an ideal candidate for multi-phase flow instrumentation. These instruments are often designed by taking advantage of the discontinuities in refractive indices between the phases. Among the available methods are photography, Particle Image Velocimetry (PIV), laser extinction, laser diffraction, Laser Doppler Anemometry or Ve-locimetry (LDA or LDV), and Phase Doppler Anemometry (PDA). The recent advances in these optical instruments can be traced to three main reasons. First, most of these methods rely upon an intense, coherent light source, and hence have only been in development since the advent in the laser in the mid 1960's. Secondly, the desired scattered signal is often buried amid a field of broadband noise which requires advanced signal processing to make accurate measurements in practical flows. Finally, these methods have also benefited from the application of increased computing power which allows exact light scattering equations to be solved.

Most applications of photography in two-phase flows are applied to flow visualiz-ation and number density measurements (Kulick et al., 1993; Longmire and Eaton, 1992). Flow visualization has time and again demonstrated to be an important tool in the study of turbulence (Winant and Browand, 1974; Brown and Roshko, 1974), as it retains the structural phase information of how the various scales of turbulence interact with one an-other. This cannot be said for all other traditional turbulence tools, such as single-point spectra (Armi and Flament, 1985) which only reflect the evolution of the amplitude of the fluctuations and completely ignore the phase information. Number density measurements are usually obtained by photographing a thin cross-section of the flow illuminated with a laser sheet and simply averaging the number of particles observed in a given region of the

image. In dense flows this is problematic, if not impossible, due to attenuation of the beam as it crosses the flow which results in a diminished probability of particle detection. The image will also be affected by the fact that the scattered light must travel through many particles to reach the camera lens, distorting the actual representation of the image.

PIV is closely related to photography, and uses the displacement of a particle image, $\Delta \mathbf{x}$, viewed at two or more different times within a short time interval, Δt, to calculate an estimated velocity, $\Delta \mathbf{u}$ (Keane and Adrian, 1992). Typically, $\Delta \mathbf{x}$ is determined by examining the spatial cross-correlation between the two images. Difficulties with this method include the fact that the measurable velocity scales are limited by the resolution of the film or CCD array used to capture the images and the fact that particles in three-dimensional flow may move out of the illuminated plane, causing an incorrect correlation. Currently, three-dimensional holographic techniques are under development to solve this problem.

Laser diffraction instruments were among the first commercial non-intrusive particle sizing instruments available (Dobbins et al., 1963; Swithenbank et al., 1977). They rely upon Fraunhoffer diffraction theory to describe the intensity of light scattered by particles present in the path of an incident laser beam. This light is collected over small scattering angles and various size distributions are iteratively selected until one is achieved which matches the measured intensity pattern with a minimum error. As this method averages over a line-of-sight of the beam's path, it works best for planar, quasi-two-dimensional flows. Deconvolution techniques must be employed when measuring cylindrically symmetric flows to obtain an actual radial profile (D. C. Hammond, 1981). Other disadvantages of this method include the fact that *a priori* assumptions about the size distribution must be made in regard to it's shape in order to make the solution of the problem tractable.

Laser extinction and PDA techniques were the primary experimental methods used in this thesis and so will receive detailed consideration in the sections that follow. These sections are intended to provide an accurate evaluation of the principles and limitations of the extinction and PDA techniques, and will provide a complete discussion of the difficulties encountered that need to be considered with these methods to obtain reliable measurements realized within conditions of the experiment.

3.2 Results for Light Extinction Theory

The extinction of incident light as it propagates through a scattering and absorbing particle can be characterized by its extinction efficiency, Q_{ext}, which is defined as the ratio of the particle's effective light-blocking area to the actual geometric cross-sectional area. For example, in the near field of an opaque object much larger than the wavelength of light (e.g. your hand, a tree, etc.) the extinction efficiency is equal to 1 and the objects simply projects its geometric shadow. For a spherical particle, Q_{ext} is independent of the polarization of the light and is related to the far field complex scattering amplitude through the expression (van de Hulst, 1981)

$$Q_{ext} = \frac{4}{\beta^2}\mathrm{Re}\{S(0)\}. \tag{3.1}$$

For the case of an opaque sphere or disk observed at distances beyond which there is a discernible geometric shadow, Huygens' principle can be used to show that

$$S(0) = \frac{\beta^2}{2}, \tag{3.2}$$

giving an extinction efficiency of 2. This reflects the fact that the opaque object is blocking πa^2 area of light and the resulting diffraction interference pattern destructively cancels another πa^2.

The analysis must be modified for a non-absorbing sphere to account for those rays which propagate through the sphere. This is readily accomplished through the use of geometric optics when $\beta \gg 1$ and $m \sim 1$, which implies that the divergence of the transmitted rays are small and that $\tau \sim \tau'$. The phase shift of the ray propagating through the sphere and exiting at the first internal reflection ($p = 1$) is then given by $\eta = 2\beta(m-1)\sin(\tau) = \varrho\sin(\tau)$ from equation (A.18) in Appendix A. When this contribution is accounted for in Huygens' formulation, the resulting expression for the complex scattering function is

$$S(0) = \beta^2 \int_0^{\pi/2} \left(1 - e^{-i\varrho\sin(\tau)}\right)\cos(\tau)\sin(\tau)d\tau \tag{3.3}$$

which can be readily integrated by parts to give

$$S(0) = \beta^2\left(\frac{1}{2} + \frac{e^{-i\varrho}}{i\varrho} - \frac{e^{-i\varrho} - 1}{\varrho^2}\right). \tag{3.4}$$
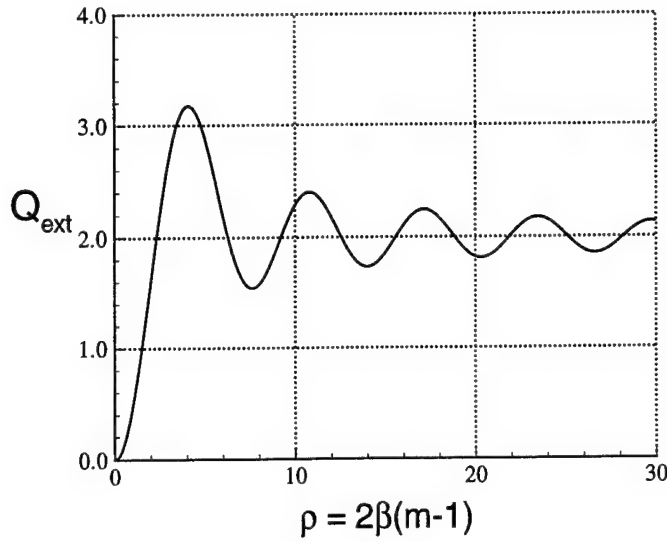
Figure 3.1: Variation of Q_{ext} as given in equation (3.5).

The efficiency factor for a single particle then becomes

$$Q_{ext} = 2 - \frac{4\sin(\varrho)}{\varrho} + \frac{4(1 - \cos(\varrho))}{\varrho^2}. \tag{3.5}$$

This function is shown in figure 3.1. It can be seen that the transmitted light alternately interferes both constructively and destructively with the diffracted pattern as ϱ is increased. Note that as $\varrho \to \infty$, Q_{ext} converges to a value of 2, implying that the transmitted rays no longer have an effect on the extinction and becomes equivalent to an opaque disk viewed from a large distance.

The extension of the preceding analysis to the case of a light beam propagating through a cloud of spherical scatters can be accomplished when the size and spacing of the particles relative to the wavelength of the radiation are such that independent scattering can be assumed. By independent scattering it is meant that the scattered waves originating from all other particles will not have a coherent phase contribution, thus eliminating interference effects and allowing the scattered intensities to be additive (Woodward, 1964). Scattering experiments have shown that this assumption is valid when the particle diameter is greater than the incident wavelength $(D > \lambda)$ and the inter-particle spacing is greater than the particle diameter $(D\alpha_p^{-1/3} > D$, where α_p is the dispersed phase volume fraction) (Hottel

et al., 1970). Furthermore, if the medium is optically thin (i.e. low volume fraction, α_p, or small distances), then multiple scattering events can be neglected and the beam's attenuation can be derived from a formulation of Beer's Law (Siegel and Howell, 1981). This law states that the ratio of scattered light intensity, dI, to the incident intensity within a small volume $dv = dx\,dy\,dz$ is proportional to the ratio of the effective scattering area of all the particles in the volume to the cross-sectional area of the incident beam:

$$\frac{dI}{I} = \frac{-dA}{A} = \frac{-\int_0^\infty \frac{\pi D^2}{4} Q_{ext}(D)\,N(D,z)dx\,dy\,dz\,dD}{dx\,dy}$$

$$= -\frac{\pi}{4}\int_0^\infty D^2 Q_{ext}N(D,z)dD\,dz$$

$$= -\sigma(z)dz \tag{3.6}$$

where $N(D,z)dx\,dy\,dz\,dD$ is the number of particles in the volume dv within the size range $D \pm dD/2$, and $\sigma(z)$ is by definition the extinction coefficient. Integrating (3.6) along the length of the beam through the particle cloud, L, gives a definition for the attenuation function,

$$\xi \equiv \ln\left(\frac{I}{I_o}\right) = -\frac{\pi}{4}\int_0^L\int_0^\infty D^2\,Q_{ext}(D)\,N(D,z)dD\,dz, \tag{3.7}$$

which is often referred to as Bouguer's Law.

Further reduction can be obtained by examining how Q_{ext} varies for a given application. As was shown in equation (3.5), Q_{ext} converges towards a constant value of 2 for large ϱ. For water droplets larger than 6 μm$(m = 1.33)$ this variation is less than 10%. Accepting this small uncertainty allows for the substitution of the constant value of 2 for Q_{ext}, giving

$$\xi = -\frac{\pi}{2}L\int_0^\infty D^2\,\overline{N}(D)dD, \tag{3.8}$$

where

$$\overline{N}(D,z)dD = \frac{1}{L}\int_0^L N(D,z)dz. \tag{3.9}$$

For the approximations made within the derivation, equation (3.8) then states that the logarithm of the beam intensity ratio is proportional to the area weighted number density

20

or average projected surface area contained within the beam volume. A more convenient form which separates the size and concentration effects can be derived by defining the particulate volume concentration, α_p, as the volume occupied by the dispersed phase per unit total volume:

$$\alpha_p = \frac{\pi}{6} \int_0^\infty D^3 \overline{N}(D)dD. \tag{3.10}$$

Applying this to equation (3.8) gives

$$\xi = -\frac{\pi}{2}L \int_0^\infty D^2 \overline{N}(D)dD \frac{6\alpha_p}{\pi \int_0^\infty D^3 \overline{N}(D)dD} = -\frac{3L\alpha_p}{D_{32}}, \tag{3.11}$$

where $D_{32} = \int_0^\infty D^3 N(D)dD / \int_0^\infty D^2 N(D)dD$ is by definition the Sauter Mean Diameter (SMD) which gives an equivalent diameter that preserves the total volume to surface area ratio of the polydispersed spray. This shows that the attenuation is then directly proportional to the volume concentration of the particulate and inversely proportional to the Sauter Mean Diameter. Most of the results will be presented in the form of a normalized attenuation

$$\frac{\xi}{\xi_\infty} = \frac{\alpha_p D_{32\infty}}{D_{32}\alpha_{p\infty}}, \tag{3.12}$$

where the subscript ∞ refers to the uniform freestream conditions.

An equivalent expression results from the definition of a normalized volume probability distribution function (pdf),

$$f(D,z)dD = \frac{D^3 N(D,z)dz}{\int_0^\infty D^3 N(D,z)dz} = \frac{\pi D^3 N(D,z)dz}{6\alpha_p(z)} \tag{3.13}$$

from which it follows that

$$\frac{\xi}{\xi_\infty} = \frac{\overline{\alpha}_p \int_0^\infty \frac{\overline{f}(D)dD}{D}}{\overline{\alpha}_{p\infty} \int_0^\infty \frac{\overline{f}_\infty(D)dD}{D}}. \tag{3.14}$$

From expression (3.12) or (3.14), it is evident that for small variation of the SMD that the attenuation can be used as a direct measure of the particle volume fraction. However, in the current measurements it will be shown that within the mixing layer the SMD can decrease as much as 50% of its freestream value, and that using ξ/ξ_∞ to represent $\alpha_p/\alpha_{p\infty}$ will be numerically off by a factor of 2. If the use of ξ is limited to a qualitative representation of α_p, then this quantitative inaccuracy may be acceptable due

to the general similarity observed in the trends of ξ and the SMD (figure 3.2). Use of ξ in the present work is therefore limited to: (1) comparison with other experiments which presented laser attenuation data, (2) qualitative discussion of the spray dispersion, and (3) estimates of α_p through the use of a measured size distribution via equation (3.12).

3.2.1   Laser Attenuation Instrumentation

The instrumentation for the laser attenuation measurements consisted of a 5 mW He-Ne laser, which was projected through the spray along the span of the test section into a United Detector Technology (PIN-6D) photodiode (figure 3.3). The output of the laser was clipped with a 3 mm circular orifice to increase the spatial resolution of the instrument, and a neutral density filter (Melles Griot, 5.012% transmittance) was used to ensure the resulting beam intensity would be within the appropriate operating range for the photodiode. The diode output current was then translated into a measurable voltage, amplified, and low-pass filtered prior to digitization with a LeCroy 8212A Data Logger. The digitizer used 12-bit analog to digital converters (ADC) and had a full-scale range of 10 V. The photodiode amplifier gain and offset were adjusted to use the entire 12-bit range of the ADC. After digitization, the data was temporarily stored in a 32K/12-bit buffer before it was transfered to a 80486 desktop computer for storage on disk.

Figure 3.4, shows the unattenuated signal time series and the autospectral power density for a typical data sample from within the mixing layer. The noise present in the baseline state is dominated by a 70 mV, 60 Hz periodicity caused by contamination from the amplifier voltage supply. Due to the periodicity of this line noise, the mean attenuation values are unaffected but the rms values are biased by approximately 1% of the mean freestream attenuation. The rest of the noise inherent to the system can be characterized from the autospectra, which shows the non-periodic component to be broad-band white noise until a roll-off is reached around 100 Hz. It can also be seen that the noise is always 1 to 2 orders of magnitude less than the data signal.

The statistical uncertainty of the processed data follows from error analysis of estimators used to find the mean and rms values (Bendat and Piersol, 1986). The mean
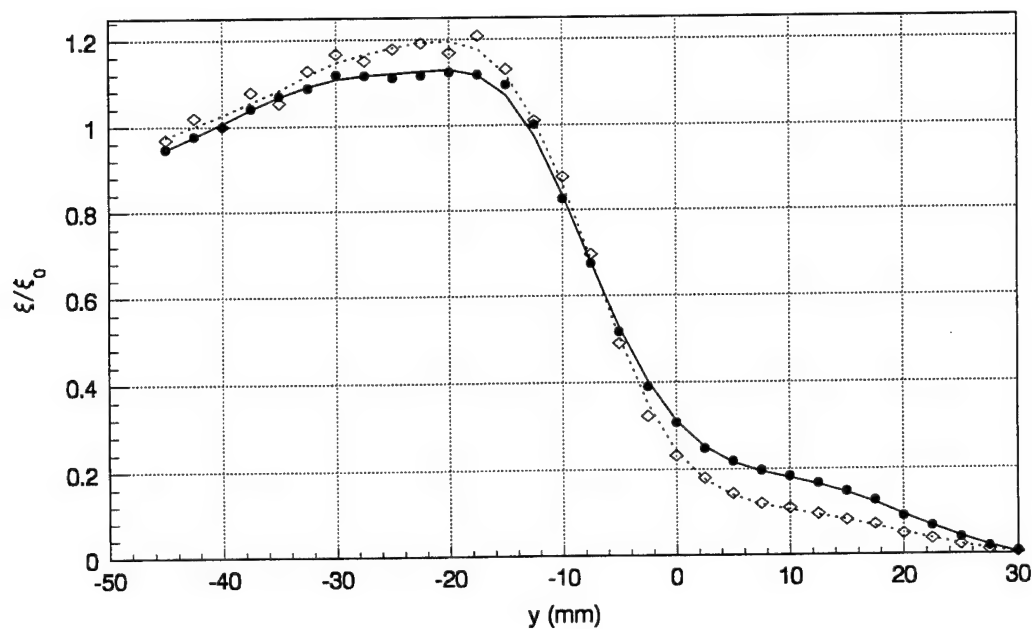
Figure 3.2: Comparison of mean attenuation (•) and mean concentration (◇) profiles.
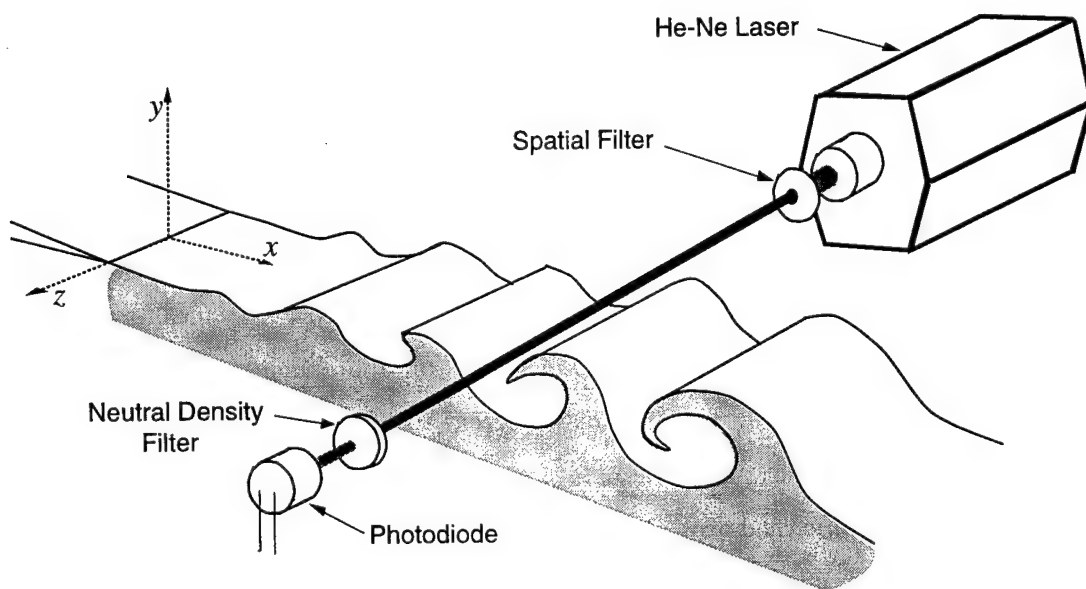
Figure 3.3: Schematic of laser attenuation instrumentation.
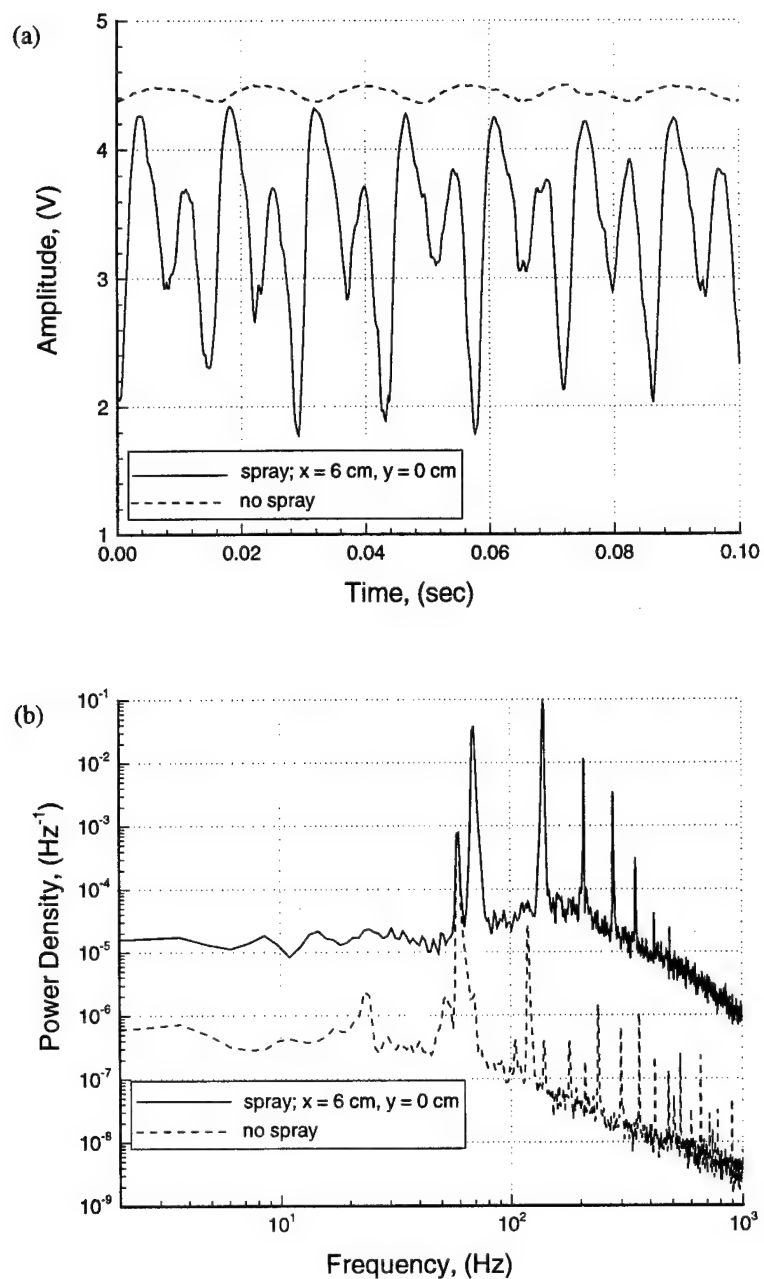
Figure 3.4: Attenuation sample time series (a), and corresponding autospectra (b) showing baseline (no spray) and typical signal amplitudes.

attenuation values were estimated using the summation

$$\overline{\xi} = \frac{1}{32768} \sum_{i=1}^{32768} \xi_i, \tag{3.15}$$

where ξ_i is the ith sample in the data series. The associated uncertainty of this estimate depends on the bandwidth of the signal, B, and the duration of the sampling period, T, which basically determines the number of independent records in the sample. All of the data was sampled at 5 kHz, with data records of 32,768 points, giving a sampling length of 6.55 sec. The bandwidth of the signal is 70 Hz, due to the strong periodic nature of the forcing signal. Using the above values, and assuming the normalized standard deviation $(\xi'/\overline{\xi})$ is bounded by 0.4 (which is observed to be valid until the outer 10% of the mean profile) gives the normalized random error to be

$$\epsilon_r(\overline{\xi}) = \frac{1}{\sqrt{2BT}} \left(\xi'/\overline{\xi} \right) \simeq 1.3\%, \tag{3.16}$$

and hence puts the 95% confidence interval within $\overline{\xi}(1 \pm 0.026)$.

The rms was estimated using

$$\xi' = \left[\frac{1}{32767} \sum_{i=1}^{32768} (\xi_i - \overline{\xi})^2 \right]^{\frac{1}{2}}, \tag{3.17}$$

which has the random error estimate

$$\epsilon_r(\xi') = \frac{1}{2\sqrt{BT}} \sim 2.3\%, \tag{3.18}$$

resulting in the 95% confidence interval $\xi'(1 \pm 0.052)$.

The phase-conditioned averages resulted in an expression similar to 3.15, with the exception that the upper limit on i was approximately 910 as each 70 Hz cycle was subdivided into 36 bins. Since the flow periodicity had no common prime factors with the 60 Hz line contamination, there was no significant bias of the phase averaged data. It was further found that the normalized rms phase averaged attenuation, $\langle \xi' \rangle / \langle \xi \rangle$ was less than 15% over the entire y/ϕ plane with the exception of the outer edge of the mixing layer, resulting in a random error estimate of

$$\epsilon_r(\langle \xi \rangle) = \frac{1}{\sqrt{2BT}} \left(\langle \xi' \rangle / \langle \xi \rangle \right) \simeq 0.5\%. \tag{3.19}$$

Similar estimates for the uncertainty of the Eulerian autocorrelation and the auto-spectra give uncertainties of approximately $\epsilon_r(R_{\xi\xi}/\xi'^2) = 10\%$ at a value of $R_{\xi\xi}/\xi'^2) = 0.35$, and $\epsilon_r(\Xi) \simeq 25\%$.

3.3   LDV/PDA Qualification and Experimental Application

Although the LDV (and to a lesser extent the PDA) has earned wide acceptance throughout the fluid mechanics community through several decades of careful research, the measurement process still requires careful consideration of the experiment at hand to obtain reliable results. In order to continue the discussion, the details of the instrument used in this experiment will first be presented, followed by the sources of measurement error considered in the context of this specific instrument.

The PDA used in this experiment was a two-component PDPA (Phase Doppler Particle Analyzer) manufactured by Aerometrics, Inc. of Sunnyvale, California. The light source consisted of a 350 mW, air-cooled, multi-line Argon ion (Ar^+) laser (Ion Lasers Inc.). The output beam was directed into a Bragg cell (which produced equal intensity unshifted/shifted beam pairs) driven at 40 MHz, followed by a dispersion prism, pickoff mirrors, and fiber-optic couplers. A 20' fiber optic cable was then used to convey the beams to the transmitter (model XMT-1204), which utilized a 50 mm clear aperture/250 mm focal length achromatic lens to focus the beams into the probe volume. The two primary wavelengths of the laser were used (green, 514 nm; blue 488 nm) to generate the orthogonal component directions. The green beams were used to measure the streamwise velocity component (x direction), and hence the transmitter was oriented such that the green beams were contained in the $x - z$ plane. The beam separations at the lens were 20.1 mm (green) and 20.3 mm (blue), giving a crossing angle, 2γ, of 4.6°. This configuration generates a probe volume which takes the form of an oblate ellipsoid with a length of $c_o = 2$ mm and a diameter of $a_o = b_o = 80$ μm.

Since the particles to be measured were transparent, non-absorbing spheres of water ranging in size from 1 to 100 μm, the dominant scattering mode to be used for sizing was the first order internal refracted beam ($p = 1$). The most advantageous collection

angle under these conditions is located as far forward (small θ) as is possible without being in a region where diffractive effects would present a problem. This, in conjunction with the limitations imposed by the girth of the test section, dictated a receiving angle of $\theta = 30°$, located in the plane of symmetry between the two incident green beams ($y - z$ plane). The receiver assembly (model RCV-2204) also used a 50 mm clear aperture/250 mm focal length achromatic lens to collect the scattered signal, which was subsequently focused (100 mm focal length lens) onto a 100 μm rectangular aperture to limit the extent of the observed probe volume. This created a sampling volume that was effectively a skewed circular cylinder with a length of $(100\,\mu m)f_1/(f_2\sin(30°)) = 500\,\mu m$ and a diameter of 80 μm. After the aperture, the green and blue signals were separated and sent to four photo-multiplier tubes (3 for velocity measurement and redundant particle sizing of the green signal, 1 for velocity measurements of the blue) which converted the scattered light intensity into a voltage signal for analysis.

The outputs of the photo-multipliers were then sent to four separate channels in the DSA. A schematic of the processor signal validation sequence is shown in figure 3.5. First, the signal was split and simultaneously sent to the digitization chain and the peak detector. En route to the peak detector, the signal passed through a high-frequency envelope filter to eliminate possible noise spikes from initiating a burst detection. The peak detector was used to provide three pieces of information: 1) It was used as a threshold to set the minimum signal amplitude required to trigger a burst detection, 2) it located the temporal location of the peak to enable sampling in the highest signal to noise region of the burst, and 3) it recorded the signal intensity to use as an additional check on the particle size. The location of the peak and its amplitude were then sent to the controller, so that it may inform the circular digitizer buffer which set of data to pass on to the main buffer for processing.

Prior to digital conversion, the signal was filtered with a 20 MHz high-pass filter and logarithmically amplified to remove the Gaussian pedestal component and heighten the slope of the remaining high-frequency AC Doppler component. The signal was then down-mixed in quadrature (two mixer signals were sent, differing only in phase by 90°) with a programmable mixer frequency (f_{mixer}), low-pass filtered to remove the $f_{Doppler} + f_{shift} + f_{mixer}$ frequency, and digitized using 1-bit analog to digital converters (ADC).
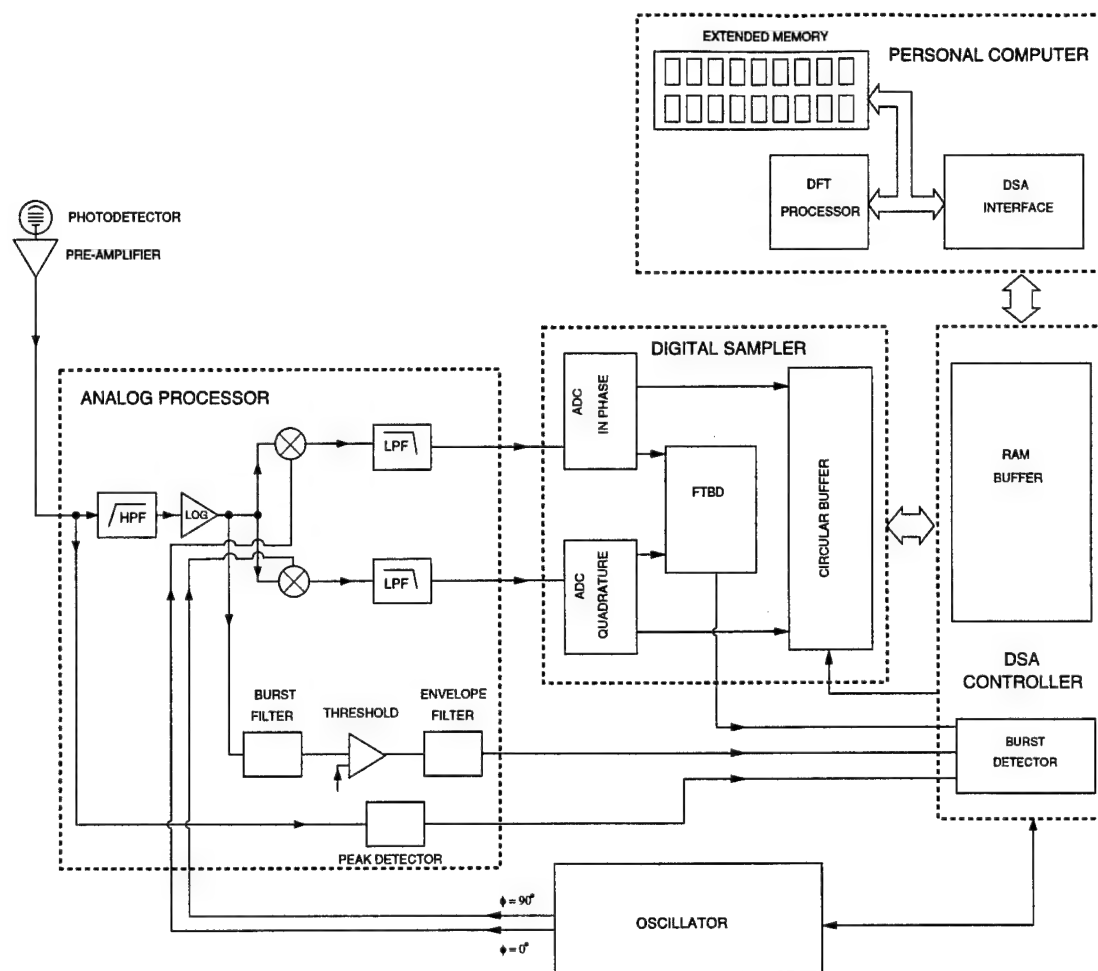
Figure 3.5: Schematic layout of the DSA burst processor.

The digitized signal had a frequency of $f_{Doppler} + f_{shift} - f_{mixer}$, which allowed greater flexibility in the available resolution of the sampling rate. Quadrature sampling allowed the region where $f_{Doppler} + f_{shift} < f_{mixer}$ to be sampled without ambiguity. A table of the sampling parameters used during this work is given in table 3.1 and 3.2.

After the signal was digitized, it was split and one branch was continuously streamed to a circular buffer which waits for information from the controller and burst detection logic to send the desired set of samples to the processor RAM buffer. The data was stored here during acquisition until it could be transfered to an Intel 80486 personal computer, where a dedicated DFT board was used to obtain the frequency (and phase shift

Transmitter:	Green	Blue
Wavelength, λ (nm)	514	488
Initial beam diameter, D_o (mm)	2	2
Initial beam separation, L_o (mm)	20.1	20.3
Beam crossing half-angle, γ	2.30°	2.32°
Probe Dimensions (μm):		
Height, a_o	81.8	77.7
Width, b_o	81.9	77.7
Length, c_o	2038	1919
Effective length, $\hat{c}_o$	500	500
Probe volume fringe spacing, $\lambda_{Doppler}$	6.37	6.01

Table 3.1: PDPA transmitter and probe volume geometry.

LDV Parameters:	Channel 1	Channel 2
Light collection angle, θ	30° forward scatter	
PMT high voltage, (V)	375	501
Threshold trigger, (mV)	11.8	11.4
# of samples per burst	128	64
Sampling frequency, (MHz)	40	20
Minimum Signal to Noise, (dB)	-10	-10
D.C. Offset voltage, (mV)	27.9	47.9
Filters & Signal Processing:		
High-pass filter, (MHz)	20	20
Down-Mixer frequency, (MHz)	38.59	38.375
Low-pass filter, (MHz)	10	5
Burst conditioning filter	50 MHz BP	40 MHz LP
Envelope filter, (ns)	300	300
Coincidence, channel 1 and 2	5%	

Table 3.2: DSA processor settings used for data acquisition.

for sizing) of the individual bursts. The other digitized signal branch was sent to a Fourier transform burst detector (FTBD), which located Doppler bursts by examining the signal to noise ratio of spectral peaks obtained from a real-time discrete Fourier transform (DFT). The FTBD was not required for operation, but does allow for increased burst detectibility in noisy environments as detection is no longer sensitive to signal amplitude or DC offset.

3.3.1 Signal Processing and Frequency/Phase Resolution

The accuracy of the velocity and size measurements are dependent upon how well the frequency and phase of the Doppler signals can be resolved in a real environment, and requires that the signal processors should operate accurately even when the signal is in the presence of a significant amount of noise. Recovery of a single frequency signal embedded in noise is optimized by processing the signal in the frequency domain through the use of Fourier analysis. It has been found that the variance of the frequency and phase obtained from Fourier analysis have lower bounds given by the Cramer-Rao bounds (Ibrahim et al., 1990)

$$var[f] = \frac{12}{(2\pi)^2 SNR\, N\,(N^2 - 1)} f_{sample}^2, \tag{3.20}$$

and

$$var[\phi] = \frac{2(2N - 1)}{SNR\, N\,(N + 1)} \tag{3.21}$$

where SNR is the signal to noise ratio, N is the number of samples used in the discreet Fourier transform, and f_{sample} is the sampling frequency.

The above bounds were for signals which had no limitations on the resolution of the amplitude. Ibrahim, Werthimer and Bachalo (Ibrahim et al., 1990) extended these results by examining the effect of 1-bit sampling on the limits of the resolution. They also allowed for the inclusion of a spectral windowing function (*e.g.* boxcar, Hamming, etc.) to decrease the amount of leakage into the side lobes of the spectra which results from the finite sample length. Further improvements were also made through the use of spectral peak interpolation, which regains an order of magnitude in frequency resolution originally lost due to the discrete frequencies used in the DFT. When these factors were accounted for,

it was shown that theoretically, the lower bounds provided by the Cramer-Rao limits can be approached with the 1-bit interpolated spectra, but in practice come within a factor of 2 to 10 depending on the signal to noise ratio and the number of points used in the DFT. The theoretical estimates compared favorably with both numerical simulation and actual experimental results obtained from the DSA. For the conditions used during the streamwise velocity measurements completed in this experiment ($N = 128$), Ibrahim, *et al* found that the normalized frequency root mean squared (rms), f'/f_{sample}, was about 0.001 at 0 dB, while the phase rms was about 2°. This frequency translates into a velocity uncertainty of approximately ± 0.25 m s^{-1} or 1.5% when referenced to the freestream velocity of 18 m s^{-1}. Note also that this is a worst case example, and that this variance decreases with increasing signal quality. For a 40 dB signal, the frequency variance is reduced to ± 0.08 m s^{-1}, while the phase is reduced to $\pm 0.7°$.

3.3.2 Particle Selection and Gas Velocity Measurement

A particle must satisfy at least three criterion to be considered a good candidate for velocity measurement of the continuous phase: 1) It must faithfully follow the flow fluctuations of interest, 2) it must scatter light efficiently in the direction of the receiver, and 3) it must be present in sufficient numbers to resolve the length scales of interest.

For gas flows seeded with liquid or solid particles, a rough measure of the particle response is given by the Stokes number, which represents the ratio of the particle's viscous response time to the time scale of the surrounding flow. It is clear that the Stokes number of seeding particles should be much less than one. Although this is adequate for some quick estimates, it still does not quantify the amplitude or phase response of the particle, and thus requires a more through analysis. Hinze (Hinze, 1971) and Hjelmfelt and Mockros (Hjelmfelt and Mockros, 1966) have obtained such results by examining the equation of particle motion in frequency space as was outlined in §2.1. If one wishes to study the complete spectral range of fluid motion in a turbulent gas, most laboratory scale flows would require particle response fidelity up to $O[10^5]$ Hz. From equation (2.21), this would require a particle that was 1 μm or smaller.

Particles that fulfill this requirement are usually either metal oxide particles (TiO$_2$,

MgO, Al_2O_3) suspended from a fluidized bed or fine oil droplets obtained from atomization and subsequent aerodynamic filtering. When used in two-phase flows, however, it becomes difficult to identify which particles are the gas seed and which are the dispersed phase. If there is a large disparity in size between the dispersed phase and the seed, it is possible to identify the particles based on the intensity of the burst. There will be a small amount of "cross-talk" due to large particles passing through the edge of the sample volume and generating a small amplitude burst (which will be interpreted as a seed particle), but this will only account for a small percentage of the bursts if the size separation is several orders of magnitude (Stock et al., 1975).

In this study, the size distribution of the dispersed phase was quite broad (extending down into the micron sized range), and hence effectively prevents the use of amplitude discrimination. In addition to this, complete spray characterization requires that the response of each size class of the dispersed phase be measured. This can be achieved by contemporary PDA techniques as long as all of the particles are spherical and are composed of material with the same index of refraction. Since the current work is only interested in the effect of velocity fluctuations due to the large eddies on the particle motion, the frequency response criterion listed above can be relaxed. This allows the gas velocity to be characterized by using all particles with a size less than a given cutoff value to represent the motion of the gas. The primary instability frequency measured in the shear layer was 140 Hz, and once more equation (2.21) can be used to show that a 10 μm droplet will respond with a $u_p/u_g > 0.96$ and a phase shift of less than 15°. It should also be pointed out that this is an *upper bound* on the particle response. The average size used to measure the gas velocity was $\sim$ 6 μm which has a fidelity $u_p/u_g > 0.99$ and a phase shift less than 6°. Thus, all measurements of the gas velocity were obtained through the measurement of particles with a diameter less than 10 μm. The quality of this response was checked by reducing the cutoff diameter from 10 μm to 5 μm and examining the effect on the mean velocity profiles. for accurate comparison, we have used the most sensitive measure of the particle response, i.e. the fluctuating component. The cross-stream rms velocity for both cutoff diameters are shown in figure 3.6. The maximum deviation is approximately 0.1 m s^{-1}, and is close to the statistical uncertainty associated with the measurement (average is formed over $\sim$ 350
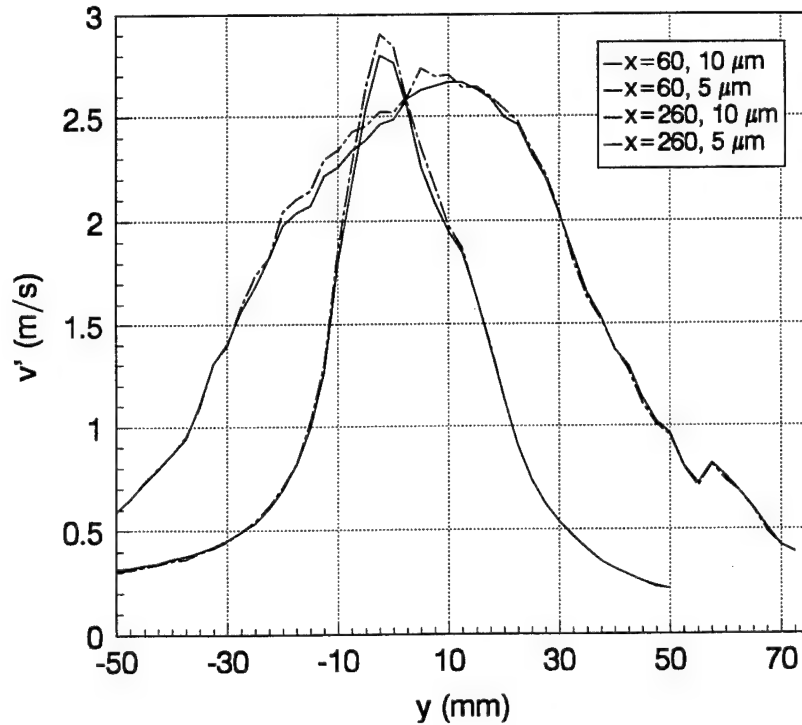
Figure 3.6: Change in cross-stream rms velocity profile at two downstream locations for $D_{max} = 5\,\mu m$ and $10\,\mu$m.

structures in the central of the mixing layer, $\pm 3\%$). Similar results are obtained for the phase-averaged quantities, with no discernible differences in the velocity vector except for minute variations due to statistical uncertainty (less than 5%). Thus, although using a cutoff size of $10\,\mu$m to represent the gas flow might not be advisable when attempting to measure the smallest flow scales, it does accurately resolve the large scales of interest in the current study as indicated by the theoretical particle response and experimental observation.

3.3.3 Velocity Bias Correction

Fringe interferometers operating in coherent burst mode require that there be only a single particle in the probe volume at any given instant in time. This requirement, coupled with the fact that particles are usually distributed randomly in space over the scale of the sampling volume, makes for an instrument that inherently records data at

random sampling intervals. If there were no correlation between the flow characteristics (i.e. particle concentration, velocity fluctuations) and the occurrence of a data sample, then an unweighted number average of the samples would give the proper ensemble or time average of the quantity in question.

However, since a measurement is dependent upon the flow to convect particles into the sampling volume, a single realization is intimately coupled to the velocity magnitude and direction, as well as the particle concentration and size variation. For example, consider measurements made between the time interval $t = 0$ and $t = 10$ sec in an unsteady, one-dimensional flow that is uniformly seeded with particles 1 particle every meter. If between $t = 0$ and $t = 5$ sec, the velocity is 1 m s^{-1}, and between $t = 5$ and $t = 10$ sec the velocity is 10 m s^{-1}, then the instrument will record five bursts at 1 m s^{-1} and 50 bursts at 10 m s^{-1}, giving an unweighted average of 9.18 m s^{-1} instead of the true time average of 5 m s^{-1}. It can be seen from this example that the instrument actually averages over the total swept volume of the probe.

McLaughlin and Tiederman (McLaughlin and Tiederman, 1973) were among the first researchers to document this fact and proposed a correction to remove the bias. Their reasoning is as follows: If the particles are uniformly distributed throughout space with a number concentration, N, then the number of particles sampled over the small interval δt is given by $\delta n = N|\mathbf{u}_p|\mathbf{A}(\mathbf{x})$, where $\mathbf{A}(\mathbf{x})$ is the cross-sectional area of the probe volume in direction $\mathbf{x} = \mathbf{u}_p/|\mathbf{u}_p|$. If it is further assumed that the sample volume has a constant cross-section in all directions (i.e. a sphere), then it follows that the probability of detecting particles of different velocity can be made independent of the velocity by dividing each individual measurement of the quantity ψ_i by the velocity magnitude

$$\bar{\psi} = \frac{\sum_{i=1}^{n_p} \psi_i/|\mathbf{u}_{p_i}|}{\sum_{i=1}^{n_p} 1/|\mathbf{u}_{p_i}|}, \tag{3.22}$$

and

$$\overline{\psi'^2} = \frac{\sum_{i=1}^{n_p} (\psi_i - \bar{\psi})^2/|\mathbf{u}_{p_i}|}{\sum_{i=1}^{n_p} 1/|\mathbf{u}_{p_i}|}, \tag{3.23}$$

where n_p is the total number of particles in the sample. At the time, very few LDV systems were capable of measuring three velocity components at once, and hence they proposed

that the vector magnitude quantities given in equation (3.22) be replaced by the velocity component in the direction of the measurement. Using stochastic measurement simulations, this method proved to be satisfactory in flows where the mean velocity coincided with the direction of measurement and the turbulence intensity was greater than 15% (values less than this do not require correction) and less than 30%. For turbulence intensities greater than 30%, the one-dimensional model very rapidly over-estimated the correction because the swept volume had significant components in the other two directions that were not measured. In practice, these corrections provide another problem, in that the sample volume is almost always a high-aspect ratio ellipsoid rather than a sphere. Thus in strong three-dimensional flows, the velocity component along the major axis of the ellipsoid will be under-represented unless further volume corrections are made.

In the current experiment, the flow was dominated by two-dimensional fluctuations which could be measured by the PDA. Furthermore, the axis of symmetry of the probe volume was aligned along the axis of symmetry of the flow, giving both dominant velocity components an equal probability of detection. Thus, provided the concentration was uniform, the corrections provided by equations (3.22) and (3.23) could be used to accurately correct for the velocity bias.

Further advancements in bias correction were made by George (George, 1976), who derived a more generalized correction which was valid for non-spherical probe volumes. This estimator is given by

$$\bar{\psi} = \frac{\sum_{i=1}^{N} \psi_i \, \Delta t}{\sum_{i=1}^{N} \Delta t}, \tag{3.24}$$

where Δt is the residence residence time of the particle within the sampling volume. This represented a significant contribution to bias correction, as it allowed accurate corrections to be made to single-component data as long as the gate time of the sampled particle could be obtained. Unfortunately in the current experiment, software limitations did not allow for the recording of the particle's gate time when the data was collected and hence, all velocity data was corrected using the 2-D McLaughlin and Tiederman correction. However, data reprocessed after a software revision allows these various velocity bias corrections to be assessed (figure 3.7). As can be observed, no bias correction is needed within the

a) mean velocity

b) rms velocity
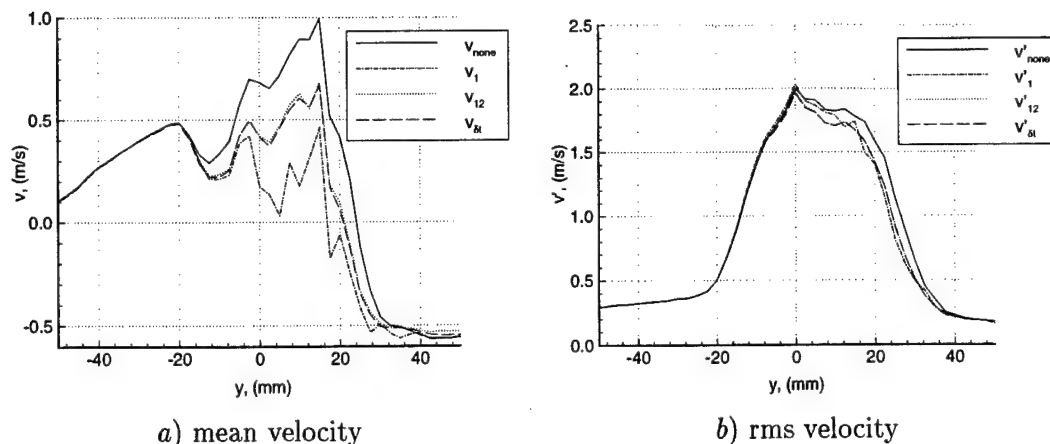
Figure 3.7: Velocity bias corrections applied to the cross-stream velocity at $x = 100$ mm.

freestream ($y < -20$ mm) due to the low turbulence intensity. Once inside the mixing region ($y > -20$ mm), the corrected profiles deviate from the unweighted estimate. Once $y > -10$ mm, the one-dimensional correction begins to grossly over correct, while the two-dimensional correction and gate time corrections produce indistinguishable results. This is in spite of the fact that use of the two-dimensional correction was strongly discouraged by a special panel of the ASME (Edwards, 1987), presumably due to the fact most generalized turbulent flows are not confined to two dimensions.

The correction posed by McLaughlin and Tiederman also implicitly assumes that the sampling volume is of equal size for all particles which pass through it. For the two phase flows measured in this experiment, this criterion is not met if the whole size range is considered at once. However, by discretizing the size distribution into several groups, this effect can be mitigated due to the fact that most particles within the same size class will have approximately the same effective probe area and also have similar velocities (If all particles had the same velocity irrespective of size, then a change in effective sampling volume would have no effect on the averaged velocity).

The last point to note is that in both of the above corrections, it was assumed that the concentration of particles remained uniform. As will be shown in the later sections, this is clearly not maintained within the mixing region of the shear layer, where particles are preferentially entrained across specific regions of the the large scales leaving other regions

nearly void of particles. This problem can be compensated through the use of conditional averaging, assuming that the concentration inhomogeneities are limited to the large scales. If the concentration is maintained at a uniform level for short times, then the above corrections can be applied independently to each of these short intervals. The total time average is then recovered by equally weighting each of the phase averaged quantities.

3.3.4 Effect of Velocity Gradients

In the preceding section, it was shown that temporal velocity fluctuations in the vicinity of the probe volume will result in a bias of the temporally averaged quantities. In a similar manner, spatial variations of the velocity will also result in a bias of the averaged measurements. If there are spatial gradients of the velocity, then the region of the sample volume in the high-velocity area will tend to produce more velocity bursts than the region occupied by the slower velocity. This is typically only a problem for continuous signal LDV applications, where many particles are scattering light from a fairly large probe volume. When instantaneous velocity gradients are present, there will be an uncertainty in the Doppler frequency (and hence limitations on the velocity resolution) due to the varying velocities of each scatter within the volume.

For burst mode LDV signals, only the mean gradient causes a problem and results in a broadening of the velocity distribution function. Kreid (Kreid, 1974) has examined both cases, and for burst mode operation gives the following estimate for the bias caused by the velocity gradient:

$$
\frac{U_{bias} - U}{U} = \frac{1}{8}\frac{a^2\,U''}{U} + \frac{1}{4}\left(\frac{a\,U'}{U}\right)^2 + \frac{1}{64}\left(\frac{a^2\,U''}{U}\right)^2 - \\
\frac{1}{32}\frac{a^2\,U''}{U}\left(\frac{a\,U'}{U}\right)^2 - \frac{1}{512}\left(\frac{a^2\,U''}{U}\right)^3 + \dots, \qquad (3.25)
$$

where U is the mean velocity, $'$ represents differentiation in the direction of the gradient, and a is the probe volume radius is the direction of the gradient. Equation (3.25) shows that the first order term in the effect of the velocity gradient depends on the probe size squared. Thus the biasing effects can be minimized by using a suitably small sampling volume. As a worst case example for the current experiment, the greatest effects will be seen in the

initial thin layer coming off the splitter plate, where the velocity changes from 0 to 18 m s^{-1} in just over 1 cm. Neglecting profile curvature and using a probe radius of 40 μmgives a resulting value of $\Delta U/U \approx 1x10^{-5}$.

3.3.5 Probe Volume/Size Bias

Due to the noise characteristics of the photo-multiplier tube and finite resolution of the processor equipment, there is an amplitude threshold which determines the minimum signal intensity required for the system to detect a burst. This implies that larger particles, which will scatter more light from the incident beam, will have a greater chance of detection than smaller ones will. Aerometrics (Aerometrics, Inc., 1994) has developed an approximate correction for this bias through the following heuristic arguments. Consider an incident laser beam that has a Gaussian intensity cross-section as described by

$$I_{incident}(r) = I_o\, e^{-4r^2/d^2_{waist}}, \tag{3.26}$$

where r is the co-ordinate normal to the beam's axis and d_{waist} is the $1/e$ beam waist diameter within the sample volume. Assuming that the incident intensity is approximately constant over the scattering particle, equation (A.15), shows that the scattered intensity depends directly on area of the droplet. In other words,

$$I_{scatter} \propto D^2\, I_o\, e^{-4r^2/d^2_{waist}}. \tag{3.27}$$

The minimum detectable intensity will be the same for each size class, and hence dictate the effective probe detection length, d_{eff}. Selecting a reference droplet size, D_{ref}, and a corresponding reference particle detection diameter, d_{ref}, then gives the relation

$$d^2_{eff} = d^2_{ref} - d^2_{waist} \ln\left(\frac{D_{ref}}{D}\right). \tag{3.28}$$

Equation (3.28) can be verified against the experimental data by calculating the effective probe diameter for each burst and plotting each record on a scatter plot. The results of such a calculation using data from the freestream of the spray ($x = 100$ mm, $y = $ -40 mm) are shown in figure 3.8. The effective probe diameter is calculated by multiplying the gate time, Δt_{gate_1}, by the velocity, u_1, measured for the streamwise component. The scatter plot clearly shows that the effective length and intensity both increase with particle size.
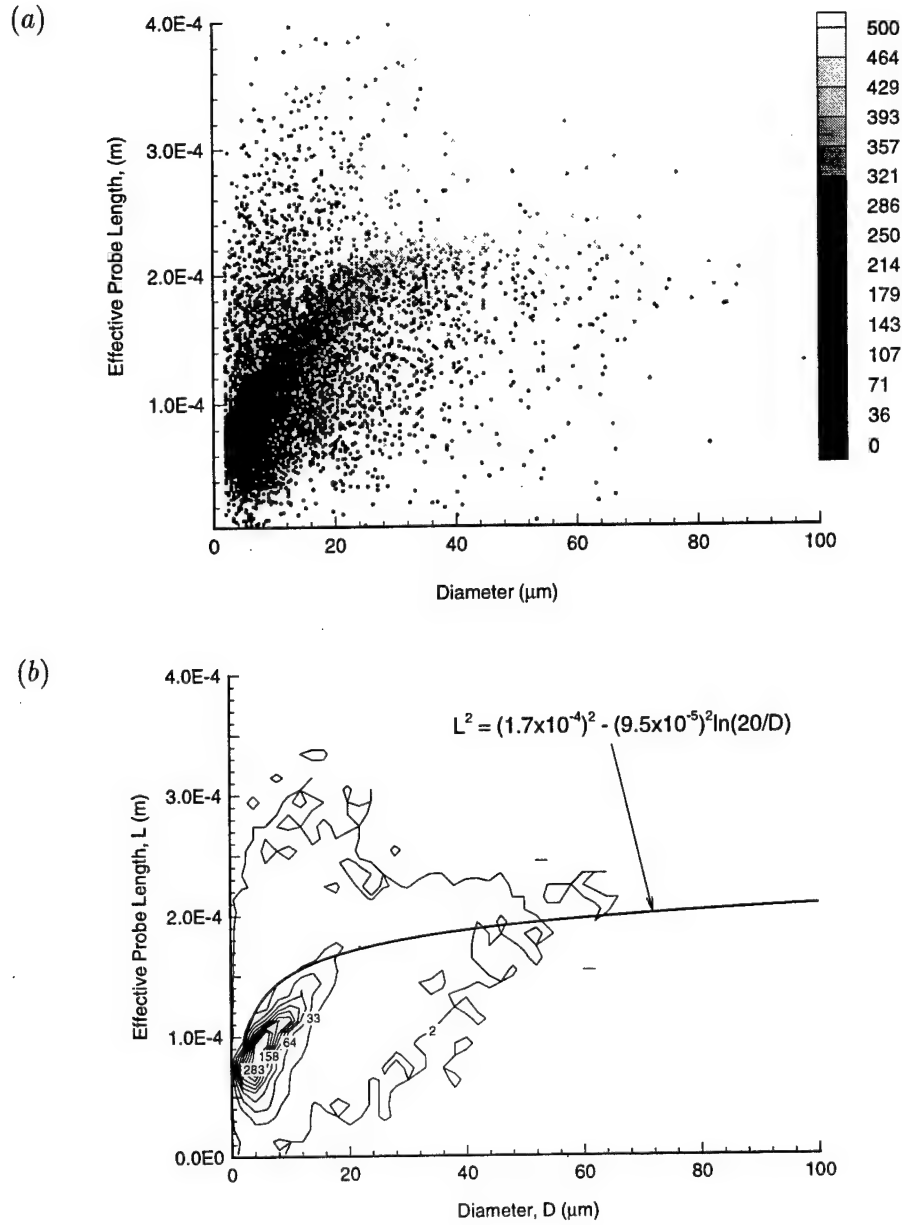
Figure 3.8: Effective probe length as a function of the particle diameter. *a*) Scatter plot of effective probe length vs. particle diameter. Grayscale of symbol corresponds to burst intensity in mV. *b*) Particle number density contours and theoretical curve fit. The pdf is non-normalized and averaged over the lengths $\Delta d_{probe} = 10 \ \mu$m and $\Delta D = 2 \ \mu$m.

In theory, equation (3.28) sets an upper bound on d_{eff} for each droplet size. Using a reference point $(D_{ref}, d_{ref}) = (20, 170)$ μm and a beam waist of 95 μm appeared to give the closest match to the upper bound visible on the number density contour plot. Although the match appears close in some regions, the overall shape of (3.28) and the observed data do not seem to agree — the bend in the knee of the fit ($D = 10$ μm, $d_{eff} = 150$ μm) is too sharp and does not match overall curvature of the observed cutoff. This could be caused by several factors: 1) the shape of the actual intensity profile is not exactly Gaussian as assumed by (3.26), and 2) the derivation of equation (3.28) assumed that the particle was illuminated uniformly, which is clearly not the case for the larger sized particles.

With these types of uncertainties involved in a possible correction formulation, no attempts were made to correct for this systematic bias. Any corrections implemented would have required extensive additional manipulation, and would most likely have increased the noise level of the resulting data.

3.3.6 Effect of Non-Uniform Illumination

The analysis of Appendix A and Appendix B assumed that the light intensity was uniform over the entire incident area of the droplet. For a small particle in a Gaussian beam distribution this seems to be a reasonable assumption, but as the particle size gets within an order of magnitude of the probe volume diameter, this is not likely to be valid. The geometric optics theory developed previously can readily be adapted to cases of non-uniform illumination, and as has been done by Sankar *et al* (Sankar and Bachalo, 1991; Sankar et al., 1992). Their results indicate that as the droplet size increases, the phase calibration curve becomes nonlinearly dependent on the trajectory of the particle through the sample volume. For example, in the case of a large water droplet, most sizing is typically performed using the light scattered by the first-order internal refraction, as it is many times greater in amplitude in the forward scatter direction than any of the other components (excluding diffraction). When large droplets move through the edge of the sample volume, however, the light incident on the particle which is sent to the receiver via refraction is coming from a very weak portion of the incident beam. The edge of the particle, which is now in the center of the beam, produces a bright reflection which is roughly equal in

amplitude with the refracted component. These two components then interfere with one another to produce a different phase shift than was expected.

This difficulty can be diminished by several factors: 1) using multiple detectors, 2) optimizing the beam crossing angle, and 3) performing intensity validation. Sankar *et al* (Sankar et al., 1992) found that by increasing the beam intersection angle from 1.8° to 5.4°, the relative phase and interference characteristics between the $p = 0$ and $p = 1$ modes were favorably reduced, and allowed for increased discrimination of those particles in off-axis trajectories. The intensity validation can be used simply to verify that the scattered light intensity is within a given range for a fixed particle size. If a very bright drop is sized and found to have a small diameter, then it is likely that it may have been a large drop on the edge of the probe volume. Some of the bright particles which were sized to be less than 30 μm in figure 3.8 may be due to this effect. Note however, that the occurrence of large diameter off-axis trajectories are rare due to the small detection cross-section of this area and the great number of smaller drops present in the current spray.

3.3.7   Small and Non-Spherical Particles

The results of the analysis in Appendix B, although illustrative, are subject to the constraints of geometric optics. For an Ar$^+$ laser, this implies that the results become suspect once the particles are smaller than 5 μm. For these small size ranges, Mie theory has been utilized to validate the calibration curves (Sankar et al., 1991). It was found that the phase/diameter calibration curves began to oscillate about the linear curve for these smaller sizes, resulting in a increased uncertainty. For the optical configuration used in this thesis, the uncertainty is approximately ± 1 μm for particles smaller than 5 μm.

The theory used in Appendix B to illustrate the operation of the PDA was also dependent upon the particle remaining spherical, as the symmetry of the problem allowed for many simplifications which made the formulation tractable. For irregularly shaped particles such as metal powders or highly deformed droplets, the derivation would be exceedingly complex and would depend strongly upon the shape and orientation of the particle. If, however, the particle is only slightly non-spherical, then a size measurement made using a reflective scattering mode would measure the local radius of curvature corresponding to

the region of the drop where the collected light was scattered. Bachalo (Bachalo, 1994) has pointed out that the same would be true for the first refractive scatter. Thus, measurements of droplets under an unsteady aerodynamic deformation loading would produce over- and under-estimates of the droplet's equilibrium state, depending upon the droplet's vibrational modes and instantaneous orientation while it was in the probe volume, and would hence result in an apparent broadening of the size distribution.

Droplet deformation will occur when external stresses (both normal and tangential) are applied to the droplet's surface. These external stresses will be resisted by both surface tension due to the interface curvature and viscous forces resulting from the internal droplet motion. The resulting surface deformation will become appreciable when the magnitude of the deforming and restoring forces are comparable. Hinze (Hinze, 1955) has examined this problem in the context of break-up processes and has suggested two non-dimensional groups to account for the various combination of dominant interactions:

$$N_{We} = \frac{\tau D}{\sigma} \qquad \text{and} \qquad N_{\nu} = \frac{\mu_p}{\sqrt{\rho_p \sigma D}},$$

where τ is the externally applied stress, σ is the droplet/air interfacial surface tension, and μ_p is the dynamic viscosity of the droplet. N_{We} corresponds to the traditional Weber number generalized to the dominant stress field, and N_{ν} is typically referred to as the Ohnesorge number which relates the ratio of the internal resisting forces. For the large droplets most likely to be deformed, $N_{\nu} \sim 0.01$, which states that the surface tension dominates the resisting force, rendering viscous forces unimportant except for damping the vibrational motion of the droplet.

If the droplet is assumed to be moving ballistically through large velocity fluctuations, with a large particle Reynolds number ($\text{Re}_p \gg 1$) such that the viscous stresses acting on the droplet are small, then the stagnation pressure ($\tau = \rho_g u_g^2$) will be the dominant force acting to imbalance the spherical symmetry imposed by surface tension. This gives a value of $N_{We} = 0.04$ for a 100 μm water droplet ($\sigma = 0.073 \, \text{Nm}^{-1}$) with a relative velocity of 5 m s^{-1}. Hinze (Hinze, 1949) has derived the following formula to describe the change in the radius of the droplet when subjected to an impulsive velocity change U'

$$\left. \frac{\Delta R}{R} \right|_{max} = -0.17 \frac{\rho_g U'^2 R}{\sigma}. \qquad (3.29)$$

Using the same conditions of the previous calculation gives the maximum deformations due to the stagnation pressure to be 0.3%. This is well below the sizing resolution of the instrument.

When the measurements are examined, however, the maximum Reynolds number attained by the largest particles is approximately 20, which is small enough to indicate that external viscous stresses on the majority of the drops will typically exceed or at least be comparable to the inertial ones (i.e. stagnation pressure). A rough estimate of the influence of these viscous stresses can be done by considering order of magnitude arguments and forming a Weber number based on the shear acting on the droplet. The force due to shear stresses acting on the surface of the droplet will be given by $\tau = \mu_g \partial U/\partial y D^2$, where μ_g is the the dynamic viscosity of the surrounding air, $\partial U/\partial y$ is the shear stress at the droplet surface, and D is the droplet diameter. The restoring forces due to surface tension are given by σD, where σ is the surface tension of the air water interface. The ratio of these two forces can be used to form a shear Weber number,

$$N_{We} = \frac{\mu D}{\sigma} \frac{\partial U}{\partial y}. \tag{3.30}$$

Using the Stokes solution to estimate the maximum normal velocity gradient on the surface of the droplet gives $\partial U/\partial y = 3\Delta U/D$. For a 100 μm droplet with a 5 m s^{-1} slip velocity, $N_{We} \sim 0.004$. Although this is not a numerical estimate of the actual droplet deformation, as was (3.29), this does state that the restoring force of surface tension is many orders of magnitude greater than the deforming forces, indicating that the particle will remain close to spherical.

3.4   Conditional Averaging

The seemingly random nature of turbulence has fostered much analysis on the statistical description of different types of turbulent flows. Traditionally, these analyses focus on the various moment distributions of the velocity probability distribution functions and their corresponding spectra and correlations. The statistical analyses are particularly successful under certain flow conditions, such as the idealized case of homogeneous, isotropic

turbulence. For most practical flows, however, the inhomogeneities and anisotropies present invalidate most of the simplifying assumptions that enabled a tractable analysis and closure modeling for the ideal flow. To this day, this is still a active area of turbulence research.

A large part of the problem with traditional statistical analysis is that the simpler descriptions (such as single point analysis) ignore the underlying structure and interaction which takes place between the diverse scales of the flow. The crucial lack of a physical connection to the flow field was recognized, and has since fostered a resurgence of methods such as flow visualization which allow for the detailed examination of the flow field structure. Among the methods which were introduced, the concept of conditional averaging has been of great value to many turbulent flows (Atta, 1974). The fundamental idea behind conditional averaging is that certain events within the turbulent flow field have a similar structure every time they occur, and if it was possible to limit the data sampling to times only during these events then it would be possible to reconstruct a portrait of the event. These similarities of the event may often times be masked by the stochastic jitter that is inherently characteristic of all turbulent flows. However, this problem can be circumvented if some quantity can be identified and measured which signals the onset of the event. Mathematically, this is expressed as

$$\langle \psi \rangle = \frac{\lim_{T \to \infty} \frac{1}{T} \int_0^T \psi(t) I(t) dt}{\lim_{T \to \infty} \frac{1}{T} \int_0^T I(t) dt}, \tag{3.31}$$

where $\langle \rangle$ denotes conditional average, ψ is the averaged quantity, T is the total sample length and I represents the so-called "conditioning function" which identifies the region to be sampled by assuming the value 1 when the condition is met and 0 otherwise. For example, at a fixed point in a boundary layer, a certain velocity magnitude significantly higher than the mean value may be selected as a "trigger" or conditioning signal. Thus when a turbulent burst occurs and brings high momentum fluid into the sublayer, the trigger will be activated and signal the temporal duration of sampling (Kovasznay et al., 1970). Admittedly, the above example is a bit simplistic — care must be used in selecting the appropriate conditioning function to ensure that resulting average is physically meaningful and actually aids in the interpretation of the events in question.

As stated in the introduction, the work of this thesis is interested in characterizing

44

how the large-scale events in the turbulent shear layer interact with the dispersed phase of droplets. The shear layer is one of several flows in which the large scales are receptive to low-amplitude forcing. That is, by introducing an artificial disturbance the jitter and randomness of the the strength and spacing of the large scale structures is greatly reduced. This enables a conditional average of the large scales to be performed, using the artificial disturbance as a phase reference or conditioning signal (hence the term phase average). Under these circumstances, the conditioning function is generalized to a periodic train of delta functions, each isolating a specific point ϕ within the disturbance signal:

$$I(\phi, t) = \delta[2\pi f(t - t(\mathrm{mod})\frac{1}{f}) - \phi], \tag{3.32}$$

where ϕ is the phase angle of the reference disturbance signal, and f is the frequency of the disturbance signal. For discretely sampled data, the duty cycle of the conditioning function must have a finite width so that the data can be averaged. The delta function is then replaced by a square wave signal with a pulse width of $\Delta\phi$ and a frequency f

$$I(\phi_i, t) = \begin{cases} 1 & \text{for } \frac{(i-1)}{P} < t \bmod \frac{1}{f} < \frac{i}{P} \\ 0 & \text{for all other } t \end{cases}, \quad i = 1 \text{ to } P \tag{3.33}$$

where P is the number of bins in one wavelength ($P = 2\pi/\Delta\phi$). The phase-average for the variable ψ then takes the form

$$\langle\psi(\phi_i)\rangle = \frac{\lim_{T\to\infty} \frac{1}{T} \int_0^T \psi(t) I(\phi_i, t) dt}{\lim_{T\to\infty} \frac{1}{T} \int_0^T I(\phi_i, t) dt} \tag{3.34}$$

where ϕ_i is the discrete phase angle of the forcing function over one period.

For records with a constant sampling interval, expression (3.34) reduces to:

$$\langle\psi(\phi_i)\rangle = \frac{1}{M} \sum_{j=1}^{M} \psi(t_j) \tag{3.35}$$

where M is the total number of samples that occurred while $I = 1$.

3.4.1 Conditional Averaging Applied to Phase Doppler Techniques

As discussed in §3.3.3, there are inherent biases present in data sets collected via burst mode laser Doppler interferometry due to the dependency of each realization upon the

particulate velocity and concentration. In most LDV applications, it is possible to maintain a uniform concentration of particles throughout the flow field through careful control of the seeding apparatus. For multi-phase sprays and dispersions however, this is not always possible as these particles have a finite inertia and are not constrained to follow the carrier phase fluctuations. This results in selective dispersion and entrainment that varies with particle size, and invariably results in a non-uniform concentration of particles across the scale of the flow field. In a strongly periodic flow, conditional averaging provides a technique to correct for this concentration bias and recover a time averaged quantity that is consistent with the standard definition.

The definition for the time average of a general quantity ψ is typically defined as

$$\overline{\psi} = \frac{1}{T} \int_0^\infty \psi(t)dt, \tag{3.36}$$

where T is the duration of the sampling interval. Consider now that the data is obtained using phase Doppler techniques, implying that each sample arrives randomly in time, and that the flow being measured is quasi-periodic with a base frequency f. The time series can then be divided by the passage of each wave into W continuous records which can be further subdivided into M bins of width $\Delta t = M/f$ (figure 3.9). This allows the averaging integral to be expressed as the sum of the average of each individual bin of all the waves in the record

$$\overline{\psi} = \frac{1}{T} \sum_{k=1}^{W} \sum_{j=1}^{M} \left(\int_{t_{j,k}}^{t_{j+1,k}} \psi(t)dt \right) = \frac{1}{T} \sum_{k=1}^{W} \sum_{j=1}^{M} \left(\overline{\psi}_{j,k} \Delta t \right), \tag{3.37}$$

where $\overline{\psi}_{j,k}$ is the time average of the individual bin. For uniform concentrations within the time Δt (which requires that $U\Delta t$ be much smaller than the flow scales causing the non-uniform concentration) this average can be expressed in the unbiased form given in equation (3.24)

$$\overline{\psi}_{j,k} = \frac{1}{\Delta t} \int_{t_{j,k}}^{t_{j+1,k}} \psi(t)dt = \frac{\sum_{i=1}^{n_{j,k}} \psi_{i,j,k} w_{i,j,k}}{\sum_{i=1}^{n_{j,k}} w_{i,j,k}}, \tag{3.38}$$

where $\psi_{i,j,k}$ is the ith sample of $n_{j,k}$ in the jth bin of the kth wave and $w_{i,j,k}$ is the corresponding weight function used to correct for the velocity bias. Expressing the total duration
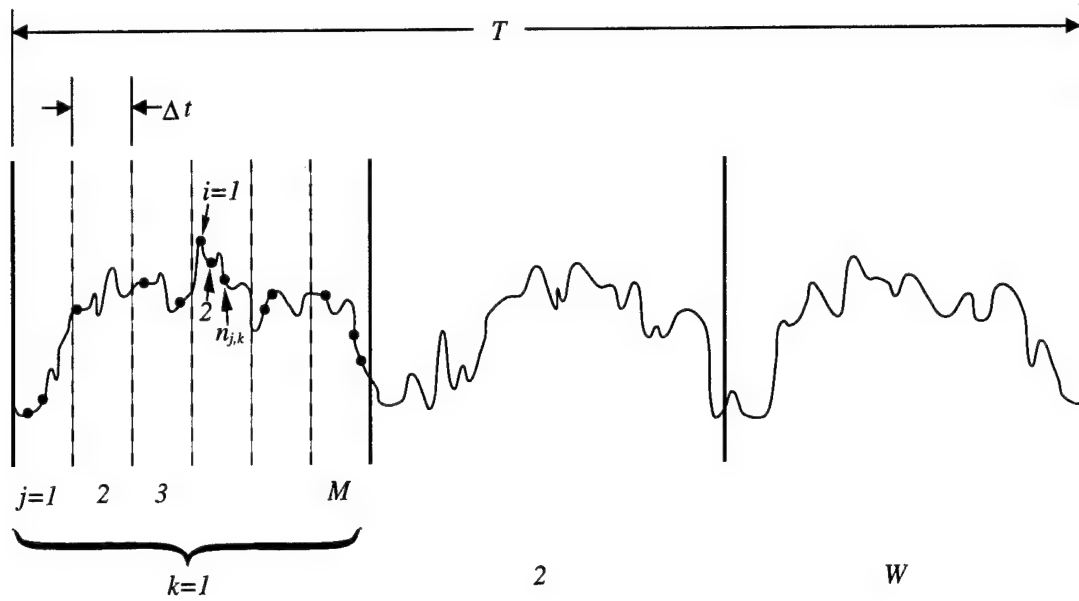
Figure 3.9: Illustration of phase Doppler data series for conditional averaging of quasi-periodic flows.

of the sample as $T = WM\Delta t$ and rearranging the order of the sums then gives

$$\overline{\psi} = \frac{1}{WM}\sum_{k=1}^{W}\sum_{j=1}^{M}\overline{\psi}_{j,k} = \frac{1}{M}\sum_{j=1}^{M}\left[\frac{1}{W}\sum_{k=1}^{W}\overline{\psi}_{j,k}\right] = \frac{1}{M}\sum_{j=1}^{M}\langle\psi_j\rangle. \qquad (3.39)$$

This last step follows from the definition of the periodic conditional average defined in equation (3.34)

$$\langle\psi_j\rangle = \frac{\frac{1}{T}\int_0^T \psi(t)I(\phi_i,t)dt}{\frac{1}{T}\int_0^T I(\phi_i,t)dt} = \frac{\sum_{k=1}^{W}\int_{t_{j,k}}^{t_{j+1,k}}\psi(t)dt}{\sum_{k=1}^{W}\Delta t} = \frac{1}{W\Delta t}\sum_{k=1}^{W}\overline{\psi}_{j,k}\Delta t. \quad (3.40)$$

Finally, if all similar bins in each wave ($j = $ constant for all k) have approximately the same concentration and therefore the same number of particles, or approximately the same average then

$$\langle\psi_j\rangle = \frac{1}{W}\sum_{k=1}^{W}\overline{\psi}_{j,k} = \frac{1}{W}\sum_{k=1}^{W}\left(\frac{\sum_{i=1}^{n_{j,k}}\psi_{i,j,k}w_{i,j,k}}{\sum_{i=1}^{n_{j,k}}w_{i,j,k}}\right) \simeq \frac{\sum_{i=1}^{N_j}\psi_{i,j}w_{i,j}}{\sum_{i=1}^{N_j}w_{i,j}}, \qquad (3.41)$$

where N_j now represents the sum of all the particles contained in the bins $j = $ constant. This last assumption is simply a statement that the overall average is equal to the sum of the averages within each wave and is exact for bins with equal number of data points, which

is a reasonable assumption for periodic flows. The final expression of the mean quantity $\overline{\psi}$ is given as

$$\overline{\psi} \;=\; \frac{1}{M}\sum_{j=1}^{M}\langle\psi_j\rangle \;=\; \frac{1}{M}\sum_{j=1}^{M}\left(\frac{\sum_{i=1}^{N_j}\psi_{i,j}w_{i,j}}{\sum_{i=1}^{N_j}w_{i,j}}\right). \tag{3.42}$$

Similar considerations for the variance of ψ result in the expression

$$\overline{\psi'^2} \;=\; \frac{1}{M}\sum_{j=1}^{M}\left(\frac{\sum_{i=1}^{N_j}(\psi_{i,j}-\overline{\psi})^2 w_{i,j}}{\sum_{i=1}^{N_j}w_{i,j}}\right). \tag{3.43}$$

This can be rearranged into the more useful form

$$
\begin{aligned}
\overline{\psi'^2} \;=\;& \frac{1}{M}\sum_{j=1}^{M}\left(\frac{\sum_{i=1}^{N_j}\psi_{i,j}^2 w_{i,j}}{\sum_{i=1}^{N_j}w_{i,j}} - 2\overline{\psi}\frac{\sum_{i=1}^{N_j}\psi_{i,j}w_{i,j}}{\sum_{i=1}^{N_j}w_{i,j}} + \overline{\psi}^2\right) + \frac{1}{M}\sum_{j=1}^{M}\left(2\langle\psi_j\rangle^2 - 2\langle\psi_j\rangle^2\right)\\[2mm]
=\;& \frac{1}{M}\sum_{j=1}^{M}\left[\frac{\sum_{i=1}^{N_j}(\psi_{i,j}^2 - 2\psi_{i,j}\langle\psi_j\rangle + \langle\psi_j\rangle^2)w_{i,j}}{\sum_{i=1}^{N_j}w_{i,j}} + \left(\langle\psi_j\rangle - \overline{\psi}\right)^2\right]\\[2mm]
=\;& \frac{1}{M}\sum_{j=1}^{M}\left[\frac{\sum_{i=1}^{N_j}(\psi_{i,j} - \langle\psi_j\rangle)^2 w_{i,j}}{\sum_{i=1}^{N_j}w_{i,j}} + \left(\langle\psi_j\rangle - \overline{\psi}\right)^2\right].\\[2mm]
=\;& \frac{1}{M}\sum_{j=1}^{M}\left[\langle\psi^{\star 2}\rangle_j + \left(\langle\psi_j\rangle - \overline{\psi}\right)^2\right]
\end{aligned}
\tag{3.44}
$$

The first term of equation (3.44) is the *phase-averaged rms* and is equal to the variance of all the data points within the phase bin j. The second term is the *coherent rms* and represents the fluctuations of the phase-averaged mean about the time-averaged mean. This term is a filtered rms that shows the contributions of the discrete frequency f and all of its higher harmonics (the frequencies up to $2^n f_s$, where f_s is the frequency of the phase average and $n = \mathrm{int}(\ln(\# \text{ of bins})/\ln(2) - 1)$, will be accurately reflected in the phase average; the harmonics higher than this will be aliased within the phase averaged mean, while all non-integer frequencies of f_s will destructively interfere with themselves and will be reflected in the phase-averaged rms).

Chapter 4

Experimental Facility and Initial Conditions

A two-phase wind tunnel facility was used to generate the droplet laden air stream and subsequent turbulent mixing layer. This facility (figure 4.1) has been used in several other two-phase shear layer studies (Lázaro and Lasheras, 1989; Lázaro and Lasheras, 1992a; Lázaro and Lasheras, 1992b). Since the current work is in some ways an extension of the previous research, care was taken to maintain the facility in a state similar to the conditions used in the previous experiments. A detailed description of the design and construction of the facility is given elsewhere (Lázaro, 1989), but a brief overview of the layout and components used are given in the following section. The last section of this chapter then characterizes the initial conditions for the dispersed and continuous phase, as well as the development of the unladen gas flow.

4.1 Facility Components

The test rig is divided into three main sections: the wind tunnel, the spray generation system, and the test section (figure 4.1). The wind tunnel portion consists of a blower, flow conditioning devices, and a two-dimensional contraction leading into the test section. The wind tunnel was powered by a 1 hp electric motor coupled to a centrifugal fan (Chicago Blowers #15 SQA 9T) designed to deliver 1700 cfm at 1400 rpm with a 1.5" of H_2O static

48
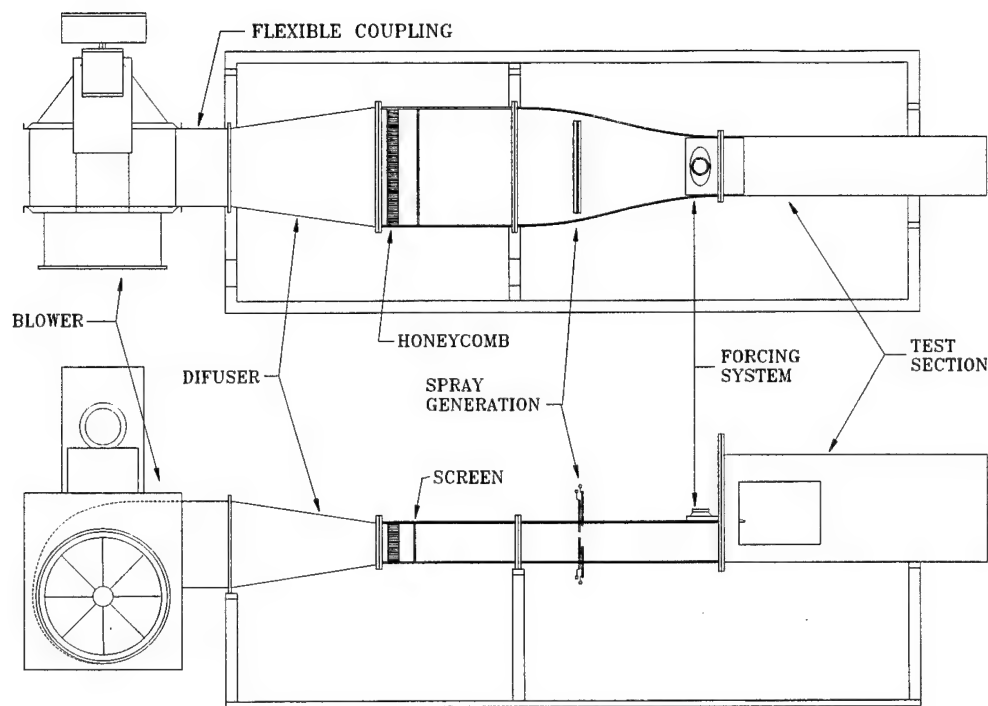
Figure 4.1: Schematic of wind tunnel facility.

pressure drop across the fan. Inlet throttling vanes were used to control the outlet velocity and pre-swirl the air entering the blower. The throttle was left in the full open position for all of the reported experiments, which provided a test section velocity of approximately $16.5 \mathrm{~m\,s^{-1}}$ (when the atomizers were not in use). To keep the vibrational noise within the test rig to a minimum, the blower assembly was secured with vibration mounts and isolated from the rest of the experiment via a flexible rubber conduit. A symmetrical sheet metal transition nozzle with a contraction ratio of 1.59:1 followed the blower, connecting it to the turbulence management section. Honeycomb (0.9 cm spacing, 0.03 cm wall thickness, 5 cm long) was placed immediately downstream of the nozzle as a flow straightener, and a wire screen (30 mesh, 40.8% open area, 0.012" diameter) was used to ensure uniformity across the width of the tunnel.

The spray generation section consisted of an array of 184 air-blast atomizers situated just upstream of the horizontal contraction. Each atomizer was supplied with de-
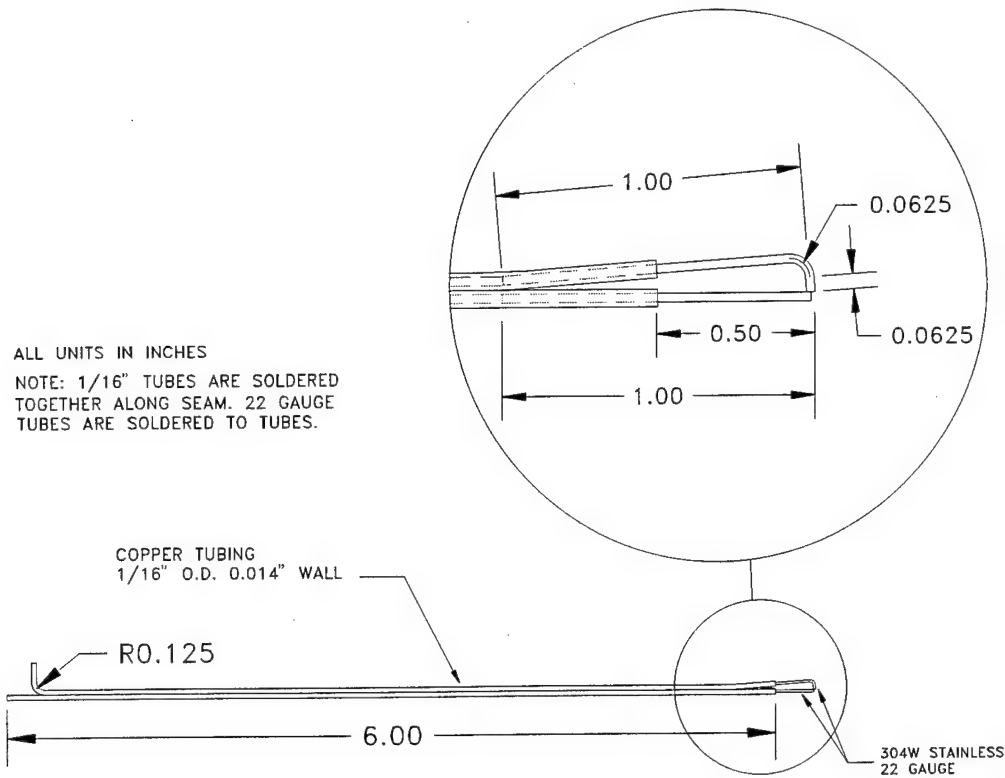
Figure 4.2: Dimensions of an individual air-blast atomizer unit.

ionized water and compressed air through 1/16" outer diameter copper tube supply stems. A 22G (0.016" inner diameter) 304 stainless steel tube was soldered to the supply stems, and the atomization took place as the pressurized air stream impinged perpendicularly upon the exiting water jet (figure 4.2). In order to ensure uniformity in the droplet loading, the atomizers were arranged in an triangular pattern (figure 4.3) with a horizontal spacing of approximately 16 mm and a spacing between rows of 12 mm. This gave an array with 8 staggered rows, alternating between 22 or 24 atomizers, covering approximately 8 cm in the cross-stream direction and 38 cm of the spanwise direction. The flowrate of water and air pressure to these eight rows was adjusted independently to obtain a uniform size and concentration distribution across the depth of the tunnel. This was done through trial and error, and the resulting flowrates were:
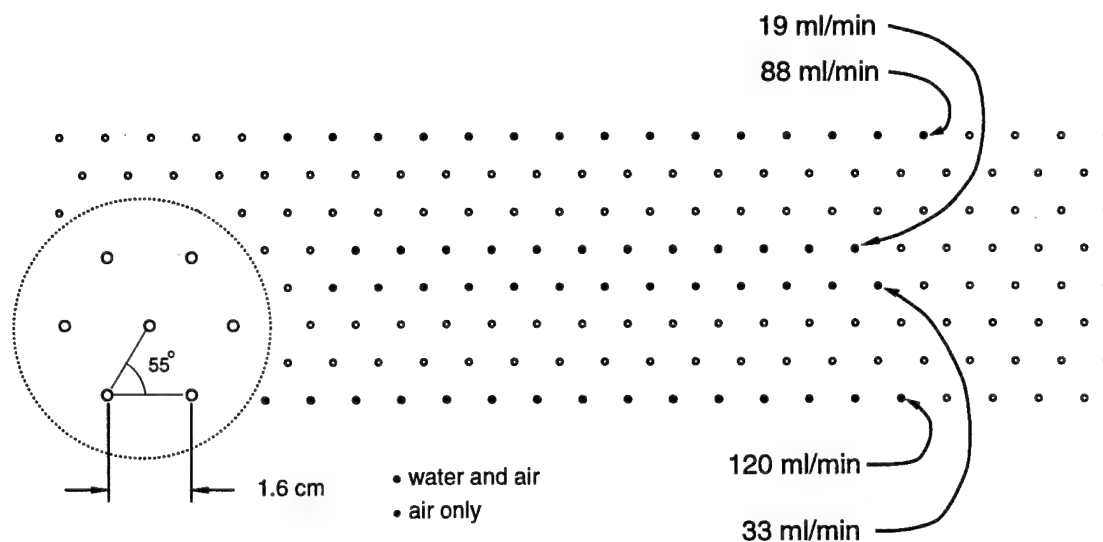
Figure 4.3: Cross-section of the spray generation device showing the spatial configuration of the atomizer array.

$$\dot{Q}_1 = 88 \text{ ml/min}, 18 \text{ psia}$$
$$\dot{Q}_4 = 20 \text{ ml/min}, 18 \text{ psia}$$
$$\dot{Q}_5 = 33 \text{ ml/min}, 20 \text{ psia}$$
$$\dot{Q}_8 = 120 \text{ ml/min}, 20 \text{ psia}$$
$$\dot{Q}_2 = \dot{Q}_3 = \dot{Q}_6 = \dot{Q}_7 = 0,$$

where $\dot{Q}_1$ is the flowrate to the top row of atomizers near the upper wall of the wind tunnel. To minimize the accumulation of water on the sidewalls, only the central 15 atomizers in each row were supplied with water. This configuration gives an effective spray cross-sectional area of approximately 10 cm x 15 cm at the entrance to the test section, which can be used to provide a rough estimate of the dispersed phase volume concentration. From the above flow rates and a resulting freestream velocity of 18 m s^{-1}, the volume fraction is calculated to be $\alpha_p \sim 1.6\,x\,10^{-5}$, which agrees quite closely with the measured value of $1.5\,x\,10^{-5}$. The high-speed gas jets of the atomizers were placed in the array such that they pointed in the direction of the surrounding gas flow. The streamwise momentum flux of these atomizers accounted for approximately 10% of the total momentum of the two-phase

flow, and increased the mean velocity of the air within the test section from $16.5 \mathrm{~m\,s^{-1}}$ to $18 \mathrm{~m\,s^{-1}}$. Hence, to maintain a uniform velocity across the test section, all of the atomizers were supplied with air (even the ones without water flow).

The two-phase (droplet laden air flow) created by the atomizers was then accelerated through a two-dimensional nozzle (contraction ratio 2:1), reducing the thickness of the boundary layers and decreasing the relative turbulence intensity which resulted from the spray generation. The length of the nozzle was designed to provide a uniform gas velocity and droplet concentration across the span of the test section. Furthermore, the residence time of the spray prior to the test section was designed to be long enough for all the droplets to equilibrate with the exiting gas velocity. Thus at the beginning of the test section the concentration was not only uniform, but the two phases had the same approximate velocity (within $0.5 \mathrm{~m\,s^{-1}}$ for the largest droplets). The test section itself consisted of a 3-sided channel which extended 100 cm in the downstream (x) direction, 45 cm in the cross-stream (y) direction, and 25.4 (cm) in the spanwise (z) direction. The upper wall surface of the test section was removed to allow unrestricted development of the shear layer and entrainment of the ambient air. Windows were cut in the test section sidewalls to allow for optical access and were fitted with sliding shutters so that only the region of interest was exposed during measurement. An optical traverse platform provided access to the first 33 cm of streamwise shear layer development and 20 cm in the cross-stream direction.

In order to increase the coherence of the naturally evolving large-scale vortices of the shear layer, a forcing system was used to add a velocity perturbation to the boundary layer at the end of the splitter plate. The system is modeled after that used by Fiedler and Mensing (Fiedler and Mensing, 1985), and consisted of a speaker attached to a small plenum chamber (25 x 25 x 2 cm) which terminated at the end of the splitter plate with a narrow spanwise slot (figure 4.4). For the low frequencies used in this experiment (less than 140 Hz), the acoustic wavelength is at least ten times the dimensions of the forcing system, preventing the formation of any significant standing wave patterns and phase shifts along the length of the slot. In other words, the pressure waves travel with a great enough speed such that the speaker acts as a set of bellows, alternately sucking and blowing air through the slot in response to the driving voltage.
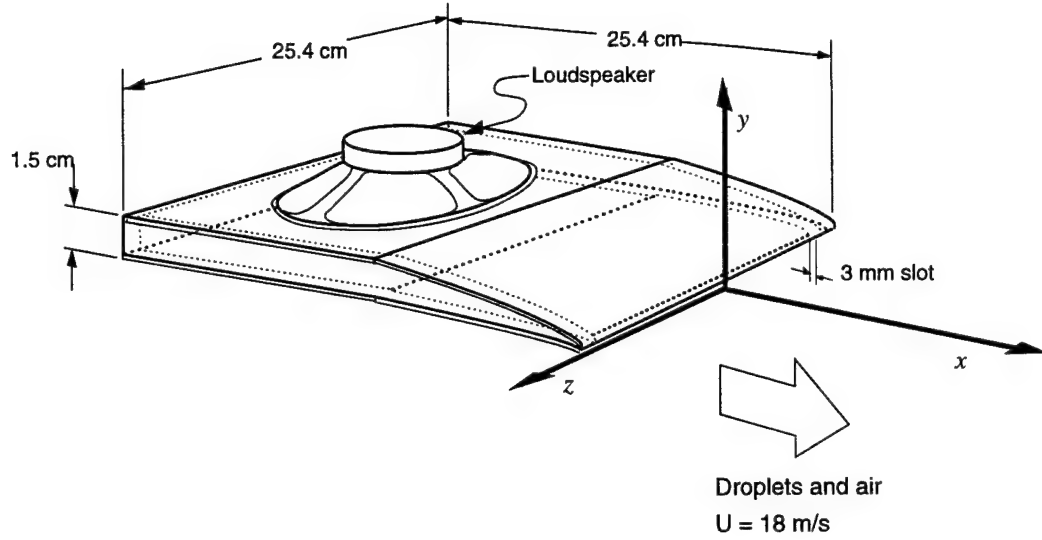
Figure 4.4: Schematic of forcing system and depiction of experimental co-ordinate system.

The forcing signal was provided by a custom-made signal generator (Lázaro, 1989), which used a programmable e-prom and a digital-to-analog converter to produce the desired waveform. The signal was then amplified by an amplifier before being sent to the speaker. To obtain a consistent pairing within the confines of the test section, the flow was forced with a combination of the the fundamental (140 Hz) and first subharmonic (70 Hz) of the naturally evolving shear layer. After sampling the amplified signal sent to the speaker, the shape of the waveform was found to have the functional form:

$$\sin(2\pi f_s t) + 1.93\sin(4\pi f_s t - \Delta\phi), \tag{4.1}$$

where the amplitude has been normalized with respect to the subharmonic component (the sampled waveform had a rms amplitude of 1.31 V), f_s is the first subharmonic frequency, and $\Delta\phi$ is the phase difference between the fundamental and subharmonic, measured to be 212°. Yang and Karlsson (Yang and Karlsson, 1991) have observed that for equal amplitude disturbance waves, $\Delta\phi \sim 90°$ results in a "tearing" growth of the vortices, whereas all other phase angles resulted in pairing events similar to the ones predominantly observed by Winant and Browand (Winant and Browand, 1974). The success of the forcing system's ability to produce a repeatable pairing event was bourn out by measurement, as will be discussed in detail in the next section. The signal generator also produced a brief

TTL timing pulse each subharmonic period which was used as a phase reference signal for the conditional averaging of the flow measurements.

4.2 Initial Conditions

The initial carrier gas phase velocity profiles, measured at $x = 0.7$ cm past the end of the splitter plate are shown in figure 4.5. The exiting stream velocity profile has a mean velocity profile of approximately $18 \, \mathrm{m \, s^{-1}}$ and an initial integral thickness of $\theta_m = 1.7$ mm, where θ_m is defined by:

$$\theta_m(x) = \int_{-\infty}^{\infty} \frac{U(y)}{U_\infty} \left(1 - \frac{U(y)}{U_\infty}\right) dy \tag{4.2}$$

According to stability theory for a hyperbolic-tangent velocity profile (Monkewitz and Huerre, 1982), the most amplified disturbance will have a Strouhal number, St $= f\theta/\overline{U}$ $= 0.032$. Since the initial profile has a slight wake component (see figure 4.8), the appropriate integral thickness to use for comparison should be somewhere after the wake has disappeared, and prior to the first vortex roll-up (Ho and Huerre, 1984). Taking the integral thickness at $x = 2$ cm gives a natural frequency of $f = 0.032(9m/s)/(0.002m) = 144$ Hz, which is consistent with the most amplified frequency obtained from flow visualization (140 Hz). The rms velocity profiles show that the freestream turbulence level due to the atomization processes have been reduced to less than 2% by the stretching action of the two-dimensional contraction. It should also be noted that the turbulence intensity within the boundary layer is substantially higher, reaching a maximum of 18% near the wall. This is indicative of the turbulent state of the boundary layer which has been tripped by the rough absorbency material used on the upper wall in addition to the fluctuations induced by the forcing system.

The optimum design conditions for the facility is to provide constant velocity and concentration profiles across the extent of the test section inlet. This, of course, is a formidable task in any practical situation due to the presence of the solid boundaries. At the surface, the velocity must satisfy a no-slip condition which leads to a velocity deficit and the development of a boundary layer. In turn, the presence of the solid boundary affects the
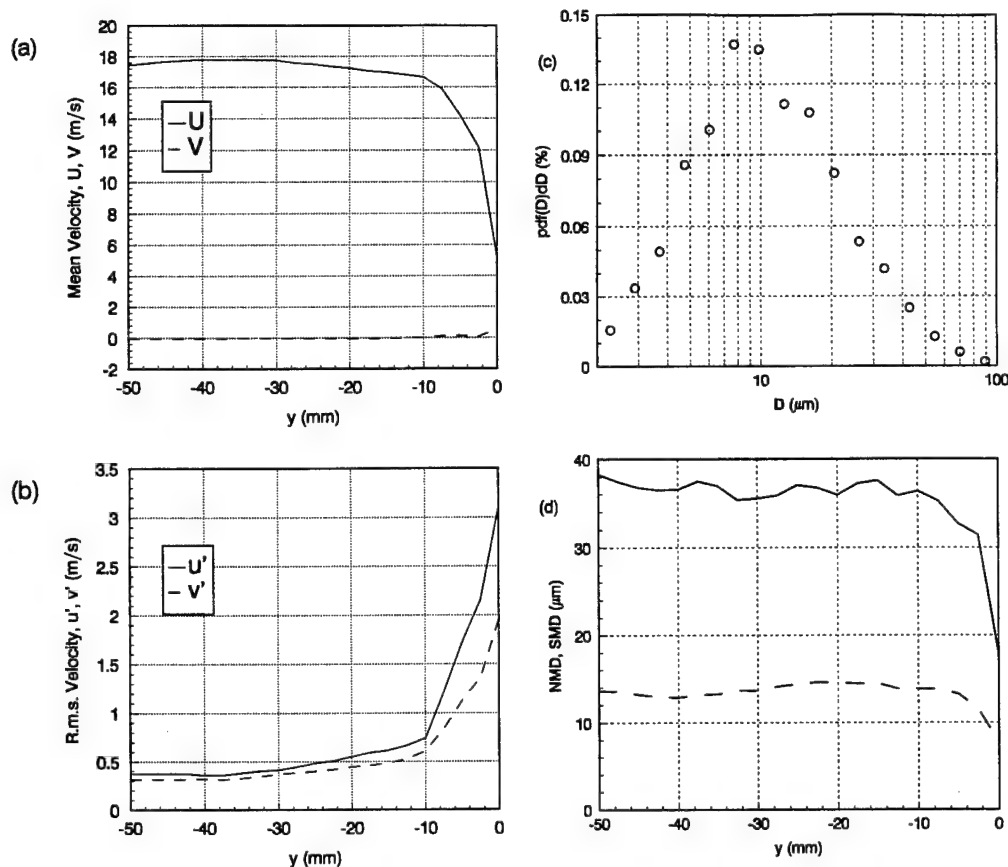
Figure 4.5: Initial conditions at entrance to the test section. (*a*) streamwise and cross-stream mean velocity, (*b*) streamwise and cross-stream rms velocity. (*c*) Number pdf at x = 0.7 cm, y = -10 mm. (*d*) Mean diameter profiles at x = 0.7 cm. ——— , SMD; ——— , NMD

particle distribution in two ways. First, the lower velocities of the boundary layer allow for increased particle sedimentation, affecting a decrease in size. Second, the boundary will act as a sink of droplets as they are absorbed on impact. To counteract these two effects the top row of atomizers was placed within 1 cm of the boundary and the water flowrate was increased. A layer of absorbency material made from a sheet of 1/8" viscose was affixed to the upper surface to prevent water from dripping back into the test section, and a suction system was used to continually remove the water from the material.

A representative size distribution from the freestream shows that the spray is quite
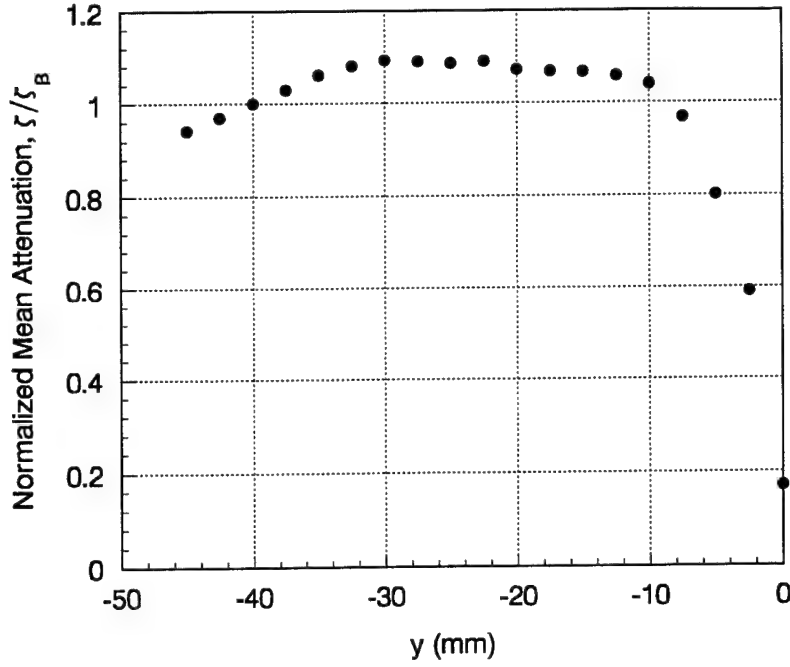
Figure 4.6: Mean attenuation profile at $x = 0$ cm.

polydispersed, with droplets ranging in size from 1 to 100 μm (figure 4.5c). The uniformity of the size distributions can be checked by examining the variation of the Sauter mean diameter (SMD) and number mean diameter (NMD) profiles across the depth of the tunnel. These quantities are defined as different moments of the size distribution

$$\text{NMD} = D_{10} \equiv \frac{\int_0^\infty D\,N(D)dD}{\int_0^\infty N(D)dD} \tag{4.3}$$

$$\text{SMD} = D_{32} \equiv \frac{\int_0^\infty D^3 N(D)dD}{\int_0^\infty D^2 N(D)dD} \tag{4.4}$$

where $N(D)dD$ is the non-normalized number probability distribution function (number of particles per unit size per unit volume). Figure 4.5d shows that the NMD and SMD remain constant throughout the freestream, indicating a uniform size distribution. The boundary layer has produced a sharp decrease in the SMD due to the increased sedimentation mentioned above. The mean attenuation (figure 4.6) indicates good concentration uniformity for -35 mm $< y <$ -10 mm (via equation (3.12) and the knowledge that the SMD is a

constant in this region), and also that the particle boundary layer has a similar thickness (~ 1 cm) to that of the initial velocity profile.

4.3   Evolution of carrier phase

The evolution of the carrier gas phase was recorded by measuring the shear layer in the absence of the water spray. During the measurements, the air supply to the atomizers was left on to maintain approximately the same mean velocity and freestream turbulence conditions that are obtained when the atomizers are producing a spray. A comparison of the initial mean and rms velocity profiles measured both with and without the spray show only a small discrepancy between the two cases (figure 4.7). Note the close agreement between both set of measurements. The small differences observed could be the result of several effects. At first thought, it seems plausible that this change in the mean and rms
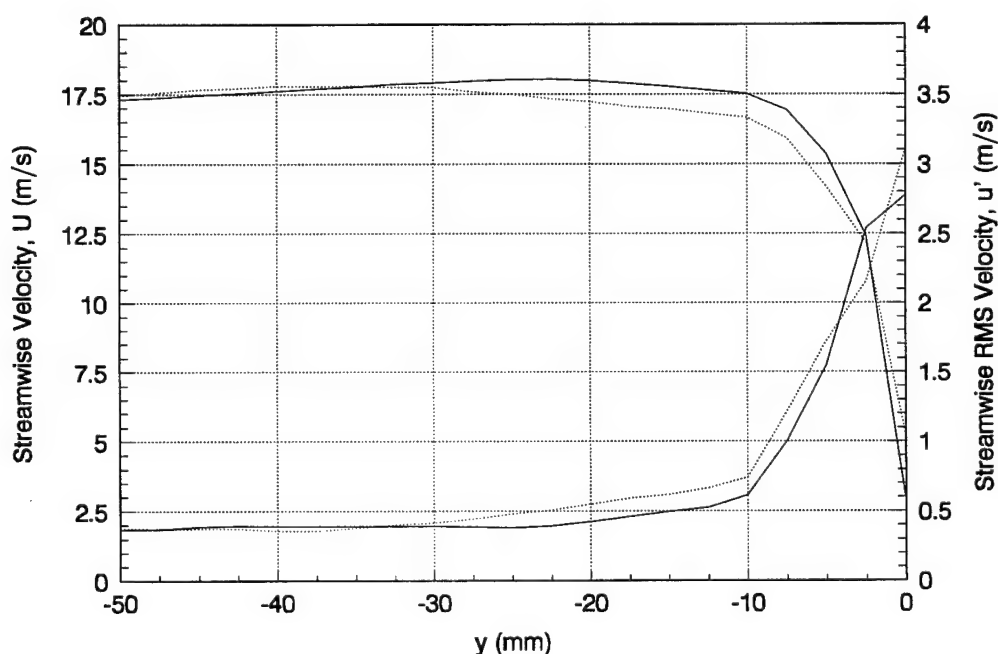
Figure 4.7: Comparison of gas velocity initial conditions with the spray on and off. ——— no water to atomizers; ········ water supplied to atomizers.

velocity may be due to particle/turbulence interaction. However, the extent of the variation is limited to the 3.5 cm closest to the plate, leaving the deep freestream unchanged. If the change were due to the different interaction of jets with the spray, then the profile would be affected uniformly. The other possibility is that the development of the two-phase boundary layer is different than that of the single phase case. Again, the extent of the change seems to rule out this possibility as well, as the concentration, size, and velocity boundary layers are all confined to a region less than 1 cm in depth. A final possibility is that there is a loss of momentum in this region due to particles being absorbed by the upper wall upon impact. Since the kinetic energy of the gas jet goes into accelerating as well as deforming the droplets, they will act as a sink of momentum to the gas if they are removed before they can relax their velocity to that of the carrier phase by virtue of viscous drag. In any event, the mean velocity deviation measured is less than 5%.

To reduce seeding bias problems, both the high-speed internal stream and the ambient entrained air were seeded with fine water droplets using several additional air-blast atomizer units. This poses a small problem for the external stream, as the far-field velocity approaches a small constant to satisfy the entrainment requirements of the shear layer, and is difficult to match precisely. A special seeding unit was fabricated for the above measurements which allowed the concentration and velocity of the seed to be adjusted to match the local entrainment conditions.

The evolution of the mean and rms streamwise velocity profiles of the carrier gas are shown in figure 4.8. The first profile, at $x = 0.7$ cm, shows a slight velocity defect due to the finite size of the splitter plate at the trailing edge (the thickness of the trailing edge is about 0.5 cm) and the finite entrainment and seeding velocity in the ambient stream. At $x = 14$ cm, there is a distinct "hump" in the low speed stream ($y = +20$ mm), indicating the occurrence of a persistent pairing (Yang and Karlsson, 1991). This is caused by each of the two distinct vortices being displaced from the centerline of the mixing region in a consistent pattern as they are convected through that particular downstream location.

Evidence of vortex displacement can also be observed in their contribution to the rms velocity (figure 4.9). This quantity, $u'_{coherent}$, is simply the square root of the variance of the phase-averaged velocity vectors as defined in §3.4.1, and is equivalent to the rms
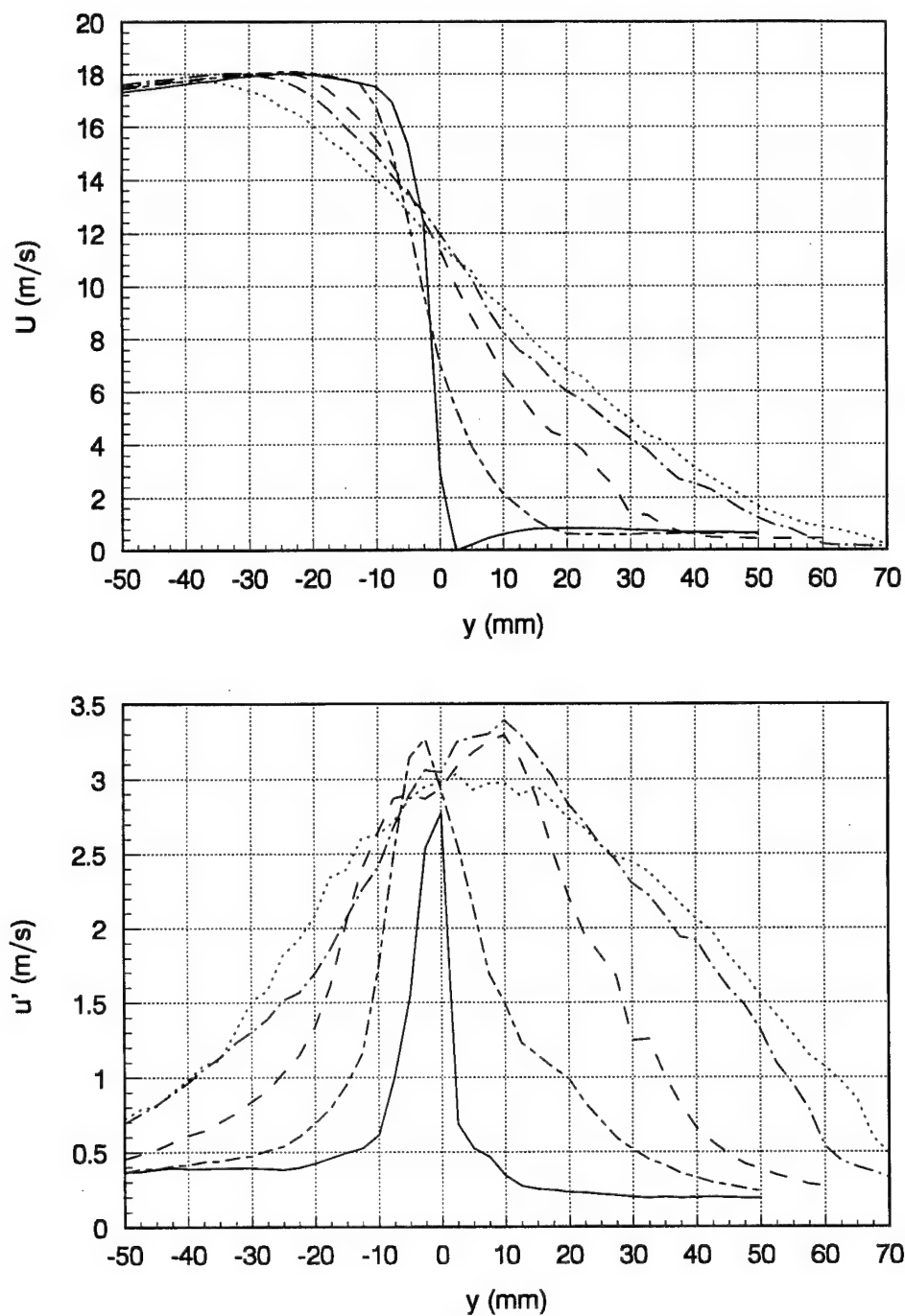
Figure 4.8: Evolution of streamwise (a) mean and (b) rms gas velocity. ——— $x = 0.7$ cm, — $\cdot$ — $x = 6$ cm, — — — $x = 14$ cm, — $\cdot$ — $x = 22$ cm, ········· $x = 30$ cm.
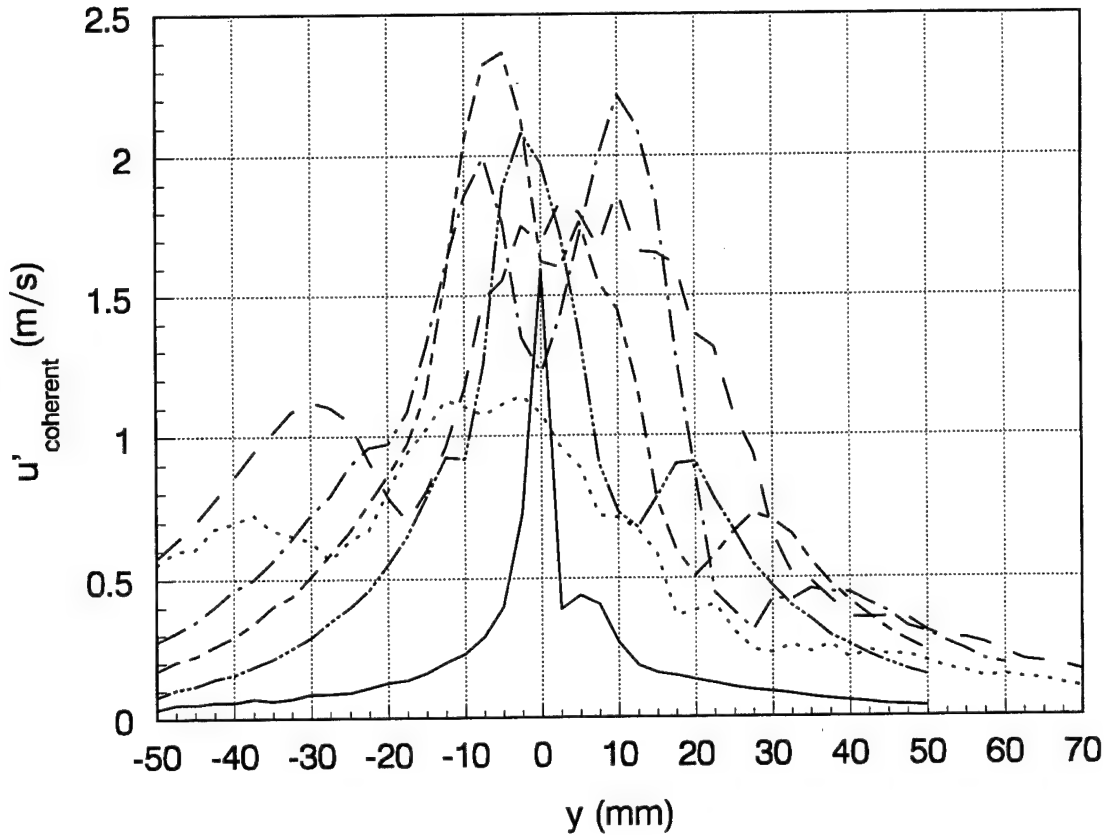
Figure 4.9: Evolution of streamwise coherent rms gas velocity. —— $x = 0.7$ cm, —··— $x = 6$ cm, ——— $x = 10$ cm, —·—— $x = 14$ cm, ——— $x = 22$ cm, ········ $x = 30$ cm.

contributions from the discrete frequency components f_s and its higher harmonics. This filtering effect removes much of the high frequency noise and shows a case similar to what is observed in a laminar shear layer (Ho and Huang, 1982). In the early development ($x = 60$ mm), there are two sharp peaks of unequal amplitude which are due to the coherent well aligned vortices which pass this location. By the time the pairing is underway ($x = 140$ mm), the vortices are displaced away from the centerline ($\pm y$) and produce a three-peaked profile. The pairing continues, and further downstream the profile reverts back to the two-peaks characteristic of a single large scale aligned along the centerline. At these locations the growth rate of the layer seems to decrease, as evidenced by the close proximity

of the two final curves of the mean velocity in figure 4.8. The streamwise rms component undergoes little amplitude development throughout the test section, primarily due to the extremely large initial amplitude coming from the boundary layer. The peak amplitude is seen to increase slightly before nearly saturating at 3.5 m s^{-1}.

The mean and rms vertical velocities show a similar evolution (figure 4.10). Again, the effect of the finite width of the splitter plate can be noted in the first profile where the strong entrainment draws air downward at over 1 m s^{-1}. In the stagnant stream, all of the mean profiles tend toward a velocity of -0.5 m s^{-1}. The rms velocity starts with a lower amplitude than the streamwise component and increases notably to a peak during the initiation of the pairing event. As the subharmonic progresses toward saturation, the rms level also decreases.

The growth of the mixing layer can be quantified by the standard definitions for the integral (equation 4.2), 0.1–0.9 level ($\delta_{0.1-0.9}(x)$), and gradient thickness ($\delta_{\partial U/\partial y}(x)$):

$$\delta_{0.1-0.9}(x) = y|_{u=0.1U_\infty} - y|_{u=0.9U_\infty} \tag{4.5}$$

$$\delta_{\partial U/\partial y}(x) = \frac{\Delta U}{\partial U/\partial y|_{max}}. \tag{4.6}$$

All three measures of the mixing layer thickness (figure 4.11) initially grow with a positive curvature until $x = 10$ cm, where the curvature changes sign and the growth rate begins to subside as the harmonic component approaches saturation (Ho and Huang, 1982). However, at this point the subharmonic is starting to grow and the pairing is initiated. This is accompanied by a sharp shift in the shear layer median location, $y_{U=0.5U_\infty}$, and another change in curvature as the displaced vortices begin to amalgamate with one another. Downstream of $x = 22$ cm, the integral and level thickness show a sharp decrease (while the maximum gradient continues to increase), indicating velocity readjustments in the outer regions of the mixing layer as the vortices continue their pairing process. Such contractions in the shear layer growth are consistent with reported evolution of shear layers undergoing a forced pairing (Yang and Karlsson, 1991; Corcos and Sherman, 1984).

To analyze the existence of a self-similar region, the shear layer growth is non-dimensionalized in similarity coordinates 4.12. A dimensional analysis of the shear layer
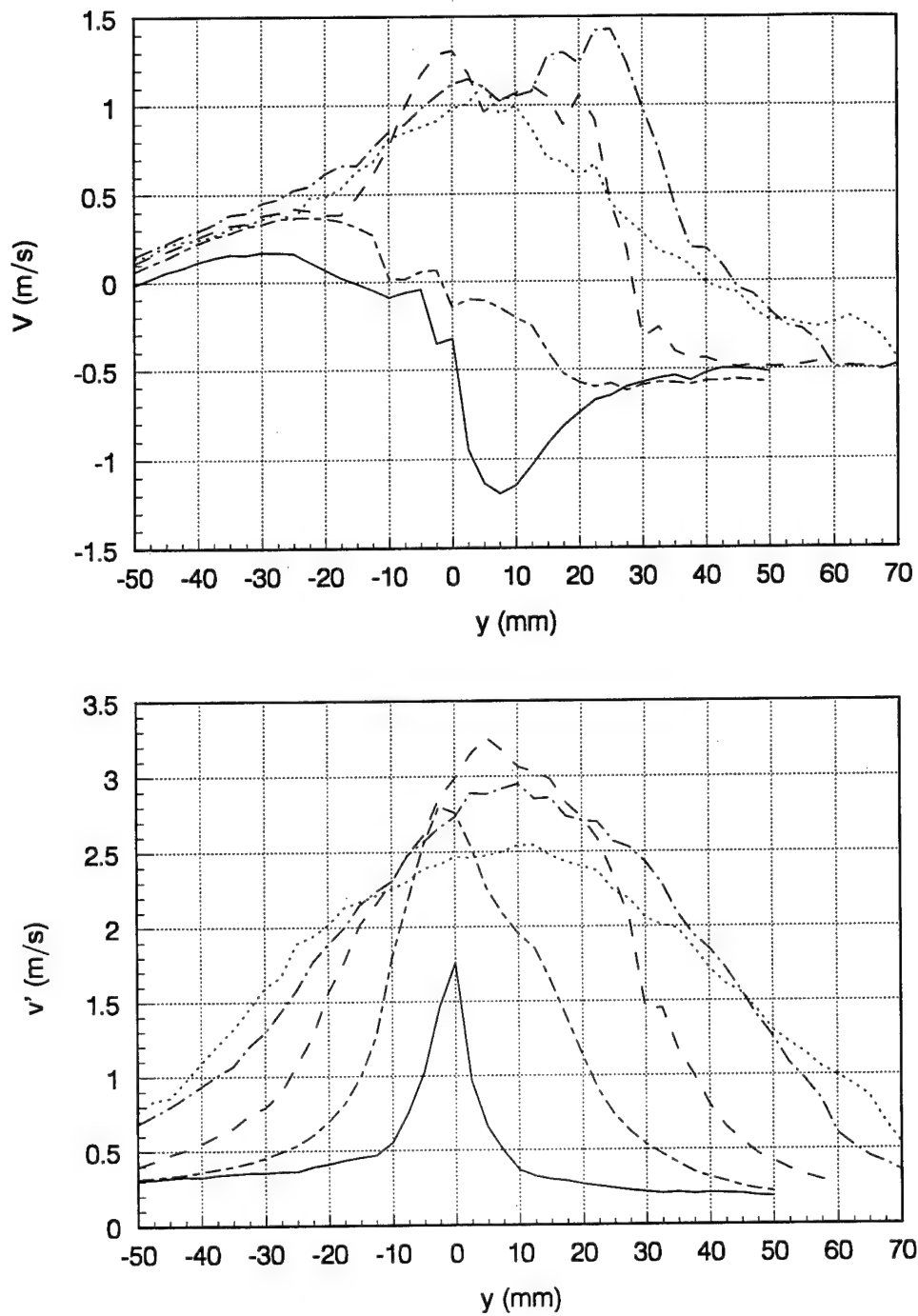
Figure 4.10: Evolution of cross-stream (*a*) mean and (*b*) rms velocity.——— $x = 0.7$ cm, —·— $x = 6$ cm, ——— $x = 14$ cm, —·— $x = 22$ cm, ········ $x = 30$ cm.
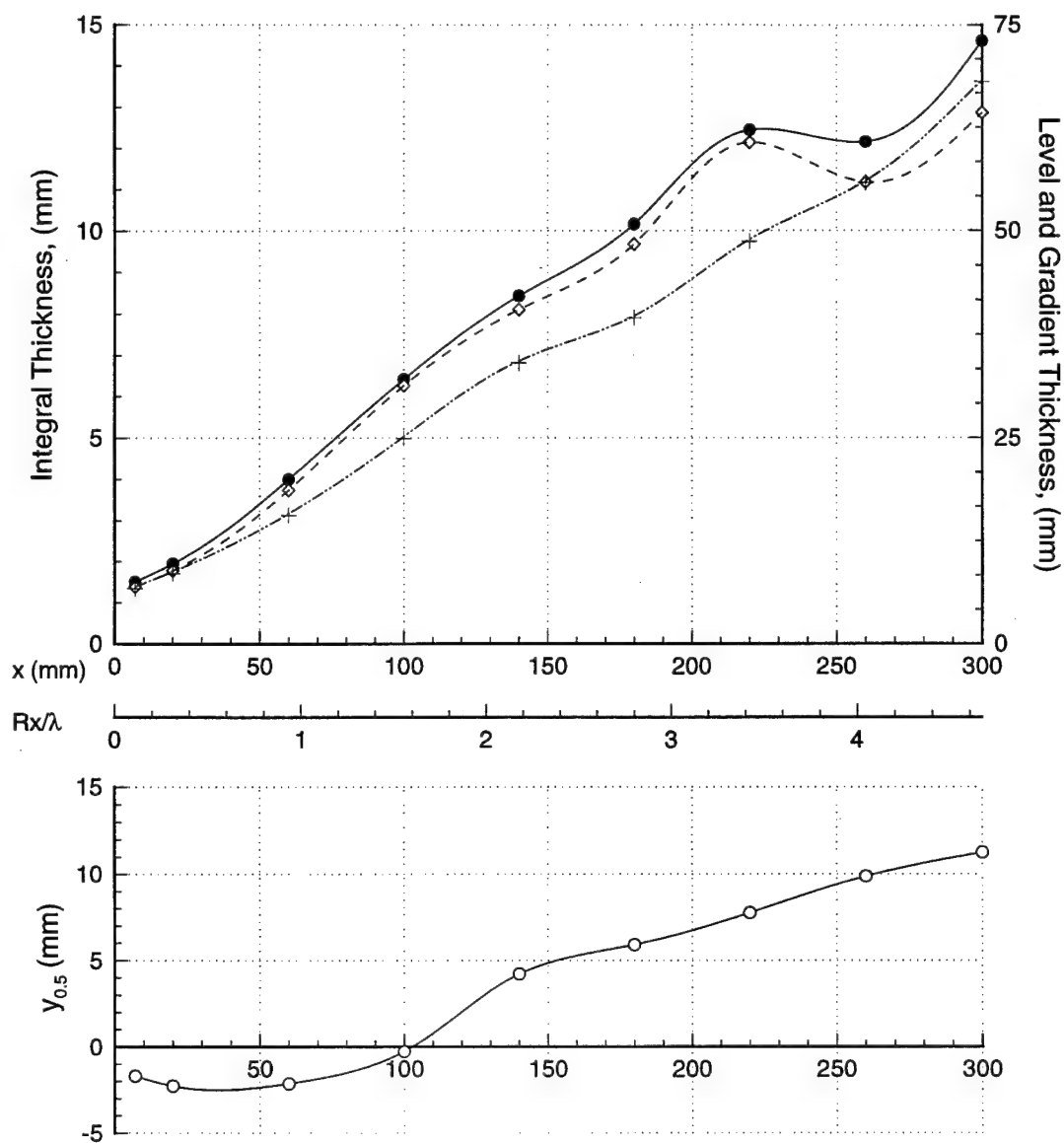
Figure 4.11: Development of the integral, level, and momentum thickness,as well as the mean velocity profile half-height, $y_{0.5} = y|_{u=0.5U_\infty}$. The scale Rx/λ is a non-dimensional development length based on the velocity ratio $R = (U_2 - U_1)/(U_2 + U_1)$ and the initial wavelength $lamba$. ——— , ● integral thickness; – – – , ◇ 0.9–0.1 level thickness; —··— , + vorticity thickness; ——— , ○ $y_{0.5}$.

problem dictates that it eventually must reach a self-similar state of development; however, it is quite clear that shear layer does not attain this state within the boundaries of the test section. This lack of similarity within the test section is not unexpected. First of all, the presence of the strong forcing component introduces several dominant length scales which prevent similarity. This forcing localizes the pairing event to a fixed spatial location, and hence prevents the profiles from converging to a fixed state. Evidence of the "hump" in the mean profile at $x = 14$ cm is a good example of this effect. In the naturally evolving shear layer, the vorticity distribution and spacing among successive vortices contains a significant amount of jitter which results in a randomization in the location of the pairing event and a self-similar mean profile. Secondly, even in a naturally evolving shear layer, there is a minimum adjustment length for the profiles to reach a self-similar state. Previous studies of axisymmetric shear layers (Hussain and Zedan, 1978) have shown that it requires a distance of about $400\theta_o - 600\theta_o$ to achieve similarity. In the current work, the farthest downstream measurements were at a location of $x = 30$ cm $= 176\theta_o$, thus implying that similarity should not be expected until $x \sim 65$ cm.

Additional physical insight into the character of the pairing process can be gained from examining the phase-averaged velocity vectors (figure 4.13) and phase-averaged rms distribution (figure 4.14). The first plots of each series show the development where the fundamental frequency is dominant. Two vortices can be clearly observed over one subharmonic wavelength, although the finite amplitude of the subharmonic and the particular phase angle used result in a disparity of the initial strengths between the two vortices. The phase averaged rms, which is the variance of the velocity with a single phase bin, represents regions of steep temporal velocity gradients (the larger the gradient, the larger the variance will be for a fixed bin size) and contributions from off-harmonic frequencies of the shear layer. As such a marker, it clearly delineates the lateral extent of the shear layer, and regions corresponding to the vortex core and braid region can be identified. From figure 4.14, the random decaying turbulent state of the freestream shows little correlation with the large scales of the mixing layer and contributes to the bulk of the total rms of 0.4–0.5 $\mathrm{m\,s^{-1}}$ measured in the mean profile. The lower edge of the mixing layer runs close to -10 to -15 mm, where there is a sharp increase in the phase-averaged rms. The cores of the
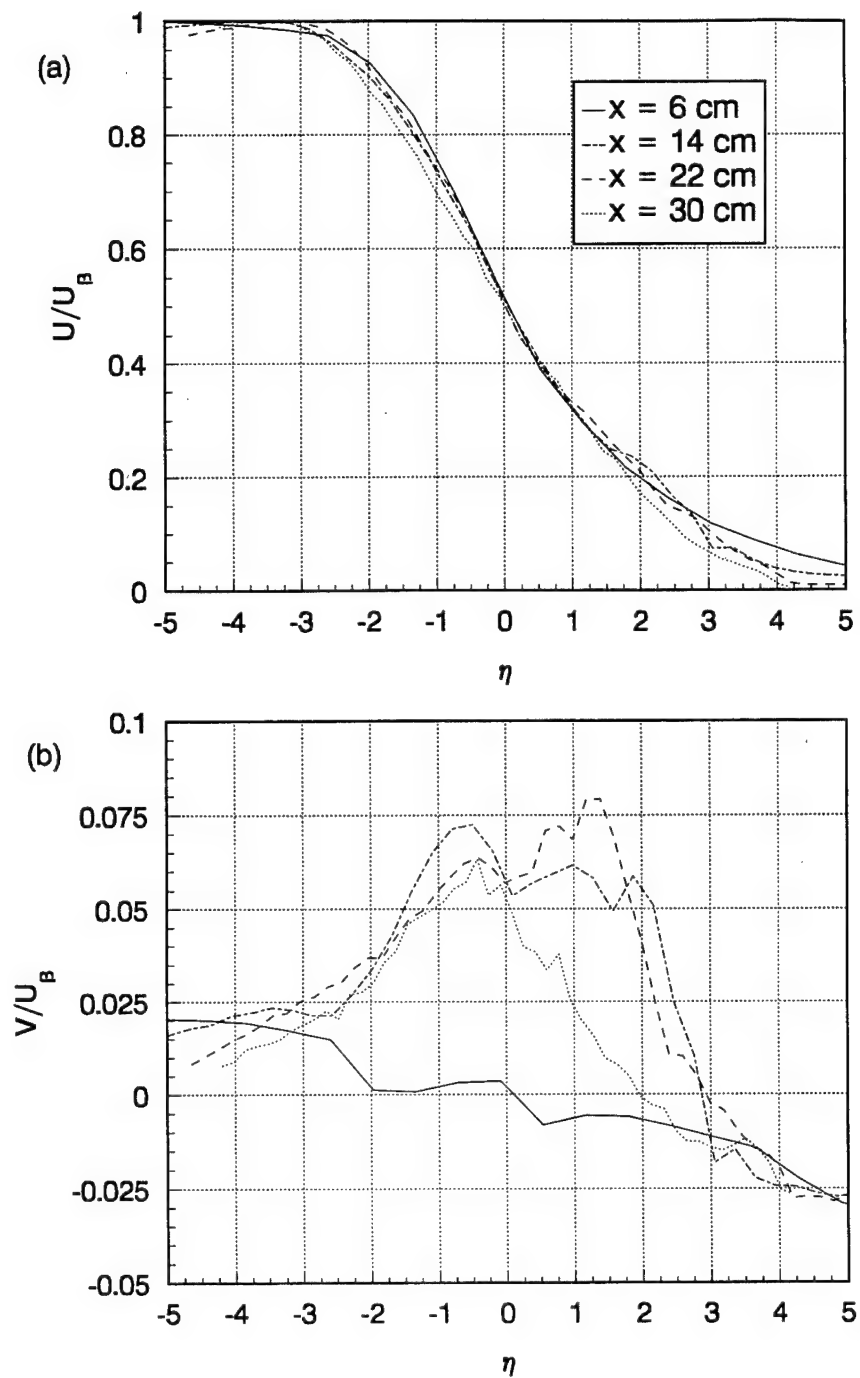
Figure 4.12: Evolution of streamwise (a) mean and (b) rms velocity in similarity co-ordinates. ——— $x = 6$ cm, ———— $x = 14$ cm, —·—— $x = 22$ cm, ········ $x = 30$ cm.
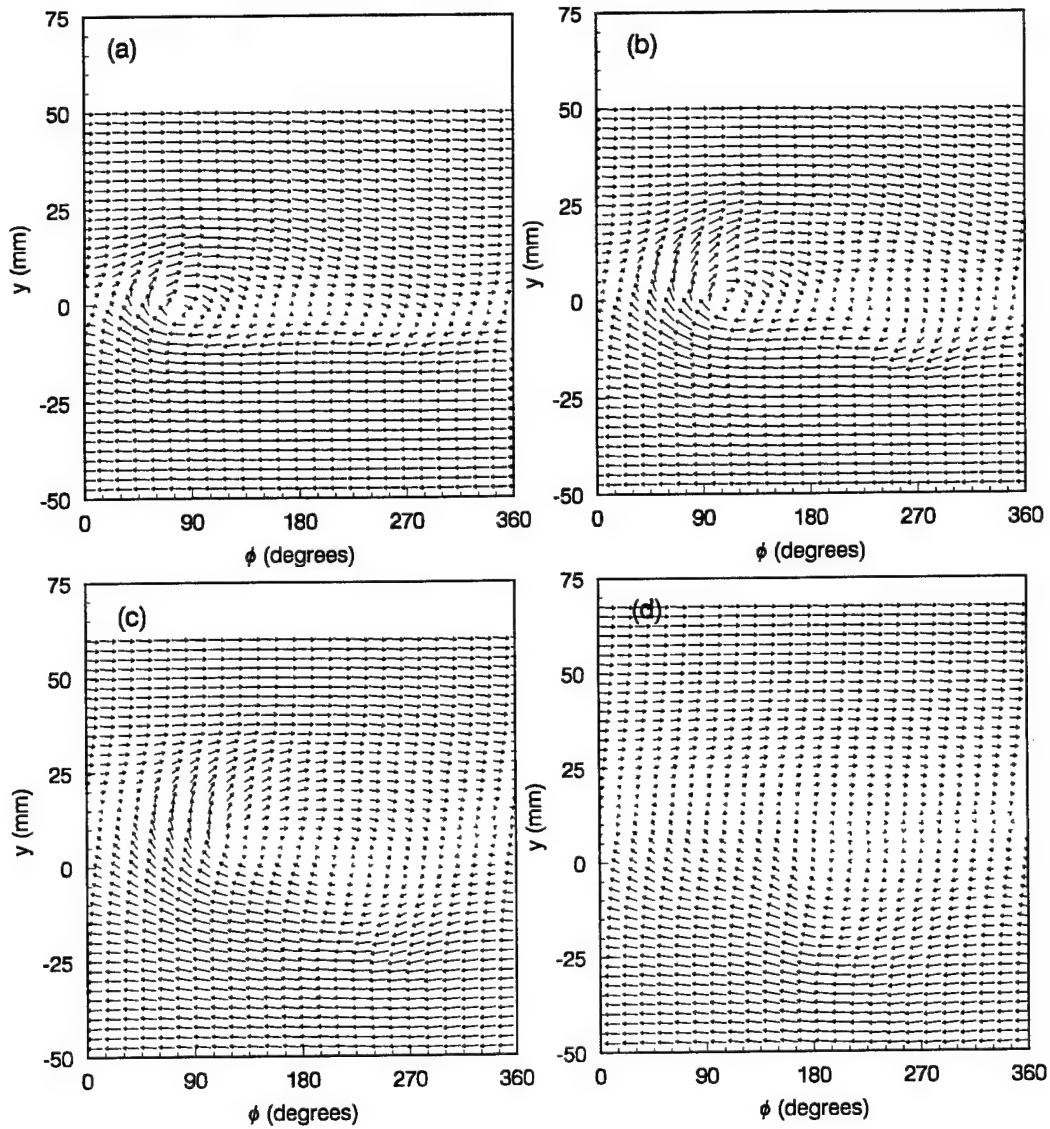
Figure 4.13: Evolution of phase-averaged gas velocity vectors at a) $x = 6$ cm, b) $x = 10$ cm, c) $x = 18$ cm, and $x = 30$ cm. The mean velocity of 9 m s^{-1} has been subtracted from the horizontal component, and a constant phase shift has been applied to center the pairing event at $\phi = 180°$. A horizontal vector with a length of 15° is equal to 9 m s^{-1}.
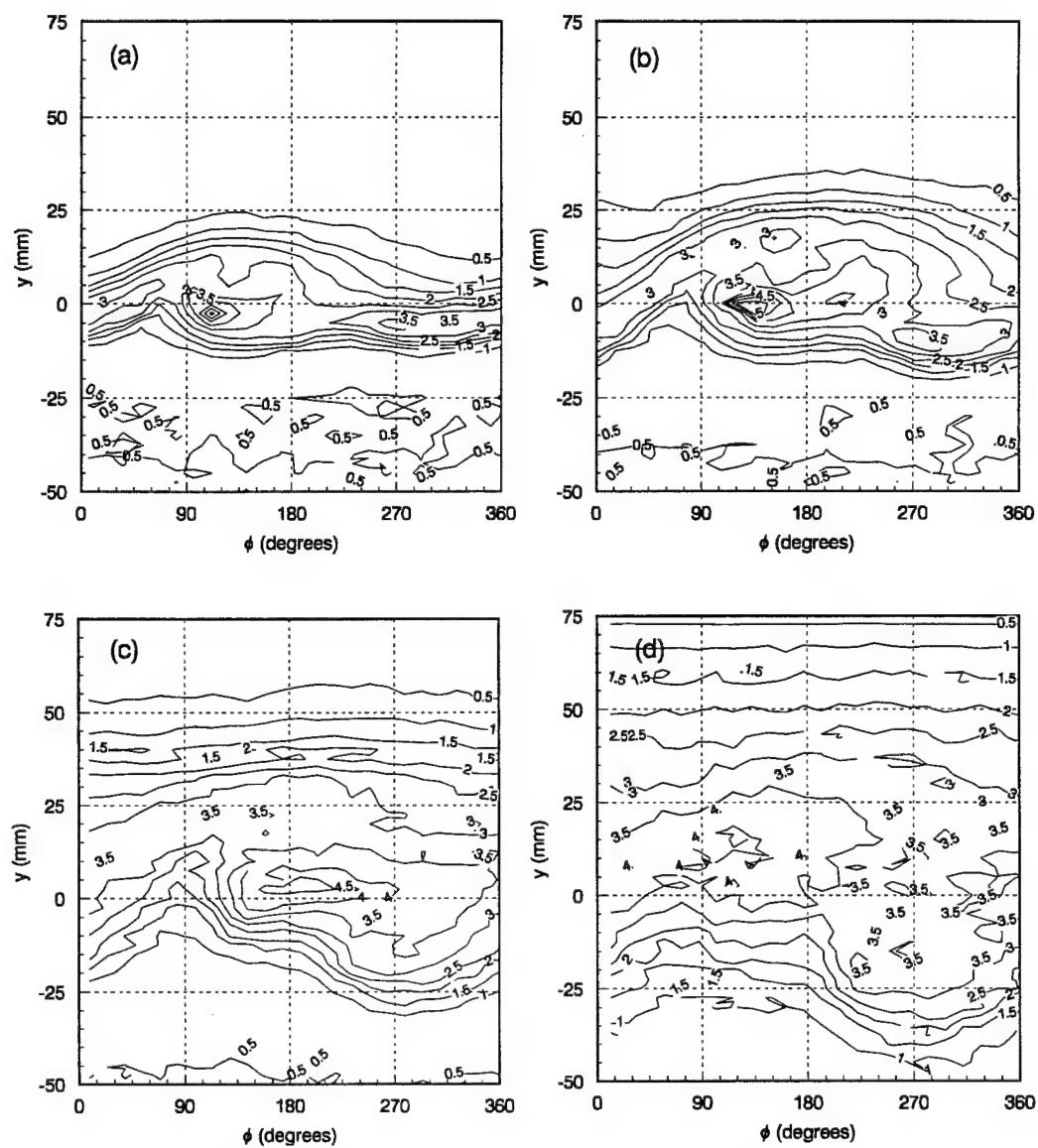
Figure 4.14: Evolution of phase-averaged gas velocity total rms at a) $x = 6$ cm, b) $x = 10$ cm, c) $x = 18$ cm, and $x = 30$ cm.

vortices are located just below $y = 0$ mm at $\phi = 110°$ and $\phi = 270°$. At $x = 10$ cm, the harmonic is still qualitatively dominant and distinct, but the effect of the subharmonic is beginning to be felt as the two vortex centers are displaced from the centerline of the shear layer. By $x = 18$ cm, the pairing is well underway and the cores of vortices are less distinct as they begin to amalgamate with one another. The last set of the series shows the core and braid region of the resulting subharmonic vortex, but reveals little of the internal detail of the structure. The corresponding velocity vectors give a similar set of information, and reveal some asymmetry across the structure. This indicates that the subharmonic has most likely not reached its final saturated state, and that some adjustment will continue further downstream prior to the next pairing event.

While most of the interactions seemed to manifest themselves as two neighboring vortices orbiting around each other and gradually merging to form a single structure twice as big as the original ones (as in the case observed by Winant and Browand (Winant and Browand, 1974)), some interactions were observed where a single vortex was stretched between its neighbors in a "tearing" or "shredding" process caused by the growing strain field of its larger neighbors (Patnaik et al., 1976). The relative frequency of occurrence for these two types of events obtained from flow visualization indicates that the pairing type of interaction makes up 90% of the two-structure interactions observed in a naturally evolving shear layer (Hernan and Jimenez, 1982). Numerical results from temporally evolving shear layers with equal amplitude disturbances in both the subharmonic and fundamental frequencies (Patnaik et al., 1976; Corcos and Sherman, 1984; Riley and Metcalfe, 1980) show that the occurrence of a tearing event is strongly dependent upon the relative phase shift, $\Delta\phi$, between the two disturbances. The numerical results, while not exhaustive, seem to indicate that the a phase shift of 180° (as referenced to the fundamental component) results in a tearing, while a phase shift of 0° results in a rapid pairing. A detailed experimental study by Yang and Karlsson (Yang and Karlsson, 1991), however, showed that the occurrence of a pure tearing event was centered in a narrow range about $\Delta\phi \approx 90°$, and a pure pairing occurred close to $\Delta\phi = 270°$. All other phase angles resulted in a combined flow, primarily dominated by the pairing event as this mode had the greatest growth rate. Thus in the current experiment, where $\Delta\phi$ was approximately 212°, the amalgamation process is

not a pure pairing event, but it is similar and thus fairly representative of a majority of the naturally occuring events.

4.3.1 Summary of Shear Layer Scales

A summary of the measured and estimated scale information of the turbulent shear layer used in the current experiment is presented in table 4.1. The integral and gradient thickness are the same quantities defined in equations (4.2) and (4.6). The Reynolds number for the shear layer is defined as

$$\text{Re}_l = \frac{\Delta U l}{\nu}. \tag{4.7}$$

where l is one of the length scale measures of the shear layer. The Taylor microscale is given by

$$\lambda_{Taylor} = \frac{\delta_{\partial U/\partial y}}{\sqrt{\text{Re}_\delta}}. \tag{4.8}$$

Due to the difficulty of measuring η_κ experimentally, an order of magnitude estimate of this scale can be obtained by (Tennekes and Lumley, 1972)

$$\eta_\kappa = \left(\nu^3/\epsilon \right)^{\frac{1}{4}}, \tag{4.9}$$

where

$$\epsilon = u^3/l, \tag{4.10}$$

Shear Layer Scale Information				
		$x = 2$ cm	$x = 10$ cm	$x = 30$ cm
Integral Thickness, θ_m	(mm)	2.0	6.7	15.6
Gradient Thickness, $\delta_{\partial U/\partial y}$	(mm)	9.3	26.7	71.6
Integral Reynolds Number, Re_θ		2400	8040	18,720
Gradient Reynolds Number, Re_δ		11,160	32,040	85,920
Taylor microscale, λ_{Taylor}	(μm)	–	150	244
Kolmogorov length scale, η_κ	(μm)	–	40	52
Kolmogorov time scale, τ_κ	(μs)	–	105	183
Kolmogorov velocity scale, v_κ	(m s^{-1})	–	0.38	0.29
Dissipation, ϵ	(m^{2}s^{-3})	–	1340	450

Table 4.1: Summary of shear layer turbulent scales

which requires the assumption of isotropy for the smallest scales and that the large scales feed their kinetic energy $(\frac{1}{2}u_g'^2)$ to the dissipation scales in one turn-over time (l/u_g'). Using the peak gas rms velocity of $u_g' \sim 3$ m s^{-1} (figure 4.8), and the gradient thickness $\delta_{\partial U/\partial y}(x)$ of 0.025 m and 0.07 m ($x = 10$ cm and 30 cm) gives a dissipation of $\epsilon|_{x=10} \sim 1100$ m^{2}sec^{-3} and $\epsilon|_{x=30} \sim 400$ m^{2}sec^{-3}. As a further check on ϵ, estimates can be made using data measured directly in a fully-developed turbulent two-dimensional mixing layer (Wygnanski and Fiedler, 1970):

$$\epsilon = \frac{0.025 U_\infty^3}{x} \tag{4.11}$$

giving $\epsilon|_{x=10} \sim 1350$ m^{2}sec^{-3} and $\epsilon|_{x=30} \sim 450$ m^{2}sec^{-3}, which are the same order of magnitude as the previous estimate. The only qualifications on the second estimate are that the mixing layer of the present study has not reached a state of similarity, and that x in (4.11) is referenced to the virtual origin. The Kolmogorov time and velocity scales then result from a dimensional analysis using viscosity and dissipation to give

$$\tau_\kappa = (\nu/\epsilon)^{\frac{1}{2}} \quad \text{and} \quad v_\kappa = (\nu\epsilon)^{\frac{1}{4}}. \tag{4.12}$$

Chapter 5

Effect of Vortex Pairing on Particle Dispersion

As mentioned in Chapter 2, the response of small, heavy particles to the unsteady motion of a carrier gas flow can be characterized by the droplet's viscous relaxation time. This is an expression of the fact that the changes in the droplet's inertia is dominated by viscous drag effects. In the turbulent shear layer there exists a range of time scales to which the particles are subjected as they are entrained across the mixing region. The largest of the time scales is due to the coherent, two-dimensional, spanwise vortices which extend across the width of the shear layer and have a period given by their spacing and the mean convective velocity. Due to their size and extent, the large scale plays a dominant role in the bulk entrainment across the mixing region. Superimposed within this structure, the turbulent flow field has a range of smaller scales which extend down to lengths small enough to rapidly dissipate the kinetic energy supplied by the mean shear of the flow field. These small scales (which for higher Reynolds number flows encompass features such as the streamwise vorticity embedded in the braid region) are typically effective at breaking down the lumps of fluid entrained across the layer by the large scales. The response of the particles to all of these different fluid time scales depends on how the particle viscous relaxation time compares with the fluid scales of interest. In the context of particle dispersion, the relevant time scale is that of the largest vortices, while the smaller scales will act to spread the particles within the large vortices (provided that the viscous relaxation time is small

71

enough for the droplets to respond to such motion).

Previous numerical (Martin and Meiburg, 1994; Chein and Chung, 1988) and experimental (Lázaro and Lasheras, 1992a; Lázaro and Lasheras, 1992b) studies have focused on the initial developing region of the shear layer. Most of these studies are conducted prior to the first pairing event and give results which describe the dispersion process dominated by large scale structures of a single frequency. In the current study, it is of interest to extend the previous work to the case of the vortex pairing event, which plays an important dynamic role in the shear layer growth by providing a transition to structures that have twice the size and time scale of the pre-pairing vortices. The droplets subsequently interact with the transitional structure during the pairing event, which results in a dispersion structure that is different from the one observed in the single frequency dominated flow.

The effect of the vortex pairing on the particle dispersion will be investigated through several methods. The first method is to directly compare measurements made in a shear layer forced with a single dominant frequency (Lázaro and Lasheras, 1992b) to measurements made in an identical shear layer forced with both the primary instability frequency and its first subharmonic. In the work of Lazáro and Lasheras (Lázaro and Lasheras, 1992b), the shear layer was forced at the first subharmonic frequency of 70 Hz with sufficient amplitude to completely suppress the formation of the fundamental wavelength. In their experiments, the high-speed air stream had a velocity of $15 \mathrm{~m\,s^{-1}}$, resulting in a wavelength of 10.7 cm. As stated in Chapter 4, the current study uses the same facility as the previous work, and forces the mixing layer with a fundamental disturbance of 140 Hz and a first subharmonic of 70 Hz (the slightly higher freestream velocity results in a longer wavelength of 12.9 cm). Due to the similarity of the facilities and the resulting time scales of the final large scale structures, comparisons between the two studies allows an evaluation of the different mechanisms which occur during the pairing process. Quantities which will be examined as a direct comparison include the phase-averaged attenuation, the mean single frequency mode forcing, whereas the results which are particular to the dispersion observed after the pairing within the current study will be noted as pairing mode forcing.

The second method to asses the effects of vortex pairing will be to compare the evolution of the dispersion structure both before and after the pairing event. In order to use

this method, the flow first is divided into three separate regions which correspond the initial developing region (with similar features to those observed in the single frequency mode), the pairing event, and the resulting subharmonic structure. This is done using a consistent but subjective definition based on the dominant frequencies observed in the attenuation spectra. Once the regions are defined, the effect of the pairing event on the dispersion of the different sized (and hence viscous relaxation time) droplets will be examined.

5.1   Time Scales and Regions of Interest

Information on the time evolution of the instantaneous particle dispersion process was obtained through measurements of the laser attenuation. The coherence of the particle concentration field in the large-scale vortices can be analyzed by the attenuation Eulerian temporal correlation coefficient, which is written as:

$$R_{\xi\xi}(\tau) = \frac{\lim\limits_{T \to \infty} \frac{1}{T} \int_0^T \xi(t)\xi(t+\tau)dt}{\lim\limits_{T \to \infty} \frac{1}{T} \int_0^T \xi(t)\xi(t)dt} \ , \tag{5.1}$$

where $\xi(t)$ is the measured attenuation as defined by equation (3.12). For the present flow, $R_{\xi\xi}$ is observed to be a periodic function composed of two frequencies (the fundamental and subharmonic) with a slightly decaying amplitude (figure 5.1). As seen by comparing the subharmonic peaks ($\tau = 14$ and 28 ms), the amplitude is never less than 0.84, indicating a very high degree of repeatability between structures. It should be remembered that the attenuation signal is an instantaneously spatially averaged measurement due to the finite width of the beam, d_{beam}. In the present set of measurements, $d_{beam} \sim 3$ mm, which is an the order of magnitude larger than the Taylor microscale ($\delta/\mathrm{Re}_o^{1/2} \sim 0.2$ mm) but is much smaller than the shear layer integral scale ($\lambda_f \sim 64$ mm). Thus $R_{\xi\xi}$ represents a filtered signal which does not resolve the high frequency content but rather emphasizes the evolution of the large scale structures. Had it been possible to make similar measurements with d_{beam} much smaller than the Taylor microscale or the Kolmogorov length, then the variability associated with these scales would have reduced the peak correlation levels. Conversely, had $d_{beam} \gg \lambda_f$, then the correlation would have always been equal to 1
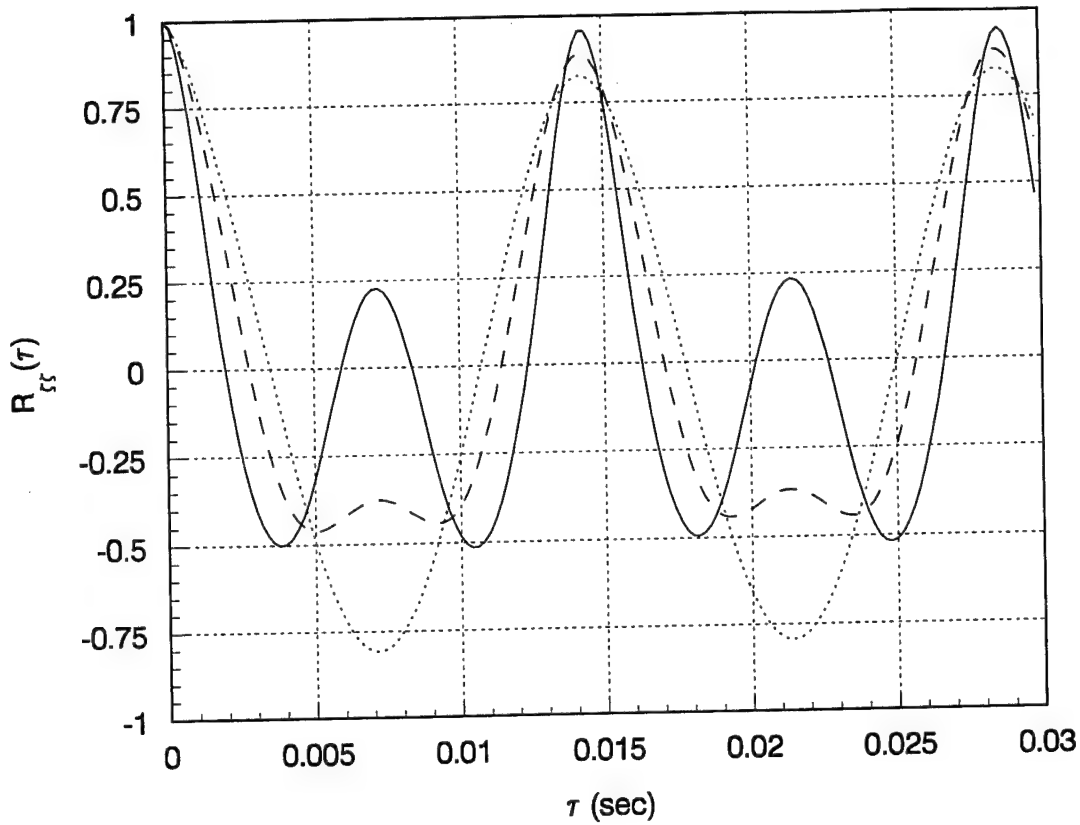
Figure 5.1: Streamwise evolution of the attenuation Eulerian temporal correlation along the coordinate $y = 0$ mm. —— $x = 2$ cm, – – – $x = 18$ cm, ········ $x = 30$ cm.

provided the flow was stationary. With this in mind, the behavior of $R_{\xi\xi}$ shows that each vortex structure convected past the measurement location is nearly identical when averaged over a scale of 3 mm.

An estimate of the variability of the vortex passage frequency can also be checked by examining the phase-averaged r.m.s. attenuation, $\left\langle \xi^{*2} \right\rangle^{1/2}$ (figure 5.2). The phase-averaged r.m.s. is typically about 5–15% of the measured freestream attenuation ($\langle \xi \rangle |_\infty \sim$ 0.26). Qualitatively, the "jitter" of the large scale vortices as they are convected past the measurement location can be observed in figure 5.2a, where the phase-averaged r.m.s. increases slightly on either side of the dispersion streak ($y \sim 0$ mm, $\phi \sim 260°$). This is caused by the small variability in the passage of each structure, and causes regions characterized by sharp changes in attenuation to have a local increase in the phase-averaged

r.m.s. attenuation. The amount variability can be estimated through the calculation of a "jitter" length which gives the distance that the phase-averaged mean surface must be moved to generate a deviation equal in magnitude to the r.m.s. attenuation. Such a length is defined by

$$l_{jitter} = \frac{\left\langle \xi^{*2} \right\rangle^{1/2}}{\nabla \left\langle \xi \right\rangle}, \tag{5.2}$$

and presented in figure 5.2b (where ∇ has been replaced by the vertical gradient, $\partial \xi / \partial y$). Equation (5.2) only has meaning where the gradient is non-zero, and hence the contours of l_{jitter} have been limited to regions within the mixing layer where the gradients are sizeable. The results indicate that the mean surface must be displaced less than 1 mm to generate the measured r.m.s. distribution. This is much less than the resolution of the instrument, and indicates that the large scale eddies are strongly phase-locked with respect to the forcing signal. Similar results can be obtained for a "jitter" time or phase period by using horizontal attenuation gradients.

The evolution of the Eulerian temporal correlation coefficient also connotes a change of dominant length scale within the test section. Initially ($x = 2$ cm), the fun-
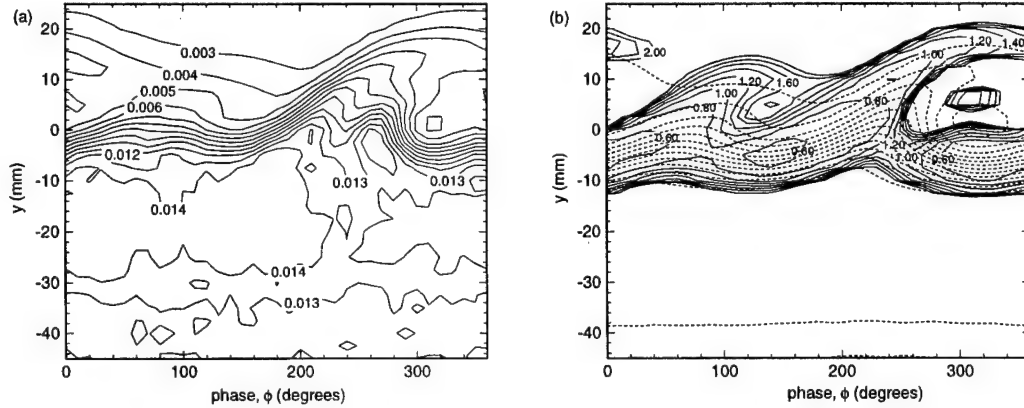
Figure 5.2: (a) Phase-averaged r.m.s. attenuation, $\left\langle \xi^{*2} \right\rangle^{1/2}$. Contours labeled in measured attenuation (unitless). (b) Phase-averaged "jitter" length, $l_{jitter} = \left\langle \xi^{*2} \right\rangle^{1/2} / \frac{\partial \langle \xi \rangle}{\partial y}$. Contour units are in mm. Dashed lines show phase-averaged attenuation contours for comparison.

76
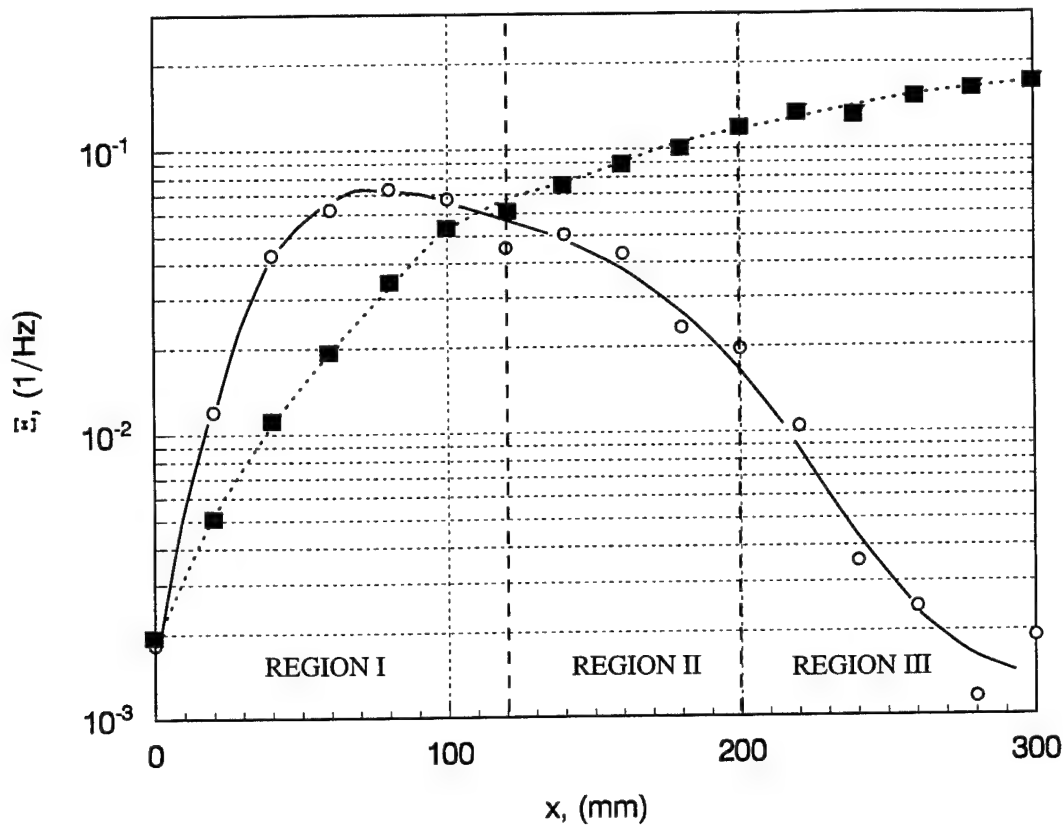
Figure 5.3: Streamwise evolution of the attenuation Eulerian spectral peak amplitude along the coordinate $y = 0$ mm. $\diamond$ $f = 140$ Hz, $\bullet$ $f = 70$ Hz.

damental frequency is dominant (as evidenced by the strong peak at $\tau = 0.007$ sec), but by the end of the test section ($x = 30$ cm) only the subharmonic remains, demonstrating the occurrence of a pairing event. The location of the pairing within the test section can be more precisely identified by analyzing the development of the fundamental and subharmonic peaks of the attenuation spectra (figure 5.3). The spectral peaks show that the fundamental is dominant throughout the first 12 cm of the shear layer, growing, saturating, and then beginning to decay. At the end of this region, the subharmonic mode becomes dominant and marks the initiation of the pairing. This then provides a criteria to be used to sub-divide the regions of interest of the flow: Region (I), the developing fundamental disturbance (from $x = 0$ to 12 cm); Region (II), the transitional pairing event (the region where the subharmonic and fundamental scales have a comparable amplitude, from $x = 12$ to 20

cm); and Region (III), the resulting subharmonic vortex (from $x = 20$ to 30 cm). Although the above criteria for locating the pairing region is not a standard definition (gas velocity spectral peaks would be more desirable, but this quantity was not measurable in the current study), it at least provides a consistent and objective definition that appears to qualitatively agree with the pairing event observable in the phase-averaged measurements of the gas velocity (figure 4.13).

5.2 Qualitative Comparison to Single Mode Forcing

The evolution of the mixing layer within Region I is comparable to the initial developing region of the single frequency forcing case (LL92b), and hence measurements of this region can be used to check with previous results as well as to compare and contrast the effects of the pairing event. Using the waveform applied to the forcing generator as a reference signal, phase-averaging techniques outlined in §3.4 were used to generate ensemble average portraits of the large-scale attenuation structure and provide an overview of the evolution of the dispersion before, during, and after the pairing event (figures 5.4 and 5.5).

In Region I of the pairing mode forcing case (figure 5.4a, b, and c), one can observe the same dispersion characteristics found in the single frequency forcing results (LL92b): namely, particle dispersion across the mixing layer is manifested in the form of a well defined streak originating near the free stagnation point, and is entrained over the core of the vortex. As the flow evolves, the streak grows, increasing in concentration and azimuthal extent as the droplets begin to respond to the coherent fluctuations. Thus, it is evident that the entrainment process due to a single dominant frequency produces strong inhomogeneities across the spanwise vortices and tends to leave their cores depleted of droplets. Although this is similar to what one might expect for the entrainment of a scalar quantity in a laminar shear layer, the small scale fluctuations in a turbulent flow would promote internal mixing and allow molecular transport to reduce the local concentration gradients between the two fluids. In the case of droplets, however, this internal mixing action will depend strongly on the viscous relaxation time of the droplets in comparison to the small scale eddy times as
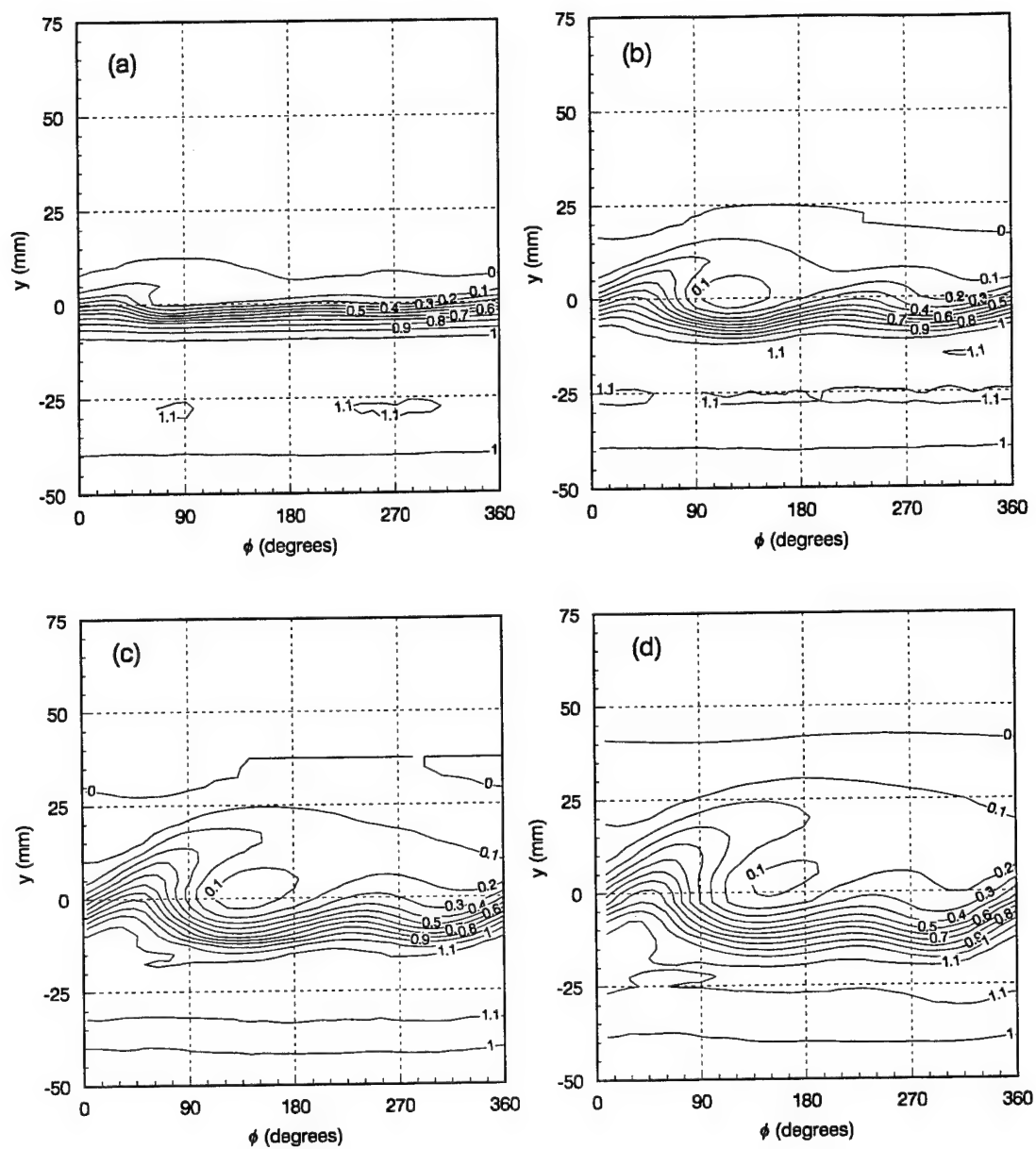
Figure 5.4: Phase averaged attenuation contours. All surfaces have been normalized by the freestream attenuation at $y = $ -40 cm. $a)$ $x = 2$ cm, $b)$ $x = 6$ cm, $c)$ $x = 10$ cm, $d)$ $x = 14$ cm,
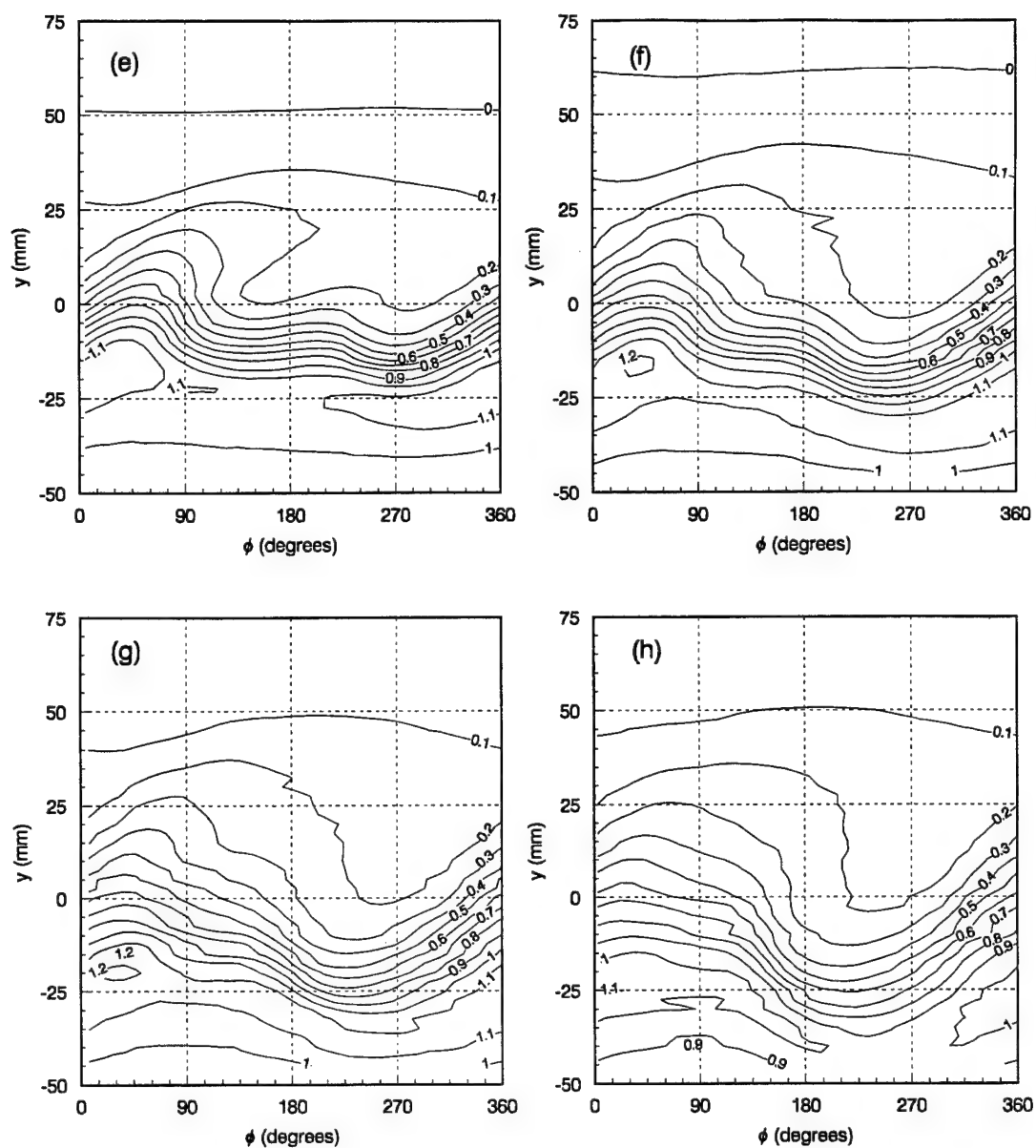
Figure 5.5: Phase averaged attenuation contours. All surfaces have been normalized by the freestream attenuation at $y = -40$ cm. *e)* $x = 18$ cm, *f)* $x = 22$ cm, *g)* $x = 26$ cm, *h)* $x = 30$ cm,

mentioned above.

In the transition region where both the fundamental and subharmonic scales coexist (Region II), the attenuation phase-averaged measurements show the extent of the droplet dispersion during the pairing process (figures 5.4d and 5.5e and f). Here the pairing is initiated, and the smaller vortex on the upstream side is subducted into the high-speed stream and brought close to the larger, downstream vortex. As the pairing takes place, the droplets that had been entrained by the smaller streak are dispersed into the rapidly evolving core of the subharmonic structure. This results in a final structure (Region III, figures 5.5g and h) that is quite different from the original one – note that the streak is now much broader and diffuse while its core is no longer depleted of droplets. Thus, it is evident that the pairing not only contributes to the dispersion lengthscale, but also leads to a homogenization effect, reducing the droplet concentration gradients within the vortex. It should be noted, however, that the droplets are not passive scalars, and each droplet size responds to the pairing process differently with a different relaxation time. These size-dependent effects are not apparent in the attenuation measurements since the attenuation reflects a variable integrated over all size classes in the flow. These considerations will be expanded upon in the next section.

Further evidence of the contrasting mixing processes between the single frequency and pairing mode cases can be seen through the evolution of the profiles of the r.m.s. attenuation (figure 5.6, and 5.7). For the single frequency forcing results of Lázaro and Lasheras (1992b), the r.m.s. profiles were found to exhibit a peak in the lower central region of the mixing layer which increased in amplitude throughout most of the test section (figure 5.7a). At $x = 20$ cm, however, the amplitude was shown to undergo a sudden decrease, and rapidly moved into the lower region of the mixing layer (figure 5.6a and 5.7c). Lázaro and Lasheras attributed this behavior to the presence of a well-developed, extended streak. In the early development ($x < 20$ cm), the largest attenuation fluctuations occurred at a cross-stream location where the beam alternatively passed through the low attenuation region in the vortex core and the high attenuation region at the base of the streak. As the streak evolved, and more particles were drawn into it, the attenuation levels increased inside the streak and correspondingly enhanced the rms level. The peak decay and the location
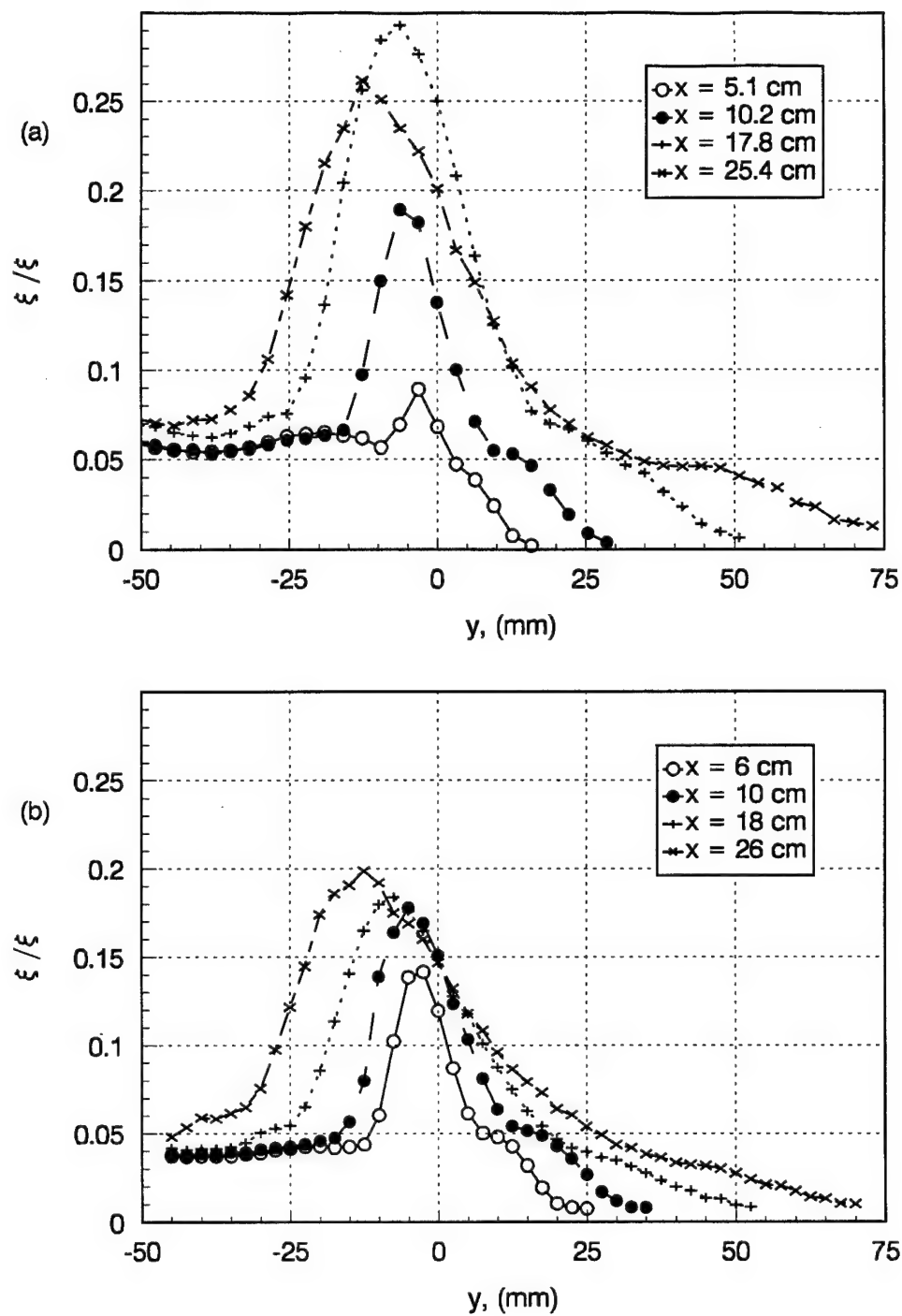
Figure 5.6: Attenuation rms profiles for *a*) single-mode forcing and *b*) pairing-mode forcing.
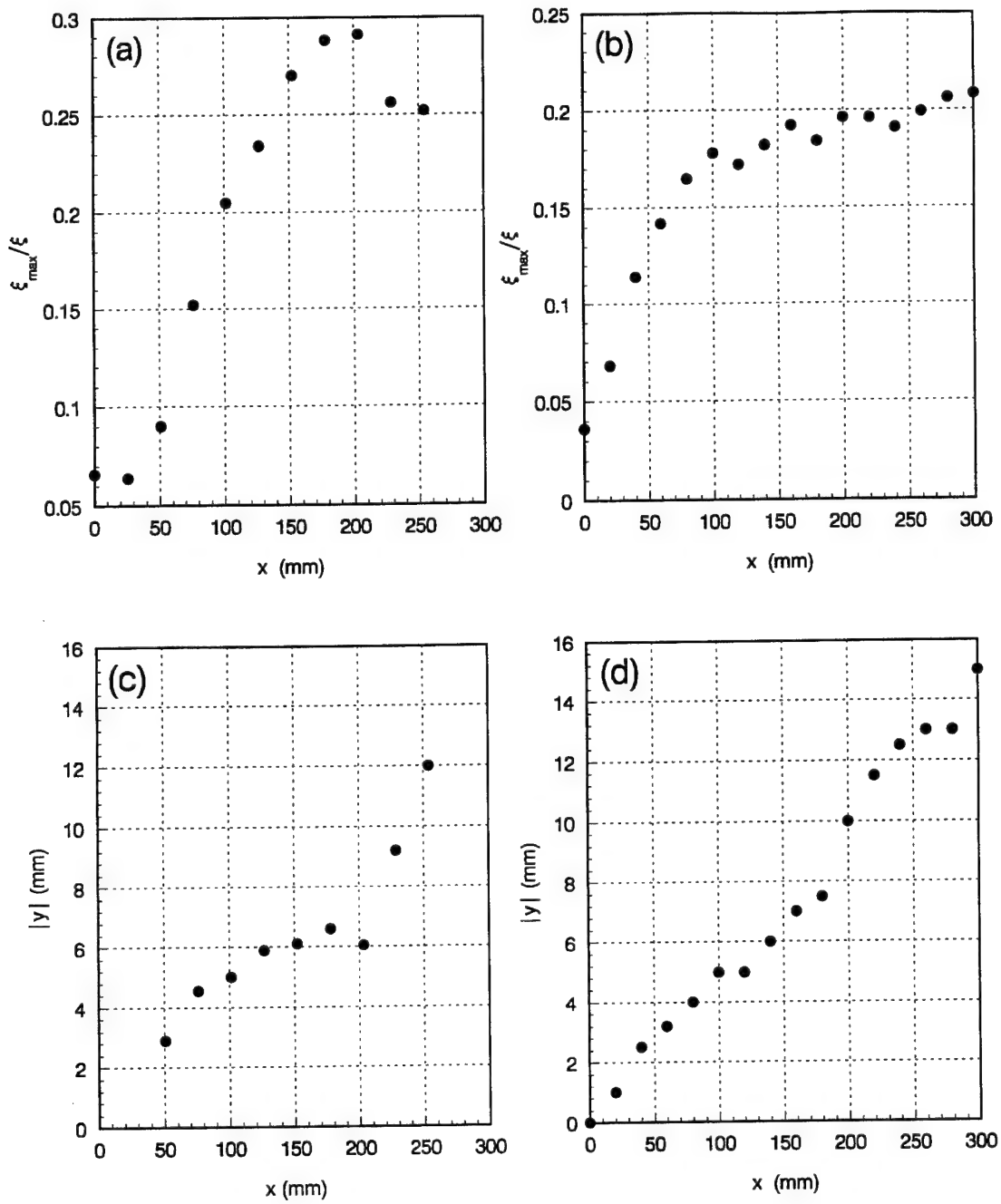
Figure 5.7: Attenuation rms (*a*) peak amplitude and (*b*) cross-stream location for single-mode forcing and rms (*c*) peak amplitude and (*d*) cross-stream location for pairing-mode forcing.

of this shift occurred when the streak impacted on the upstream neighboring vortex. The r.m.s. level was then reduced due to the lengthened duty cycle of the heightened attenuation and the maximum shifted to a location deeper in the spray. The existence of an external plateau was also attributed to an extensive streak development, as the r.m.s. was stabilized by the increased signal duty cycle and attenuation decay along the streak.

Comparing the above results with the forced pairing mode case shows the similarities and differences between the two cases. It is not surprising that the initial profiles have the same shapes composed of a peak and a plateau (figure 5.6b, compare the profiles at $x \sim 10$ cm for both cases), due to the fact that Initially the development in both cases is dominated by a single frequency. Further downstream, the peak continues to grow monotonically with no sudden shifts in location (figure 5.7b and d), while the prominent plateau is erased during the pairing event.

The above results indicate that the streak development is considerably changed by the pairing, and that the streak reconnection observed in the single frequency forcing case never occurs once the pairing is initiated. This hypothesis is confirmed in each of the two cases by comparing the evolution of the streak location and attenuation amplitude (figures 5.8, 5.9, 5.10, and 5.11). The location of the streak centerline was identified by graphically finding the path of steepest ascent along the attenuation contours in the y/ϕ plane, starting from the tip of the streak in the outer region of the mixing layer. The phase coordinate was then translated into a length through multiplication by $\frac{1}{360}\frac{\overline{U}}{f}$, and both coordinates were given an origin referenced to the streak's emergence location from the spray stream. The results of the single frequency forcing case (Lázaro, 1989) show a streak emerging from the spray with an angle close to 45° which increases slightly as the vortex grows downstream (figure 5.8). Once the streak has been drawn out of the high-speed stream, it is then extended streamwise over the core of the vortex. Noting that the fundamental vortex wavelength for this case was 10.7 cm, it can be seen that the streak is identifiable over 65% of the vortex length. The centerline attenuation (figure 5.9) exhibited an initial sharp decrease along the streak emergence region, followed by a relaxation in the outer region where it was drawn over the vortex core. As the evolution continues and more droplets are entrained into the streak, the attenuation shows a corresponding increase over
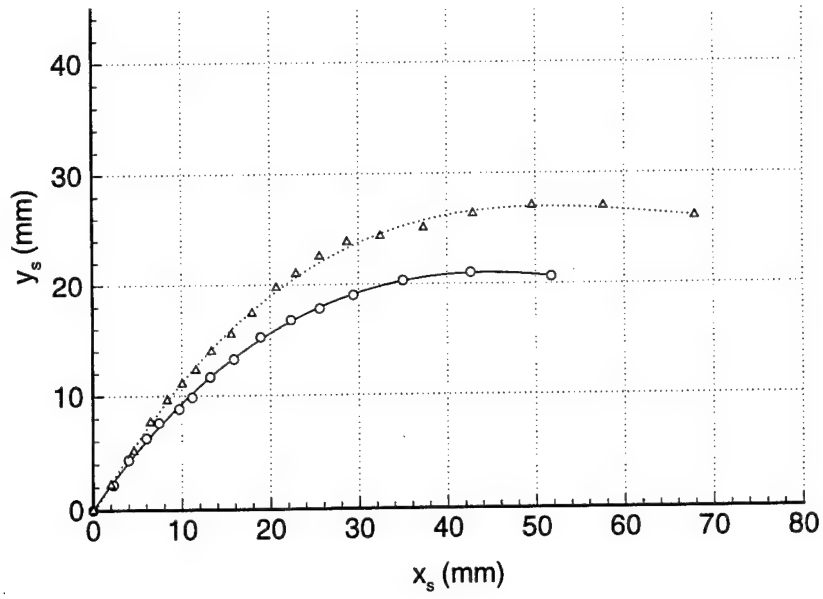
Figure 5.8: Dispersion streak shape evolution for single frequency forcing, from Lázaro 1989. o,
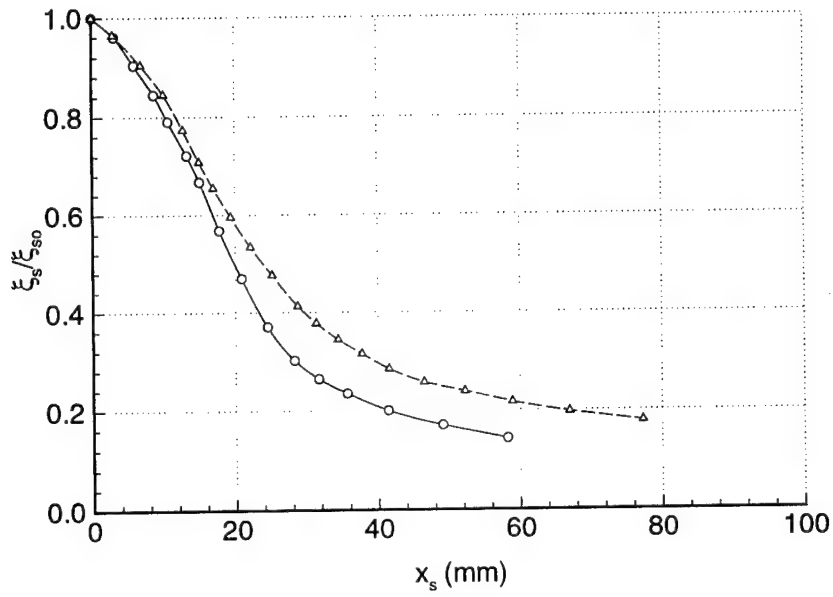
Figure 5.9: Attenuation along the length of the streak for single frequency forcing, from Lázaro 1989. Normalized by the attenuation at the streak origin, ξ_{so}.o, —— $x = 10.2$ cm; $\triangle$, ⋯⋯ $x = 20.3$ cm.
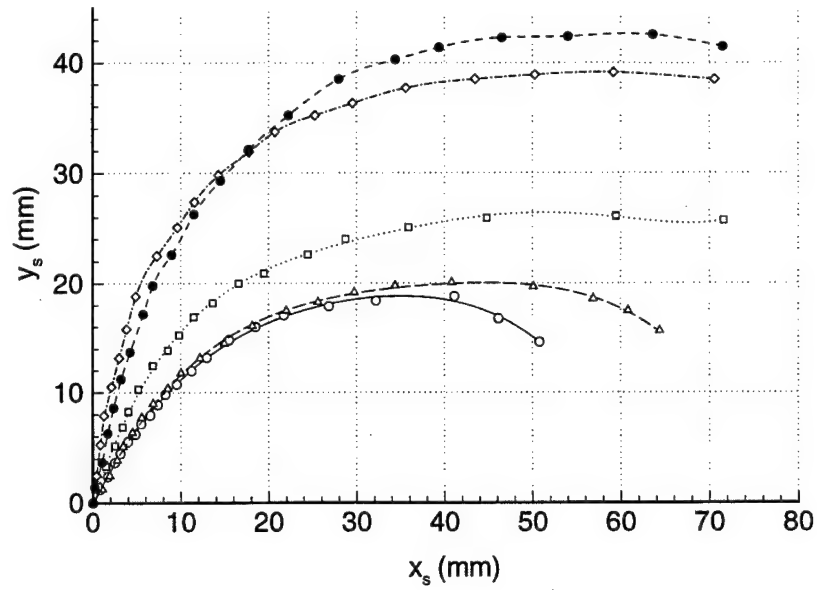
Figure 5.10: Dispersion streak shape evolution for pairing mode forcing. ○, ——— $x = 6$ cm; △, — —

Figure 5.11: Attenuation along the length of the streak for pairing mode forcing. Normalized by the attenuation at the streak origin, ξ_{so}. ○, ——— $x = 6$ cm; △, — — $x = 10$ cm; □, ········ $x = 18$ cm; ◇, — · — $x = 26$ cm; ●, — — — $x = 30$ cm.

the entire length of the streak (figure 5.9).

Examining the development of the larger streak in Region I of the pairing mode case gives a similar development (figure 5.10). Again, the streak starts with an emerging at an angle close to 45° and continues to elongate as the fundamental disturbance is amplified. The relative azimuthal development of the streak appears to be greater for the current results than for those shown in figure 5.8, and is most likely due to the smaller initial particle concentration boundary layer of the current experiment (having an increased supply of particles close to the mixing region will enhance the initial streak definition), as well as the increased strength of the vortex. Noting that for this case the wavelength associated with the fundamental is 6.4 cm, it is observed that both curves are very similar in cross stream extent and shape up to the $0.65\lambda_f$ point ($x_s = 40$ mm in figure 5.10). At this location the pairing mode streak then continues development and is drawn back towards the mixing region, covering the entire length of the fundamental disturbance. Observing the streak that will remain after the pairing, the streak's emergence angle increases dramatically as the pairing event is initiated. This angle reaches a maximum of 75° at $x = 26$ cm, where it begins to decrease as the streak readjusts to the pairing event. Given sufficient time, it seems plausible that this angle may decrease back to it's original value, but there was not sufficient development length within the test section to observe this. It should also be noted that during and after the pairing event the streamwise extent of the identifiable streak region remains more or less constant. Since the wavelength of the carrier flow field doubles during the pairing, it causes a decrease in the *relative* length of the streak, which now occupies approximately 56% of the subharmonic structure. Finally, the attenuation along the streak (figure 5.11) shows similar characteristics as the single frequency mode, with the exception that the attenuation grows very little along the streak after the pairing has occurred. This is indicative of a reduced entrainment immediately after pairing has occurred.

Thus, it is already becoming evident that the final subharmonic structure produced by the pairing is not similar to the one Initially produced by dispersion due to a single length scale. The history of the flow through the transitional process has significantly altered the final distribution structure. This gives additional support to the somewhat subjective characterizations shown in the attenuation images.
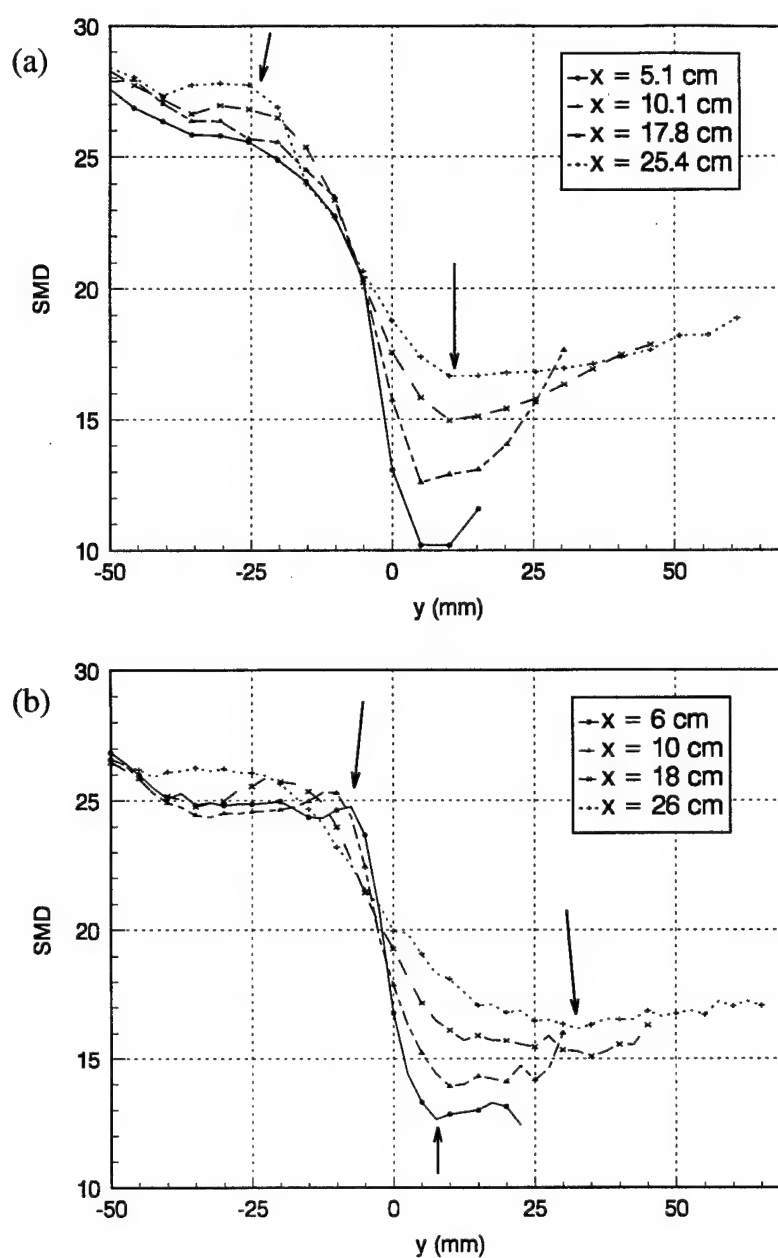
Figure 5.12: Comparison of Sauter Mean Diameter profiles for (a) single-mode forcing from Lázaro and Lasheras (1992b) and (b) pairing-mode forcing (only every other data point shown). Note size overshoot in the lower free-stream and the shift in the minimum diameter location after the pairing.

The last set of measurements to be presented as a direct comparison with the single frequency forcing results are those of the time averaged SMD (figure 5.12). The original measurements were performed with a Malvern 2600 laser diffraction particle sizer, and the same instrument was used for the sake of comparison between the two cases. For the single frequency forcing case, the initial profile decays sharply through the mixing region and then increases slightly at the external edge of the shear layer. Further downstream, the baseline level of the 'valley' region increases, all the while maintaining a minimum close to the center of the shear layer. The valley is a result of averaging over the depleted core region, which contains only the smallest size droplets. The external recovery can then be attributed to the presence of larger particles in the streak region. As the flow evolves, larger particles continue to respond and migrate through the base of the streak, increasing the minimum size of the 'valley'. In the lower sublayer of the spray (from $y = -35$ to -15 mm), a small overshoot is evident during the late stages of development. This is due to the very large droplets' inability to follow the flow through the stagnation point and results in an accumulation of the larger sizes (as will be clearly evident in the next section).

Comparing our measurements to these results, the main differences in the SMD resulting from the pairing are:

(i). The location of the minimum starts in a similar position as the single frequency forcing case ($y = 10$ mm), but after the pairing moves to a location on the outside region of the shear layer ($y = 35$ mm).

(ii). The minimum size in the 'valley' is initially 10-20% greater than the single frequency case, but eventually relaxes to similar sizes.

(iii). The overshoot in the lower sublayer is much more pronounced. (*cf.* $x = 6$ cm, $y = -5$ to -10 cm)

Point (i) gives additional evidence to the argument that larger particles entrained by the smaller streak previous to pairing are subsequently deposited into the core of the emerging subharmonic vortex structure. With a greater number of large droplets in this area, the average Sauter mean diameter will increase, shifting the minimum towards the external

edge of the mixing layer. The last two points are most likely due to differences in the initial forcing conditions and slight changes in the initial particle concentration boundary layer thickness. From these two figures it can be seen that the single frequency results of Lázaro and Lasheras (1992b) have a thicker boundary layer with respect to the mean diameter ($\sim$ 2.5 cm as opposed to $\sim$ 1 cm). A ready supply of larger droplets in the boundary layer would easily increase the SMD in the initial mixing region. Also, the sharper boundary layer and higher initial frequency would accentuate the size overshoot development.

5.3 Size Dispersive Effects of Vortex Pairing

In the preceding section, the quantification of how the different sized droplets were dispersed during the pairing was limited to the evolution of the time averaged SMD profiles. While these results were valuable as a direct comparison with previous experimental data, they do not give detailed information about how the various droplet sizes are dispersed through the mixing layer. This information, however, can be observed in the phase-averaged quantities of the number mean diameter, $\langle D_{10}(\phi_j, \mathbf{x}) \rangle$, and the normalized number frequency, $\eta(D_i, \phi_j; \mathbf{x})$.

The first of these quantities, $\langle D_{10}(\phi_j, \mathbf{x}) \rangle$, was obtained by conditionally averaging the arithmetic mean diameter of the recorded droplets:

$$\langle D_{10}(\phi_i, \mathbf{x}) \rangle = \frac{1}{N_j} \sum_{k=1}^{N_j} D(t_k, \mathbf{x}), \qquad (5.3)$$

where N_j is again the number of samples that occur when $I(\phi_i, t_k) = 1$. This is simply the average diameter of all the particles occurring in the phase angle range $\phi_i \pm \Delta\phi/2$.

The second quantity is defined from the statistics gathered by the PDPA through the construction of a joint probability distribution function between the phase angle and the droplet size:

$$g(D_i, \phi_j; \mathbf{x}) = \frac{N_{i,j}(\mathbf{x})}{\sum_{i=1}^{S} \sum_{j=1}^{M} N_{ij}(\mathbf{x})} \qquad \begin{aligned} i &= 1 \text{ to } S \text{ (number of size classes)} \\ j &= 1 \text{ to } M \text{ (number of phase bins)} \end{aligned} \qquad (5.4)$$

where $N_{i,j}(\mathbf{x})$ is the number of particles occurring within the size range $D_i \pm D/2$ and within the phase angle $\phi_j \pm \phi/2$ at the location $\mathbf{x}$. Looking at a fixed streamwise co-ordinate, x,

the normalized number frequency is given by:

$$\eta(D_i, \phi_j, y) = \frac{g(D_i, \phi_j; y)}{\frac{1}{M} \sum_{j=1}^{M} g(D_i, \phi_j; y = -4 \text{ cm})} \qquad (5.5)$$

By normalizing in this manner, deviations in η from unity indicate changes (with respect to the undisturbed free stream) in the probability of finding a particle of size D_i over the y and ϕ domain in any given sample. It should be noted that η is not a reflection of the particle *concentration*, but instead is a measure of the relative *probability* of finding a given size droplet at a given phase angle with respect to the uniform freestream conditions. Measurements of particle concentration using only the PDPA require a knowledge of the swept volume history of the measuring probe, which is difficult to define for low particle concentrations and is hampered by the size biasing effects inherent to the PDPA.

In the present work, $M = 15$ and $S = 4$, with the size ranges divided as given in table 5.1. Here the Stokes number, St (which is the ratio of the droplet's viscous response time to that of the flow fluctuation time scale, St $= \frac{\rho_p D^2}{18\rho_g \nu \tau_g}$), of each size class was based upon the fundamental frequency and the average size of the droplets within the given size range. The choice of size range for each class was a compromise to keep the sampling bins large enough to contain a reasonable number of droplets and at the same time be able to discern variations in their development due to the size differences. Even with these compromises, the initial droplet size distribution was heavily weighted towards the scalar and small size classes, leaving few particles available to represent the largest size. Considering that each sample contained 10,000 measurements, the sparsity of large droplets does present a sizeable amount of statistical uncertainty in the largest size range (approximately 20%). In order to eliminate some of the statistical noise and to highlight the large scale features, the probability

Size Range			Assigned Size "Name"	Stokes Number, St	% Number, $y = -45$ mm
2	$< D_0 <$	10 μm	scalar	0.016	55%
10	$< D_1 <$	20 μm	small	0.098	28%
20	$< D_2 <$	40 μm	intermediate	0.39	13%
40	$< D_3 <$	100 μm	large	1.56	4%

Table 5.1: Size discretization used for phase averaged PDPA data

surfaces were convolved with a spatial low-pass filtering kernel. The convolution generated a smoothed data point based on the weighted average of a 3x3 block of the original data, where the weighting components were selected to be 0.5 for the center point of the block and 0.1 for the other 8. The resulting smoothed surface had a maximum average correction of 10% and standard deviation of 15%. It will be observed, though, that even with this handicap, clear trends for the large size are obtained.

5.3.1   Size dispersion evolution in the presence of a single length scale. Region I.

Contours of $\langle D_{10} \rangle$ at the end of Region I (figure 5.13a, b) show results that are characteristic to single frequency dispersion and are briefly summarized as follows:

(i). There is a size decay along the streak centerline, and also a size increase with radial displacement from the vortex core.

(ii). The mean droplet size begins to increase above the surrounding free stream value beneath the free stagnation point on the spray side of the mixing layer.

(iii). The minimum diameter region occurs at approximately the same phase location as the attenuation (concentration) minimum, but is displaced vertically upwards relative to the attenuation minimum.

(iv). There is a size increase in the external region of the mixing layer, just behind the free stagnation point.

Explanations of the above features are aided by the examining the normalized number frequency in Region I (figure 5.14) which isolates the structure's interaction with each size class. As each one of the surfaces shows, the large-scale streak forms a peaked high-probability ridge, which moves further away from the vortex core and closer to the spray free stream as the size is increased. For the largest size, the same peak occurs within the high-speed stream itself and shows very little significant development along the streak. This feature is responsible for points (i) and (ii), and is consistent with previous experimental (Lázaro and Lasheras, 1992a; Longmire and Eaton, 1992) and numerical findings (Martin
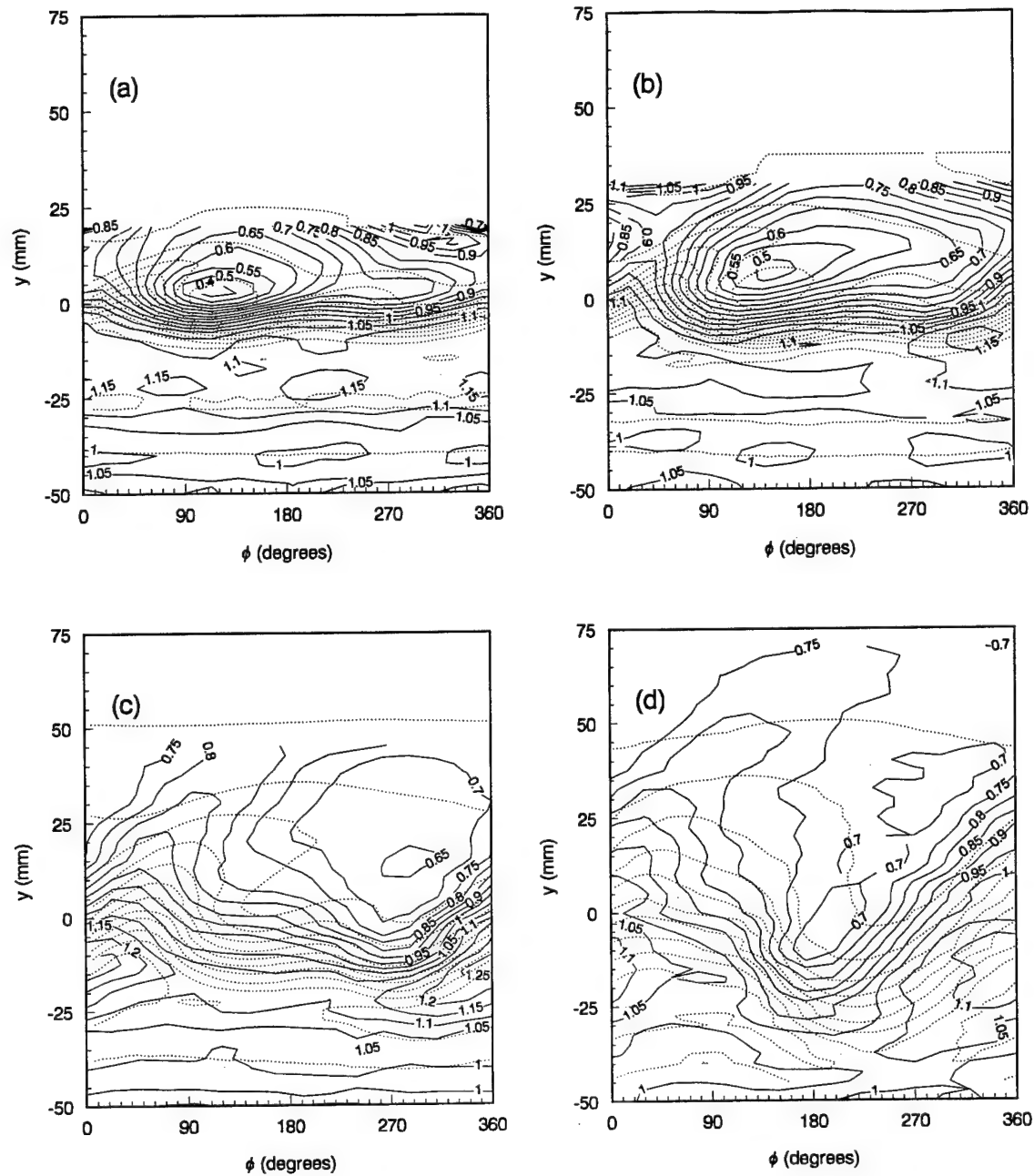
Figure 5.13: Normalized Number Mean Diameter contours for (a) $x = 6$ cm, (b) $x = 10$ cm, (c) $x = 18$ cm, and (d) $x = 30$ cm. Note the development of a size overshoot in lower braid region ($\phi = 320°$, $y = -10$ mm) of figure b. Measurements have been normalized by their average freestream value at $y = -40$ mm and attenuation contours are shown for comparison.
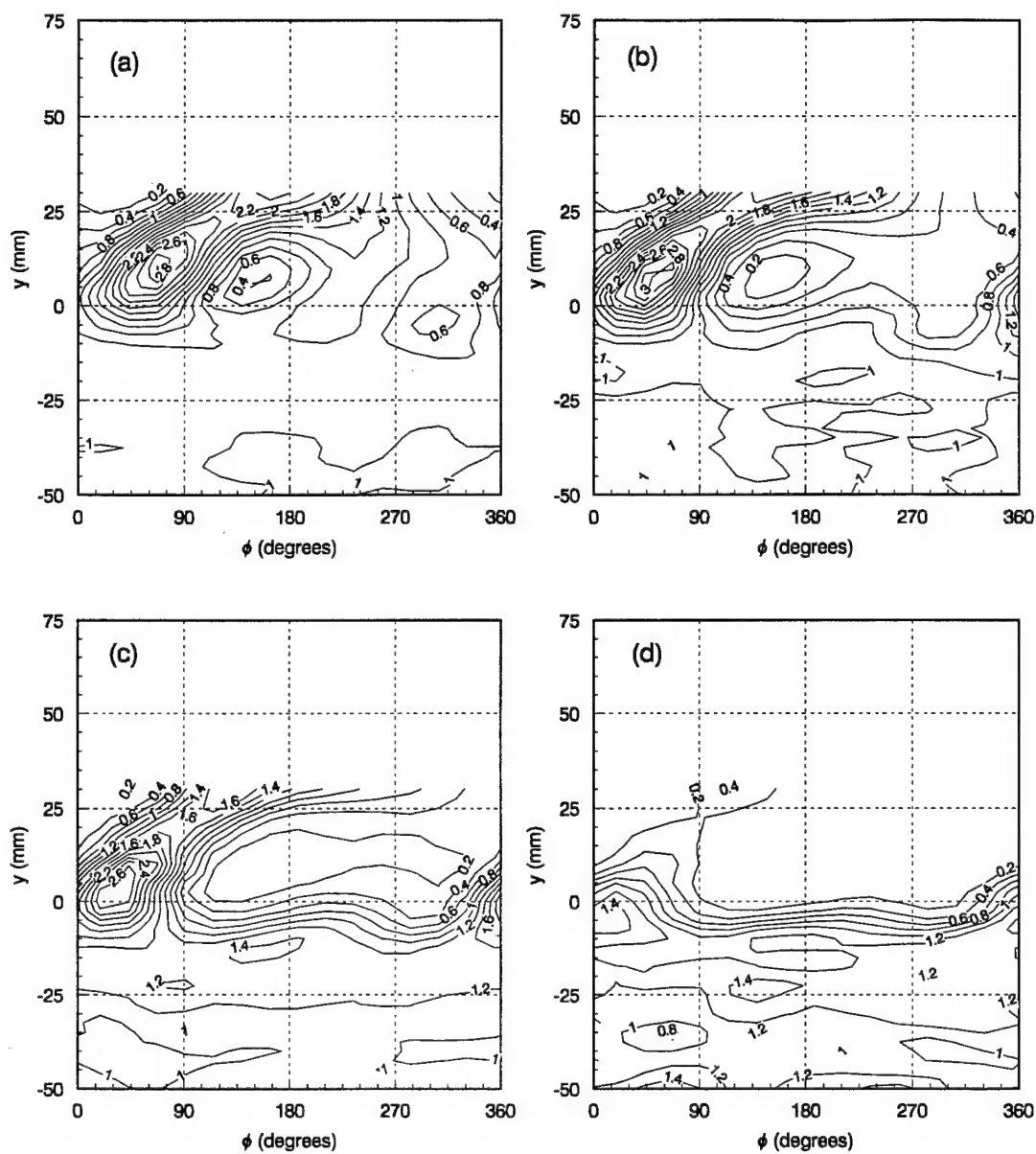
Figure 5.14: Normalized number frequency contours at $x = 10$ cm, region I. (a) scalar size class, D_0; (b) small size class, D_1; (c) intermediate size class, D_2; and (d) large size class, D_3.

and Meiburg, 1994; Chein and Chung, 1988). From the previous work, it is known that this size dependent dispersion can be parameterized by the Stokes number and is a result of increasing inertial effects in the presence of a combined vortex and stagnation point flow. For small Stokes number ($St \ll 1$) the particles follow the flow closely and are entrained along the full length of the streak and into the vortex core. As the size, and hence Stokes number, is increased, the particles are no longer able to follow the flow and require a longer time to adjust to the disturbance. Hence, the extent of the large droplet azimuthal entrainment is retarded compared to droplets of smaller Stokes number and they tend to move along the outer edge of the vortex due to centrifugal effects. Additionally, as a particle with a slow response time is entrained towards a stagnation point, it's trajectory will deviate from the fluid streamlines and overshoot into the opposing stream (Martin and Meiburg, 1994). This causes the droplet to oscillate between the two streams, slowing its entrainment away from the stagnation point and results in the accumulation of larger sizes, as observed above (figure 5.13b). The final two points have not been explained previously (or noted in numerical simulations) but are observable in the experimental data of Lázaro and Lasheras (1992b) (Lázaro and Lasheras, 1992b).

5.3.2 Size dispersion effects of vortex pairing. Region II and III.

The details of the droplet dispersion during the pairing event can be determined by examining the conditionally-averaged diameter, $\langle D_{10} \rangle$, and η at a location in the transitional region, $x = 18$ cm (figures 5.13c and 5.15). As the pairing initiates, the size minimum moves upstream to the core of the smaller vortex as the previous minimum (large vortex core) experiences an increase in mean particle size. The overshoot at the free stagnation point increased to approximately 1.25 times the initial freestream size, and the external overshoot previously noted has now disappeared. Examining the individual size number frequency distributions, one can observe that as the smaller vortex is induced downward, the scalar-sized particles are drawn down into the freestream. This is substantiated by the formation of a decreased probability "hole" on the lower right side of figure 5.15a ($y = -15$ mm, $\phi = 290°$). The larger particles cannot respond to the pairing this quickly and are disturbed only a small amount (figure 5.15d), which amplifies the overshoot of the mean
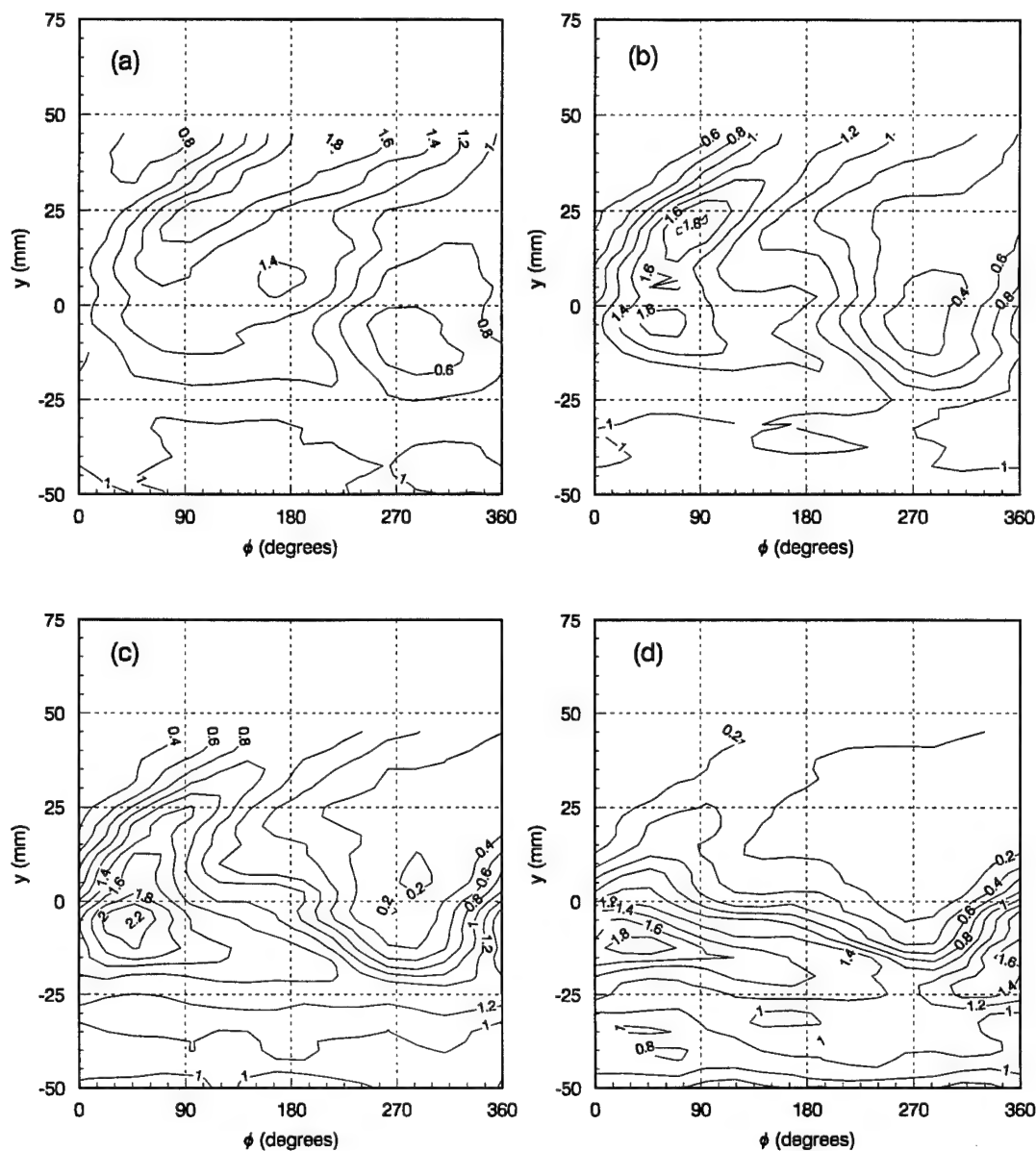
Figure 5.15: Normalized number frequency contours at $x = 18$ cm, region II. (a) scalar size class, D_0; (b) small size class, D_1; (c) intermediate size class, D_2; and (d) large size class, D_3.
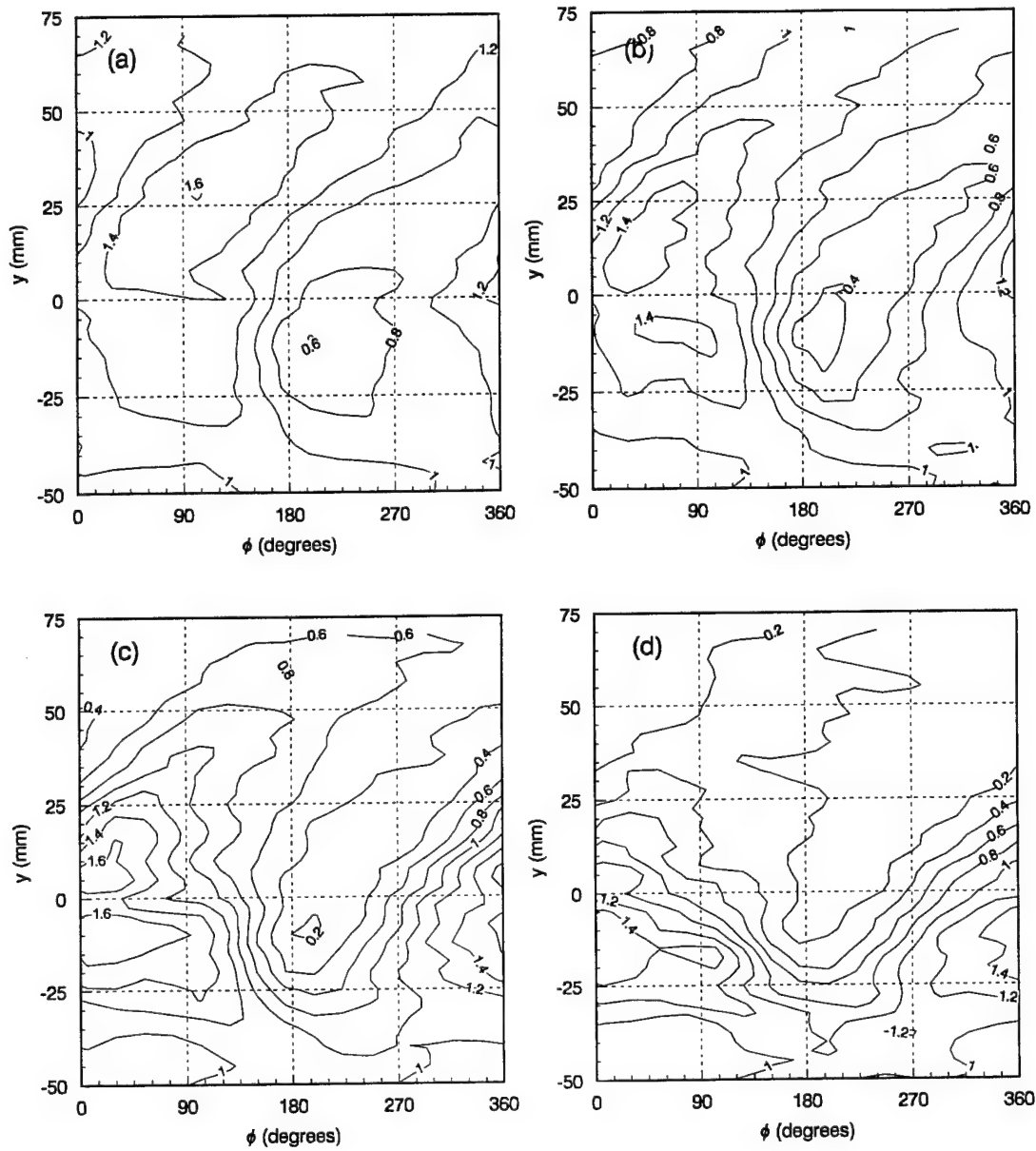
Figure 5.16: Normalized number frequency contours at $x = 30$ cm, region I. (a) scalar size class, D_0; (b) small size class, D_1; (c) intermediate size class, D_2; and (d) large size class, D_3.

diameter near this region. The shifting of the minimum diameter location is a result of the small and intermediate sized droplets being deposited in the core of the subharmonic vortex, which had only been previously occupied by the scalar sized droplets (the smallest droplets were mixed through the core of the vortex by the small scale eddies). For the largest size particles, the pairing process is reduced to the amalgamation of the two underdeveloped streaks in a manner somewhat similar to that observed by Longmire and Eaton (Longmire and Eaton, 1992).

The resulting subharmonic size distribution is also observed to be dissimilar in comparison to structures created by a single dominant frequency. For the mean diameter, the difference is manifested in the shape of the core minimum which is no longer an isolated region surrounded by the streak. Instead the minimum region runs parallel to the streak and extends towards the external free stream. This attests to the weakened streak development that is produced by the interruption of the pairing and also explains the shift in the minimum of the time averaged SMD profile.

Examining the number frequency of each size class (figure 5.16) shows what a diverse impact the pairing has produced. The scalar size has experienced a very pronounced homogenization – peak probability values now fluctuate about 30% at any fixed cross-stream location as compared with 150% during the single frequency region. This is to be expected for particles with St $\ll$ 1, as their quick response time will allow them to follow the stirring motion of the eddies and the strong mixing that occurs due to the rotating strain field of the vortices during the pairing process. As the size increases, the resulting homogenization decreases. For the intermediate and large sizes, we once again see the streak and depletion regions that are characteristic of coherent-structure dispersion (albeit with a shape slightly different as remarked above). Thus, it is noted that the homogenizing influence of the pairing is strongly linked to the response time of the droplets and the driving frequencies of the flow, resulting in complex separation effects.

At this point, it should be noted that the above dispersion measurements are the result of the pairing event produced by the particular combination of phase and amplitude used for the forcing signals. Even so, the trends observed are fairly general and would be qualitatively similar for most other forcing conditions (with the exception of the range of
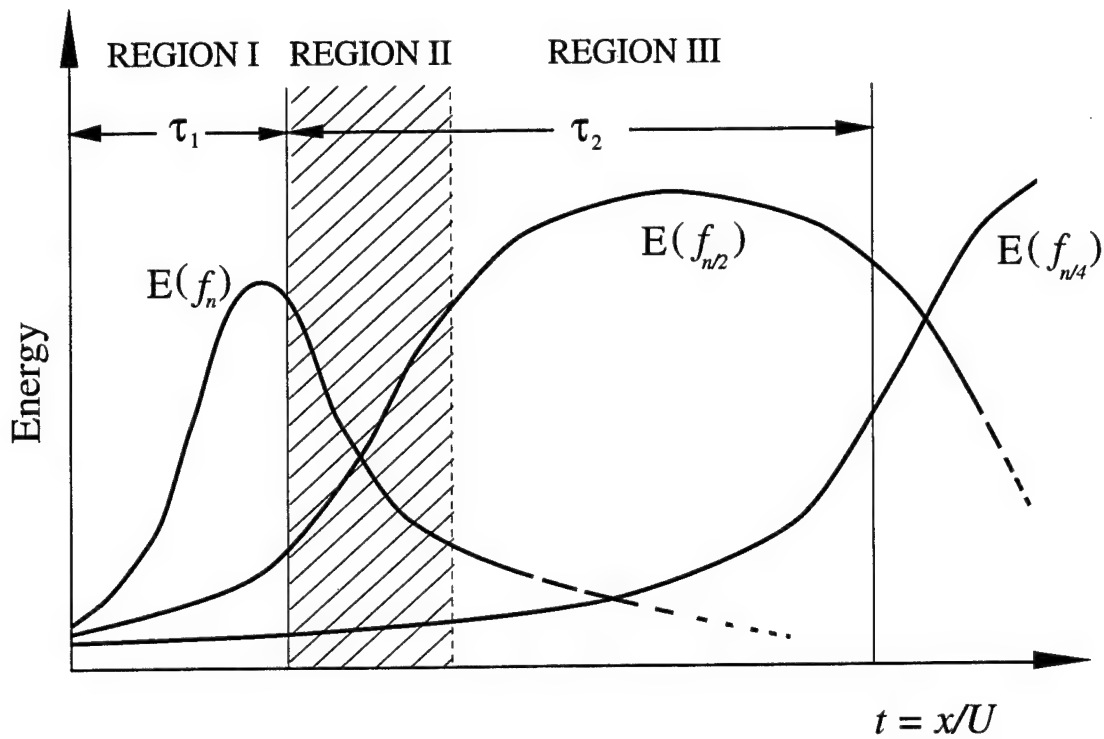
Figure 5.17: Illustration of pairing timescale influence on particle dispersion.

phase shifts which produce a tearing event rather than a pairing). The quantitative differences would then stem from parameters controlling the dispersion that are associated with the details of the pairing event. In addition to the Stokes numbers based on the dominant frequencies (St_1, and St_2), the other two parameters that impact on the dispersion of the individual size classes are: the fundamental development time, τ_1, and the subharmonic lifetime, τ_2 (figure 5.17).

As was discussed earlier, and shown in the results of Lázaro and Lasheras (Lázaro and Lasheras, 1992b), increasing Stokes number particles require additional time to adequately respond to fluctuations. This size dependent time lag was responsible for the azimuthal streak variation in the fundamental dominated region. If the fundamental growth had been allowed more time prior to pairing (larger τ_1), then there would have been more

extensive streak development and larger particle dispersion in the intermediate sizes (St ~ 0.4). This would have resulted in a more complete homogenization for this size during the pairing, as the inner streak is dispersed in the core of the paired vortex. Also, with an increased fundamental development time, there would have been more homogenization in the scalar class even before the pairing event, although to what relative extent cannot readily be determined.

The second parameter of importance, namely the subharmonic lifetime, would determine how long the particles can interact with the paired structure before the next pairing takes place. This is of significance for the larger particles (St ~ 1) ingested during the pairing event; namely, if given a sufficient amount of time they would once again be centrifuged towards the periphery of the vortex structure. This expulsion process, however, was not observed in our case due to the lack of significant large-particle development prior to pairing.

It has been noted that particles with a large scale Stokes number of the order unity tend to be dispersed by the coherent structures further than corresponding fluid elements (Crowe and Troutt, 1988; Chung and Troutt, 1988; Chein and Chung, 1987). As discussed above, amplified dispersion was not observed to occur in the current measurements (*cf.* figures 5.14d, 5.15d, and 5.16d). This is in contrast to numerical results obtained by Chein and Chung (Chein and Chung, 1987), who found that the pairing event increases particle dispersion in comparison to the pre- and post-pairing flows. Our findings, however, do not contradict their results, but instead reflect the fact that their simulations considered groups of particles that were released in small regions in space and time, while our flow continually disperses droplets from all regions in the high-speed stream. Thus, even though certain regions of the structure may be very effective at dispersing particles, the net effect of the whole structure does not result in amplified dispersion properties. This is confirmed by the numerical simulations of Martin and Meiburg (Martin and Meiburg, 1994), who showed that dispersion integrated over the subharmonic wavelength during the pairing event exhibits a reduced value in comparison to single frequency forced flows. Their results did indicate that some amplified dispersion did eventually occur, but only well after the pairing event had completed.

As a final remark, it is noted that the preceeding discussion intrepreted the experimental data with the assumption that the Stokes drag force was the dominant force acting on the particle. Of the other forces acting on the particle, only the body force due to gravity and the lift force are likely to make a slight contribution to the motion of the droplet (added mass and the pressure force are negligible due to the large density ratio, and the Basset history term is a higher order effect that is important at large Stokes numbers). The influence of gravitational effects can be estimated by comparing the ratio of the body force, $m_p \Delta \rho \mathbf{g}$, to the Stokes drag giving:

$$\frac{\mathbf{F}_g}{\mathbf{F}_D} = \frac{\frac{4}{3}\pi a^3 (\rho_p - \rho_g)\mathbf{g}}{6\pi\mu a(\mathbf{u}_g - \mathbf{u}_p)} = \frac{2}{9}\frac{a^2 \Delta \rho g}{\mu \Delta U}, \tag{5.6}$$

where a is the radius of the droplet. From equation (5.6), the importance of the gravitational effects scale with the diameter squared and will therefore be most prominent for the largest sizes. A balance of these forces ($\mathbf{F}_g/\mathbf{F}_D = 1$) for the largest droplets in the spray (100 μm) requires a slip velocity of 0.3 m s^{-1}. Typical slip velocities for the large size class are an order of magnitude larger (1 to 3 m s^{-1}), indicating that the drag force will be 3 to 10 times that due to gravity. Even for the worst case example just calculated, the effect of gravity on the dispersion will be small, due to the short residence time of the eddies within the test section. At the average convective velocity of 9 m s^{-1}, the gravitational force will only alter a 100 μm droplet's vertical velocity by 0.33 m s^{-1} by the time it has exited the test section (0.3 m). Thus the effects of gravity will only be dominant in the outer regions of the shear layer where the lower velocities and longer residence times allow its effects to be felt.

An estimate of the importance of the lift force can be determined in the same way as the gravitational force:

$$\frac{\mathbf{F}_L}{\mathbf{F}_D} = \frac{\frac{1}{2}\rho_g \Delta U^2 A_p C_L}{6\pi\mu a(\mathbf{u}_g - \mathbf{u}_p)} = \frac{C_L \mathrm{Re}_D}{24}, \tag{5.7}$$

where by definition $C_L = \mathbf{F}_L/\frac{1}{2}\rho_g \Delta U^2 A_p$, $A_p = \pi a^2$ is the cross-sectional area of the particle, and $\mathrm{Re}_D = D\Delta U/\nu$ is particle slip Reynolds number. Currently, there is little agreement between the theoretical predictions and experimental measurement of C_L (Sridhar and Katz, 1995), other than the fact that it should somehow be dependent upon the slip

Maximum Lift to Drag by Size				
	$D = 10 \ \mu$m	$D = 20 \ \mu$m	$D = 40 \ \mu$m	$D = 100 \ \mu$m
Max. slip velocity, $(\mathrm{m\,s^{-1}})$	0.3	1	1.5	3
Reynolds number, Re_D	0.2	1.4	4	20
Drag coefficient, C_D	120	18	6	1.2
Lift coefficient, C_L	0.38	0.34	0.36	0.39
F_L/F_D	0.3%	2%	6%	30%

Table 5.2: Maximum lift to drag estimates

velocity and the local vorticity. Theories have been put forth for both viscous (Saffman, 1965) and inviscid (Auton, 1987) predictions of the lift force, with the result that the theoretical solutions under-predict the lift coefficients by as much as 1 to 2 orders of magnitude. In light of such discrepancies, C_L will be estimated using the correlation (Sridhar and Katz, 1995)

$$C_L = 0.59 \left(\frac{a\omega}{\Delta U} \right)^{0.25} \qquad (5.8)$$

where ω is the local vorticity. The local vorticity will be most intense in the streamwise vortical structures embedded in the braid region, which result from a convective/diffusive balance in the high strain region between the vortices and scale as $\delta/\sqrt{\mathrm{Re}}$. Using the estimated Taylor length scale of $\lambda_{Taylor} \sim 0.1$ mm, and a velocity scale of 1 m s^{-1} provides an estimate of the vorticity to be $\omega = 10^4$ s^{-1}. The estimates lift/drag ratios for the maximum droplet diameter of each size class is given in table 5.2. The results indicate that the lift force will also play a secondary role in the motion of the droplet, with the most significant contribution occuring for the largest droplets. Thus, for the particular turbulence scales and droplets sizes used in the current experiment, the assumption of dominant drag seems reasonable with the exception of the largest sizes in limited isolated regions (i.e. slow speed stream and intense small scale vortices in the braids) where gravitational and lift forces may make a noticeable secondary effect.

Chapter 6

Two-Phase Kinetic Energy Transfer

One of the most pressing obstacles in the analysis of two-phase, turbulent flows is to effectively model the transfer of linear momentum and kinetic energy between the two phases. Often in the numerical computation of two-phase flows, the transfer models rely on algebraic, first- and second-moment closures (Elghobashi and Abou-Arab, 1983; Viollet and Simonin, 1994), and require either an educated guess or a fit to limited experimental data to obtain the model coefficients. In order to gain an understanding of the underlying physical processes and to assess the validity of any such closure models, it is important to obtain experimental information on the instantaneous fluctuations of all the flow variables. This would enable one to have direct information on how the cross-moments vary throughout the flow, and judge the performance of the models. Unfortunately, current experimental methods do not allow for such detailed, complete measurements. However, in turbulent shear layers (where large-scale structures are receptive to controlled perturbation), conditional sampling offers an effective tool to produce ensemble-averaged portraits of how the closure terms are affected by the large-scale structures.

The energy budget for a turbulent two-phase spray in practical applications, e.g. combustors, is in general quite complicated, and involves terms which account for the turbulent kinetic energy of both phases, surface deformation, heat conduction, vaporization, and chemical reaction. If the conditions are restricted to a dilute, dispersed, isothermal spray of droplets in an incompressible carrier phase, the problem can then be reduced to considerations of the kinetic energy contained within and exchanged between the two phases.

For the dilute spray and the turbulent shear layer considered within the current work, the total kinetic energy of the flow at the inlet to the test section is given by

$$\text{KE}_{total} = \frac{1}{2}\rho_p\alpha_p\boldsymbol{v}^2 + \frac{1}{2}\rho_g\alpha_g\boldsymbol{u}^2. \tag{6.1}$$

In the standard Reynolds averaging sense ($\boldsymbol{u} = \boldsymbol{U} + \boldsymbol{u'}$; $\overline{\boldsymbol{u}} = \boldsymbol{U}$), this energy is divided between a mean kinetic energy, $\frac{1}{2}(\rho_p\overline{\alpha}_p\boldsymbol{V}^2 + \rho_g\overline{\alpha}_g\boldsymbol{U}^2)$, and a fluctuating component, $\frac{1}{2}(\rho_p(\overline{\alpha}_p\overline{\boldsymbol{v'}^2} + 2\boldsymbol{V}\cdot\overline{\alpha_p'\boldsymbol{v'}} + \overline{\alpha_p'\boldsymbol{v'}^2}) + \rho_g(\overline{\alpha}_g\overline{\boldsymbol{u'}^2} + 2\boldsymbol{U}\cdot\overline{\alpha_g'\boldsymbol{u'}} + \overline{\alpha_g'\boldsymbol{u'}^2}))$. With the exception of the thin boundary layer region on the splitter plate, the kinetic energy of the flow will initially reside mainly in the mean component. As the shear layer forms, the mean kinetic energy of the gas is converted to fluctuating kinetic energy through shear instabilities and turbulent processes normally found in single-phase flows (assuming that the presence of the particles does not significantly alter the formation of the shear layer). The changes in mean and turbulent kinetic energy of the gas are then transmitted to the dispersed phase through the interfacial forces, which will result in a redistribution of the mean and fluctuating components of the droplets' kinetic energy as well as a transport and feedback of kinetic energy into the gas as the droplets are dispersed throughout the flow.

Although the standard Reynolds averaging procedure results in quantities which are useful to design work, they completely obscure the physical structure of the flow which is often times crucial to understanding the processes involved. Conditional averaging (also called phase-averaging in the current experiment) offers a partial solution to the problem by selectively averaging discrete scales within the flow to present an ensemble mean of the flow structure. This solution is partial in the sense that it does not resolve all of the scales which may be important to the problem being studied. In the current experiment, conditional averaging is a useful tool to examine the kinetic energy because the large scales resolved by the phase-average contain a major portion of the turbulent kinetic energy of the shear layer, and hence they may play a dominant role in the transfer processes between the phases. This does not imply that the small scales are unimportant. Quite to the contrary, in cases of strong coupling, the small scales which are not resolved will most likely be the first structures affected by the feedback of energy to the gas (Elghobashi and Truesdell, 1993).
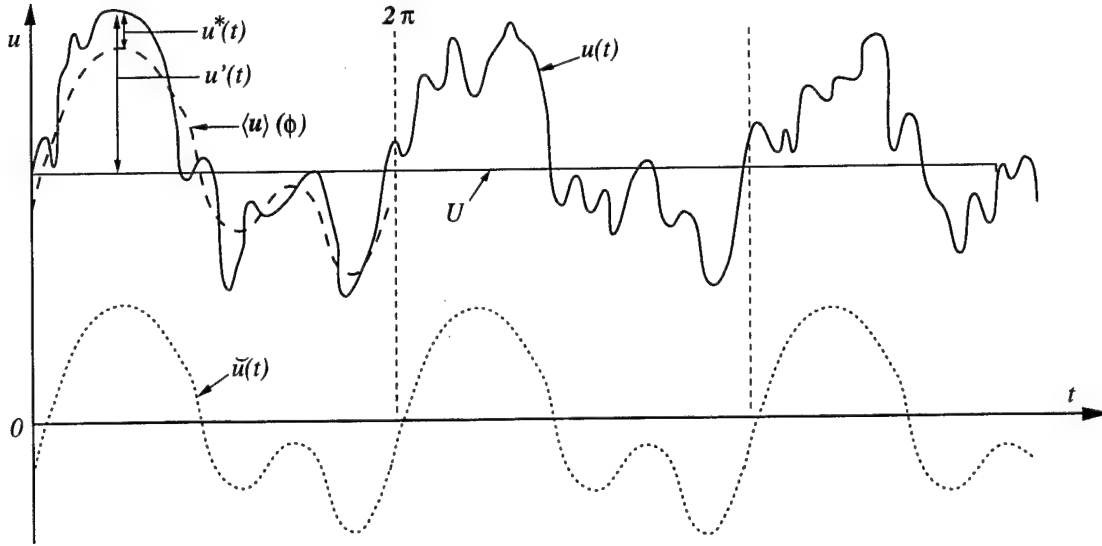
Figure 6.1: Definition of phase-averaged variables.

The standard Reynolds averaged quantities can be expressed in terms of phase-averaged quantities by redefining the fluctuating component, $u'(t)$, to be the sum of a periodic fluctuation that has a zero mean, $\breve{u}(t)$, and a random component, $u^\star(t)$, which is the difference between u' and $\breve{u}$ (figure 6.1):

$$u'(t) \;=\; \breve{u}(t) \,+\, u^\star(t) \tag{6.2}$$

The periodic fluctuating component, $\breve{u}(t)$, is defined as the phase-average signal minus the time average mean,

$$\langle \breve{u}(\phi) \rangle \;\equiv\; \langle u(\phi) \rangle \,-\, U. \tag{6.3}$$

Here the notation $\langle u(\phi) \rangle$, has been adopted to represent the resultant phase-averaged quantity of u (which is a function of ϕ), as opposed to $\langle u(t) \rangle$ which represents the phase-averaged operator acting on $u(t)$. As a result of definition (6.3), it follows that

$$\langle u^\star(t) \rangle \;=\; \Big\langle u(t) - U - \breve{u}(t) \Big\rangle \;=\; \langle u(t) \rangle - U - \langle \breve{u}(t) \rangle \;=\; 0. \tag{6.4}$$

It is important to note that $\breve{u}(t)$ is constant with respect to the phase-averaging operator due to its periodicity. This gives the useful result:

$$\langle \breve{u}(t)^2 \rangle \;=\; \langle \breve{u}(\phi) \rangle^2 \quad \text{and} \quad \langle \breve{u}(t)\,u^\star(t) \rangle \;=\; \langle \breve{u}(\phi) \rangle \langle u^\star(t) \rangle \;=\; 0. \tag{6.5}$$

The relation between the discrete phase-average (finite bin width) and the Reynolds average was derived in §3.4. The finite bin phase-average can be extended to the case of a continuous phase-averaged function by allowing the bin width, $\Delta\phi$, go to zero. In this case, the time average of $\boldsymbol{u}(t)$ is given by

$$U = \overline{\boldsymbol{u}(t)} = \frac{1}{2\pi} \int_0^{2\pi} \langle \boldsymbol{u}(t) \rangle \, d\phi = \frac{1}{2\pi} \int_0^{2\pi} \langle \boldsymbol{u}(\phi) \rangle \, d\phi, \tag{6.6}$$

which implies that

$$\begin{aligned}
\overline{\boldsymbol{u}(t)'^2} &= \frac{1}{2\pi} \int_0^{2\pi} \left\langle (\breve{\boldsymbol{u}}(t) + \boldsymbol{u}^\star(t))^2 \right\rangle d\phi \\
&= \frac{1}{2\pi} \int_0^{2\pi} \left(\left\langle \breve{\boldsymbol{u}}^2(t) \right\rangle + 2 \langle \breve{\boldsymbol{u}}(t) \boldsymbol{u}^\star(t) \rangle + \left\langle \boldsymbol{u}^{\star 2}(t) \right\rangle \right) d\phi \\
&= \frac{1}{2\pi} \int_0^{2\pi} \left(\langle \breve{\boldsymbol{u}}(\phi) \rangle^2 + \left\langle \boldsymbol{u}^{\star 2}(\phi) \right\rangle \right) d\phi
\end{aligned} \tag{6.7}$$

This shows that the total r.m.s. is the sum of the variance of the periodic phase-averaged signal and the variance of the random fluctuations about the mean phase-average. For the case of discrete phase-averaging, the quantity $\langle \boldsymbol{u}^{\star 2} \rangle$ will depend on the gradients of $\langle \boldsymbol{u}(\phi) \rangle$ and the bin width used for sampling. The quantity should converge to the continuous value once $\Delta\phi(\partial \langle \boldsymbol{u}(\phi) \rangle / \partial\phi) \ll \langle \boldsymbol{u}^{\star 2}(\phi) \rangle$.

The turbulent kinetic energy of (6.1) can be redefined as a phase-averaged quantity which will then represent the kinetic energy of the fluctuations associated with the averaging scale periodicity plus the mean kinetic energy. This can be verified by using relations (6.2)–(6.5) to link the phase-averaged kinetic energy to the standard Reynolds averaged quantities:

$$\begin{aligned}
\frac{1}{2\pi} \int_0^{2\pi} \left(\frac{1}{2} \rho_g \langle \boldsymbol{u} \rangle^2 \right) d\phi &= \frac{1}{2\pi} \int_0^{2\pi} \frac{1}{2} \rho_g \left(U^2 + 2U \langle \breve{\boldsymbol{u}} \rangle + \langle \breve{\boldsymbol{u}} \rangle^2 \right) d\phi \tag{6.8} \\
&= \frac{1}{2} \rho_g \left(U^2 + \frac{1}{2\pi} \int_0^{2\pi} \langle \breve{\boldsymbol{u}} \rangle^2 \, d\phi \right) \\
&= \frac{1}{2} \rho_g \left(U^2 + \overline{\boldsymbol{u}'^2} - \frac{1}{2\pi} \int_0^{2\pi} \left\langle \boldsymbol{u}^{\star 2} \right\rangle d\phi, \right).
\end{aligned}$$

While observation of the dispersed and continuous phase kinetic energy is useful, it alone does not give much insight into the coupling between the two phases. The more instructive quantities to examine are the terms which produce the transfer of kinetic energy from one phase to the other. These terms stem from three general sources: The rate of work being done on the particle owing to forces generated by its relative motion, called **kinetic**

energy transfer; the rate of kinetic energy lost to shear deformation work in the surrounding continuous phase due to the particle motion, called **particle dissipation**; and the rate of work done by body forces and the far field pressure gradients on the particle, called **buoyant energy transfer**(see Maxey, Chang, and Wang (1994) and Rightley (1995) for the importance of buoyant energy transfer in bubbly flows). In the current work, the inertia of the droplets throughout most of the flow is large enough such that the buoyant energy transfer is of secondary importance (Chapter 5). The following chapter will therefore focus on an examination of the mean phase-average kinetic energy transfer and mean phase-averaged particle dissipation, starting with the definition and formulation of these terms, followed by the method of experimental realization, and finally resulting in a detailed examination of their evolution within the shear layer.

6.1 Framework for Study of Kinetic Energy Transfer

In the limit of dilute flows with particles smaller than the continuous fluid scales, the effect of the dispersed phase on the carrier flow evolution can be examined by decomposing the motion of the carrier fluid about an isolated droplet into two components as in Chapter 2 (Maxey and Riley, 1983): u, which describes the flow field that would exist if there were no drop present in the fluid, and u_ε, which specifies the perturbation caused by the relative motion and presence of the droplet. The decomposition for the total fluid velocity, $\tilde{u}$, can be expressed as

$$\tilde{u} = u + u_\varepsilon \tag{6.9}$$

with the supplemental boundary conditions

$$u_\varepsilon \rightarrow 0 \qquad \text{as } r \rightarrow \infty$$

$$u_\varepsilon = v - u \qquad \text{at } r = a, \text{ the surface of the droplet,}$$

The disturbance flow will generate a force on the particle which will be given by

$$f_\varepsilon = \oint \sigma_\varepsilon \cdot \mathbf{n} dS \tag{6.10}$$

where $\boldsymbol{\sigma}_\varepsilon$ is the stress tensor of the disturbance flow

$$\boldsymbol{\sigma}_\varepsilon = -p_\varepsilon \mathbf{I} + \mu(\nabla \boldsymbol{u}_\varepsilon + \nabla \boldsymbol{u}_\varepsilon{}^T). \tag{6.11}$$

The disturbance force that is transmitted across the surface of the drop (and its corresponding reaction force on the carrier fluid) is one of the terms of interest in the coupling problem between the phases. Taking the dot product of the disturbance force with the velocity of the droplet gives the rate of work performed on the droplet by the gas to change its kinetic and potential energy:

$$\mathbf{P} = \boldsymbol{f}_\varepsilon \cdot \boldsymbol{v} \tag{6.12}$$

Note that $\mathbf{P}$ can be either a positive or negative quantity, and hence can represent a source or sink of kinetic energy to the droplet depending on the sign of the above dot product.

In addition to the transfer of kinetic energy which occurs from the force acting on the interface, there will also be dissipative losses due to deformation work done on the gas within the disturbance flow field. Since it is assumed that the particles are smaller than the smallest fluid scales of the undisturbed flow, the frictional dissipation of the disturbance flow can be treated separately from the undisturbed flow (Wang and Maxey, 1993a) to give

$$\epsilon_p = \int_0^{2\pi} \int_0^\pi \int_a^\infty (2\nu \mathbf{s}_\varepsilon : \mathbf{s}_\varepsilon) \, r^2 \sin\theta \, dr \, d\theta \, d\phi, \tag{6.13}$$

where r is the radial component of a coordinate system centered on the droplet, a is the droplet radius, θ is the polar angle measured from the axis of relative motion, ϕ is the azimuthal coordinate, ν is the kinematic viscosity, and $\mathbf{s}_\varepsilon = \frac{1}{2}\left(\nabla \boldsymbol{u}_\varepsilon + \nabla \boldsymbol{u}_\varepsilon^T\right)$ is the strain rate tensor of the disturbance flow. Note here that $\mathbf{s}_\varepsilon : \mathbf{s}_\varepsilon$ is a positive definite quantity, and hence ϵ_p will always act as a sink of energy to the carrier phase. Thus as energy is transferred either to or from the particle by $\mathbf{P}$, ϵ_p will act as an additional drain on the kinetic energy of the carrier flow.

In the limit of dilute sprays of small heavy particles ($\alpha_p \ll 1$, $D_p < \eta_\kappa = $ the Kolmogorov scale, and $\rho_g/\rho_p \ll 1$) it can be shown (Chapter 2) that the Stokes drag force is the dominant effect determining the motion of the droplet and hence describes the disturbance flow field in the vicinity of the droplet (provided that the Reynolds number

based on slip velocity, Re_p, is less than one). The velocity field for this solution is given by

$$u_{r_\epsilon} = (u - v)\cos\theta \left(1 - \frac{1}{2}\left[\left(\frac{a}{r}\right)^3 - 3\left(\frac{a}{r}\right) + 2\right]\right) \qquad (6.14)$$

$$u_{\theta_\epsilon} = -(u - v)\sin\theta \left(1 - \frac{1}{4}\left[-\left(\frac{a}{r}\right)^3 - 3\left(\frac{a}{r}\right) + 4\right]\right). \qquad (6.15)$$

Use of equations (6.15) in the integration of (6.10) and (6.13) gives the kinetic energy transfer rate per unit volume to be

$$\mathbf{P} = 3\pi\mu D(\mathbf{u} - \mathbf{v}) \cdot \mathbf{v} = \mathbf{f}_\varepsilon \cdot \mathbf{v}, \qquad (6.16)$$

and a particle dissipation per unit volume of

$$\rho_g \epsilon_p = 3\pi\mu D(\mathbf{u} - \mathbf{v})^2 = \mathbf{f}_\varepsilon \cdot (\mathbf{u} - \mathbf{v}), \qquad (6.17)$$

Expression (6.17) shows that the calculated dissipation is exactly equal to the force acting on the droplet multiplied by the relative slip velocity. Under more generalized flow conditions, the expression for $\mathbf{f}_\varepsilon$ contains other forces such as added mass and the Basset history term, and in flows where these terms are comparable to the Stokes drag, $\mathbf{f}_\varepsilon \cdot (\mathbf{u} - \mathbf{v})$ represents energy that is lost to the disturbance flow and presumed to be rapidly dissipated in the smallest scales (see Chapter 2).

The applicability of the above formulation to the current experimental conditions can be checked by examining the carrier gas velocity field, particulate velocity field, and the size distribution of the spray. The requirement of a dilute spray ($\alpha_p \ll 1$) is equivalent to having a large inter-particle spacing in comparison to the droplet diameter such that the Stoke's solution for a single particle may be applied without having to be concerned with the effect of nearby droplets. The measured freestream volume concentration of approximately $2 \, x \, 10^{-5}$ gives an average inter-particle spacing of 37 mean particle diameters – at half this distance the velocity disturbance is only 4% of the total slip velocity, which implies that interference effects due to the neighboring droplets will not be important.

The requirement of having droplets smaller than the Kolmogorov length scale, η_κ, stems from the fact that the Stokes solution was derived for a steady uniform flow. Thus the temporal and spatial gradients seen by the particle must be very small, which is

satisfied provided that $D \ll \eta_\kappa$. Using the estimates from §4.3.1 give $\eta_\kappa|_{x=6} = 42\ \mu m$ and $\eta_\kappa|_{x=30} = 54\ \mu m$, which is larger than all of the size classes except for the largest one, D_3. For the large particles, use of (6.17) will give a first order estimate of the dissipation as higher order corrections are needed to account for the non-uniformity of the surrounding flow. Corrections for the unsteady motion result in the added mass and Basset history term, while weak velocity gradients give the so-called Faxen corrections (Maxey and Riley, 1983). Except in cases of very high frequency motion, the unsteady terms result in only small corrections to particle response for large density ratios (see Chapter 2). The Faxen corrections are of order $D^2 U_o / L^2$ (U_o/L is the typical velocity gradient) smaller than the Stokes drag term, and are thus typically much smaller than the Stokes drag provided $(u - v)/U_o < a^2/L^2$ which should hold for even the larger particles due to their large slip velocity.

Finally, the stipulation of a small slip Reynolds number ensures the applicability of the Stokes solution for the flow around the droplet. Examination of the phase averaged slip velocity shows that only the intermediate and large size classes ($D_2 \sim 30\ \mu m$, $D_3 \sim 60\ \mu m$) exceed this requirement in the regions of high slip velocity where Re_p can reach maximum values around 2 and 10, respectively. Use of equation (6.17) in these regions results in an underestimation of the drag force (and dissipation) of approximately 50% in comparison to the standard drag curve for the largest size class. It should be remembered that this is a maximum deviation which results in a conservative estimate of dispersed phase coupling influence. The droplets influence on the carrier phase may be a factor of 2 greater if the largest sizes have a dominant effect.

6.2 Multiple Particles and Experimental Measurement

The total kinetic energy transfer and particle dissipation caused by the spray can be extended from the single particle expression by multiplying (6.16) and (6.17) by the number density of each size and integrating over the size range to obtain

$$P(x,t) = \int_0^\infty 3\pi\mu D\Big(u(x,t) - v(D,x,t)\Big) \cdot v(D,x,t)\, N(D,x,t)\, dD, \qquad (6.18)$$

110

and

$$\epsilon_p(\boldsymbol{x}, t) = \int_0^\infty 3\pi\nu D\Big(\boldsymbol{u}(D, \boldsymbol{x}, t) - \boldsymbol{v}(D, \boldsymbol{x}, t)\Big)^2 N(D, \boldsymbol{x}, t)\, dD. \tag{6.19}$$

Limiting the discussion for the moment to the kinetic energy transfer, information regarding the large-scale contribution can be obtained by taking a phase-average of (6.18), resulting in:

$$\langle P(\phi) \rangle = \int_0^\infty 3\pi\mu D \left\langle (\boldsymbol{u} - \boldsymbol{v}) \cdot \boldsymbol{v} N \right\rangle dD. \tag{6.20}$$

The experimental characterization of this quantity poses great difficulties since there is no instrument available that can instantaneously measure the gas velocity, the particulate velocity, and the size distribution. Therefore, the discussion will be limited to observation of the mean phase-averaged quantities as given by:

$$\int_0^\infty 3\pi\mu D \left(\langle \boldsymbol{u} \rangle - \langle \boldsymbol{v} \rangle\right) \cdot \langle \boldsymbol{v} \rangle \langle N \rangle\, dD. \tag{6.21}$$

In the limit of laminar periodic flow and infinitesimal bin width ($\Delta\phi \to 0$), this is equivalent to (6.20) due to the fact that all higher-order fluctuating moments, such as $\langle n^\star \boldsymbol{u}^\star \boldsymbol{v}^\star \rangle$, are identically zero. In the current experiment, where most of the fluctuations are contained in the resolved scales of the mean phase-average, (6.21) will be a good approximation to (6.20).

The interpretation of the above mean phase-averaged kinetic energy transfer terms can be aided by examining what contribution they make to the mean kinetic energy equation and the turbulent kinetic energy budget for the carrier gas phase. Limiting the discussion for the moment to the consideration of a dispersed phase with a uniform particle size D, the mean kinetic energy equation for the carrier gas is

$$\boldsymbol{U} \cdot \nabla \frac{1}{2} U^2 = -\nabla \cdot \left(\frac{PU}{\rho_g} - 2\nu \boldsymbol{U} \cdot \mathbf{S} + \frac{1}{2}\overline{\boldsymbol{u}'\boldsymbol{u}'} \cdot \boldsymbol{U} \right) - 2\nu\overline{\mathbf{S}:\mathbf{S}}$$
$$+ \overline{\boldsymbol{u}\boldsymbol{u}}:\mathbf{S} - \left(\overline{N}\,\boldsymbol{F}_\varepsilon + \overline{N'\boldsymbol{f}_\varepsilon'} \right) \cdot \boldsymbol{U} \tag{6.22}$$

and the turbulent kinetic budget is given by:

$$\boldsymbol{U} \cdot \nabla \frac{1}{2}\overline{u'^2} = -\nabla \cdot \left(\frac{\overline{p'\boldsymbol{u}'}}{\rho_g} - 2\nu\overline{\boldsymbol{u}' \cdot \mathbf{s}'} + \frac{1}{2}\overline{u'u'^2} \right) - 2\nu\overline{\mathbf{s}':\mathbf{s}'}$$
$$- \overline{\boldsymbol{u}\boldsymbol{u}}:\mathbf{S} - \overline{N\,\boldsymbol{f}_\varepsilon' \cdot \boldsymbol{u}'} - \boldsymbol{F}_\varepsilon \cdot \overline{\boldsymbol{u}'N'} - \overline{N'\boldsymbol{f}_\varepsilon' \cdot \boldsymbol{u}'}, \tag{6.23}$$

where $f_\varepsilon = F_\varepsilon + f_\varepsilon'$ is the force acting on the particles as given by (6.16), and $N = \overline{N} + N'$ is the concentration. Equation (6.22) was obtained by taking the Reynolds average of the instantaneous momentum equation for the gas phase (equation 2.28) and multiplying by the mean velocity. The turbulent kinetic energy budget then resulted from the dot product of the instantaneous gas phase momentum equation with u, Reynolds averaging, and subtracting the mean kinetic energy equation. With the exception of the last two terms in (6.22) and the last three in (6.23), the equations are the same as the single-phase mean and turbulent kinetic energy equations (cf. Tennekes and Lumley, 1972, p. 63), and are subject to the same interpretations of kinetic energy transport and dissipation. The last few terms represent how the mean and kinetic energy of the gas is coupled to the dispersed phase. The exact nature of the interaction is not clear, as interpretation of higher-order correlations is usually speculative at best. Some progress, however, can be made by examining the particle/turbulence coupling terms in a phase-averaged sense. The mean transfer terms are expressed as:

$$\overline{N}\, F_\varepsilon \cdot U + \overline{N f_\varepsilon'} \cdot U \;=\; \frac{1}{2\pi} \int_0^{2\pi} \left[U \cdot \left(\langle f_\varepsilon \rangle \langle N \rangle + \langle f_\varepsilon^\star N^\star \rangle \right) \right] d\phi, \qquad (6.24)$$

while the terms appearing in the turbulent kinetic energy budget are given by

$$\overline{N\, f_\varepsilon' \cdot u'} + F_\varepsilon \cdot \overline{u' N'} + \overline{N' f_\varepsilon' \cdot u'} \;=$$
$$\frac{1}{2\pi} \int_0^{2\pi} \Big[\langle N \rangle \langle u \rangle \cdot \langle f_\varepsilon \rangle \;-\; U \cdot \left(\langle f_\varepsilon \rangle \langle N \rangle + \langle f_\varepsilon^\star N^\star \rangle \right) + \langle N \rangle \langle f_\varepsilon^\star \cdot u^\star \rangle$$
$$\langle u \rangle \cdot \langle f_\varepsilon^\star N^\star \rangle + \langle f_\varepsilon \rangle \cdot \langle u^\star N^\star \rangle + \langle N^\star f_\varepsilon^\star \cdot u^\star \rangle \Big] d\phi. \quad (6.25)$$

Again there are many higher-order correlation terms which are not readily meaningful, but in the case of large, coherent structures they may represent a much smaller contribution than the resolved phase-averaged quantities and could thus possibly be neglected. It is also of interest to note that once they are phase-averaged, the particle interaction terms of the mean kinetic energy equation are identical in form but opposite in sign to the second term in the turbulence energy budget. Thus, these quantities represent an additional mechanism by which energy can be indirectly transferred between the mean and fluctuating gas components. Of the seven phase-averaged quantities shown in (6.24) and (6.25) which compose

112

the two-phase coupling terms, only two could be measured in the current experiment – one of which will be presented and is the subject of the current chapter. The term which is not presented, $U \cdot \langle f_\varepsilon \rangle \langle N \rangle$, is part of the turbulent kinetic energy conversion process mentioned above, while the second quantity to be measured, $\langle N \rangle \langle u \rangle \cdot \langle f_\varepsilon \rangle$ represents a turbulent exchange process between the dispersed and continuous phase. This term is directly related to the phase-averaged kinetic energy transfer and dissipation discussed in §6.1:

$$
\begin{aligned}
\langle N \rangle \langle u \rangle \cdot \langle f_\varepsilon \rangle &= \langle N \rangle \langle f_\varepsilon \rangle \cdot \langle v \rangle + \langle N \rangle \langle f_\varepsilon \rangle \cdot \langle u - v \rangle \\
&= 3\pi\mu D \langle N \rangle \left(\langle u \rangle - \langle v \rangle \right) \cdot \langle v \rangle + 3\pi\mu D \langle N \rangle \left(\langle u \rangle - \langle v \rangle \right)^2 .
\end{aligned}
\tag{6.26}
$$

Thus equations (6.23), (6.25), and (6.26) make clear the fact that the phase-averaged kinetic energy transfer and the phase-averaged particle dissipation are kinetic energy coupling terms related to the mean motion of the large, coherent eddies and are responsible for the production and destruction of turbulent kinetic energy within the carrier gas phase.

To calculate the above terms from the experimental measurements, the data was first divided according to the size groups of table 5.1, and then the velocity was phase-averaged by size to obtain $\langle v(D_i, \mathbf{x}, \phi) \rangle$, $i = 0, 1, 2, 3$. Since the current calculations are only concerned with resolving the mean phase-averaged fluctuations, the velocity of the scalar sized droplets can be used to faithfully represent the velocity of the carrier gas as was shown in §3.3.2. It then remains to calculate $\langle N(D_i, \mathbf{x}, \phi) \rangle dD$, the conditionally-averaged concentrations of the different size classes. This can be done using laser attenuation data in conjunction with the coarse number distributions obtained from the PDPA. Converting the PDPA number pdf's to volume pdf's and using (3.12) and (3.14), the volume concentration of droplets can be written as:

$$
\alpha = \frac{\xi D_{32}}{3L} = \frac{\xi}{3L \int_0^\infty \frac{pdf(D)}{D} dD}.
\tag{6.27}
$$

The volume fraction of particles within the size range of $D \pm dD/2$ is given by:

$$
\alpha(D) = \alpha \, pdf(D) dD.
\tag{6.28}
$$

Similarly, the number concentration of this size class is the volume fraction divided by the average volume of a single particle within that size class:

$$
N(D)dD = \frac{\alpha_p(D)}{\frac{\pi}{6}D^3} = \frac{2\xi D_{32} \, pdf(D) \, dD}{\pi L D^3} = \frac{2\xi \, pdf(D) \, dD}{\pi L D^3 \int_0^\infty \frac{pdf(D)}{D} dD}.
\tag{6.29}
$$

The right hand side of (6.29) needs to be conditionally-averaged to get $\langle N(D, \mathbf{x}, \phi)\rangle \, dD$. One way to estimate this quantity is to substitute the individually averaged quantities into the expression:

$$\langle N(D_i)\Delta D_i\rangle \;=\; \frac{2\,\langle \xi\rangle\,\langle pdf(D_i)\Delta D_i\rangle}{\pi L\langle D_{30_i}^3\rangle \displaystyle\sum_{j=0}^{3} \frac{\langle pdf(D_j)\Delta D_j\rangle}{\langle D_{30_i}^3\rangle^{1/3}}}. \tag{6.30}$$

Here the volume mean diameter (D_{30_i}) of the size bin has been used to represent the average diameter of bin i. Thus, the experimental realization of the kinetic energy transferred to size D_i per unit volume per unit time is given by:

$$\langle P(D_i, \phi)\rangle \;=\; \frac{6\mu\,\langle \xi\rangle\,\langle pdf(D_i)\Delta D_i\rangle}{\pi L\langle D_{30_i}^3\rangle^{\frac{2}{3}} \displaystyle\sum_{j=0}^{3} \frac{\langle pdf(D_j)\Delta D_j\rangle}{\langle D_{30_i}^3\rangle^{1/3}}} \Big(\langle \boldsymbol{u}\rangle - \langle \boldsymbol{v}\rangle\Big)\cdot\langle \boldsymbol{v}\rangle, \tag{6.31}$$

and the total power transfer per unit volume can then be calculated

$$\langle P\left(\boldsymbol{x}, \phi\right)\rangle \;=\; \sum_{i=1}^{3} \langle P\left(D_i, \boldsymbol{x}, \phi\right)\rangle. \tag{6.32}$$

Using an expression analogous to (6.21) and (6.30) gives the large scale contribution to the dissipation of size class D_i to be

$$\langle \epsilon_p(D_i, \phi)\rangle \;=\; \frac{6\nu\,\langle \xi\rangle\,\langle pdf(D_i)\Delta D_i\rangle}{\pi L\langle D_{30_i}^3\rangle^{\frac{2}{3}} \displaystyle\sum_{j=0}^{3} \frac{\langle pdf(D_j)\Delta D_j\rangle}{\langle D_{30_i}^3\rangle^{1/3}}} \Big(\langle \boldsymbol{u}\rangle - \langle \boldsymbol{v}\rangle\Big)^2, \tag{6.33}$$

and the total dissipation to be

$$\langle \epsilon_p\left(\boldsymbol{x}, \phi\right)\rangle \;=\; \sum_{i=1}^{3} \langle \epsilon_p\left(D_i, \boldsymbol{x}, \phi\right)\rangle. \tag{6.34}$$

Before proceeding to discuss the measurements, it should first be pointed out that there are several sources of error associated with using (6.31) and (6.32) to measure the conditionally-averaged kinetic energy transfer given by (6.20). The first source of error is the statistical uncertainty of the data. The largest size had the fewest samples, ranging from 45 to 5 samples per phase bin. As a worst case example, the uncertainty in the velocity of the largest size was then estimated at 4% in the regions where the energy transfer was

114

sizable[a]. For the small droplets, this uncertainty was much smaller, having an average value of 1%. The statistical uncertainty will also contribute to the uncertainty in the estimation of N. Again, to reduce the high-frequency random noise associated with this statistical uncertainty, the low-pass spatial kernel used for the normalized number frequency measurements of §5.3 was convolved with the data. The upperbound on the average smoothing correction introduced by this procedure was about 0.8 W m^{-3} with a standard deviation of 1.4 W m^{-3} for the individual size classes and $1.4 \pm 2.4 \text{ W m}^{-3}$ for the total energy.

The last two deviations have to do with how the PDPA measures the pdf distributions. The first of these errors is due to the fact that the effective probe detection volume increases with the size of the droplet due to its increased scattering cross-section. As mentioned in §3.3.5, the Aerometrics PDPA uses an empirical algorithm to correct for this error during post-processing. We did not perform similar corrections as the small benefits gained would be outweighed by the increase in error caused by the added manipulations. The second discrepancy results from the fact that the PDPA measures the size distribution in a swept volume, whereas the attenuation uses the instantaneous volume occupied by the entire beam. If there is a large mean velocity bias between the various sizes, then the pdf will be skewed toward the higher-speed particles in proportion to the velocity differences between the sizes. In this experiment, the effect will only be sizable when the mean velocity becomes close to the same order of magnitude as the slip velocity between different sizes, say $|(\boldsymbol{v}(D_i) - \boldsymbol{v}(D_j))| / |\boldsymbol{v}(D_j)| < 0.2$, which will not occur until one reaches the low-speed portion of the mixing layer where the concentration of droplets, and hence the energy transfer, approaches zero.

Even taking into account the above shortcomings, it is clear that the conditional-averaged data measured in this way shows distinctive trends which reveal the underlying physics of the particle dynamics, and which also represent the best currently available data for modeling purposes. In the remaining sections the conditional-averaged kinetic energy transfer between the liquid and gas phases will be discussed as a function of particle size, beginning with the evolution of the dominant fundamental disturbance, leading through the

---

[a]The uncertainty peaked around 20% in the external region of the shear layer, but here the concentration of droplets was extremely small, and hence the energy transfer went to zero.

pairing event, and finishing with the later developing stages of the resulting subharmonic structure. This will be followed by a similar discussion of the particle dissipation.

6.3 Mean Phase-Averaged Kinetic Energy Transfer

6.3.1 Fundamental dominated flow: role of a single vortex

The total kinetic energy transfer between the phases (equation 6.32) in the initial flow region exhibits the relevant features of the transfer processes that are basic characteristics of the large-scale structures present in the shear layer (figure 6.2). Perhaps the most surprising fact is that the preponderance of the energy exchange does not take place in the central region of the mixing layer as might be expected, but instead occurs in a sublayer just outside the mixing region and extends deep into the freestream of the spray. It is readily apparent that the transfer in this region is characterized by large, structured inhomogeneities with both positive and negative transfer regions which form as the dispersed phase locally absorbs and restores energy to the carrier fluid. Comparing the energy transfer plot with those of the attenuation (figure 5.4) and the velocity field (figure 4.13) indicates that the positive peak is located under the core of the vortex structure, while the negative peak occurs beneath the free stagnation point located in the braid region between successive vortices. Upon further comparison with the r.m.s. velocity field in figure 4.14, it is found that the kinetic energy transfer maxima are also outside the region of the peak velocity fluctuations, which is in contrast to what might be assumed in more traditional turbulence modeling. This then poses an interesting question: if the turbulent Reynolds stresses are not the primary contributors to this energy exchange, then what is the source of the maxima? All of the above experimental evidence indicates that the kinetic energy transfer peaks are the result of two effects:

(i). The droplet concentration field is inhomogeneous across the mixing layer and quite dilute in the external region of the flow.

(ii). There are peaks in the slip velocity field due to the droplets' response to a periodic forcing by distributions of lumped vorticity in the mixing layer.
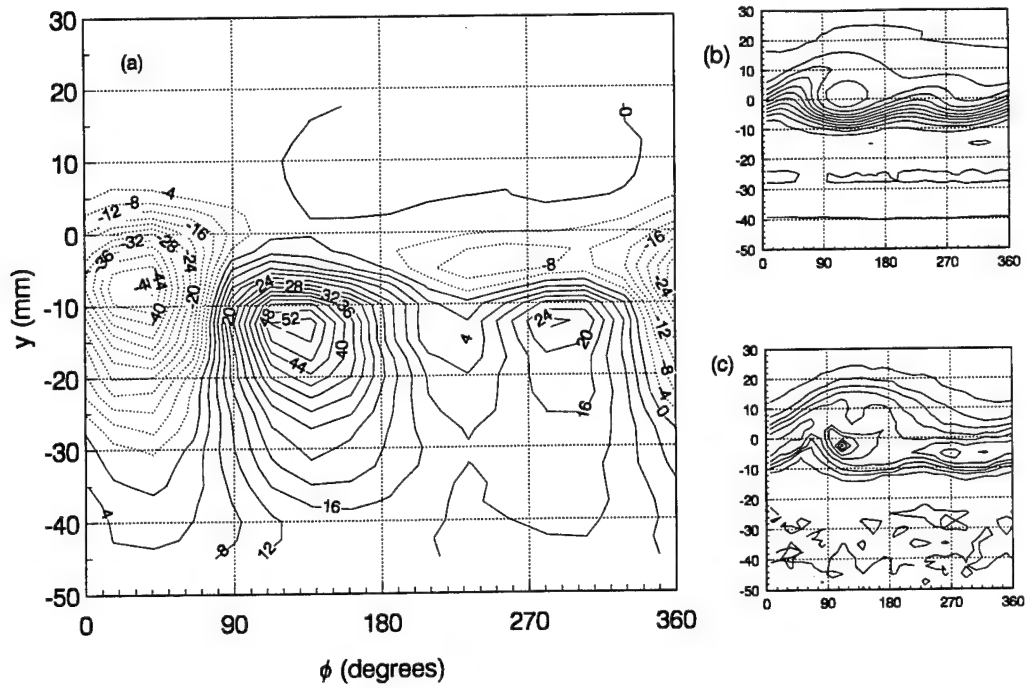
116

Figure 6.2: Phase averaged total kinetic energy transfer at $x = 6$ cm. —— positive, energy transfer to the droplets; ⋯⋯ negative, energy transfer from the droplets. Contour values are in $\mathrm{W\,m^{-3}}$.

The presence of the vortices create an irrotational perturbation velocity in the freestream that decays inversely with distance from the mixing region (figure 6.3). For the streamwise velocity component, this perturbation will be a maximum beneath the vortex core, with a corresponding minimum beneath the stagnation region between the two vortices. If it is assumed that the coherent structures are moving at approximately the mean speed of the two layers, then the particles outside the shear layer in the uniform stream will be convected past them at a relative frequency of $f_{rel} = f\frac{(U_2-U_1)}{(U_2+U_1)}$. When a droplet initially moving at a steady velocity is exposed to this alternating velocity field, it will try to follow the disturbance with varying amounts of success depending on its relative Stokes number, $St_{rel} = \frac{\rho_l D^2 f_{rel}}{18\rho_g \nu}$. This sets up slip velocities in the direction of the particle's motion and creates the observed pattern of the kinetic energy transfer. Additional evidence of this will be presented when we consider the effects of the droplet size on the kinetic energy transfer.
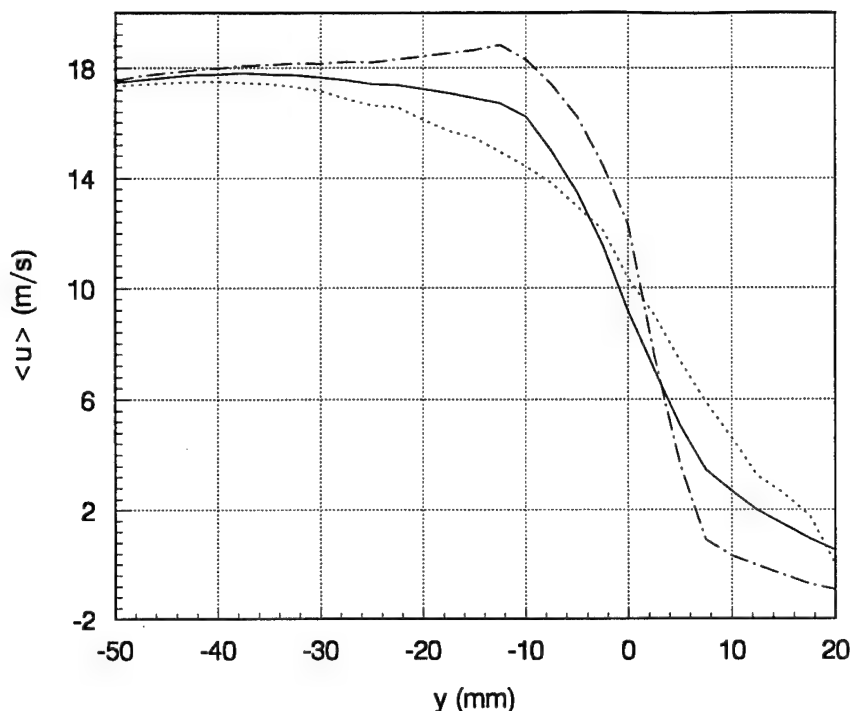
Figure 6.3: Phase averaged streamwise velocity profiles at $x = 6$ cm, showing the average velocity increase at the core, $-\cdot-\ \phi = 121°$, and the deficit at the braids, $\cdots\cdots\ \phi = 25°$ in comparison to the mean velocity ——— .

The fact that this mechanism of kinetic energy transfer exists should come as no surprise; rather, the interesting point is what *prevents* the central mixing region (with the maximum fluctuation levels) from making a sizable contribution? The answer to this lies in the details of the concentration field (approximately given by the attenuation, figure 5.4) and the dot product of the droplet velocity with the slip velocity (figure 6.4). There it can be seen that even though the slip velocity is at a maximum in the external mixing region (approximately twice the corresponding value at the observed energy transfer peaks), the absolute value of the droplet velocity and the droplet concentration is so low that it does not produce any significant energy transfer. Additionally, in between the two peaks there is a region where the concentration and slip velocity is large, but the vector product $(\boldsymbol{u} - \boldsymbol{v}) \cdot \boldsymbol{v}$ is small due to the strong lateral velocity fluctuations of the vortex. Finally, there is a region in the central mixing layer on the lower edge of the vortex core where the velocity vector

118

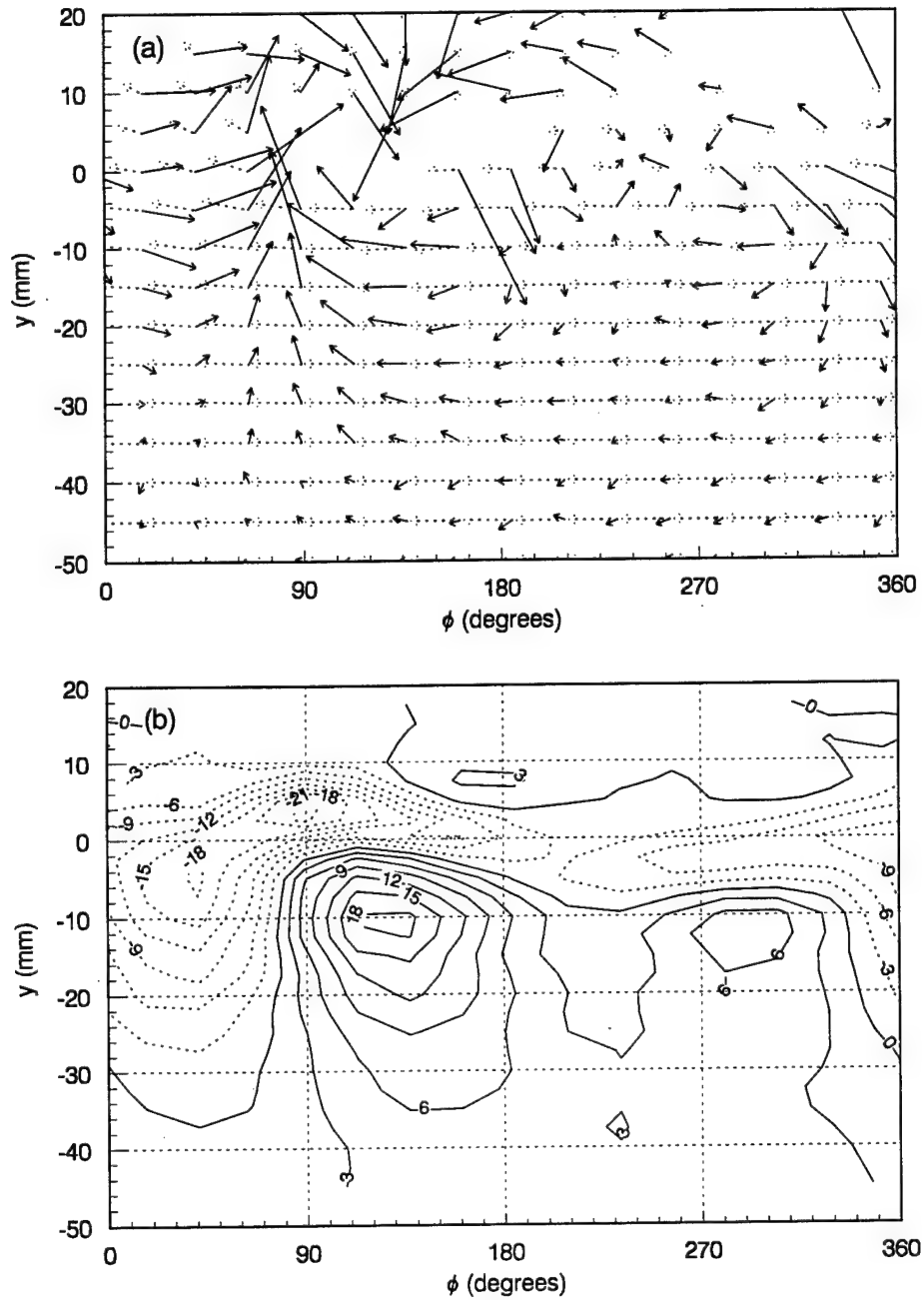Figure 6.4: Phase averaged velocity vectors of the relative slip velocity and absolute velocity of the intermediate size class at $x = 6$ cm. (a) Solid vector: slip velocity, horizontal vector of length $24° = 1$ m s^{-1}; Dotted vector: absolute velocity, horizontal vector of length $24° = 18$ m/s. (b) Contours of the velocity dot product $(\boldsymbol{u} - \boldsymbol{v}) \cdot \boldsymbol{v}$. Units are in $m^2 s^{-2}$.

product does exhibit a peaked minimum ($y = 4\,\text{mm}$, $\phi = 90°$), but again the concentration is too small to produce a sizable kinetic energy transfer. This negative vector product peak results from the steep velocity gradients around the core as well as the particle's inertial 'memory' of the high-speed freestream. In the initial developing region, the concentration of particles in the streak near the core is too low for this mechanism to have any impact, but as will be seen, this region makes a contribution in the later development and alters the characteristic transfer process.

Since it has been shown in the previous sections that the particle size plays a dominant role in the dispersion process, it is of paramount interest to also determine how the different size classes contribute to the total kinetic energy transfer. Upon examination of the energy transfer for each of the sizes (figure 6.5), it is seen that the overall pattern of the peaks and valleys is preserved for each size, with slight differences in the location and relative proportion of each size's contribution. When comparing the magnitudes of the these peaks, it is evident that there is a distinct ordering of the magnitude based on size, with the greatest contribution coming from the intermediate size, followed by the largest size, and then finally the smallest. The ordering of the peak magnitude is influenced by the Stokes number through its connection to the slip velocity. The larger the Stokes number, the greater the slip velocity and hence greater energy transfer. The drop-off in concentration of the largest Stokes number droplets then eventually balances the increased slip velocities and results in a specific ordering of the peaks as noted above. In addition to the differences in magnitude, the locations of the peaks all shift downstream (lower phase angles) as the size is increased. This temporal shift of the peak's location can also be consistently explained by Stokes number arguments. For the three size classes considered, the average relative Stokes number based on $f_{rel_1} = 140$ Hz are approximately 0.1, 0.4, and 1.6 for the small, intermediate, and large classes respectively. Using the equation of motion for an isolated particle, it is possible to obtain analytical expressions that describe the steady state response of the particle to a periodic disturbance (Hjelmfelt and Mockros, 1966). The results of such an analysis for the given particles result in phase differences of 28°, 60°, and 70° (14°, 30°, and 35° on the subharmonic scale shown in the figure) between the scalar sized droplets and the larger size classes. Examining the particle response velocity measured in the flow
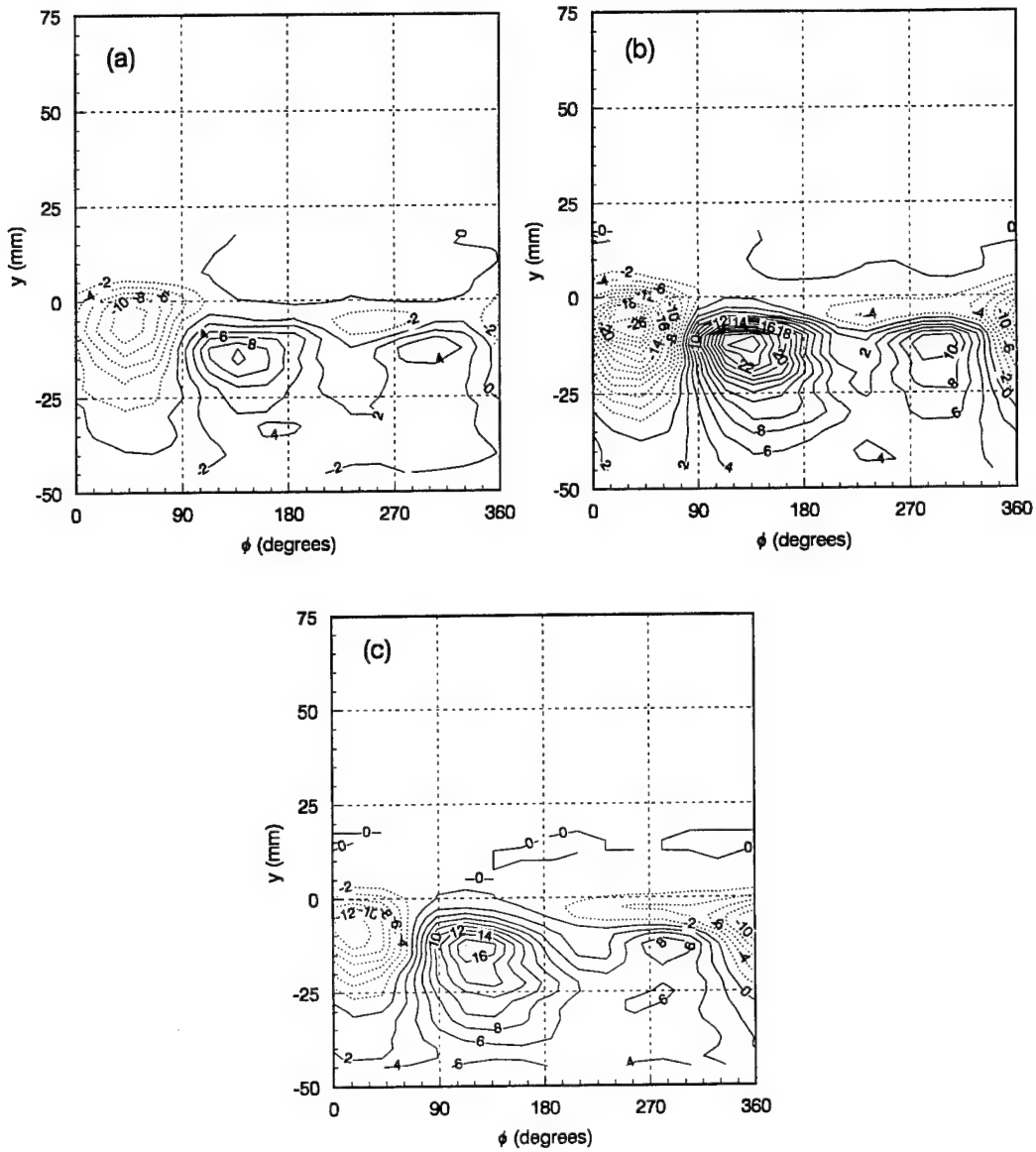
Figure 6.5: Phase averaged kinetic energy transfer at $x = 6$ cm. (a) small size class, D_1; (b) intermediate size class, D_2; (c) large size class D_3. —— (positive), energy transfer to the droplets; ⋯⋯ (negative), energy transfer from the droplets.
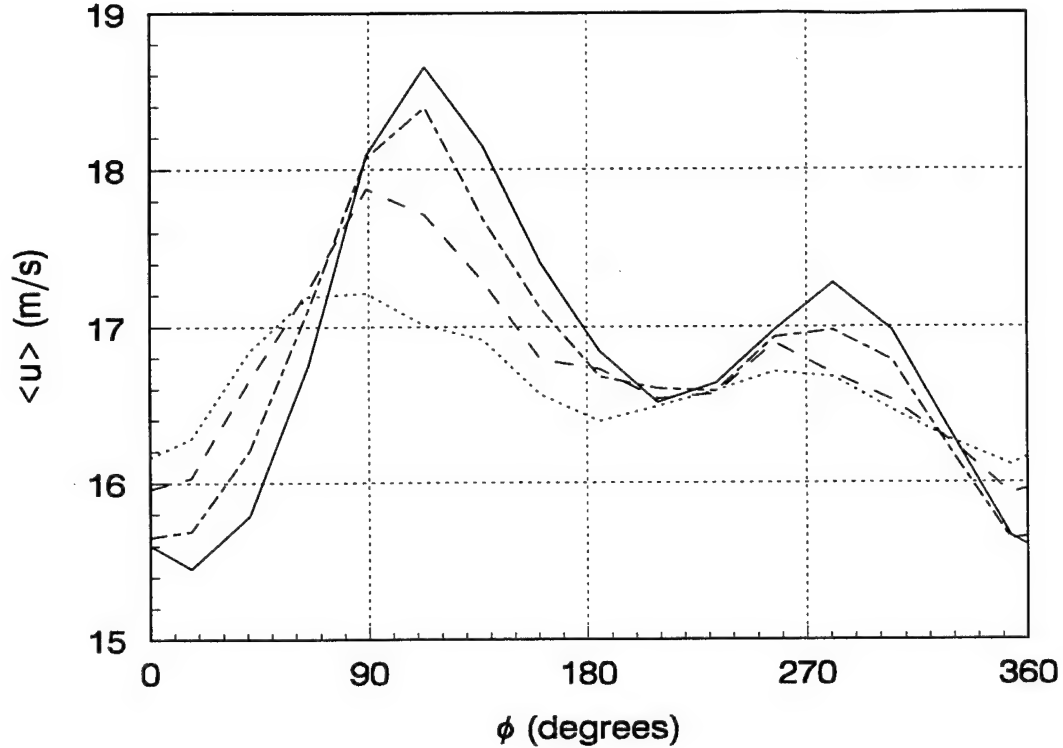
Figure 6.6: Phase averaged streamwise velocity component for each size class at $x = 10$ cm, $y = $ -15 mm, showing the amplitude decrease and phase lag between the sizes.

(figure 6.6) shows that the measured phase lags are approximately 15°, 25°, and 45° ($\pm 7°$ based on bin width) which agrees quite closely with the predictions. Discrepancies between the results can be explained by the uncertainty in the waveform shape and the fact that the larger particles do not have a sufficient response time to achieve a steady state before the structures change significantly.

6.3.2 Vortex pairing event and resulting subharmonic structure

Knowing that the vortex pairing plays a dominant role in the dispersion properties of the droplets depending on their size, it is also of interest to quantify how the energy transfer occurs during this transition. Questions that are raised by knowledge gained in the previous chapter include: how does the competition of a second flow scale affect the kinetic energy transfer process? Once the flow is back to a single dominant scale (this time
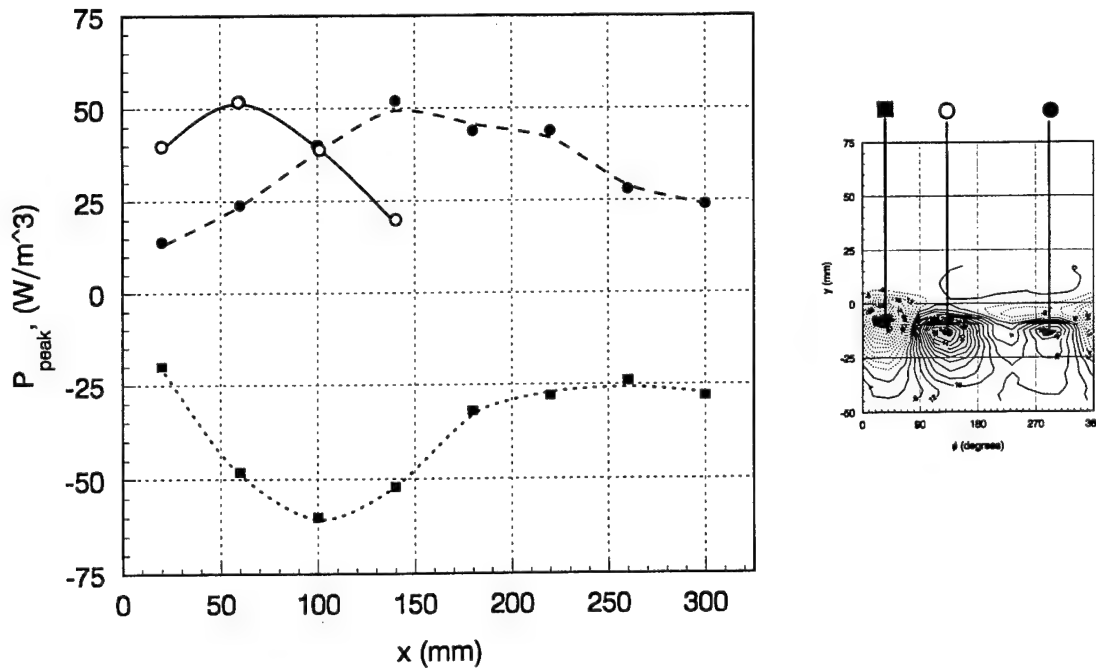
Figure 6.7: Amplitude evolution of the dominant kinetic energy transfer peaks identified over one subharmonic wavelength.

twice as large), will the mechanism still be the same? Finally, can we use this information to infer what might take place further downstream in the mixing layer, after several pairings have occurred?

During the initial stages of the shear layer development, the peaks of the energy transfer identified in the previous section displayed a continual increase in magnitude (figure 6.7). From the mechanism described previously this can be ascribed to an increase in the circulation within the core of the spanwise rollers as they continually remove vorticity from the braid region (Corcos and Sherman, 1984). This vorticity intensification increases the strength of the vortex and hence heightens the fluctuating velocities perceived by the droplets in the freestream. When the pairing initiates, the peak levels are observed to decrease and maintain a reduced amplitude throughout the rest of the test section. The reason for this decrease can be explained primarily by the growth of the subharmonic length scale and the resulting decrease in the relative Stokes number, increasing the particles' ability to

Figure 6.8: Phase/location evolution of the dominant kinetic energy transfer peaks identified over one subharmonic wavelength.

respond to the fluctuations. In addition to this, the vorticity in the core after the pairing does not immediately attain the same concentrated distribution that it had after the initial roll-up, and hence could also contribute to a loss of velocity fluctuation in the freestream.

If one follows the location of the peaks throughout the pairing (figure 6.8) it can be seen that the peaks track with the location of the dominant vortex core and stagnation points of the flow, all the while remaining close to the edge of the sublayer. The positive peak initially formed by the larger fundamental vortex is seen to be obliterated in the early stages of the pairing event, and instead favors the growth of the positive peak located under the smaller vortex. By the end of the pairing, we are left with a positive peak located well into the freestream, and a negative peak that appears to have encroached somewhat deeper into the large-scale streak structure shown earlier.

The pairing event also has an effect on the magnitude of the peaks for each size class and produces a reshuffling of the size responsible for the dominant energy transfer. In

our case the flow conditions were such that the large size became the dominant transfer group for the positive peak (figure 6.9a). This is again consistent with a reduction of the relative Stokes number, and the low-pass filtering characteristics of the droplet's amplitude response (see Lázaro and Lasheras, 1989). This reshuffling, however, did not appear to occur in the negative peak (figure 6.9b). Instead, all three peak levels seemed to reach somewhat similar values. The equalization of the negative peaks can be consistently explained by the increased concentration of smaller sizes in the core due to the pairing event. As was noted earlier, the velocity vector product exhibited a strong minimum in this region, and hence, the increased concentration of the small droplets shifts the peak kinetic energy transfer towards the vortex core. The large sizes, however, accumulate near the stagnation point and thus reduce the peak energy transfer near the core (figure 6.10), resulting in similar amplitude contributions for each size class.

In many situations, it is useful to quantify the time-averaged or mean flow quantities to try and answer questions about the bulk characteristics of the flow. Very little additional information, however, was gained from this procedure for the kinetic energy transfer (figure 6.11). These profiles do reflect the influence of the two-peaked sublayer transfer pattern, as can be seen by the net positive and negative energy transfers centered about the sublayer; however, the averaging procedure also obscures the actual degree of coherent inhomogeneity present in the temporal flow by attenuating the peak transfer levels. One interesting observation to note is that the net negative transfer region grows with an increasing rate once the pairing is initiated (compare the first two profiles with the last two).

What then, does this imply for the continued evolution of energy transfer in the mixing layer? The results of the above section indicate that the peaked sublayer pattern is a dominant transfer mechanism as long as the vortices maintain a minimum intensity and the relative Stokes numbers of the particles in the spray are at least $O[1]$. Successive pairings increase the structure size and continually decrease the relative Stokes number. As this occurs, the sublayer transfer by the smaller particles decreases to negligible values, leaving contributions mainly due to the larger droplets. Eventually, the large-scales grow to a point where all droplet sizes of the spray are affected. When this occurs, a secondary
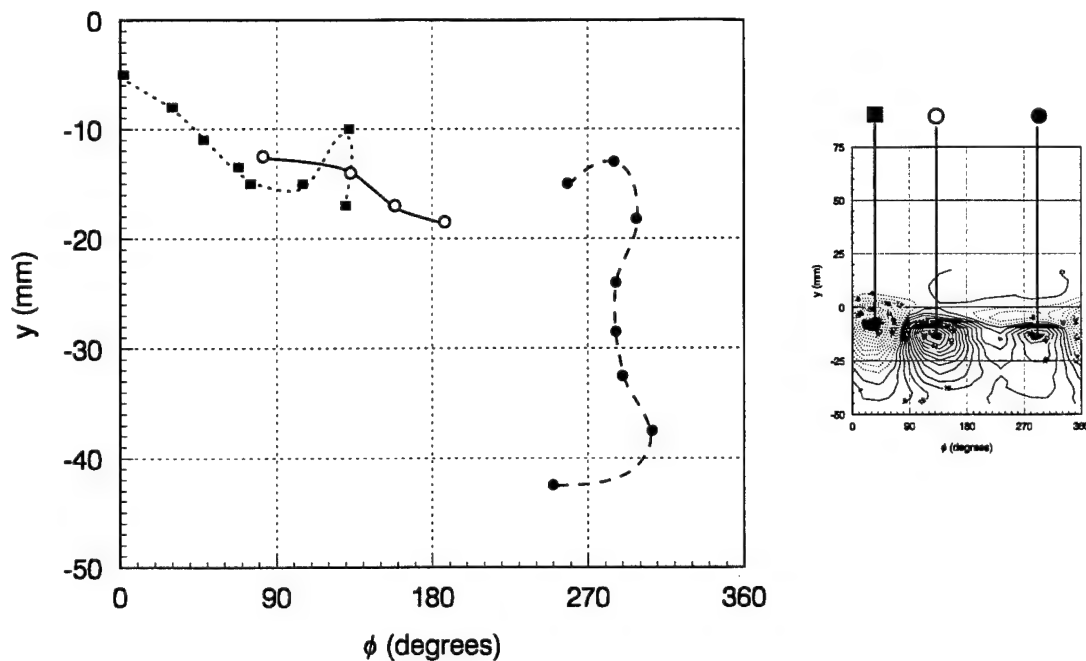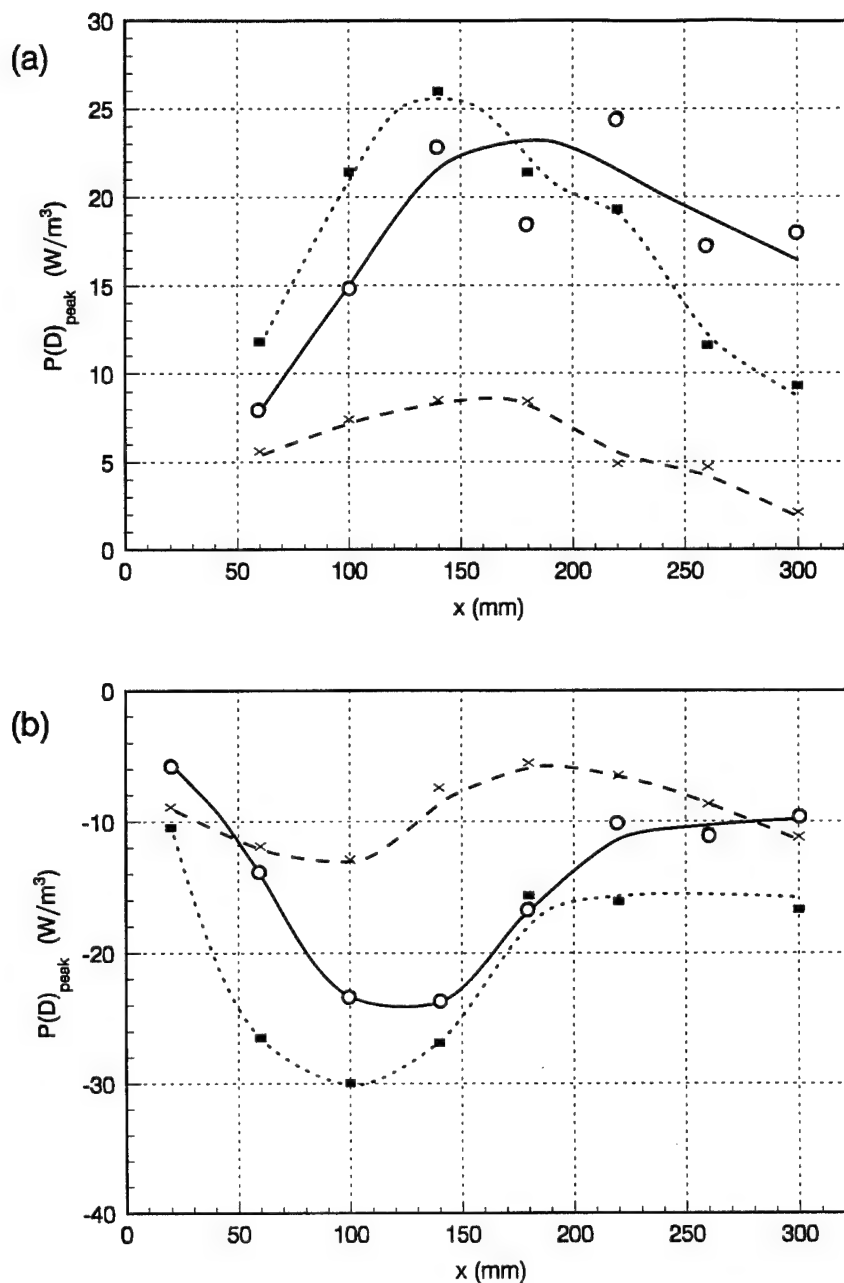
Figure 6.9: Phase/location evolution of the dominant kinetic energy transfer peaks of each size class identified over one subharmonic wavelength. (a) positive peak originating at $x = 6$ cm, $(y, \phi) = (-15\,\text{mm}, 285°)$, (b) negative peak originating at $x = 2$ cm, $(y, \phi) = (-5\,\text{mm}, 0°)$. x, D_1; ■, D_2; ○, D_3.
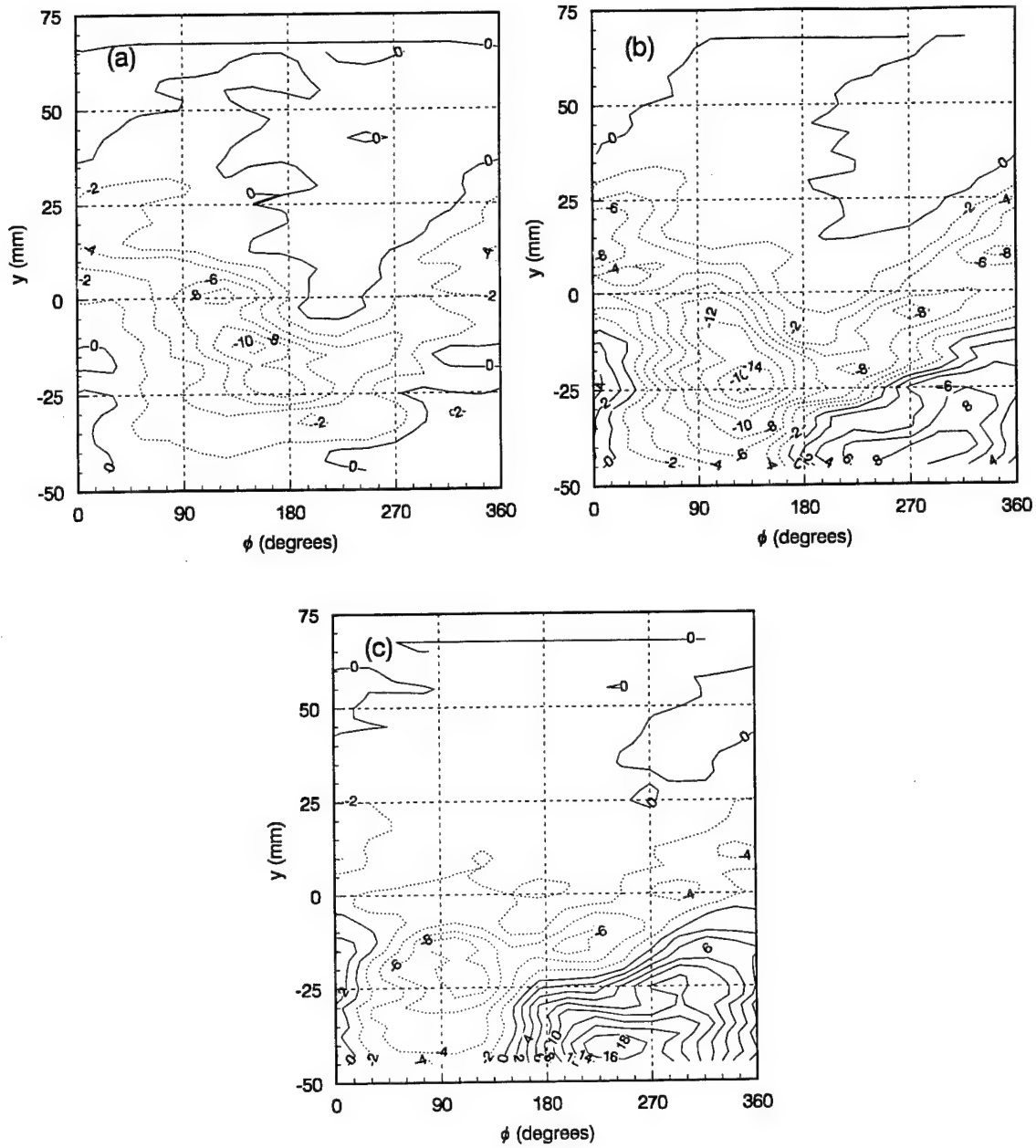
Figure 6.10: Phase averaged kinetic energy transfer at $x = 30$ cm. (a) small size class, D_1; (b) intermediate size class, D_2; (c) large size class D_3. —— (positive), energy transfer to the droplets; ········ (negative), energy transfer from the droplets.

mechanism may be responsible for the kinetic energy transfer between the phases as the Stokes number will most likely be $O[1]$ for some scales present in a turbulent mixing layer. This is further aided by the fact that the homogenization of particles throughout the large-scale structure is greatly enhanced by the decrease in the relative Stokes number, creating increasing concentrations in regions where the particulate interact with the smaller scales. In the case of high void fractions, this may result in a transfer process which could affect the development of the flow as kinetic energy is redistributed into a region near the braids from beneath the core of the vortex.

6.4   Evolution of the Phase-Averaged Droplet Dissipation

The evolution of the total phase-average dissipation due to particle motion as calculated from (6.34) is shown in figure 6.12. During the initial stages of the fundamental

Figure 6.11:   Time average of the phase-averaged kinetic energy transfer, $\frac{1}{2\pi} \int_0^{2\pi} \int_0^\infty 3\pi\mu D(\langle u \rangle - \langle v \rangle) \cdot \langle v \rangle \, dD \, d\phi$.

development (figure 6.12a and b), the dissipation is concentrated into the high shear region separating the two flows and beneath the core and streak of the larger vortex. The broader peak on the left hand side is in the same region as the kinetic energy transfer peaks observed in the previous section, only now the two distinct peaks are joined as a broad ridge. This is bec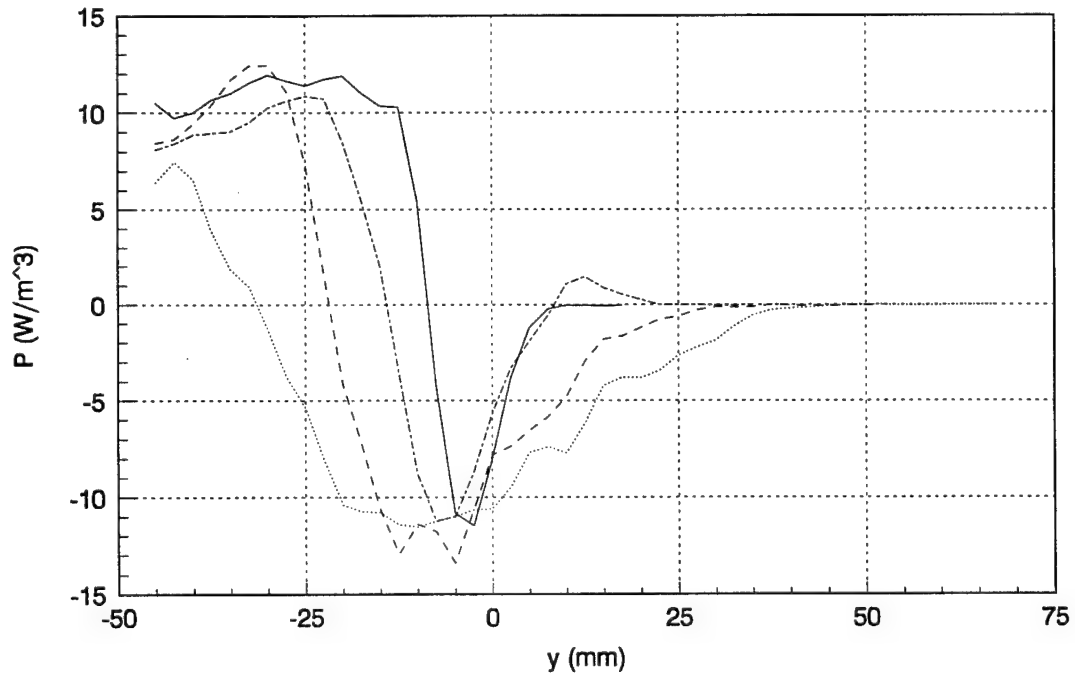ause the phase-averaged dissipation measurements depend on $(\langle v \rangle - \langle u \rangle)^2$ and not on the dot product $(\langle v \rangle - \langle u \rangle) \cdot \langle v \rangle$, which goes to zero as the direction of the particle motion and the drag force become perpendicular. The major contribution of the smaller vortex at this point of development is limited to a narrow band in the center of the mixing region where larger, fast-moving particles encounter the slower gas velocity. The peaks visible beneath the core of the smaller vortex in the kinetic energy transfer case (figure 6.32) are not as readily appearent as in the dissipation due to the scaling selected for the contours – the discrepancy in slip velocities beneath either core of the vortices is amplified by taking the square of its magnitude.

A more detailed comparison of the total mean kinetic energy transfer rate and mean particle dissipation is shown in figure 6.13, which presents several phase averaged profiles of both quantities. In general, the peaks occur at similar cross-stream (y) locations, but the high dissipation region does not extend as deep into the freestream as that of the mean phase-averaged kinetic energy transfer. The dissipation peaks tend to be narrower and centered more towards the middle of the mixing layer. Quantitatively, the width of the peaks at 20% of their peak amplitude measure 35% greater for the kinetic energy transfer than for the dissipation. Also note that there is a small but noticable dissipation peak in the external region of the mixing layer for $\phi = 137°$, which is not present in the energy transfer, and that the second dissipation peak for $\phi = 281°$ ($y = -2.5$ mm) is twice the magnitude of the first one ($y = -12.5$ mm), which is the exact opposite trend found for the mean phase-averaged kinetic energy transfer. The cause of these changes will be investigated further when the dissipation of the individual size classes is calculated.

The magnitude of the profiles show that the phase-averaged dissipation rate due to the particles is typically about 10% or more of the local phase-averaged kinetic energy transfer rate. This implies that whenever phase-averaged kinetic energy is added to or removed from the dispersed phase, there will be an additional loss of phase-averaged kinetic
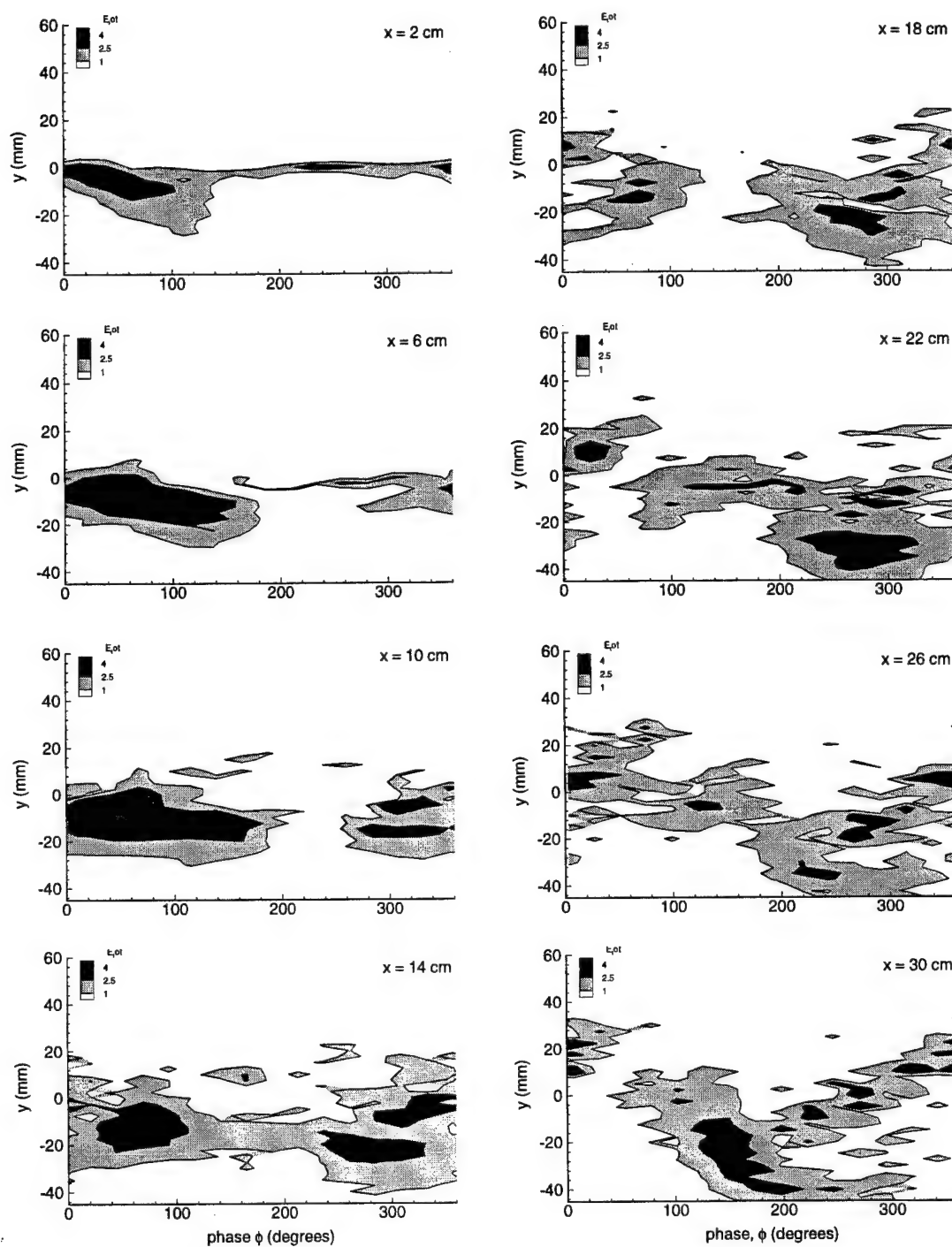
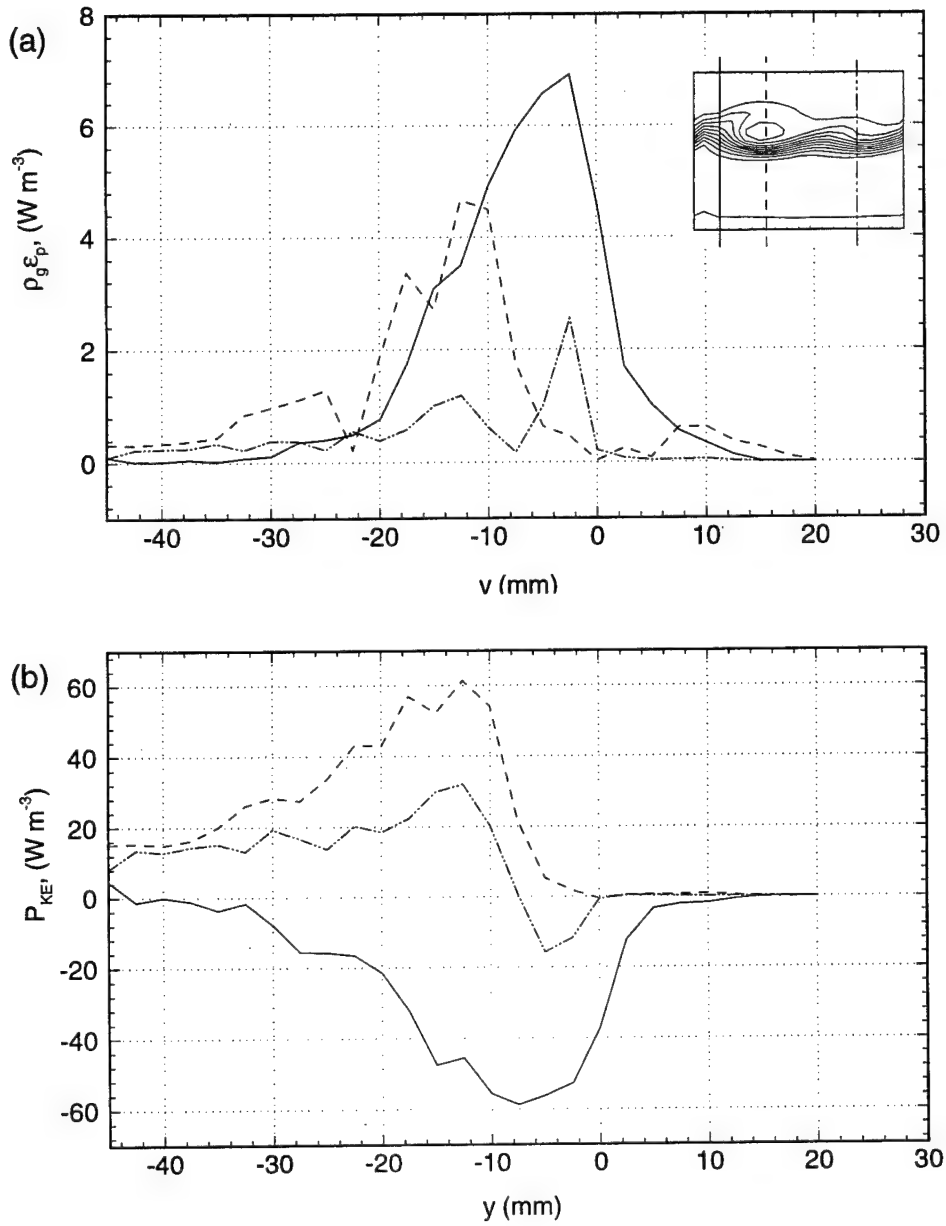Figure 6.12: Total kinetic energy dissipation due to droplet motion.

Figure 6.13: Phase averaged profiles of (a) dissipation per unit volume, $\rho_g \epsilon_p$ and (b) kinetic energy transfer at $x = 6$ cm. (——— , $\phi = 41°$; – – – , $\phi = 137°$; –··– , $\phi = 281°$).

energy in the gas due to the particle dissipation. The ratio of phase-averaged dissipation to kinetic energy transfer is observed to increase in the external region of the mixing layer where the kinetic energy transfer rapidly goes to zero. There are also regions where the particle dissipation becomes comparable to the kinetic energy transfer as the slip velocity is large but perpendicular to the droplet's direction of motion.

It is also of interest to compare the calculated mean phase-averaged particulate dissipation with the magnitude of the dissipation that would occur in the shear layer without any particles present. Due to the turbulent nature of the shear layer, the dissipation will occur primarily in the fluctuations of the smallest scales (the mean dissipation is approximately $1/\text{Re}_\delta$ less than the turbulent dissipation), and is therefore a quantity that could not be measured. The magnitude of the turbulent dissipation rates were estimated in §4.3.1, however, giving values of $\epsilon|_{x=10} = 1340\, m^2 s^{-3}$ and $\epsilon|_{x=30} = 450\, m^2 s^{-3}$. This indicates that the additional dissipation due to the presence of the droplets as they interact with the large scales is roughly $O(10^{-2})$ of the average turbulent dissipation of the continuous phase, and is the same order of magnitude as the mass loading.

This is in contrast to one-way coupling numerical DNS results obtained by Wang and Maxey (Wang and Maxey, 1993b), who estimated that for similar size particles (40 μm), mass loadings (5%), and density ratio ($\rho_p/\rho_g = 900$) that the average dissipation due to the presence of the particles in a homogeneous turbulent flow could be as much 30% of the average turbulent gas phase dissipation. They noted that the particle dissipation was not homogeneously distributed throughout the flow, but was typically concentrated into isolated structures similar in size to the Kolmogorov scale, some of which attained dissipation levels 100 times greater than the local turbulent dissipation. However, their study differed from the current experiment not only in the type of underlying turbulent flow, but also in the fact that they focused on the effects of monodispersed droplets with a viscous relaxation time which was similar to the Kolmogorov time scale. Other results (Wang and Maxey, 1993a; Squires and Eaton, 1990) also indicate that particles which are 'tuned' to the Kolmogorov scale ($\tau_a/\tau_\kappa \sim 1$) show the strongest tendency to accumulate in regions of low vorticity (upwards 20 to 30 times the average concentration). This preferential concentration, coupled with regions of large slip in the low vorticity regions is what resulted in a enhanced particle

dissipation. In comparison to this mechanism, the current experimental evidence as well as numerical simulations (Martin and Meiburg, 1994) indicate that preferential concentration due to the large scales is not as intense, and never seems to exceed values more than twice the initial freestream concentration. Thus the regions of isolated particle dissipation in the current study are due to strong variations in the slip velocity across the large scales as opposed to regions of enhanced particle accumulation.

As mentioned in the introduction to this chapter, the evolution of the mean phase-averaged kinetic energy also depends on the small scale structures of the flow given by terms like $\left(\langle N^\star \boldsymbol{u}^\star \rangle - \langle N^\star \boldsymbol{v}^\star \rangle\right) \cdot \boldsymbol{U}$. Other moments of the r.m.s. phase-averaged variables will also contribute to the Reynolds averged turbulent dissipation, and thus it is of some importance to try and estimate the magnitude of their influence within context of the current flow. The study of Wang and Maxey (1993b) suggests that the contribution from particles which have a viscous relaxation time comparable to the Kolmogorov scale may have a disproportionate effect on the dissipation due to their tendency to accumulate in clusters of increased concentration. The only size class in which the response time is of the same order as the Kolmogorov scale is the "scalar" size class, $D_0 \sim 6~\mu$m, used to measure the gas velocity fluctuations of the large scales. This size class has a response time of $\tau_a \sim 83~\mu$s, comparable to $\tau_\kappa|_{x=10} \sim 100~\mu$s. Assuming the slip velocity for this size will be 1/2 the Kolmogorov velocity scale, $v_\kappa = (\epsilon\nu)^{1/4} \sim 0.4~\mathrm{m\,s^{-1}}$, requiring the small scale particle dissipation contribution to be at least 10% of the large scale peak value (7 W m^{-3}) determines the level of droplet concentration to be

$$
\begin{aligned}
N &= \frac{\epsilon_p}{3\pi\rho_g\nu D(u_p - u_g)^2} \\
&= \frac{0.7~\mathrm{W~m^{-3}}}{3\pi(1.2\,\mathrm{kg~m^{-3}})(1.5\,x\,10^{-5}\,\mathrm{m^2~s^{-1}})(6\,x\,10^{-6}\,\mathrm{m})(0.2\,\mathrm{m~s^{-1}})^2} \\
&= 2\,x\,10^{10}\,\mathrm{droplets/m^3}.
\end{aligned}
$$

The measured freestream concentration of droplets is around $2\,x\,10^9$ for the "scalar" size class, which is within a factor of 10 of the required concentration. Thus it seems plausible that the interaction with the small scales may contribute to a small fraction of the measured large-scale dissipation, but it seems unlikely that the small scale particle dissipation

From Table I, II, and figure 2, Elghobashi & Truesdell, 1993		
Mass fraction, ϕ_m	τ_p/τ_κ	$(\epsilon_p/\epsilon_{\phi_m=0})_{max}$
0.23	$1.3 \Rightarrow 0.4$	~ 0.10
0.45	$2.3 \Rightarrow 0.8$	~ 0.25
0.91	$5.1 \Rightarrow 1.5$	~ 0.50
From Table III, Squires & Eaton, 1990		
Mass fraction, ϕ_m	τ_p/τ_e	$\epsilon_p/\epsilon_{\phi_m=0}$
0.1	0.15/0.52	0.12/0.17
0.5	0.15/0.52	0.39/0.65
1.0	0.15/0.52	0.69/1.06

Table 6.1: Comparison of particle dissipation effects in homogeneous turbulence DNS simulations. For Elghobashi & Truesdell (1993), $(\epsilon_p/\epsilon_{\phi_m=0})_{max}$ was estimated from the maximum ratio observed in the dissipation evolution.

mechanism has attained a comparable level that was observed in the simulaitons of Wang and Maxey (1993a), as this would require a concentration increase of over 3000 times the freestream value. Thus even with the possibility of enhanced concentration, the mass fraction of this size class is too small (0.0002) to make a significant contribution. Other results (Elghobashi and Truesdell, 1993; Squires and Eaton, 1990) of particle/turbulence interaction which included two-way coupling effects, however, seem to indicate that the level of dissipation due to the random small scale structures is about an order of magnitude smaller than what is estimated by Wang and Maxey (1993b), and roughly the same order of magnitude as the mass loading (table 6.4). Elghobashi and Truesdell (1993) performed DNS simulations of decaying homogeneous turbulence and studied the effect of particle viscous response time, volume fraction and gravity, while Squires and Eaton (1990) studied forced homogeneous turbulence with no body forces and examined the effect of response time and mass loading with an emphasis on the structure of the turbulent flow. Squires and Eaton (1990) showed that the amount of preferential concentration exhibited by the particles which were in resonance with the small scale decreased with increasing mass loading, which most likely accounts for the order of magnitude difference in the particle dissipation estimated by Wang and Maxey (1993). The observation of dissipation scaling with the mass loading has an important implication for polydispersed sprays - namely, the turbulent scales which are

in resonance with the viscous relaxation time of the particles whose size are in the peak of the volume size p.d.f. will tend to dominate the particle dissipation. Thus, as the evolution of the shear layer continues and the large scales grow to the extent where the larger droplets follow their fluctuations, the importance of the small scale interactions will play a much more dominant role, particularly with the embedded streamwise features found in the braid region which can have a fairly organized and intense structure.

Returning to the evolution of the total dissipation (figure 6.12), the region near the end of the external streak begins to show a measurable contribution just at the end of the fundamental development ($x = 10$ cm, $y \sim +10$ mm, $100° < \phi < 300°$). As the pairing is initiated, the streak tip region (10 mm$< y < 20$ mm, $\phi > 100°$) increases somewhat and then begins to decay until it disappears by the end of the pairing. The peak beneath the core of the vortices is observed to follow a similar evolution as the kinetic energy transfer peak in that it shifts to the right hand vortex as the pairing is initiated ($x = 14$ cm, $y = -20$ mm, $\phi = 280°$), reaches a maximum around $x = 22$ cm, and begins to decay as the pairing completes. The last feature to note is that the dissipation near the larger streak on the left hand side undergoes an unusual transformation starting around $x = 14$ cm. As the pairing starts, the peak contribution splits into two distinct portions – one stays close to the core of the vortex, while the other remains on the outer edge, leaving the center of the streak (which is a local maximum in the concentration) as a relatively inactive zone.

A comparison between the kinetic energy transfer and the dissipation after the pairing now show slightly more of a separation of the peak locations through most of the vortex (figure 6.14). The only peak that remain colocated is the one beneath the core of the vortex ($y = -40$ mm, $\phi = 246°$). The other concentrated dissipation regions are shifted more into the shear layer by about 10 mm. The amplitude of both quantities has decreased by approximately a factor of two.

The formation of the distinct dissipation regions observed in figure 6.12 are clearly linked to the dynamics of the particles as they interact with the large scales. The cause of these different regions can be explained through the examination of the contribution made by the various size classes. The intermediate size class is ideal for this aspect of the discussion, as it makes a sizeable contribution to the dissipation and contains features observed in both
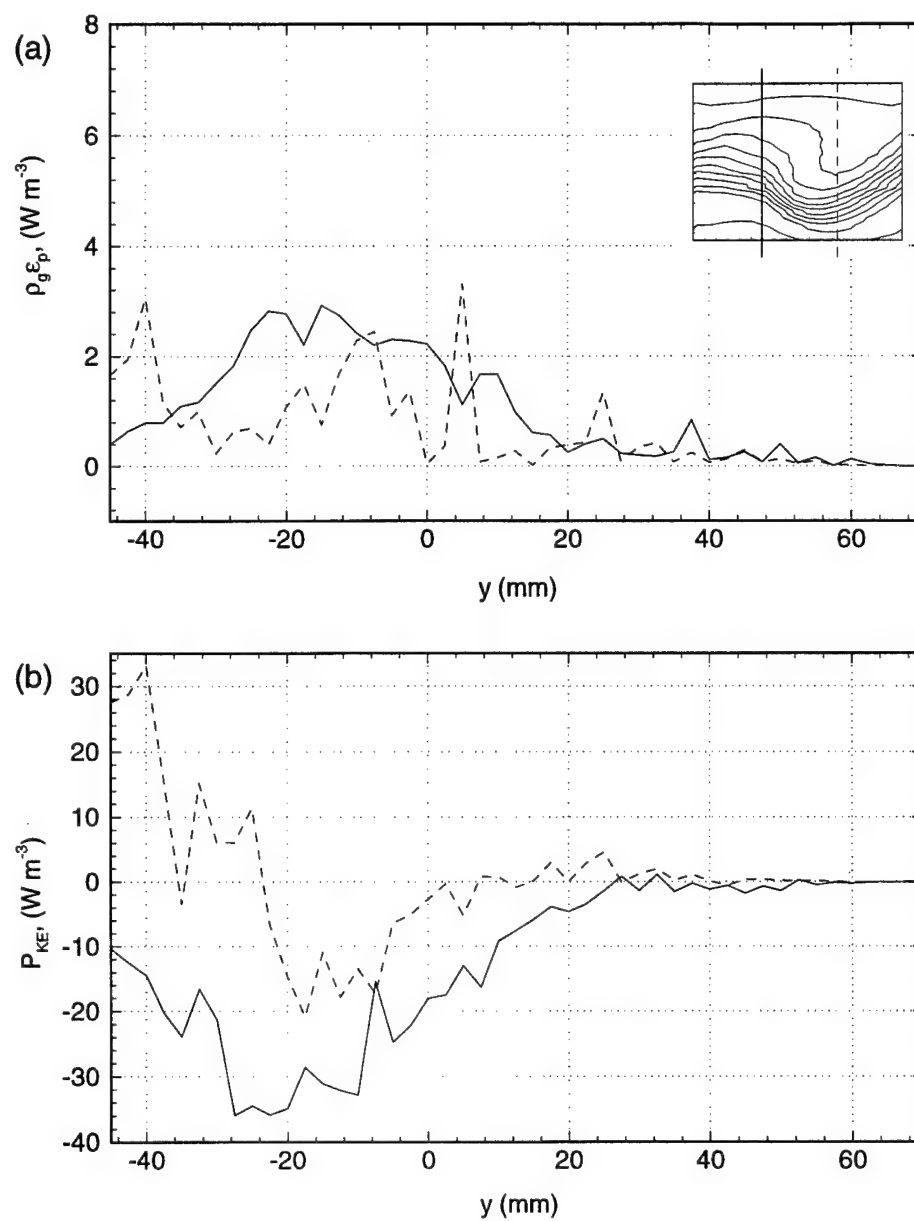
Figure 6.14: Phase averaged profiles of (a) dissipation per unit volume, $\rho_g \epsilon_p$ and (b) kinetic energy transfer at $x = 30$ (cm. ——— , $\phi = 126°$; – – – , $\phi = 246°$).
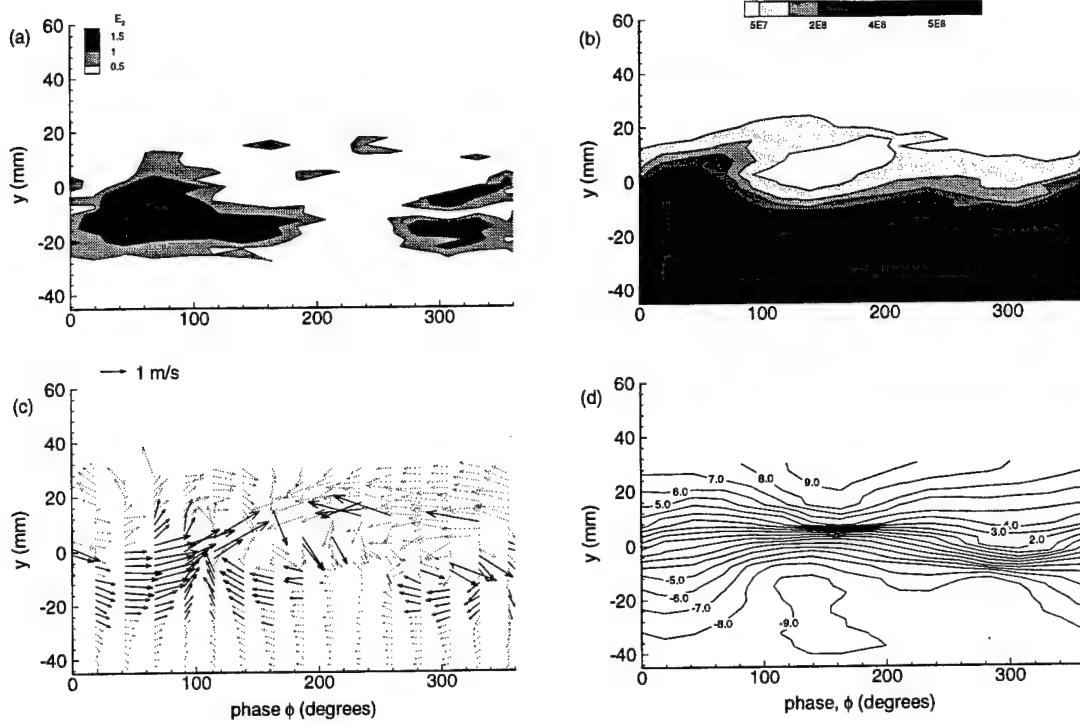
Figure 6.15: Phase averaged (a) dissipation, (b) concentration, (c) slip velocity, for the intermediate size class, D_2, and (d) streamwise gas velocity contours at $x = 10$ cm. Bold vectors correspond to the region where the dissipation is greater than 0.5 W m^{-3}.

the large and small size classes. Examining $\rho_g \epsilon_p(D_2)$ just prior to the pairing at $x = 10$ cm (figure 6.15) allows the identification of four distinct regions of localized dissipation:

(i). Freestream core acceleration region. $100° < \phi < 220°$, -25 mm $< y < 0$ mm and $260° < \phi < 350°$, -20 mm $< y < $ -10 mm

(ii). Inner streak edge deceleration region. $0° < \phi < 100°$, -25 mm$< y < 5$ mm

(iii). Outer streak edge deceleration region. $260° < \phi < 380°$, -10 mm$< y < 5$ mm

(iv). External streak tip acceleration region. $160° < \phi < 360°$, 7.5 mm$< y < 20$ mm

These regions are classified by the type of interaction which they exhibit with the vortical structure as they are entrained into the mixing layer, and are made evident by the slip velocity vector field (figure 6.15c). Since the slip velocity is predominantly aligned with the

streamwise axis, most of the dissipation is caused by particles crossing strong gradients of streamwise velocity – either through lateral transport in strong cross-stream gradients or downstream advection through streamwise gradients. This is verified by the streamwise gas velocity contours (figure 6.15d). The above naming conventions corresponds to the direction of the streamwise slip velocity component. As flow is from right to left for the high-speed stream, slip velocities pointing from right to left denote a force acting on the droplet which tries to increase its velocity, and is hence called an acceleration. Region (i) corresponds to an acceleration by the concentrated core vorticity trying to increase the streamwise velocity of the droplets, and corresponds to the same dynamical event identified in §6.3.1 which produces a positive kinetic energy transfer peak in the same location. The difference in the cross-stream shape observable in figure 6.13 is due to the dissipation's quadratic dependence on the slip velocity in comparison to the energy transfer's linear dependence (since the streamwise velocity is constant in this region). Region (ii) is caused by the lack of vorticity in the braid region, and a resulting deceleration of the gas flow as identified for the negative kinetic energy transfer peak discussed in §6.3.1. Region (iii) occurs along the dividing streamline of the free stagnation point, and is a region where particles with finite inertia can cross the boundary and move into a region of reversed flow, and hence feel a strong deceleration. Finally, region (iv) results from the droplets which have been decelerated as they were entrained along the streak. As they pass the core of the vortex, the streamwise gas velocity increases (again due to the reduced level of vorticity in the braid region between the vortices) and the particles are accelerated.

After the pairing event (figure 6.16), the core acceleration region for the intermediate size has been markedly reduced due to the decreased vorticity levels and the doubling in fluid timescale. There is also a corresponding decrease in the streak tip acceleration region, as the streamwise velocity gradients along the end of the streak have been reduced by the wider distribution of the vorticity (the weaker vorticity is evident by the uniformity of the $u_g = 6$ and 7 m s^{-1} contours). The primary contributors to the dissipation for this size class come from the inner and outer streak edge deceleration regions as the particles are brought into the streak and cross over the stagnation boundary. It is somewhat surprising that the peak dissipation does not occur in the center of the streak where the concentration
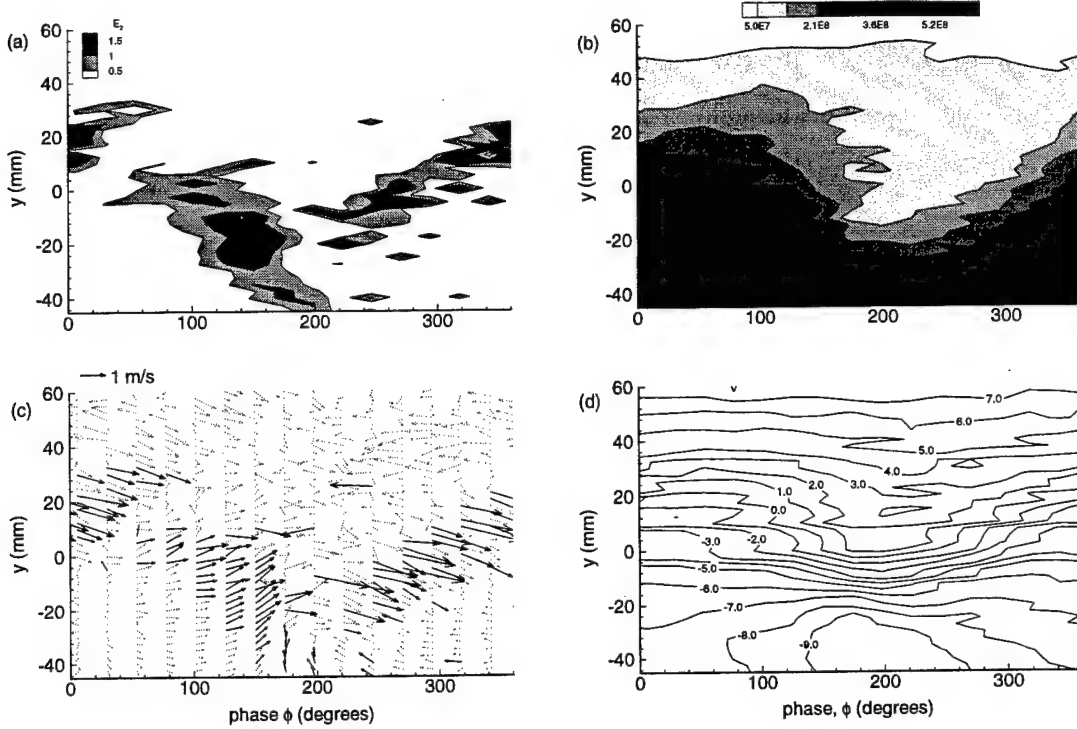
Figure 6.16: Phase averaged (a) dissipation per unit volume, $\rho_g \epsilon_p$, (b) number concentration, (c) slip velocity, for the intermediate size class, D_2, and (d) streamwise gas velocity contours at $x = 30$ cm. Bold vectors correspond to the region where the dissipation is greater than 0.5 W m^{-3}.

is the greatest, but the streamwise velocity contours reveal that the structure has evolved such that the particle's velocity vector is aligned with the contours.

The complete evolution of the dissipation due to the intermediate size class, D_2, along with the other two sizes are given in figures 6.17, 6.18, and 6.19. The small size class, D_1, contributes little to the total dissipation via large scale coupling, as would be expected from the disparity of the viscous relaxation time and the large scale period. Initially, what contribution it does make is limited mostly to the inner streak deceleration region (ii) and the streak tip acceleration region (iv), with a small fraction in the core acceleration region (i). The lack of substantial core acceleration follows from the particles low Stokes number with respect to the fundamental frequency, as this peak is mainly a result of streamwise temporal fluctuation as the droplets are advected past the large scale structures. The prominence of

Figure 6.17: Evolution of phase averaged dissipation per unit mass, $\rho_g \epsilon_p$, for small size class, D_1. (a) $x = 2$ cm, (b) $x = 6$ cm, (c) $x = 10$ cm, (d) $x = 14$ cm, (e) $x = 18$ cm, (f) $x = 22$ cm, (g) $x = 26$ cm, (h) $x = 30$ cm.

Figure 6.18: Evolution of phase averaged dissipation per unit mass, $\rho_g \epsilon_p$, for intermediate size class, D_2. (a) $x = 2$ cm, (b) $x = 6$ cm, (c) $x = 10$ cm, (d) $x = 14$ cm, (e) $x = 18$ cm, (f) $x = 22$ cm, (g) $x = 26$ cm, (h) $x = 30$ cm.
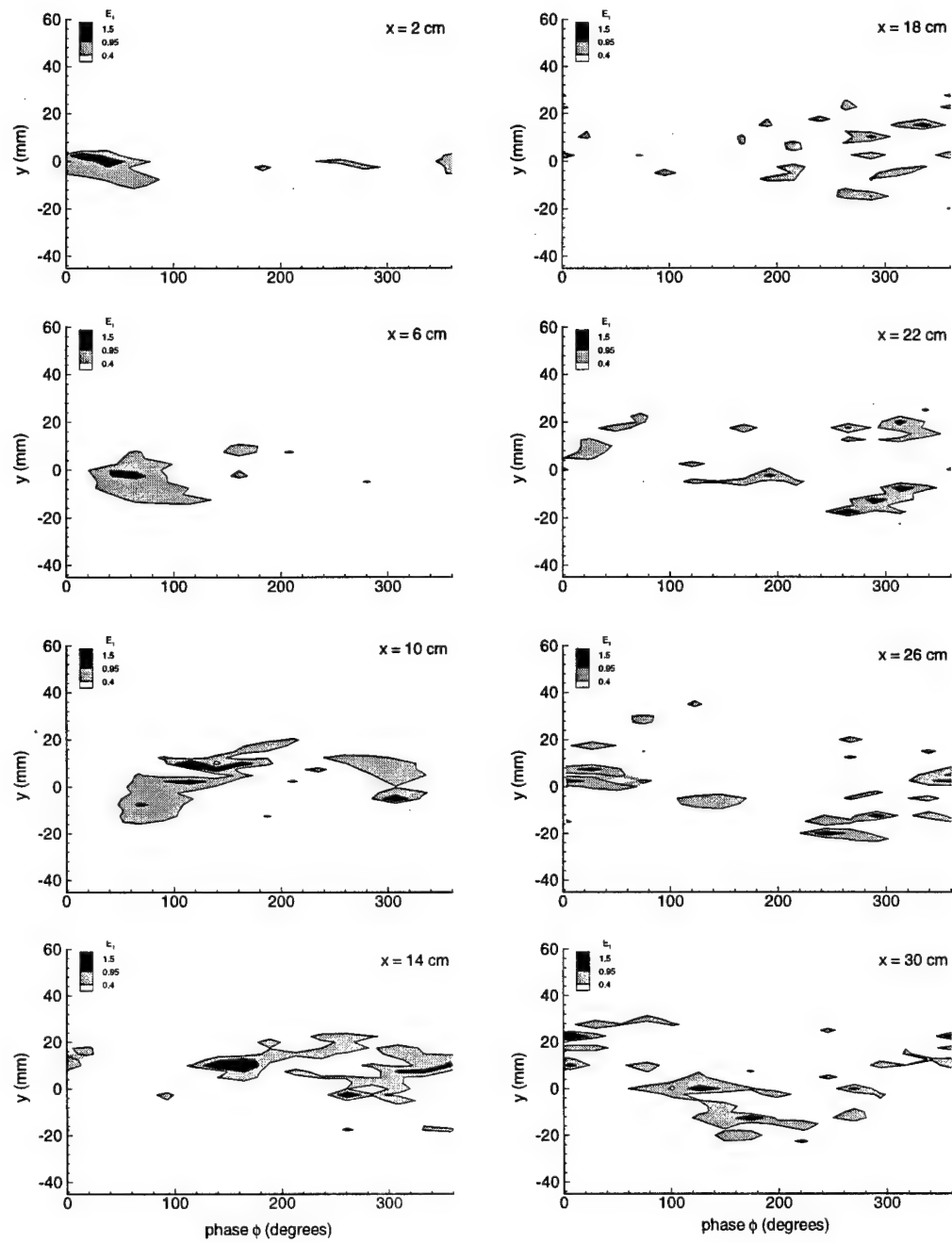
Figure 6.19: Evolution of phase averaged dissipation per unit mass, $\rho_g \epsilon_p$, for large size class, D_3. (a) $x = 2$ cm, (b) $x = 6$ cm, (c) $x = 10$ cm, (d) $x = 14$ cm, (e) $x = 18$ cm, (f) $x = 22$ cm, (g) $x = 26$ cm, (h) $x = 30$ cm.
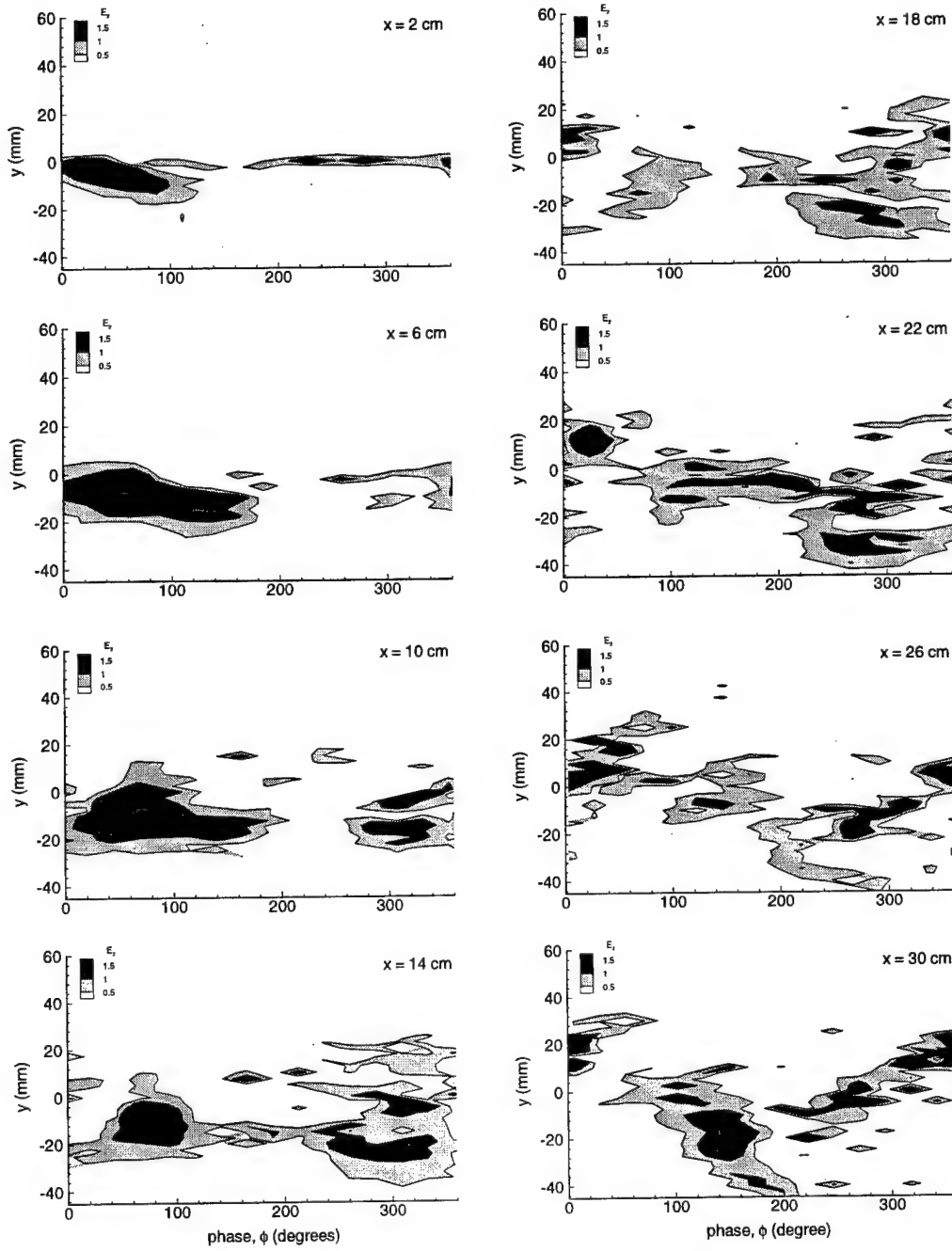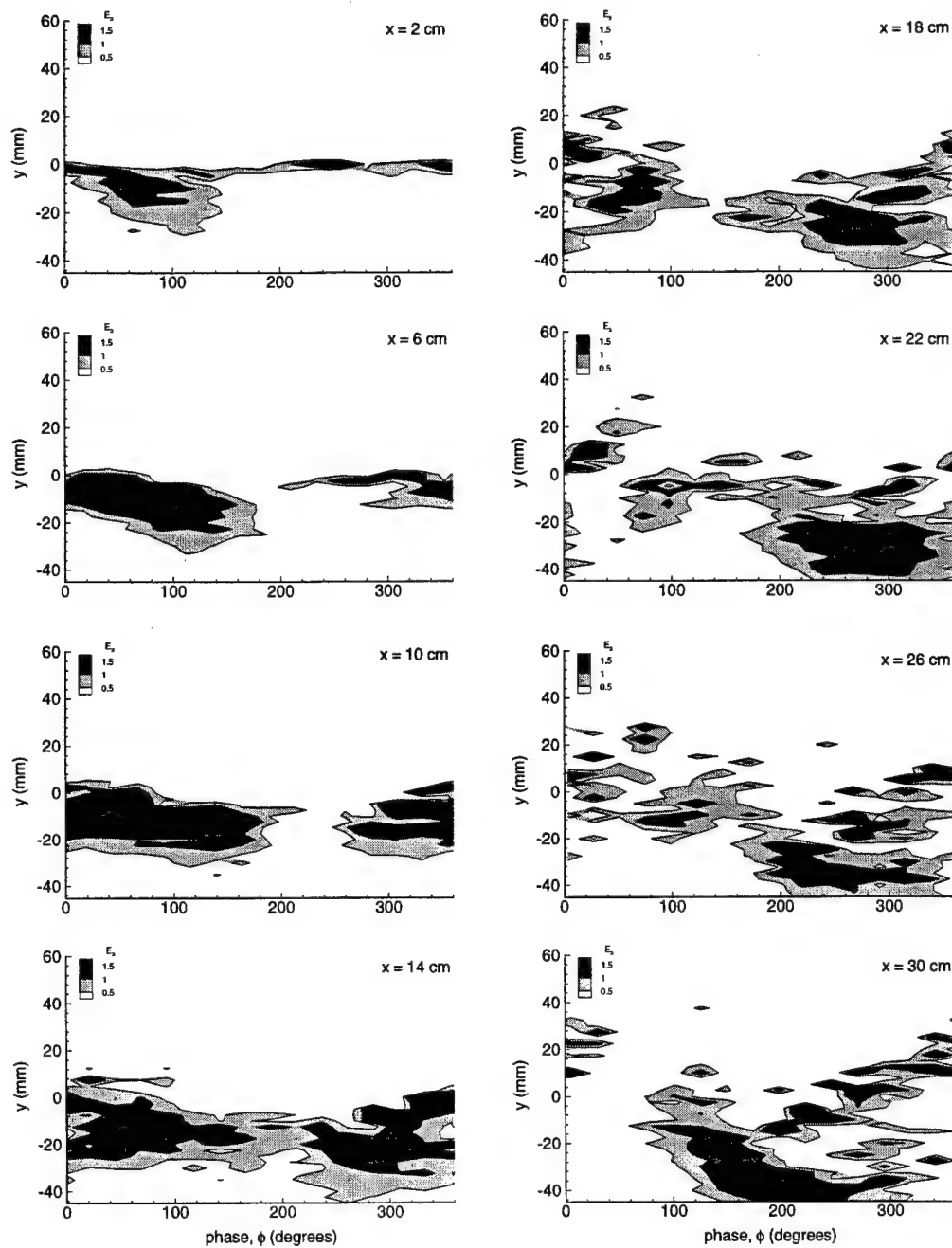
the inner deceleration corresponds to the sharp divergence of the streamwise gas velocity contours, creating a strong deceleration. The outer streak tip acceleration is at a maximum with the smallest size, due to its greatest concentration in the external region. Even so, the prominence of this region decreases after the pairing has occurred, leaving almost no trace at $x = 26$ and 30 cm. The evolution after the pairing has started is limited mainly to the narrow regions along the streak edges as observed for the intermediate size. As mentioned earlier, it is likely that this size class will interact with the other turbulence scales present in the flow.

The largest size class (figure 6.19) is characterized by almost the opposite trends observed for the smallest size class. Namely, throughout the entire evolution the dissipation for this size is dominated by the core acceleration region, and shows no evidence whatsoever of an external streak tip acceleration. The lack of external accelerations comes as little surprise, due to the reduced dispersion for this size class – there are simply too few large particles in the external streak for this mechanism to make a contribution, and what particles do get into this region are still experiencing strong decelerations as they attempt to relax to the surrounding gas velocity. The streak edge decelerations are also exaggerated for this size class, due to their greater inertia and lack of response as they pass through the gradients in these regions.

Thus the mean phase-averaged dissipation is observed to have an inhomogeneous structure across the large-scale eddies of the shear layer, localized in most cases to regions of localized mean phase-averaged kinetic energy transfer. The two quantities differ in the fact that the total phase-averaged particle dissipation is typically about 10% of the total phase-averaged kinetic energy transfer between the phases, but in a few isolated regions where the particle velocity is perpendicular to the slip velocity (such as in the region between the core and braid of the eddies), the particle dissipation can exceed the particle kinetic energy transfer. Comparisons with the estimated turbulent gas dissipation for the shear layer indicate that the total mean phase-averaged particle dissipation is of $O(10^{-2})$, which is the same order of magnitude as the mass loading.

Simulations of homogeneous turbulence (Elghobashi and Truesdell, 1993; Squires and Eaton, 1990) also display increased dissipation levels which are on the order of the

mass loading. Use of these results allowed for estimates of the particle dissipation caused by the smaller scales, which indicate that their contribution will not be initially comparable to levels of the large scales owing to small mass fraction of particles which are able to respond to those scales. As the large-scales increase with successive pairings, however, the importance of the large-scale phase-averaged particle dissipation will be diminished, and the small-scale interactions will dominate. The observation that the mass loading is an important factor further implies that those particles sizes in the peak of the volume p.d.f. will tend to be the dominant contributor to the particle/turbulence interaction, and the time scales of import to determining the structure of the interaction will follow the viscous relaxation time of these particles.

Chapter 7

Conclusion

The measurements of the velocity and particle concentration fields in a polydispersed, particle-laden, turbulent mixing layer confirm the early observations that the large-scale eddies are primarily responsible for the particle dispersion process. In addition, it is found that through the mechanism of vortex pairing the particle concentration field is progressively homogenized as particles entrained by nearby vortices are redistributed inside the resulting subharmonic structure. The homogenization resulting from this process indicated not only a strong dependence on the particle size and dominant eddy time scale, but also on the time between pairing events. Specifically, the fundamental development time, τ_1, controls the growth of each size class along the initial streak and hence the amount of homogenization attained after the pairing. The time between pairing, τ_2, determines whether or not the subharmonic structure will redistribute larger particles away from the core where they had been deposited by the pairing process.

It was also found that both prior to and during the vortex pairing event, the kinetic energy transfer between the phases is a highly anisotropic process. In the early stages of the evolution, where the flow is dominated by a single, large, eddy scale, we found the somewhat surprising results that most of the kinetic energy exchanged between the phases occurs in a region outside of the mixing layer and does not coincide with the regions of the maximum velocity fluctuations or peak vorticity regions of the carrier gas. Instead, the transfer is manifested as clearly defined positive and negative peaks existing beneath cores and free stagnation points of the vortices. This mechanism is the result of the particulate's

144

response to the irrotational velocity perturbation fields set up in the free stream by the array of large-scale vortices. Furthermore, it is found that the central region is excluded as a prominent transfer area due to its lower concentrations as well as regions of strong lateral slip velocity which are not aligned with the droplet's velocity.

The contribution of each size class to the kinetic energy transfer is also linked to the size as well as the concentration of each size family. The maximum contribution is produced by the balance between increasing slip velocity due to particle inertia and the eventual decrease in concentration dictated by the spray's size distribution. The pairing event results in a decrease of the energy transfer, as the growth of the subharmonic introduces a reduced relative Stokes number that is twice as small as the initial one. The doubling of the dominant scale also changes the size class which is responsible for the dominant energy transfer as a new slip velocity and concentration balance is formed.

Finally, it is speculated that the above mechanism will remain a significant source of kinetic energy transfer as long as the large scales are maintained and the relative Stokes numbers are of order unity. As the pairing continues to reduce the large-scale slip velocities and the homogenization of the particles is increased, additional sources of transfer will likely take place in the braid region where the concentration is increasing due to the origin of the dispersion streaks.

Measurements of the mean phase-averaged particle dissipation were observed to have an inhomogeneous structure across the large-scale eddies of the shear layer, localized in most cases to the same regions prominent mean phase-averaged kinetic energy transfer. The two quantities differ in the fact that the total phase-averaged particle dissipation is typically about 10% of the total phase-averaged kinetic energy transfer between the phases, but in a few isolated regions where the particle velocity is perpendicular to the slip velocity (such as in the region between the core and braid of the eddies), the particle dissipation can exceed the particle kinetic energy transfer. Comparisons with the estimated turbulent gas dissipation for the shear layer indicate that the total mean phase-averaged particle dissipation is of $O(10^{-2})$, which is the same order of magnitude as the mass loading.

Simulations of homogeneous turbulence (Elghobashi and Truesdell, 1993; Squires and Eaton, 1990) also display increased dissipation levels which are on the order of the

mass loading. Use of these results allowed for estimates of the particle dissipation caused by the smaller scales, which indicate that their contribution will not be initially comparable to the large-scale effects owing to small mass fraction of particles which are able to respond to the smallest scales. As the large-scales increase with successive pairings, however, the importance of the large-scale phase-averaged particle dissipation will be diminished, and the small-scale interactions will dominate. The observation that the mass loading is an important factor further implies that those particles sizes in the peak of the volume p.d.f. will tend to be the dominant contributor to the particle/turbulence interaction.

The current study has focused specifically on the role of the large scales in the shear layer, and the results of the eddy's dynamical interaction on the droplet dispersion and the inter-phase kinetic energy transport. While this has afforded considerable insight into the dispersion and coupling problem, it remains incomplete in that the effects of the smaller turbulent scales could not be addressed in detail. Although in the current study the viscous response time of the particles which dominate the inter-phase transfer was comparable to the large eddy turn-over times, there are many applications where this would not be the case. Therefore future work should be concentrated on the features of the smaller scales and their particular structure within the shear layer.

Other aspects of interest to the study of multi-phase turbulent flows include extending the measurement of the inter-phase coupling terms to greater mass (and volume) fractions to observe how the feedback affects the evolution of the turbulent flow. Studies of this nature have been completed for jet, channel, and boundary layer flows, but to date have had only limited success in determining the structure of the coupling mechanisms between the phases.

Appendix A

Light Scattered by a Spherical Particle

In the view of classical continuum mechanics, light consists of electro-magnetic waves which are described analytically by Maxwell's equations. For the case of propagation through a non-dissipative medium, the governing relationships reduce to the well-known vector wave equation. Two important solutions of this equation are given by

$$\mathbf{E}(\mathbf{x}, t) = \mathbf{E}_0(\mathbf{x}, t)e^{(-i\mathbf{k}\cdot\mathbf{x} + \omega t)} \tag{A.1}$$

and

$$\mathbf{E}(\mathbf{r}, t) = \frac{\mathbf{E}_0(\mathbf{r}, t)}{\mathbf{k}\cdot\mathbf{r}}e^{(-i\mathbf{k}\cdot\mathbf{r} + i\omega t)}. \tag{A.2}$$

Equation (A.1) and (A.2) represent the motion of the electric field vector, $\mathbf{E}$, in the form of a planar and spherical traveling wave. In these equations, $\mathbf{E}_0$ is the complex amplitude, $\mathbf{k} = \frac{2\pi}{\lambda}\mathbf{e}_k$ is the wavenumber and points in the direction of wave propagation, ω is the wave frequency, $\mathbf{x}$ and $\mathbf{r}$ are the position vectors in cartesian and spherical coordinates, and t is the time. The magnetic field is a vector quantity, and as such can be represented by two the orthogonal components

$$\mathbf{E}(\mathbf{x}, t) = E_\perp(\mathbf{x}, t)\mathbf{e}_\perp + E_\parallel(\mathbf{x}, t)\mathbf{e}_\parallel. \tag{A.3}$$

The direction vectors $\mathbf{e}_\perp$ and $\mathbf{e}_\parallel$ are defined to be those components of the electric field which are perpendicular and parallel respectively to a scattering surface. For a wave propagating

147

in free space, their exact orientation is immaterial.

Due to the high frequency of its fluctuation ($\omega \approx 10^{14}\, s^{-1}$), it is impossible to make a direct measurement of $\mathbf{E}$. Instead, most instruments typically register a time average of the incident radiant energy, defined by

$$I = nc\epsilon_o \|\mathbf{E}^2\| = nc\epsilon_o \mathbf{E}\mathbf{E}^* = nc\epsilon_o(E_\perp E_\perp^* + E_\| E_\|^*). \tag{A.4}$$

Here n is the absolute index of refraction, c is the speed of light, ϵ_o is the permittivity of free space, and * denotes the complex conjugate. Due to the separability of the electric field and intensity into the contribution of the perpendicular and parallel components, only one of the components will be represented in following discussion unless the results for the other component warrant special attention.

Appendix A.1 Scattering Function for a Spherical Particle

Light scattering by spherical particles has been studied in depth by van de Hulst (van de Hulst, 1981), and much of the following formulation follows directly from his work. When considering problems involving light scattered by a single particle from a distant source, we shall assume that the incident light can be described as a monochromatic, linearly polarized, planar wave as given by (A.1) with the assumption that $\mathbf{E}_0(\mathbf{x}, t) = \mathbf{E}_{inc}$, a constant. The amplitude of perpendicular component of the scattered light can then be defined by the spherical wave

$$E_\perp(r, \theta) = S_\perp(\theta)\frac{e^{(-i\mathbf{k}\cdot\mathbf{r} + \omega t)}}{i\mathbf{k}\cdot\mathbf{r}}. \tag{A.5}$$

This equation provides the definition for the complex scattering amplitude function, $S(\theta)$, which depends only on the scattering angle, θ, as defined in figure Appendix A.1. The energy intensity follows from (A.4),

$$I_\perp = nc\epsilon_o\frac{S_\perp(\theta)S_\perp^*(\theta)}{(kr)^2} = nc\epsilon_o\frac{i_\perp}{(kr)^2} \tag{A.6}$$

This allows the complex amplitude to be expressed in polar form, with a real amplitude and phase shift, $\sqrt{i_\perp}$ and σ.
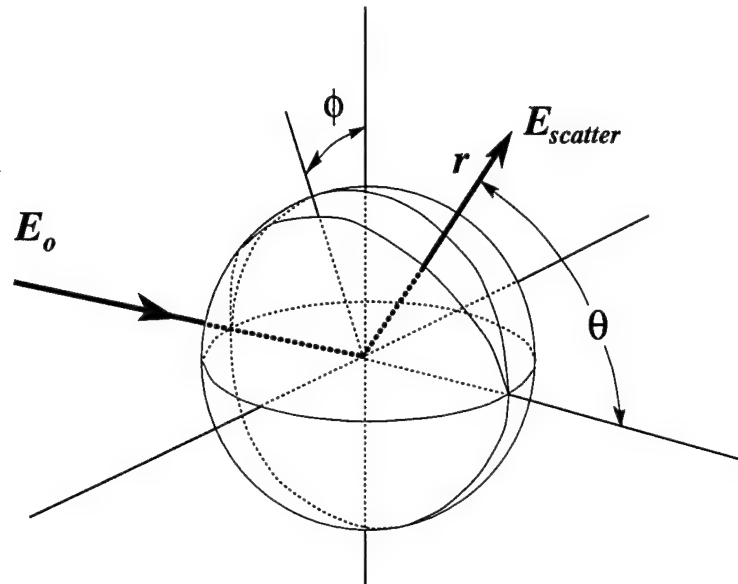
Figure Appendix A.1: Coordinate system defined for single particle light scattering.

The rigorous solution of Maxwell's equations for light scattered by a spherical particle illuminated by a uniform incident beam is known as Mie theory. Unfortunately, Mie's solution is expressed as an infinite sum of Legendre polynomials, and as such it is amiable to complete analysis for a only a few special cases and asymptotic geometries. Realization of the intensity and phase of the scattered light is either obtained from tabulated summation or numerical computation.

For the case of very large spheres in comparison with the wavelength of the incident light, van de Hulst (van de Hulst, 1981) has shown that the results obtained from geometric optics is equivalent to the asymptotic solution of Mie theory. This regime requires that the wavelength of the incident light be much larger than the size of the sphere ($\beta = \pi D / \lambda \gg 1$) and that the phase lag caused by propagation through the sphere is large ($\varrho = 2\beta(m-1) \gg 1$). Under these conditions, incident light beams can be viewed as distinct separable rays whose path can be traced throughout the sphere and described by the Fresnel equations of reflection and refraction, as is typically done for geometric optics. Implicit to this technique is the fact that the effects of diffraction must also be separable from those of reflection and refraction. Diffraction is the component of light which is scattered by the formation of an incomplete wavefront due to the blocking presence of the particle boundary. For $\beta \gg 1$,

the far field diffraction pattern is intense but is limited to a very narrow angular range that is described by Fraunhoffer diffraction theory. In contrast, the light scattered through the sphere is dispersed in a broad angular pattern and is of moderate intensity. This is what allows for the separation of the distinct phenomenon. As the size of the sphere is decreased, the diffraction intensity pattern is reduced and spread over a broader angular distribution similar to the distribution resulting from the internally refracted light. In this regime, the geometrical optics approximations are no longer valid, and the general Mie theory must be used to obtain the complete solution.

In addition to the above conditions on the size of the particle, there are some additional limitations where the geometric optics approximation breaks down. This occurs wherever several rays converge to form a focal point. In these regions the energy carried by the beam is contained in a vanishingly small area, and for geometric optics, results in an infinite amplitude. There are numerous focal points within the particle and the near field, but for practical instrumentation the far-field focal points are the ones of concern. It is these points which give rise to the well known phenomenon of rainbows and the glory, which for water are located at $\theta = 138°$, $129°$ (first and second rainbow) and $\approx 175°$ (glory).

With the above considerations in mind, geometric optics will be used then in the following derivations due to its applicability to most sprays encountered in two-phase flows (the drops are usually big enough for the approximation to hold) and because of the physical explanations which can be clearly illustrated.

The assumption that the scattered light can be independently divided into contributions due to diffraction and reflection/refraction allows the complex amplitude to be divided into the sum of the individual components:

$$S_\perp(\theta) = S_{\perp_{diff}}(\theta) + S_{\perp_{refl,refr}}(\theta). \qquad (A.7)$$

For the conditions above, the diffraction pattern is equivalent to that around a circular disk and is given by (Hecht, 1987)

$$S_{diff}(\theta) = S_{\perp_{diff}}(\theta) = S_{\|_{diff}}(\theta) = \beta^2 \frac{J_1(\beta \sin(\theta))}{\beta \sin(\theta)}. \qquad (A.8)$$

Where $J_1(\ )$ is the Bessel function of the first kind. A similar result can be derived from Mie theory which differs from (A.8) by replacing $\sin(\theta)$ with θ.
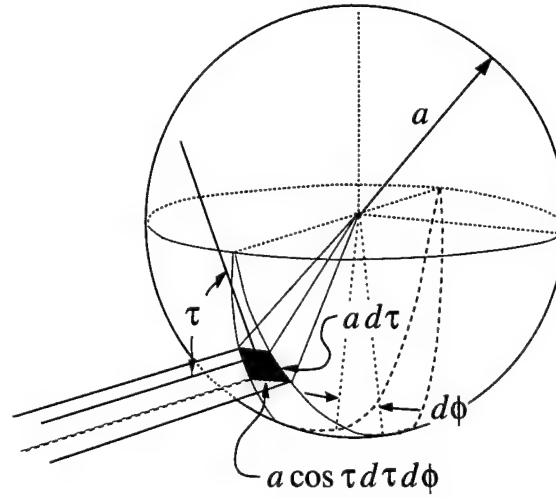
Figure Appendix A.2: Diagram of incident light ray considered for geometrical scattering.

The reflected and refracted components are then obtained by considering the energy flux contained in a thin incident ray as shown in figure Appendix A.2:

$$\mathcal{F} = I_o a^2 \cos(\tau) \sin(\tau) d\tau d\phi, \tag{A.9}$$

where I_o is the intensity of the incident wave, τ is the angle between the incident ray and the surface of the sphere, and ϕ is the azimuthal angle. Once the ray intersects the sphere's surface, it will subsequently be divided into a reflected and refracted component whose geometry is described by Snell's Law,

$$m \cos(\tau') = \cos(\tau), \tag{A.10}$$

and whose intensity is governed by the Fresnel equations,

$$R_\perp = \left(\frac{E_{refl_\perp}}{E_{o_\perp}} \right) = \frac{\sin(\tau) - m\sin(\tau')}{\sin\tau + m\sin(\tau')}, \tag{A.11}$$

and

$$R_\parallel = \left(\frac{E_{refl_\parallel}}{E_{o_\parallel}} \right) = \frac{m\sin(\tau) - \sin(\tau')}{m\sin\tau + \sin(\tau')}, \tag{A.12}$$

where m is the relative index of refraction, and $R_\perp$ and $R_\parallel$ are the amplitude ratios of the reflected electric field vector components relative to the incident components in the planes perpendicular and parallel to the plane of scattering. The intensity of the first reflected
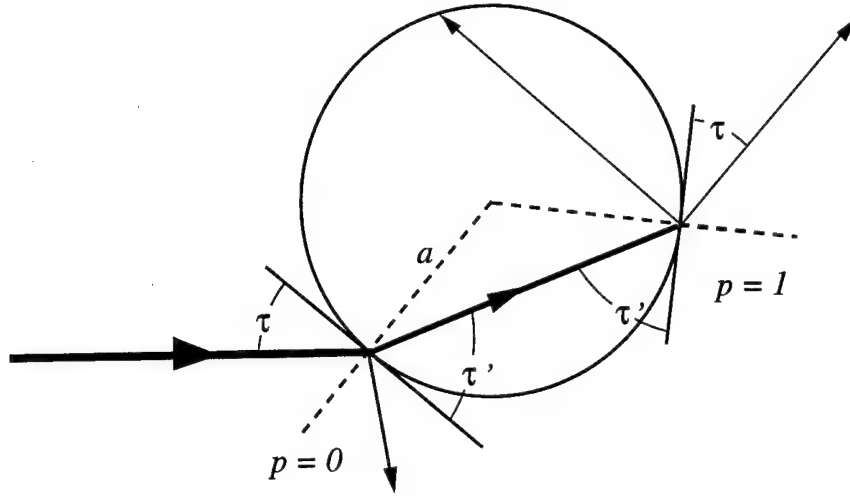
Figure Appendix A.3: Geometry definition for scattering rays.

ray will therefore be given by $R_\perp^2$ (for the perpendicular component). Once the incident ray has been refracted by the first surface, it will continue through the sphere with an intensity of $1 - R_\perp^2$ until it encounters a new interface where it will undergo a second reflection/refraction and repeat the process again (see figure Appendix A.3). The second emigrant ray will have the intensity of $(1 - R_\perp^2) - R_\perp^2(1 - R_\perp^2) = (1 - R_\perp^2)^2$. The amplitude and direction of the pth order emerging ray can then be expressed as

$$
\begin{aligned}
\varepsilon_\perp^2 &= R_\perp^2 & \text{for } p = 0. \\
\varepsilon_\perp^2 &= (1 - R_\perp^2)^2(-R_\perp)^{2(p-1)} & \text{for } p = 1,2,3\ldots
\end{aligned}
\tag{A.13}
$$

and

$$
\theta = 2\tau - 2p\tau'.
\tag{A.14}
$$

Equation (A.14) follows from the symmetry of the scattering (e.g. $\tau_0' = \tau_1' = \tau'$, which also implies that τ is the same at every interaction by equation (A.10)).

The scattered light is then spread over an area given by $r^2 sin(\theta)d\theta d\phi$. Normalizing the outgoing energy flux by this area then gives the scattered radiation intensity:

$$
I_\perp(\theta, p) = \frac{\varepsilon_\perp^2 I_{o_\perp} a^2 \cos(\tau)\sin(\tau)d\tau d\phi}{r^2 sin(\theta)d\theta d\phi} = \frac{a^2}{r^2}\varepsilon_\perp^2 I_{o_\perp}\Lambda,
\tag{A.15}
$$

where

$$\Lambda = \frac{\cos(\tau)\sin(\tau)}{sin(\theta)|d\theta/d\tau|} = \frac{\cos(\tau)\sin(\tau)}{sin(\theta)|2 - 2p\frac{\tan(\tau)}{\tan(\tau')}|}. \tag{A.16}$$

Comparing this with equation (A.6) then gives the real amplitude of $S_\perp$ to be

$$S_\perp(\theta) = \sqrt{i_\perp}e^{(i\sigma)} = \beta\varepsilon_\perp\sqrt{I_o\Lambda}e^{i\sigma}. \tag{A.17}$$

The phase shift, σ, caused by the scattering must now be considered to complete the formulation. These phase changes can be categorized into three different sources: reflections, passage through focal points, and variation of optical path length. The first of these stems from the fact that reflection will change the sign of the electric field (as can be seen from an examination of equations (A.11) and (A.12)),which is equivalent to a phase change of π. Passing the ray through a focal line advances its phase by $\pi/2$, and by π when it passes through a focal point (which can be thought of as a superposition of two focal lines of infinitesimal extent). The last contribution is the one that turns out to be the most important for PDA applications, and is caused by the effective change in wavelength as the light travels through the particle with an index of refraction m. Typically, this phase shift is referenced to an equivalent undisturbed ray traveling through the same location $a\cos(\tau)$. This phase shift can be determined geometrically from examination of figure Appendix A.4, and is given by

$$\eta = \overline{AB} - \overline{AC} = 2\beta(sin(\tau) - mp\sin(\tau')). \tag{A.18}$$

With these results, the complete expressions for the scattered electric field can be written

$$E_\perp(r,\theta) = \frac{\beta\varepsilon_\perp\sqrt{I_{o\perp}\Lambda}}{i\mathbf{k}\cdot\mathbf{r}}e^{i(-\mathbf{k}\cdot\mathbf{r}+\omega t+\varphi_{reflc}+\varphi_{focus}+\eta)}. \tag{A.19}$$

A similar expression can also be written for $E_\parallel$.
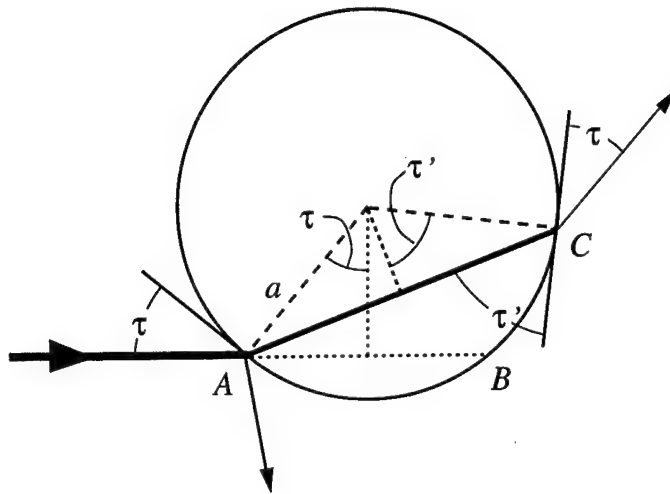
Figure Appendix A.4: Phase shift due to change in optical path length.

Appendix B

Dual Beam Interferometry: Velocity and Size Measurement

One of the most pervasive uses of optical instrumentation applied to fluid mechanics research over the past two decades has to be that of dual beam interferometry. These methods rely upon information that can be extracted from the scattered interference patterns generated when two coherent light sources are incident upon the scattering particle. The first and simplest instruments were able to measure the velocity of scattering particles by capitalizing on of the Doppler effect (Yeh and Cummins, 1964). About a decade later, dual-beam spherical particle sizing development began by measuring the amplitude ratio between the high-frequency Doppler intensity and the low-frequency or "pedestal" component (also known as the signal visibility) (Bachalo, 1980). Although this method was an improvement over other techniques which measured just the amplitude, its accuracy was strongly dependent on ensuring that both incident laser beams were of identical intensity, and its dynamic range was limited to less than a decade. This technique was improved once it was realized that the particle diameter was linearly related to the size of the projected interference fringe pattern (Bachalo and Houser, 1984). Multiple receivers were then used to record the spatial pattern as a time lag which was created when the particle moved through the probe volume. With the advent of advanced signal processing and high-speed dedicated discrete Fourier transform (DFT) boards, reliable measurements could be made in realistic sprays. Currently, research is focusing on extending the instrument to be able to identify

the index of refraction of the scattering material (Bachalo, 1994; Naqwi et al., 1991), and also to make the instrument more robust and reliable in a wider variety of applications such as bubbly flows and combustible sprays.

The fundamental geometric layout of the LDV and the PDA are identical and consists of two linearly polarized monochromatic coherent beams of equal amplitude (but possibly slightly different frequency and wavelength) E_1 and E_2 which are crossed at a small angle (figure B.1). The ellipsoidal region of intersection is referred to as the probe volume and its dimensions are dictated by the initial beam width, spacing at the transmitter lens, and the focal length of the transmitter lens. The probe volume dimensions can be found by examining diffractive interference effects within the converging beam, which prevents the light from being focused into an infinitesimal point. The results of such consideration give (Drain, 1980)

$$
\begin{aligned}
a_o &= \frac{4f\lambda}{\pi D_o} \\
b_o &= \frac{a_o}{\cos(\gamma)} \\
c_o &= \frac{a_o}{\sin(\gamma)},
\end{aligned}
\tag{B.1}
$$

where f is the focal length of the lens, D_o is the beam diameter incident on the lens, and λ is the wavelength of the light. Particles within this volume will scatter light from both beams to create the desired interference pattern. The probe volume, however, is not always identical to the measurement volume as often times an aperture is placed within the receiver optics to limit the extent of the measurement region. The scattered light is collected over the receiver lens and focuses onto several photo-multiplier tubes where it is transformed into an electrical signal.

The results from Appendix A can now be used to find the intensity of the combined scattered light from beams 1 and 2. Most systems are polarized in the plane which bisects the beams and collect the scattered signal in the same plane (figure B.1). This defines the incident electric field components

$$
E_1 = E_o \cos(\phi_1)\mathbf{e}_{\parallel} + E_o \sin(\phi_1)\mathbf{e}_{\perp}.
\tag{B.2}
$$

The above condition implies that the parallel component (i.e. in the plane of scatter)

will be the dominant contributor to the signal, and hence will be the component used in the following derivation. A similar expression can also be obtained for the perpendicular component. Summing the electric field component contributions from beam 1 and 2 gives

$$E_{\|} = E_{\|_1} + E_{\|_2}. \tag{B.3}$$

Dropping the $\|$ notation, the resulting scattered intensity is

$$
\begin{aligned}
I \propto EE^* &= (E_1 + E_2)(E_1^* + E_2^*) \\
&= \frac{S_1 S_1^*}{r^2 k_1^2} + \frac{S_2 S_2^*}{r^2 k_2^2} + \frac{S_1^* S_2}{r^2 k_1 k_2} e^{-i(k_2-k_1)r+i(\omega_2-\omega_1)t} + \frac{S_1 S_2^*}{r^2 k_1 k_2} e^{i(k_2-k_1)r-i(\omega_2-\omega_1)t}.
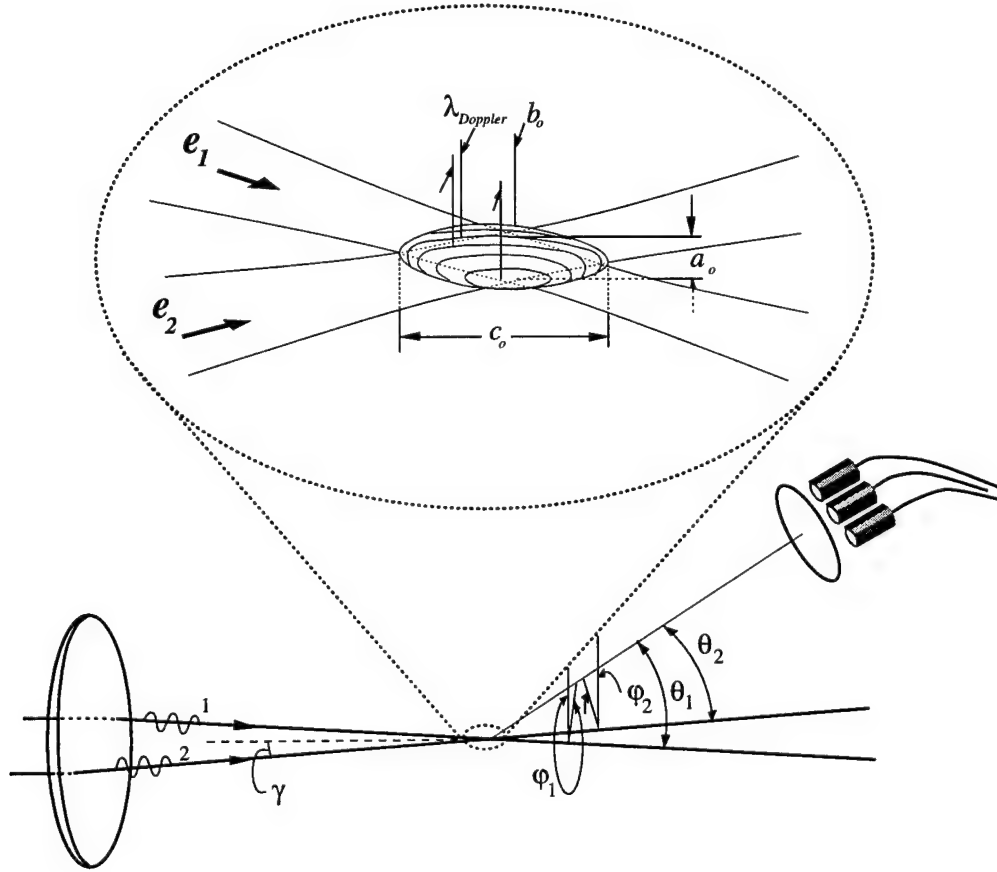\end{aligned} \tag{B.4}
$$

Figure Appendix B.1: Geometry and coordinate system defined for dual-beam or fringe interferometry.

From equation (A.17) it follows that

$$
\begin{aligned}
S_1 S_1^* &= & \beta^2 \varepsilon_1^2 I_{o_1} \Lambda_1 & & = & \; i_1 \\
S_2 S_2^* &= & \beta^2 \varepsilon_2^2 I_{o_2} \Lambda_2 & & = & \; i_2 \\
S_1^* S_2 &= & \beta^2 \varepsilon_1 \varepsilon_2 \sqrt{I_{o_1} I_{o_2} \Lambda_1 \Lambda_2} e^{i(\sigma_2 - \sigma_1)} & & = & \; \sqrt{i_1}\sqrt{i_2} e^{i(\sigma_2-\sigma_1)} \\
S_1 S_2^* &= & \beta^2 \varepsilon_2 \varepsilon_1 \sqrt{I_{o_1} I_{o_2} \Lambda_1 \Lambda_2} e^{-i(\sigma_2 - \sigma_1)} & & = & \; \sqrt{i_1}\sqrt{i_2} e^{-i(\sigma_2-\sigma_1)}
\end{aligned}
\tag{B.5}
$$

Combining equations (B.4) and (B.5) gives the final desired scattering intensity:

$$
I(\theta_1, \theta_2) = \frac{i_1}{r^2 k_1^2} + \frac{i_2}{r^2 k_2^2} + \frac{\sqrt{i_1}\sqrt{i_2}}{r_2 k_1 k_2} \cos\left[(\omega_2 - \omega_1) t + (\sigma_2 - \sigma_1) - (\mathbf{k}_2 - \mathbf{k}_1) \cdot \mathbf{r} \right], \tag{B.6}
$$

where

$$
\begin{aligned}
\omega_1 - \omega_2 &= \quad \text{frequency difference between the beams,} \\
& \qquad \text{and is responsible for the for the Doppler} \\
& \qquad \text{beat frequency used to detect velocity.} \\
\sigma_2 - \sigma_1 &= \quad \text{scattered phase shift difference between} \\
& \qquad \text{the two beams, and is used for particle size} \\
& \qquad \text{detection.} \\
(\mathbf{k}_2 - \mathbf{k}_1) \cdot \mathbf{r} &= \quad \text{spatial phase distribution; typically} \\
& \qquad \text{negligible.}
\end{aligned}
$$

In order to explain how the frequency difference is related to the operation of the LDV, it is first necessary to explain the origin of the Doppler shift. A moving particle will shift the frequency of the scattered light due to the Doppler effect. This frequency shift can be determined by considering the results from two simpler cases: (a) finding the frequency shift of a moving observer relative to a stationary source (the shift in the incident light as perceived by the particle), and (b) combining it with the frequency shift observed by a stationary receiver and a moving transmitter (the shift in the light scattered by the moving particle). These results can be obtained from considerations of elementary wave physics (Resnick and Halliday, 1977).

To find the shift for case (a), consider a stationary source emitting a series of spherical waves. If the observer is moving with a velocity $\mathbf{u}_p$ away from a source emitting a frequency ν_o, then it will receive $\mathbf{u}_p \cdot \mathbf{e}_s \, \Delta t / \lambda_o$ ($\mathbf{e}_s$ is the unit vector from the source to the observer) fewer wave fronts than a stationary observer would during the time interval Δt ($c \, \Delta t / \lambda_o$ for the stationary observer). Thus the total number of waves observed, $\nu' \Delta t$, gives the frequency perceived by the moving particle,

$$
\nu' = \nu_o \left(1 - \frac{\mathbf{u}_p \cdot \mathbf{e}_s}{c} \right). \tag{B.7}
$$

Considering now case (b), a moving transmitter emitting with a frequency ν' will compress $\nu' \Delta t$ wave fronts into a length shortened by the motion of the emitter, $\nu' \Delta t \lambda' - \mathbf{u}_p \cdot \mathbf{e}_r \Delta t$ (where $\mathbf{e}_r$ is the unit vector pointing from the moving emitter to the stationary receiver). The effective wavelength is then

$$\lambda = \frac{\nu' \Delta t \lambda' - \mathbf{u}_p \cdot \mathbf{e}_r \Delta t}{\nu' \Delta t}. \tag{B.8}$$

Substituting $\lambda = c/\nu$ and $\lambda' = c/\nu'$ gives

$$\nu = \frac{\nu'}{\left(1 - \frac{\mathbf{u}_p \cdot \mathbf{e}_r}{c}\right)}. \tag{B.9}$$

The total frequency shift incurred by a moving scatter is then obtained by combining (B.7) and (B.9) to give

$$\nu = \nu_o \frac{\left(1 - \frac{\mathbf{u}_p \cdot \mathbf{e}_s}{c}\right)}{\left(1 - \frac{\mathbf{u}_p \cdot \mathbf{e}_r}{c}\right)} \tag{B.10}$$

Returning to the LDV, the scattering particle will produce a Doppler shift with each of the two beams, $\mathbf{e}_1$ and $\mathbf{e}_2$. Assuming that the particles will not introduce any further frequency shifts (e.g. fluorescent emission), we can write

$$\omega_1 = \omega_{1_o} \frac{\left(1 - \frac{\mathbf{u}_p \cdot \mathbf{e}_1}{c}\right)}{\left(1 - \frac{\mathbf{u}_p \cdot \mathbf{e}_r}{c}\right)} \quad \text{and} \quad \omega_2 = \omega_{2_o} \frac{\left(1 - \frac{\mathbf{u}_p \cdot \mathbf{e}_2}{c}\right)}{\left(1 - \frac{\mathbf{u}_p \cdot \mathbf{e}_r}{c}\right)}. \tag{B.11}$$

Their difference is then

$$
\begin{aligned}
\omega_2 - \omega_1 &= \frac{\left[\omega_{2_o}\left(1 - \frac{\mathbf{u}_p \cdot \mathbf{e}_2}{c}\right) - \omega_{1_o}\left(1 - \frac{\mathbf{u}_p \cdot \mathbf{e}_1}{c}\right)\right]}{\left(1 - \frac{\mathbf{u}_p \cdot \mathbf{e}_r}{c}\right)} \\
&= \frac{\left[(\omega_{2_o} - \omega_{1_o}) + \frac{\mathbf{u}_p \cdot \mathbf{e}_1}{\lambda_{1_o}} - \frac{\mathbf{u}_p \cdot \mathbf{e}_2}{\lambda_{2_o}}\right]}{\left(1 - \frac{\mathbf{u}_p \cdot \mathbf{e}_r}{c}\right)} \\
&\simeq \left[(\omega_{2_o} - \omega_{1_o}) + \frac{\mathbf{u}_p \cdot (\mathbf{e}_1 - \mathbf{e}_2)}{\lambda}\right]. \tag{B.12}
\end{aligned}
$$

The last step assumes that the typical particle velocities are small in comparison to the speed of light, c, and that $\Delta \omega_o / \omega = (\omega_2 - \omega_1)/\omega \ll 1$. This allows the term in the denominator to be ignored ($|\mathbf{u}_p|/c$ is typically $\ll 10^{-5}$), and permits the simplification

$$\frac{1}{\lambda_{2_o}} = \frac{1}{\lambda_{1_o} + \Delta \lambda} = \frac{1}{\lambda_{1_o}}\left(1 + \frac{\Delta \lambda}{\lambda_{1_o}}\right)^{-1} = \frac{1}{\lambda_{1_o}}\left(1 - \frac{\Delta \lambda}{\lambda_{1_o}} + \ldots\right) \simeq \frac{1}{\lambda_{1_o}} = \frac{1}{\lambda} \tag{B.13}$$

For typical applications $\Delta\omega_o$ is $O[10^7]$, which implies that $\Delta\lambda/\lambda_{1_o} \sim 10^{-7}$ for the green wavelength of an Ar^+ laser (514 nm). Considering the geometry of the probe volume, equation (B.12) can be rewritten

$$\omega_2 - \omega_1 = \left[\Delta\omega_o + \frac{2u_{p_\perp}\sin(\gamma)}{\lambda}\right]. \qquad (B.14)$$

Here $u_{p_\perp}$ represents the component of the particle's velocity which is in the plane of the incident beams and perpendicular to their bisector. The resulting frequency of oscillation is typically $O[10^5 - 10^8]$, which is much lower than that of the individual Doppler signals due to each beam alone. This heterodyne effect is what makes LDV a practical reality. It should be noted that expression (B.14) is also independent of the scattering angle, and thus allows for convenient observation from any direction (usually determined by the experiment and the angular scattering intensity distribution).

Although not identical, the above derivation gives many results which are equivalent to a heuristic description whereby a moving particle scatters light from within a standing wave interference pattern. If two monochromatic coherent beams are crossed at a small angle, it is simple to show from wave mechanics that they will form a standing wave pattern known as an interference fringe which has a spacing $\lambda_{Doppler} = \lambda/2\sin(\gamma)$. As a particle moves through this fringe pattern, it will scatter light when it is within the regions of constructive interference and will remain dark in the regions of destructive interference, thus producing a temporal oscillation frequency of $u_{p_\perp}/\lambda_{Doppler}$.

It is also apparent from (B.14) that if there is no frequency shift between the original beams ($\Delta\omega_o = 0$), then the direction of the particle through the probe volume is indeterminate due to the fact that $\cos()$ is an even function. This can cause a problem in unsteady reversing flows as all negative samples will be mapped to a positive value. To alleviate this problem, a frequency shift is usually introduced into one of the two beams through the use of an acousto-optic (Bragg) cell. With this method, particles traveling through the opposite direction will simply produce a lower frequency, and the actual velocity can be obtained from $u_{p_\perp} = (f_{measured} - f_{shift})\lambda/2\sin(\gamma)$.

Particle sizing is performed by utilizing the linear relationship which exists between the phase shift $\Delta\sigma$ and the particle diameter. Considering for the moment the case of a

single dominant scattering component p (either reflection or first order refraction), then from equation (A.18),

$$
\begin{aligned}
\Delta\sigma &= \eta_2 - \eta_1 \\
&= \frac{2\pi}{\lambda}[\sin(\tau_2) - \sin(\tau_1) - mp(\sin(\tau_2') - \sin(\tau_1'))]D \qquad \text{(B.15)} \\
&= \frac{2\pi G(\tau_1, \tau_2, \tau_1', \tau_2')D}{\lambda}.
\end{aligned}
$$

The phase changes due to reflection and passage through a focal point have been omitted, due to the fact that they will be the same for the components for each beam and will hence cancel. If the distance to the receiver is large, then for a single fixed point in the receiver plane τ_1, τ_2, τ_1', and τ_2' will be fixed constants, giving a linear relationship between the particle size and the phase shift. With only one detector, however, it is impossible to distinguish a phase shift as there is no temporal frame of reference. This can be alleviated through the use of two detectors. The phase shift between two detectors a and b is then given by

$$
\phi_{ab} = \Delta\sigma_a - \Delta\sigma_b = \frac{2\pi}{\lambda}\left(G(\tau_{1_a}, \tau_{2_a}, \tau_{1_a}', \tau_{2_a}') - G(\tau_{1_b}, \tau_{2_b}, \tau_{1_b}', \tau_{2_b}')\right)D. \quad \text{(B.16)}
$$

If more than a single order is included, however, additional interference effects between the different order refractions and reflections result in a more complicated distribution pattern and creates high-frequency oscillations in the phase vs. size calibration curves. This difficulty can be ameliorated by collecting the light over a carefully selected aperture, which spatially averages the high-frequency oscillations and restores the linear phase/diameter relationship (Sankar and Bachalo, 1991).

References

Aerometrics, Inc. (1994). *Phase Doppler particle analyzer user's manual.* Aerometrics, Inc.

Armi, L. and Flament, P. (1985). Cautionary remarks on the spectral interpretation of turbulent flows. *J. Geophys. Res.*, 90(C6):11,779–11,782.

Atta, C. W. V. (1974). Sampling techniques in turbulence measurements. *Ann. Rev. Fluid. Mech.*, 6:75–91.

Auton, T. R. (1987). The lift force on a spherical body in a rotational flow. *J. Fluid Mech.*, 183:199–218.

Auton, T. R., Hunt, J. C. R., and Prudhomme, M. (1988). The force exerted on a body in inviscid unsteady non-uniform rotational flow. *J. Fluid Mech.*, 197:241–257.

Bachalo, W. D. (1980). Method for measuring the size and velocity of spheres by dual-beam light-scatter interferometry. *Appl. Optics*, 19(3):363–370.

Bachalo, W. D. (1994). Experimental methods in multiphase flows. *Int. J. Multiphase Flow*, 20, *suppl.*:261–295.

Bachalo, W. D. and Houser, M. J. (1984). Phase/doppler spray analyzer for simultaneous measurements of drop size and velocity distributions. *Opt. Engng.*, 23(5):583–590.

Bendat, J. S. and Piersol, A. G. (1986). *Random Data, 2nd ed.* John Wiley & Sons, New York.

Brown, G. L. and Roshko, A. (1974). On density effects and large structure in turbulent mixing layers. *J. Fluid Mech.*, 64:775–816.

Chein, R. and Chung, J. N. (1987). Effects of vortex pairing on particle dispersion in turbulent shear flows. *Int. J. Multiphase Flow*, 13:785–802.

Chein, R. and Chung, J. N. (1988). Simulation of particle dispersion in a two-dimensional mixing layer. *AIChE Journal*, 34:946–954.

Chung, J. N. and Troutt, T. R. (1988). Simulation of particle dispersion in an axisymmetric jet. *J. Fluid Mech.*, 186:199–223.

Corcos, G. M. and Lin, S. J. (1984). The mixing layer: deterministic models of a turbulent flow. part 2. the origin of the three-dimensional motion. *J. Fluid Mech.*, 139:67–95.

Corcos, G. M. and Sherman, F. S. (1984). The mixing layer: deterministic models of a turbulent flow. part 1. introduction and the two-dimensional flow. *J. Fluid Mech.*, 139:29–65.

Corrsin, S. and Lumley, J. (1956). On the equation of motion for a particle in turbulent fluid. *Appl. Sci. Res.*, 6:114–116.

Crowe, C. T. and Troutt, T. R. (1988). Particle mixing in free shear layers. *Prog. Energy Combust. Sci.*, 14:171–194.

D. C. Hammond, J. (1981). Deconvolution techniques for line-of-sight optical scattering measurement in axisymmetric sprays. *Appl. Optics*, 20:493.

Delhaye, J. M., Giot, M., and Riethmuller, M. L. (1981). *Thermohydraulics of two-phase systems for industrial design and nuclear engineering.* Hemisphere Publishing Company, Washington.

Dobbins, R. A., Crocco, L., and Glassman, I. (1963). Measurement of mean particle sizes of sprays from diffractively scattered light. *AIAA Journal*, pages 1882–1886.

Drain, L. E. (1980). *The laser Doppler technique.* John Wiley & Sons, New York.

Drew, D. A. (1983). Mathematical modeling of two-phase flow. *Ann. Rev. Fluid. Mech.*, 15:261–291.

Edwards, R. V. (1987). Report of the special panel on statistical particle bial problems in laser amemometry. *Jour. of Fluids Eng.*, 109:89–93.

Elghobashi, S. and Truesdell, G. C. (1993). On the two-way interaction between homogeneous turbulence and dispersed solid particles. i: Turbulence modification. *Phys. Fluids A*, 5:1790–1801.

Elghobashi, S. E. and Abou-Arab, T. W. (1983). A two-equation turbulence model for two-phase flows. *Phys. Fluids*, 26:931–938.

Fiedler, H. E. and Mensing, P. (1985). The plane turbulent shear layer with periodic excitation. *J. Fluid Mech.*, 150:281–309.

George, W. K. (1976). *The Accuracy of flow measurement by laser Doppler methods*, chapter Limitations to measuring accuracy inherent in the laser Doppler signal, pages 20–63. Skovlunde: Proceedings LDA-Symposium Copenhagen 1975, 1976.

Hecht, E. (1987). *Optics, 2nd ed.* Addison-Wesley Publishing Co., Reading, Massachusettes.

Hernan, M. A. and Jimenez, J. (1982). Computer analysisof a high-speed film of the plane turbulent mixing layer. *J. Fluid Mech.*, 119:323–345.

164

Hetsroni, G. and Sokolov, M. (1971). Distribution of mass, velocity, and intensity of turbulence in a two-phase turbulent jet. *J. Appl. Mech.*, 32(2):315–327.

Hinze, J. O. (1949). Critical speeds and sizes of liquid globules. *Appl. Sci. Res.*, A1:273–288.

Hinze, J. O. (1955). Fundamentals of the hydrodynamic mechanism of splitting in dispersion processes. *AIChE Journal*, 1(3):289–295.

Hinze, J. O. (1971). *Prog. heat/mass trans.*, volume 6, chapter Turbulent fluid and particle interaction, pages 433–452. Pergamon press.

Hinze, J. O. (1972). *Turbulence, 2nd Edition.* McGraw-Hill, Inc., New York.

Hjelmfelt, A. T. and Mockros, L. F. (1966). Motion of discrete particles in a turbulent fluid. *Appl. Sci. Res.*, 16:149–161.

Ho, C. and Huang, L. (1982). Subharmonics and vortex merging in mixing layers. *J. Fluid Mech.*, 119:443–473.

Ho, C. and Huerre, P. (1984). Perturbed free shear layers. *Ann. Rev. Fluid. Mech.*, 16:365–424.

Hottel, H. C., Sarofim, A., Vasalos, I. A., and Dalzell, W. H. (1970). Multiple scatter: camparison of theory with experiment. *J. Heat Transf.*, 92:285–291.

Hussain, A. K. M. F. and Zedan, M. F. (1978). Effects of the initial condition on the axisymmetric free shear layer: Effects of the initial momentum thickness. *Phys. Fluids*, 21:1100–1112.

Ibrahim, K. M., Werthimer, G. D., and Bachalo, W. D. (1990). Signal processing considerations for laser doppler and phase doppler applications. In *5th International Symposium on the Application of Laser Techniques of Fluid Mechanics*, Lisbon, Portugal.

Ishii, M. (1975). *Thermo-fluid dynamic theory of two-phase flow.* Eyrolles, Paris.

Keane, R. D. and Adrian, R. J. (1992). *Flow visualization and image analysis*, chapter Theory of cross-correlation analysis of PIV images, pages 1–25. Kluwer Academic Press, Dordrecht.

Kovasznay, L. S. G., Kibens, V., and Blackwelder, R. F. (1970). Large scale motion in the intermittent region of a turbulent boundary layer. *J. Fluid Mech.*, 41:283–325.

Kreid, D. K. (1974). Laser-doppler velocimeter measurements in non-uniform flow: error estimates. *Appl. Opt,*, 13(8):1872–1881.

Kulick, J. D., Fessler, J. R., and Eaton, J. K. (1993). On the interaction between particles and turbulence in a fully-developed channel flow in air. Technical Report MD-66, Stanford University; Thermosciences Division of Department of Mechanical Engineering.

Lasheras, J. C. and Choi, H. (1988). Three-dimensional instability of a plane free shear layer: an experimental study of the formation and evolution of streamwise vortices. *J. Fluid Mech.*, 189:53–86.

Lasheras, J. C. and Maxworthy, T. (1987). Structure of the vorticy field in a plane free shear-layer. In *Turbulent shear flows 5*, pages 124–133. Springer.

Lázaro, B. J. (1989). *Particle dispersion in turbulent free shear flows.* PhD thesis, University of Southern California.

Lázaro, B. J. and Lasheras, J. C. (1989). Particle dispersion in a turbulent, plane, free shear layer. *Phys. Fluids A*, 235:143–178.

Lázaro, B. J. and Lasheras, J. C. (1992a). Particle dispersion in the developing free shear layer. part 1. unforced flow. *J. Fluid Mech.*, 235:143–178.

Lázaro, B. J. and Lasheras, J. C. (1992b). Particle dispersion in the developing free shear layer. part 2. forced flow. *J. Fluid Mech.*, 235:179–221.

Longmire, E. K. and Eaton, J. K. (1992). Structure of a particle-laden round jet. *J. Fluid Mech.*, 236:217–257.

Lu, Q. Q., Fontaine, J. R., and Aubertin, G. (1993). A langrangian model for solid particles in turbulent flows. *Int. J. Multiphase Flow*, 19:347–367.

Marble, F. E. (1970). Dynamics of dusty gases. *Ann. Rev. Fluid. Mech.*, 2:397–447.

Martin, J. E. and Meiburg, E. (1994). The accumulation and dispersion of heavy particles in forced two-dimensional mixing layers. i: The fundamental and subharmonic cases. *Phys. Fluids*, 6:1116–1132.

Maxey, M. R., Chang, E. J., and Wang, L.-P. (1994). Simulation of interactions between microbubbles and turbulent flows. *Appl. Mech. Rev.*, 47(6).

Maxey, M. R. and Riley, J. J. (1983). Equation of motion for a small rigid sphere in a nonuniform flow. *Phys. Fluids*, 26(4).

McLaughlin, D. K. and Tiederman, W. G. (1973). Biasing correction for individual realization of laser anemometer measurements in turbulent flows. *Phys. Fluids*, 16:2082–2088.

Mei, R. (1992). An approximate expression for the shear lift force on a spherical particle at finite reynolds number. *Int. J. Multiphase Flow*, 18:145–147.

Mei, R., Adrian, R. J., and Hanratty, T. J. (1991). Particle dispersion in isotropic turbulence under stokes drag and basset force with gravitational settling. *J. Fluid Mech.*, 225:481–495.

Monkewitz, P. A. and Huerre, P. (1982). The influence of velocity ratio on the spatial instability of mixing layers. *Phys. Fluids*, 25:1137–43.

166

Naqwi, A., Durst, F., and Liu, X. (1991). Two optical methods for simultaneous measurement of particle size, velocity, and refractive index. *Appl. Optics*, 30(33):4949–4959.

Patnaik, P. C., Sherman, F. S., and Corcus, G. M. (1976). A numerical simulation of kelvin-hemholtz waves of finite amplitude. *J. Fluid Mech.*, 73:215–240.

Resnick, R. and Halliday, D. (1977). *Physics, 3rd ed.* John Wiley & Sons, New York.

Rightley, P. M. (1995). *Bubble dispersion and interphase coupling in a free shear flow.* PhD thesis, University of California, San Diego.

Riley, J. J. and Metcalfe, R. W. (1980). Direct numerical simulation of a perturbed turbulent mixing layer.

Saffman, P. G. (1965). The lift on a small sphere in a slow shear flow. *J. Fluid Mech.*, 22:385.

Sankar, S. V. and Bachalo, W. D. (1991). Response characteristics of the phase doppler particle analyzer for sizing spherical particles larger than the light wavelength. *Applied Optics*, 30(12):1487–1496.

Sankar, S. V., Inenaga, A. S., and Bachalo, W. D. (1992). Trajectory dependent scattering in phase doppler interferometry: Minimizing and eliminating sizing errors. In *Sixth International Symposium on the Application of Laser Techniques to Fluid Mechanics*, Lisbon, Portugal.

Sankar, S. V., Weber, B. J., Kamemoto, D. Y., and Bachalo, W. D. (1991). Sizing fine particles with the phase doppler interferoemtric technique. *Applied Optics*, 30(33):4914–4920.

Siegel, R. and Howell, J. R. (1981). *Thermal radiation heat transfer, 2nd ed.* Hemisphere Publishing Corporation, Washington.

Soo, S. L. (1967). *Fluid dynamics of multi-phase systems.* Blaisdell, Waltham, Massachusetts.

Squires, K. D. and Eaton, J. K. (1990). Particle response and turbulence modification in isotropic turbulence. *Phys. Fluids*, pages 1191–1203.

Sridhar, G. and Katz, J. (1995). Drag and lift forces on microscopic bubbles entrained by a vortex. *Phys. Fluids*, 7(2):389–399.

Stock, D. E., Jurewicz, J. T., Crowe, C. T., and Eschback, J. E. (1975). Measurement of both gas and particle velocity in turbulent two-phase flow. In *Proc. 4th Biennial Symposium of Turbulence in Liquids*, Princeton, New Jersey.

Swithenbank, J., Beer, J. M., Taylor, D. S., Abbot, D., and McCreath, G. C. (1977). *Experimental diagnostics in gas phase combustion systems*, volume 53 of *Progess in Astronautics and Aeronautics*, chapter A laser diagnostic technique for the measurement of droplet and particle size distribution, pages 420–447. AIAA.

Tchen, C. M. (1947). *Mean value and correlation problems connected with the motion of small particles suspended in a turbulent fluid.* PhD thesis, Delft.

Tennekes, H. and Lumley, J. L. (1972). *A first course in turbulence.* The MIT Press, Cambridge, Massachusettes.

van de Hulst, H. C. (1981). *Light scattering by small particles.* Dover Publications, Inc., New York.

Viollet, P. L. and Simonin, O. (1994). Modelling dispersed two-phase flows: closure, validation and software development. *Appl. Mech. Rev.*, 47(6):S80–S84.

Wang, L.-P. and Maxey, M. R. (1993a). Interactions of heavy particles with small-scale flow structures in homogeneous isotropic turbulence. In *Proc. 5th Intl. Symp. on Gas-solid Flows*, Washington, D.C.

Wang, L.-P. and Maxey, M. R. (1993b). Settling velocity and concentration distribution of heavy particles in homogeneous isotropic turbulence. *J. Fluid Mech.*, 256:27–68.

Winant, C. D. and Browand, F. K. (1974). Vortex pairing: The mechanism of turbulent mixing-layer growth at moderate renolds number. *J. Fluid Mech.*, 63:237–255.

Woodward, D. H. (1964). Multiple light scattering by spherical dielectric particles. *J. Opt. Soc. Am.*, 54(11):1325–1331.

Wygnanski, I. and Fiedler, H. E. (1970). The two-dimensional mixing region. *J. Fluid Mech.*, 41:327–361.

Yang, Z. and Karlsson, S. (1991). Evolution of coherent structures in a plane shear layer. *Phys. Fluids A*, 3:2207–2219.

Yeh, H. and Cummins, H. Z. (1964). Localized fluid flow measurements with he-ne laser spectrometer. *Appl. Phys. Lett.*, 4:176.